

**THERMAL AND ELECTROCHEMICAL MODELS FOR BATTERIES  
DURING HIGH RATES OF DISCHARGE**

A Resubmitted Final Report

For

ONR Grant N00014-98-1-0554

USC Account Number 15510 F102

By

**John W. Van Zee, Ph.D.**  
**Professor**  
**Department of Chemical Engineering**  
**University of South Carolina**  
**Columbia, SC 29208**

Phone: (803) 777-2285  
Fax: (803) 777-8142  
Email: [vanzee@enr.sc.edu](mailto:vanzee@enr.sc.edu)

**August 15, 2004**

Prepared for

**Program Officer; Code 33**  
**Office of Naval Research**  
**Ballston Center Tower One**  
**800 North Quincy Street**  
**Arlington, VA 22217-5660**

20040917 129

REPORT DOCUMENTATION PAGE					Form Approved OMB No. 0704-0188	
The public reporting burden for this collection of information is estimated to average 1 hour per response, including the time for reviewing instructions, searching existing data sources, gathering and maintaining the data needed, and completing and reviewing the collection of information. Send comments regarding this burden estimate or any other aspect of this collection of information, including suggestions for reducing the burden, to Department of Defense, Washington Headquarters Services, Directorate for Information Operations and Reports (0704-0188), 1215 Jefferson Davis Highway, Suite 1204, Arlington, VA 22202-4302. Respondents should be aware that notwithstanding any other provision of law, no person shall be subject to any penalty for failing to comply with a collection of information if it does not display a currently valid OMB control number.						
PLEASE DO NOT RETURN YOUR FORM TO THE ABOVE ADDRESS.						
1. REPORT DATE (DD-MM-YYYY) 15-08-2004		2. REPORT TYPE FINAL TECHNICAL			3. DATES COVERED (From - To) 01-MAY-98 - 31-DEC-01-	
4. TITLE AND SUBTITLE  THERMAL AND ELECTROCHEMICAL MODELS FOR BATTERIES DURING HIGH RATES OF DISCHARGE				5a. CONTRACT NUMBER		
				5b. GRANT NUMBER N00014-98-1-0554		
				5c. PROGRAM ELEMENT NUMBER		
6. AUTHOR(S)  Van Zee, John, W., Ph.D.				5d. PROJECT NUMBER 98PR05313-00		
				5e. TASK NUMBER		
				5f. WORK UNIT NUMBER		
7. PERFORMING ORGANIZATION NAME(S) AND ADDRESS(ES)  University of South Carolina Office of Sponsored Programs 901 Sumter Street, Columbia, SC 29208					8. PERFORMING ORGANIZATION REPORT NUMBER 15510-F102	
9. SPONSORING/MONITORING AGENCY NAME(S) AND ADDRESS(ES) Office of Naval Research Regional Office Atlanta 100 Alabama Street NW Suite 4R15 Atlanta, GA 30303-3104					10. SPONSOR/MONITOR'S ACRONYM(S) ONR	
					11. SPONSOR/MONITOR'S REPORT NUMBER(S)	
12. DISTRIBUTION/AVAILABILITY STATEMENT Approval for Public Release; Distribution is Unlimited						
13. SUPPLEMENTARY NOTES This report is resubmitted because the final report that was not received by ONR in 2002.						
14. ABSTRACT The first of the three parts of this work documents the effort toward the original objective of the grant: understanding how commercial software could be modified to understand the three dimensional thermal and electrochemical gradients in a silver/zinc battery during high rates of discharge. This objective had broad applications for accelerated design of new batteries if we could use the mathematical solvers in commercial software packages because these software packages have automatic grid generation procedures. Unfortunately the state of the art of those software packages in 2000 required extensive custom modification and we concluded that the complex models of battery required too much computation time to be useful for transient behavior of the Ag/Zn system. The second part documents where an understanding of the 3-D transient behavior can be obtained with commercial software modified to account for the electrochemistry. The third part of this report documents the experimental work on transient behavior of fuel cells. In this third part, we were able to demonstrate how complete 3-D models may lead to improved design and operation.						
15. SUBJECT TERMS  <b>BEST AVAILABLE COPY</b>						
16. SECURITY CLASSIFICATION OF:			17. LIMITATION OF ABSTRACT  UU	18. NUMBER OF PAGES  231	19a. NAME OF RESPONSIBLE PERSON John W. Van Zee, Ph.D.	
a. REPORT  U	b. ABSTRACT  U	c. THIS PAGE  U			19b. TELEPHONE NUMBER (Include area code) 803-777-2285	

## Table of Contents

<b><u>Topic</u></b>	<b><u>Page</u></b>
<b>FORM SF 298.....</b>	<b>2</b>
<b>Summary.....</b>	<b>3</b>
<b><u>Part I: Models and Predictions for the Ag/Zn Battery.....</u></b>	<b><u>4</u></b>
Presentation at the Electrochemistry S&T Review for ONR & AFOSR February 14-16, 2000.....	5
Prediction of Performance and Temperature Rise of a Silver-Zinc Cell During Discharge: A Mathematical Model.....	20
<b><u>Part II: Models and Predictions for the Fuel Cells.....</u></b>	<b><u>99</u></b>
Predicting the Energy Transport Inside A Serpentine Flow-Field PEM Fuel Cell.....	100
Predicting The Transient Response Of A Serpentine Flow-Field PEMFC. I: Excess To Normal Fuel And Air.....	151
Predicting The Transient Response Of A Serpentine Flow-Field PEMFC. II: Normal To Minimal Fuel And Air.....	182
Advances in Computational Fluid Dynamics Modeling for PEM Fuel Cells.....	200
<b><u>Part III: Experimental Observations of the Transient Behavior of Fuel Cells.....</u></b>	<b><u>207</u></b>
The Effect of Stoichiometry on Dynamic Behavior of a Proton Exchange Membrane Cell (PEMFC) During Load Change.....	208
The Effect of Reservoirs and Fuel Dilution on the Dynamic Behavior of a PEMFC.....	220
<b>Distribution List.....</b>	<b>230</b>
<b><u>END OF REPORT.....</u></b>	<b><u>231</u></b>

REPORT DOCUMENTATION PAGE					Form Approved OMB No. 0704-0188	
<p>The public reporting burden for this collection of information is estimated to average 1 hour per response, including the time for reviewing instructions, searching existing data sources, gathering and maintaining the data needed, and completing and reviewing the collection of information. Send comments regarding this burden estimate or any other aspect of this collection of information, including suggestions for reducing the burden, to Department of Defense, Washington Headquarters Services, Directorate for Information Operations and Reports (0704-0188), 1215 Jefferson Davis Highway, Suite 1204, Arlington, VA 22202-4302. Respondents should be aware that notwithstanding any other provision of law, no person shall be subject to any penalty for failing to comply with a collection of information if it does not display a currently valid OMB control number.</p> <p><b>PLEASE DO NOT RETURN YOUR FORM TO THE ABOVE ADDRESS.</b></p>						
1. REPORT DATE (DD-MM-YYYY) 15-08-2004		2. REPORT TYPE FINAL TECHNICAL			3. DATES COVERED (From - To) 01-MAY-98 - 31-DEC-01-	
4. TITLE AND SUBTITLE  THERMAL AND ELECTROCHEMICAL MODELS FOR BATTERIES DURING HIGH RATES OF DISCHARGE					5a. CONTRACT NUMBER	
					5b. GRANT NUMBER N00014-98-1-0554	
					5c. PROGRAM ELEMENT NUMBER	
6. AUTHOR(S)  Van Zee, John, W., Ph.D.					5d. PROJECT NUMBER 98PR05313-00	
					5e. TASK NUMBER	
					5f. WORK UNIT NUMBER	
7. PERFORMING ORGANIZATION NAME(S) AND ADDRESS(ES)  University of South Carolina Office of Sponsored Programs 901 Sumter Street, Columbia, SC 29208					8. PERFORMING ORGANIZATION REPORT NUMBER 15510-F102	
9. SPONSORING/MONITORING AGENCY NAME(S) AND ADDRESS(ES) Office of Naval Research Regional Office Atlanta 100 Alabama Street NW Suite 4R15 Atlanta, GA 30303-3104					10. SPONSOR/MONITOR'S ACRONYM(S) ONR	
					11. SPONSOR/MONITOR'S REPORT NUMBER(S)	
12. DISTRIBUTION/AVAILABILITY STATEMENT Approval for Public Release; Distribution is Unlimited						
13. SUPPLEMENTARY NOTES This report is resubmitted because the final report that was not received by ONR in 2002.						
14. ABSTRACT The first of the three parts of this work documents the effort toward the original objective of the grant: understanding how commercial software could be modified to understand the three dimensional thermal and electrochemical gradients in a silver/zinc battery during high rates of discharge. This objective had broad applications for accelerated design of new batteries if we could use the mathematical solvers in commercial software packages because these software packages have automatic grid generation procedures. Unfortunately the state of the art of those software packages in 2000 required extensive custom modification and we concluded that the complex models of battery required too much computation time to be useful for transient behavior of the Ag/Zn system. The second part documents where an understanding of the 3-D transient behavior can be obtained with commercial software modified to account for the electrochemistry. The third part of this report documents the experimental work on transient behavior of fuel cells. In this third part, we were able to demonstrate how complete 3-D models may lead to improved design and operation.						
15. SUBJECT TERMS						
16. SECURITY CLASSIFICATION OF:			17. LIMITATION OF ABSTRACT		18. NUMBER OF PAGES	
a. REPORT U	b. ABSTRACT U	c. THIS PAGE U	UU		231	
					19a. NAME OF RESPONSIBLE PERSON John W. Van Zee, Ph.D.	
					19b. TELEPHONE NUMBER (Include area code) 803-777-2285	



## Summary

This report describes the accomplishments obtained at the University of South Carolina for ONR Grant N00014-98-1-0554, entitled "Thermal and Electrochemical Models for Batteries during High Rates of Discharge." This report is resubmitted because the final report that was not received by ONR in 2002. Copies of that original report have not been found and the PI has reconstructed that report as documented below. During this reconstruction, the most recent internal reports, documents, and published papers were included here.

This report consists of three parts. The first part documents the effort toward the original objective of the grant: understanding how commercial software could be modified to understand the three dimensional thermal and electrochemical gradients in a silver/zinc battery during high rates of discharge. This objective had broad applications for accelerated design of new batteries if we could use the mathematical solvers in commercial software packages because these software packages have automatic grid generation procedures. These grid generation packages that allow for direct importation of electronic drawings of material parts and thereby reduce the complexity and the delivery time of predictions of performance. Unfortunately during the second year of the grant, those software packages required extensive custom modification and we concluded that the complex models of battery required too much time to be useful for transient behavior. The conclusion from this part of the grant was that approximation models should be used at that time (i.e., FY 2000) for the Ag/Zn system.

The second part documents the work where an understanding of the 3-D transient behavior can be obtained with commercial software modified to account for the electrochemistry. In this part of the grant, we switched mathematical solvers and software from these based on finite element techniques to those based on control volume techniques. Here we were successful in demonstrating that with relative ease, subroutines can be written that allow a relatively seamless transfer from electronic drawings of fuel cell components to numerical predictions of the performance of those components.

The third part of this report documents the experimental work on transient behavior of fuel cells. These experiments were initiated during the final year of the no-cost extension. The experiments were suggested by the numerical predictions of part two. The most outstanding feature of this work is the prediction and subsequent experimental observation of second-order phenomena during changes in the load of the fuel cell. These might be experienced during acceleration of a vehicle and these results were unexpected. These predictions could not be observed with less complex models. Thus, in this third part, we were able to demonstrate how complete 3-D models may lead to improved design and operation.

**Long-term Research Objective:** The long-term objective of this project was to develop computer-based design tools that can be used to reduce the cost and delivery time for batteries. We sought to change the paradigm for the development of new battery designs *from* one based solely on expensive trial & error building of prototypes *to* a methodology that is aided by computer simulations of new designs. These tools will reduce the time required to have a mission- ready battery or fuel cell once newly developed materials and chemistries are developed. The methodology captures the three-dimensional aspects of the design and it allows for integration of the mechanical engineering of the battery or fuel cell and system components with predictions of the thermal and electrochemical behavior. The methodology is based on a fundamental understanding of the rate processes, the electrochemistry, and the thermal response of materials as verified with statistically designed experiments. We began with analyses of designs that manage the thermal characteristics of AgO-Zinc batteries during high rates of discharge. The methodologies developed here were then applied to PEM fuel cell designs.

## **Part I: Models and Predictions for the Ag/Zn Battery**

# Thermal and Electrochemical Models for Batteries Under High Rates of Discharge

John W. Van Zee



Department of Chemical Engineering  
University of South Carolina

J.W. Van Zee, Feb. 14-16, 2000  
Electrochemistry S&T Review for ONR & AFOSR

Department of Chemical Engineering  
University of South Carolina  
Columbia, SC 29208



## Objective

- Reduce the Cost & Delivery Time for New and Mission Specific Batteries
  - Develop Computer- Based Design Tools
  - 3-D Mathematical Models in Time
  - Integrate Thermal & Electrochemical Behavior
  - Integrate Mechanical Design of System & Components

J.W. Van Zee, Feb. 14-16, 2000  
Electrochemistry S&T Review for ONR & AFOSR

Department of Chemical Engineering  
University of South Carolina  
Columbia, SC 29208



## Methods

- Develop & Demonstrate Software Techniques
- Allow for Easy Upgrades
  - with Understanding of Electrochemistry
  - with New Materials
  - with New Missions
  - with New Size Constraints

J.W. Van Zee, Feb. 14-16, 2000  
Electrochemistry S&T Review for ONR & AFOSR

Department of Chemical Engineering  
University of South Carolina  
Columbia, SC 29208



## Outline: Two Battery Chemistries

### AgO-Zn

- Missions:
  - Targets, Mars Rover
- Problem: Rate Limited by Heat Transfer
- Solution: Test New Designs
  - Electrode Sizes
  - Tab Location
  - Battery Case Materials
  - Battery Case Size

### Li-ion

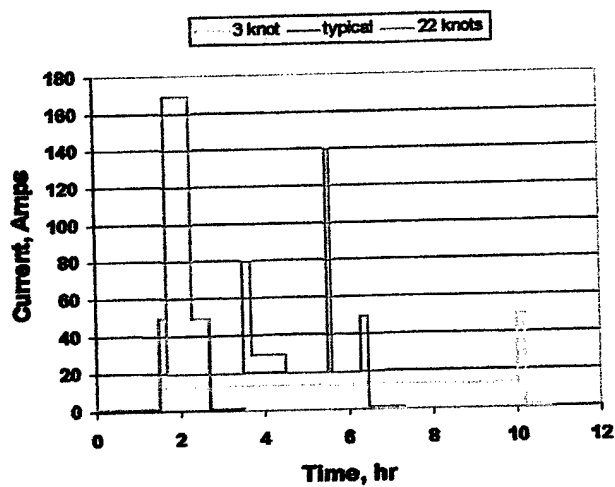
- Missions:
  - One Size Doesn't Fit All
- Problem: Low Rates, Developing Materials
- Solution: Test New Designs
  - Particle Size Distributions
  - Tab Locations
  - Thermal Management
    - -40C to 80C

J.W. Van Zee, Feb. 14-16, 2000  
Electrochemistry S&T Review for ONR & AFOSR

Department of Chemical Engineering  
University of South Carolina  
Columbia, SC 29208



## Discharge Profiles



J.W. Van Zee, Feb. 14-16, 2000  
Electrochemistry S&T Review for ONR & AFOSR

Department of Chemical Engineering  
University of South Carolina  
Columbia, SC 29208



## Models for AgO-Zn Batteries

- Requirements of Model
- Electrode Reactions
- Prototype Battery
- Model Development
- Model Predictions
  - Concentration Distributions
  - Heat Generation Rates

J.W. Van Zee, Feb. 14-16, 2000  
Electrochemistry S&T Review for ONR & AFOSR

Department of Chemical Engineering  
University of South Carolina  
Columbia, SC 29208



## Model Requirements

- Determine Local Heat Generation Rates
  - function of  $x, y, z$  in a cell
  - function of plate position
  - function of time & discharge rate
  - function of cycle
  - function of charge rate
- For Heat Removal:
  - Consider Alternate Grid Designs
  - External Cooling

J.W. Van Zee, Feb. 14-16, 2000  
Electrochemistry S&T Review for ONR & AFOSR

Department of Chemical Engineering  
University of South Carolina  
Columbia, SC 29208



## Prototype Battery

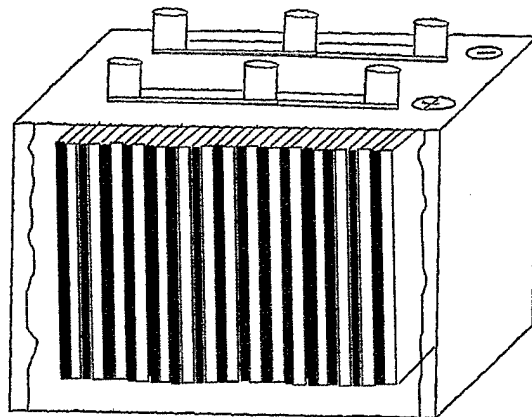
- 135 A-h Capacity
- 3-25 knots
- 50 -250 Amps                      10 -100 mA/cm<sup>2</sup>
- 250 V
- 168 cells @ 24 cells/case = 7 cases
- 15 in<sup>2</sup>
- Nylon, Cellophane, FRSC = 0.130 in.
- AgO, Zn thick. = 0.039, 0.060 in.

J.W. Van Zee, Feb. 14-16, 2000  
Electrochemistry S&T Review for ONR & AFOSR

Department of Chemical Engineering  
University of South Carolina  
Columbia, SC 29208



Schematic of a 135 A-hr Zn/AgO Battery  
(Only 15 of the 24 positive (Ag) and 25 negative (Zn) plates are shown  
separators not shown)

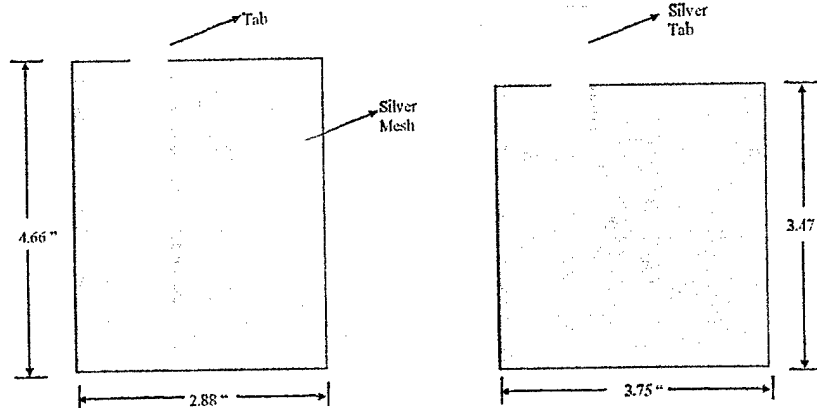


J.W. Van Zee, Feb. 14-16, 2000  
Electrochemistry S&T Review for ONR & AFOSR

Department of Chemical Engineering  
University of South Carolina  
Columbia, SC 29208



## Alternate Electrode Designs

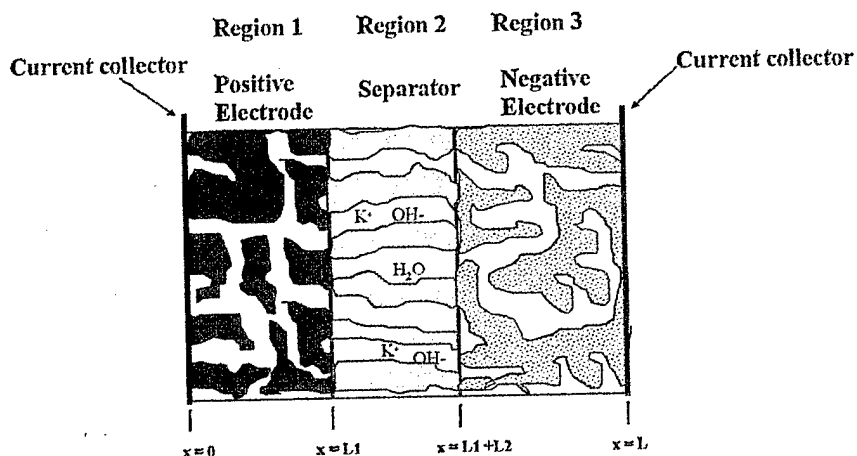


J.W. Van Zee, Feb. 14-16, 2000  
Electrochemistry S&T Review for ONR & AFOSR

Department of Chemical Engineering  
University of South Carolina  
Columbia, SC 29208



## Schematic of a silver-zinc cell.

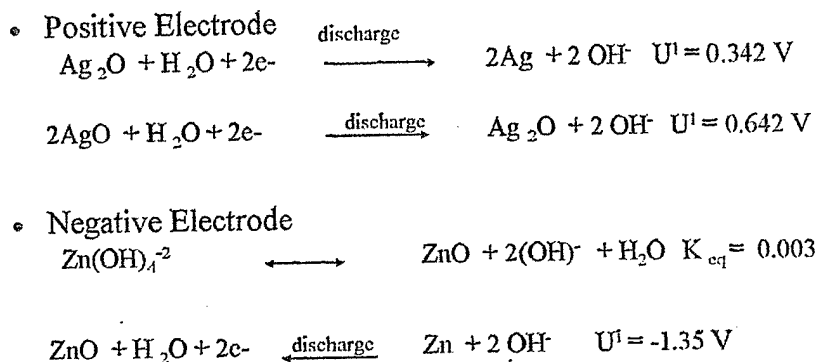


J.W. Van Zee, Feb. 14-16, 2000  
Electrochemistry S&T Review for ONR & AFOSR

Department of Chemical Engineering  
University of South Carolina  
Columbia, SC 29208



## Electrode Reactions



J.W. Van Zee, Feb. 14-16, 2000  
Electrochemistry S&T Review for ONR & AFOSR

Department of Chemical Engineering  
University of South Carolina  
Columbia, SC 29208





## Governing Equations- in Zn electrode

$$\varepsilon_{Zn} \frac{\partial C_{K^+}}{\partial t} = -\nabla \cdot N_{K^+}$$

$$\varepsilon_{Zn} \frac{\partial C_{OH^-}}{\partial t} = -\frac{a_{OH^-} i_n}{nF} - \nabla \cdot N_{OH^-} + 2R$$

$$\varepsilon_{Zn} \frac{\partial C_{Zn(OH)_4^{2-}}}{\partial t} = -\frac{a_{Zn(OH)_4^{2-}} i_n}{nF} - \nabla \cdot N_{Zn(OH)_4^{2-}} - R$$

J.W. Van Zee, Feb. 14-16, 2000  
Electrochemistry S&T Review for ONR & AFOSR

Department of Chemical Engineering  
University of South Carolina  
Columbia, SC 29208



## One-dimensional flux expression

$$\frac{N_i}{\varepsilon} = -\frac{D_i}{\tau} \frac{\partial C_i}{\partial x} - \frac{Fz_i D_i C_i}{\tau RT} \frac{\partial \phi}{\partial x}$$

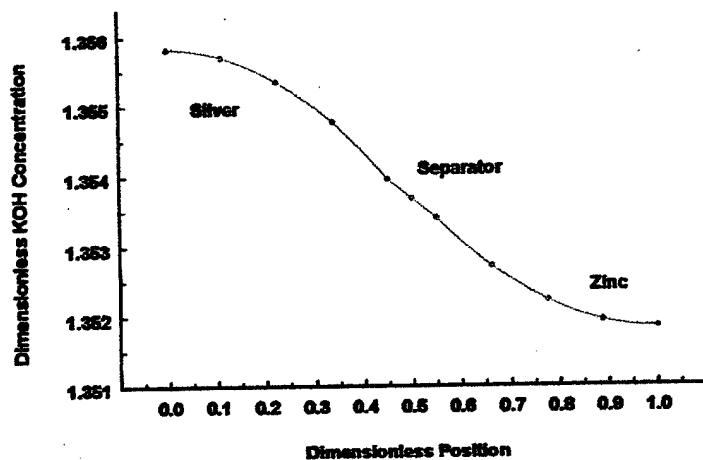
## Butler-Volmer Equation; Porous Media

J.W. Van Zee, Feb. 14-16, 2000  
Electrochemistry S&T Review for ONR & AFOSR

Department of Chemical Engineering  
University of South Carolina  
Columbia, SC 29208



## First Principles Model - KOH Profile

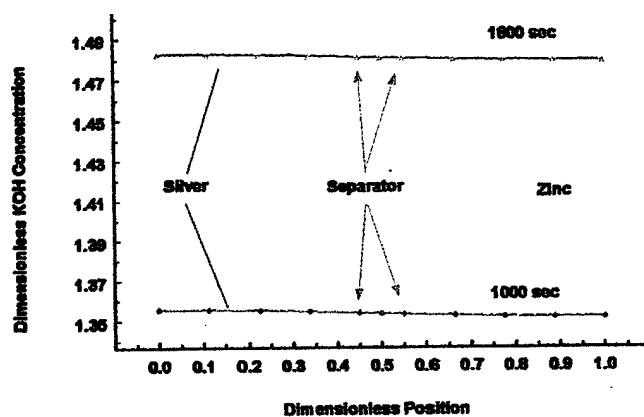


J.W. Van Zee, Feb. 14-16, 2000  
Electrochemistry S&T Review for ONR & AFOSR

Department of Chemical Engineering  
University of South Carolina  
Columbia, SC 29208



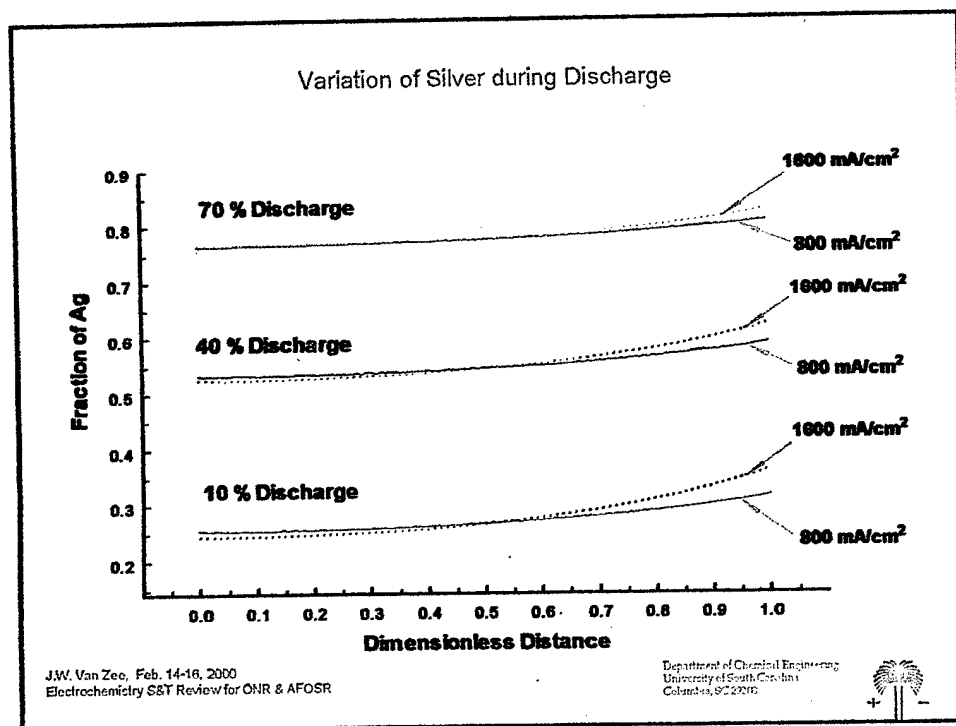
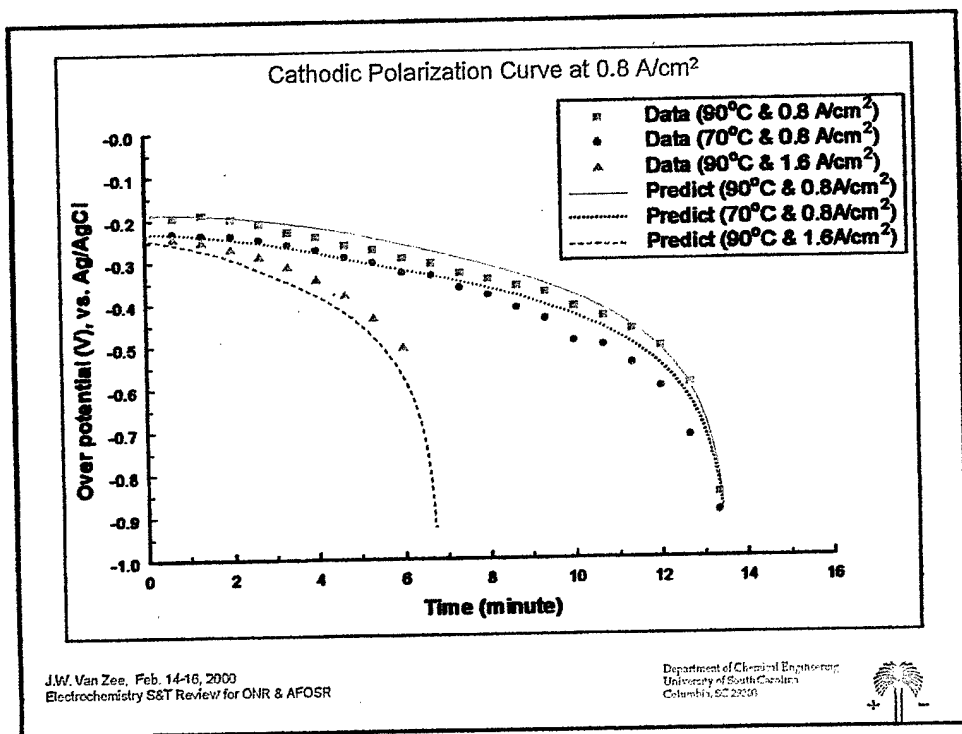
## - Transient KOH Profiles

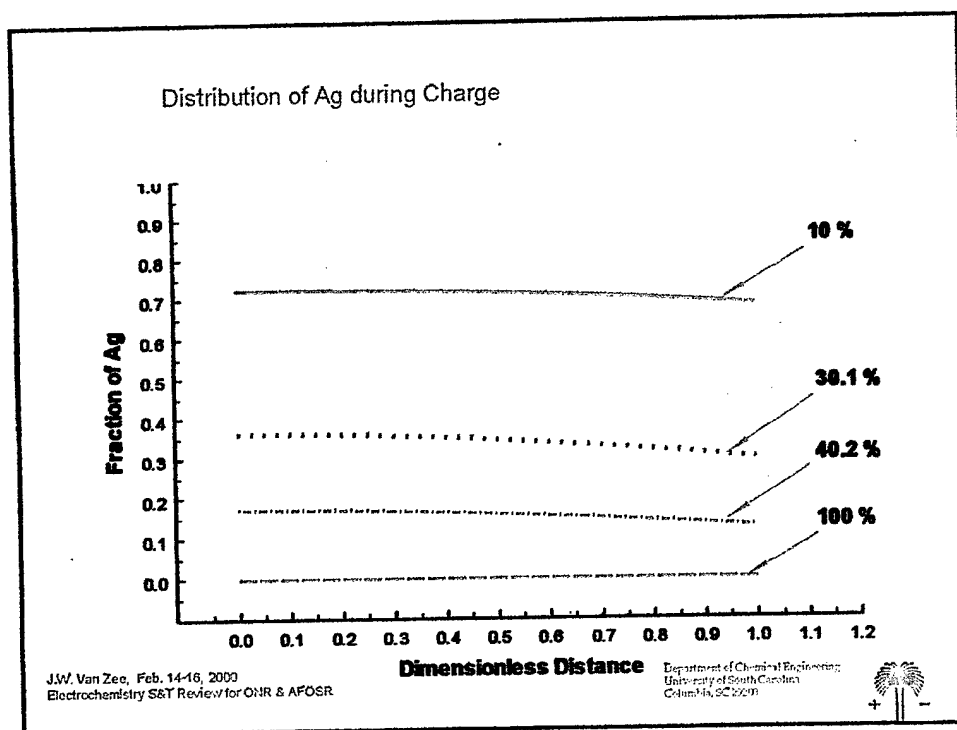
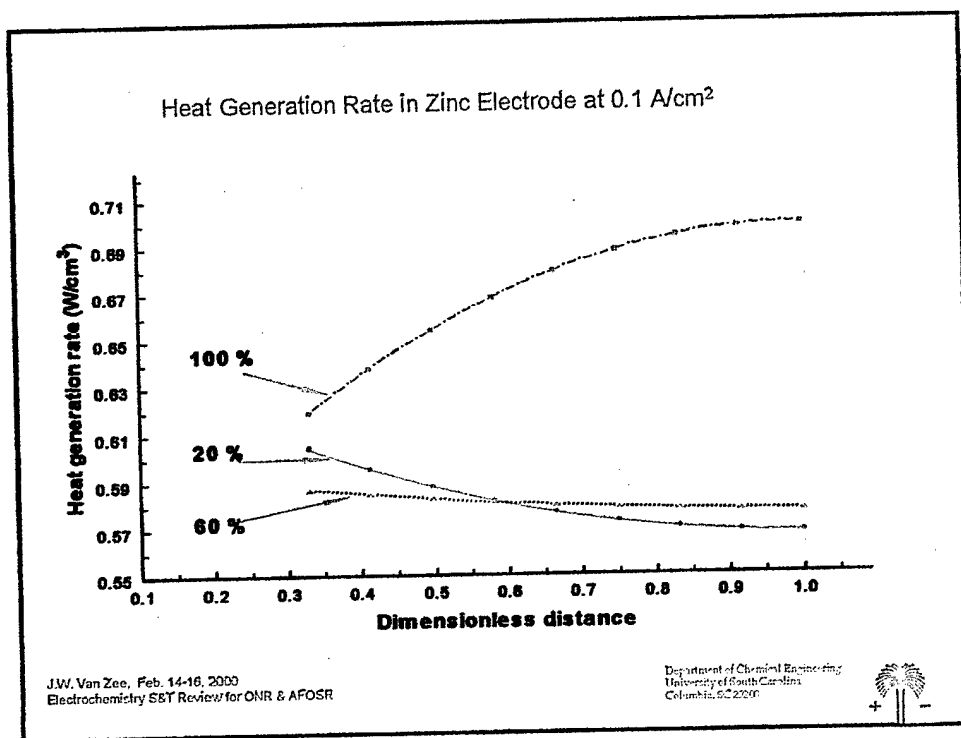


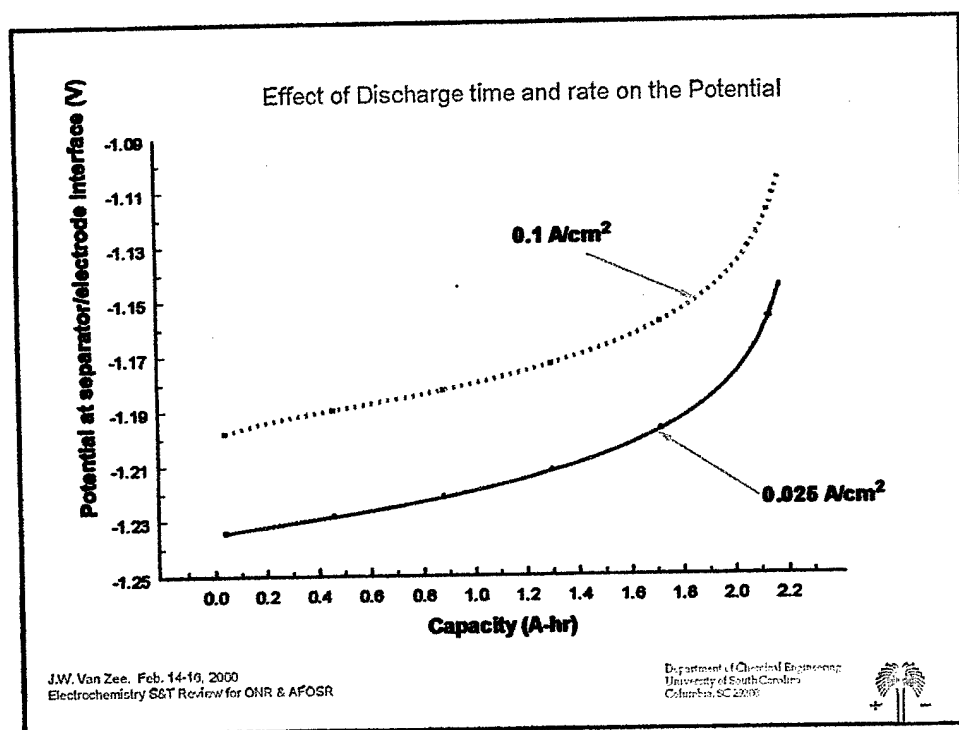
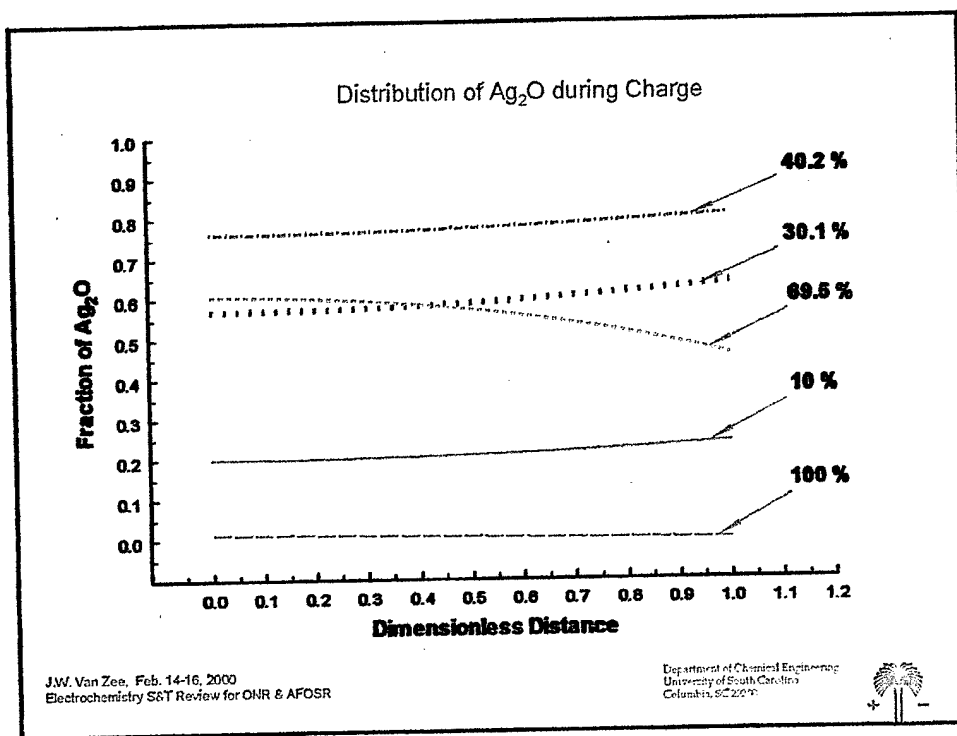
J.W. Van Zee, Feb. 14-16, 2000  
Electrochemistry S&T Review for ONR & AFOSR

Department of Chemical Engineering  
University of South Carolina  
Columbia, SC 29208

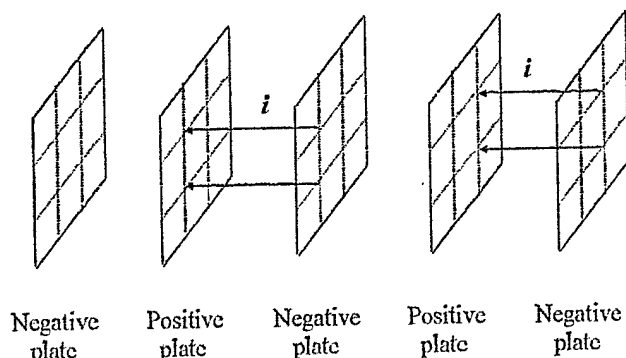








## Cell Design and Computation Scheme

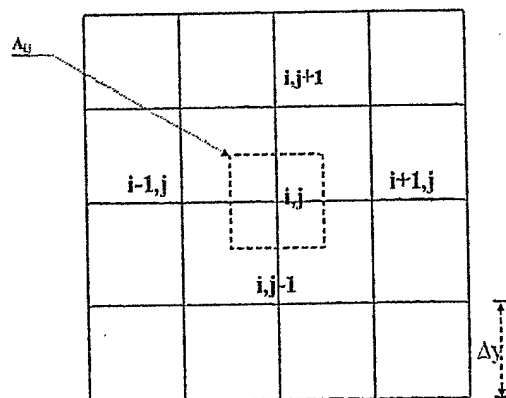


J.W. Van Zee, Feb. 14-16, 2000  
Electrochemistry SST Review for ONR & AFOSR

Department of Chemical Engineering  
University of South Carolina  
Columbia, SC 29208



## Schematic of the grid

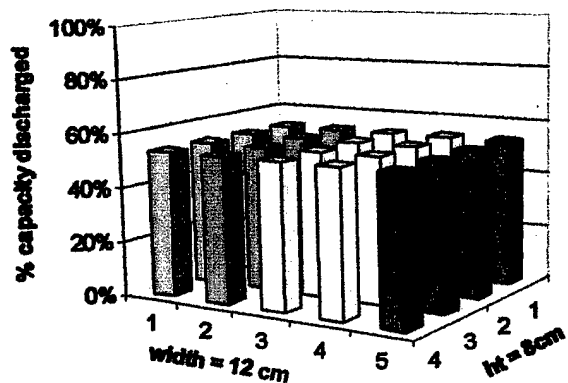


J.W. Van Zee, Feb. 14-16, 2000  
Electrochemistry SST Review for ONR & AFOSR

Department of Chemical Engineering  
University of South Carolina  
Columbia, SC 29208



### Distribution of Capacity in Grid Plane at 3 knots

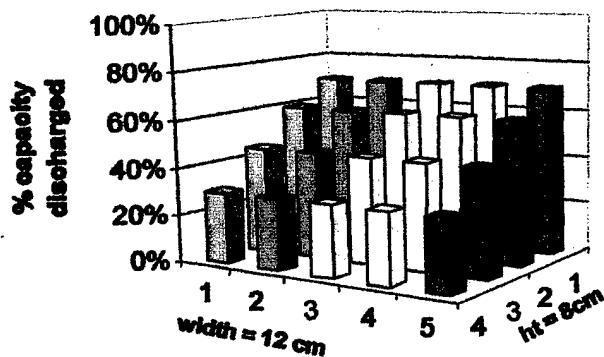


J.W. Van Zee, Feb. 14-16, 2000  
Electrochemistry S&T Review for ONR & AFOSR

Department of Chemical Engineering  
University of South Carolina  
Columbia, SC 29208



### Distribution of Capacity in Grid Plane at 0.1 A/cm<sup>2</sup>



J.W. Van Zee, Feb. 14-16, 2000  
Electrochemistry S&T Review for ONR & AFOSR

Department of Chemical Engineering  
University of South Carolina  
Columbia, SC 29208



## Summary & Future Work

- First Principles Model Developed
- Local Isothermal Heat Generation Predicted
- Include Temperature Feedback
  - Kinetics, conductivity, thermodynamics
- Extend to 3-D Current Distribution
- Solve 3-D Temperature Distribution

J.W. Van Zee, Feb. 14-16, 2000  
Electrochemistry S&T Review for ONR & AFOSR

Department of Chemical Engineering  
University of South Carolina  
Columbia, SC 29208



## Information Technology Design Tools

### Dynamic Load Scenario

**Desired System Performance**  
**Mission Specific**

### Design Specifications

**Fixed Geometry**  
**Fixed Average Capacity**  
**Fixed Power or Rates**

### Constraints: Cost

**Manufacturing Equipment**  
**Manufacture's Paradigm**  
**Materials**

### IT Constraints:

**Model Developers: 1-D**  
**I/O Interfaces not Standard**  
**Rapid Solutions of Equations**

J.W. Van Zee, Feb. 14-16, 2000  
Electrochemistry S&T Review for ONR & AFOSR

Department of Chemical Engineering  
University of South Carolina  
Columbia, SC 29208





## How commercial software may speed development

### Ex: Finite Element Package

#### **Advantages:**

- Input Mechanical Drawing
- Generates Grid
- Equation Solver Efficient
- Heat Transfer (3D in Time)
- Familiarity
- Standard Input/Output

#### **Disadvantages**

- Need Subroutines for Electrochemical Equations

J.W. Van Zee, Feb. 14-16, 2000  
Electrochemistry S&T Review for ONR & AFOSR

Department of Chemical Engineering  
University of South Carolina  
Columbia, SC 29208



## Acknowledgments

- Naval Underwater Warfare Center, Newport  
S. Tucker, E. Dow, C. Egan, M. Mederios
- J.R. Moden, JRM Inc., Bristol, RI
- Woo-kum Lee, USC
- R. Spotnitz, Battery Design Co.,  
Pleasanton, CA
- Danielle Brooks, NCA&T

J.W. Van Zee, Feb. 14-16, 2000  
Electrochemistry S&T Review for ONR & AFOSR

Department of Chemical Engineering  
University of South Carolina  
Columbia, SC 29208



**Prediction of Performance and Temperature Rise of a Silver-Zinc Cell  
During Discharge: A Mathematical Model**

**Van Zee Group Technical Memorandum # 9**

**By**

**Murali Venkatraman and J.W. Van Zee**

**January 1, 2002**

### **Abstract**

A mathematical model has been developed to study the performance and thermal behavior of the silver-zinc cell during discharge. It has been shown that the rates of reactions in the cathode (silver electrode) could be used to explain the cell-voltage – time curve. A reaction front is observed in the anode (zinc electrode) and a study of influence of parameters (the exchange current density, initial electrolyte concentration and diffusivity of OH<sup>-</sup> ions) have been presented. The temperature rise for cell stack was predicted with the heat generation rates calculated through one-dimensional model. Dilute solution theory and Newman's macro homogenous theory of porous electrodes were used to predict the results.

## Model development

The assumptions needed to develop the model are presented first, followed by a discussion on the formulation of governing equations and boundary conditions.

### Assumptions:

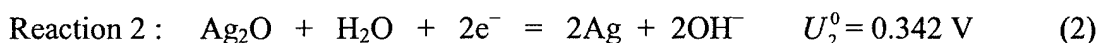
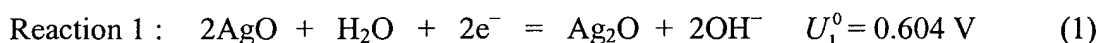
The schematic of a single cell is given in Fig.1. It features a cathode made of silver-silver(I) oxide-silver(II) oxide ( $\text{Ag-Ag}_2\text{O-AgO}$ ). The separator material used is a combination of nylon, cellophane and FRSC, with a wrap of each material one above the other forming a three layer structure. But for the modeling purposes, the separator will be considered a single entity with average properties. To the right of the separator is the anode made of zinc-zinc oxide ( $\text{Zn-ZnO}$ ). Himy [24] gives a good description about the preparation of the two electrodes emphasizing that the reproducibility in case of zinc electrode preparation is low. This justifies the investigation of the parameters especially the specific surface area ( $a$ ), the exchange current density ( $i_0$ ) and open circuit potential for the anode. It is also assumed in the present that the single cell under study is adiabatic (i.e. thermally insulated from the ambience) and hence the temperature rise we may expect from the model is the highest one may encounter.

The length ( $L$ ) and width ( $W$ ) are very large compared to the gap between the electrodes. The model considers one-dimension for the transport between the electrodes. A good reason for not considering the multi-dimensional problems presently is the high thermal and electrical conductivities of the materials involved in the cell. When the cell discharges, the cathode gets richer in silver and this increases the conductivity. At any point of time the anode has silver oxides and/or silver which are highly conductive. However the case is not the same with the anode. The zinc oxide formed during the

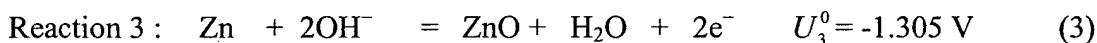
course of discharge is an insulator, but there is always excess zinc in the cathode by design. This ensures that the conductivity of the cathode matrix is high always. It is also assumed that the Nernst-Einstein relation ( $u_i = D_i/RT$ ) relates the mobility of ionic species to the diffusion coefficient and that Butler-Volmer kinetics would express the relations between the transfer currents and the overpotentials. Choi et al [11] have suggested a capacity correction factor to be added to the Butler-Volmer expression, but a more comprehensive expression was developed with more than just one correction factor.

#### Model:

On discharge, the following reactions are assumed to occur at the cathode:

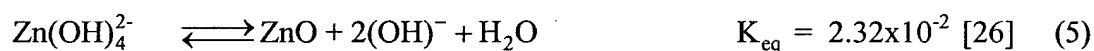


and in the anode:



The zinc electrode operates according to a dissolution-precipitation reaction mechanism.

The reaction mechanism is as follows:



During the discharge process of a battery, zinc is oxidized to  $\text{Zn}(\text{OH})_4^{2-}$ , zincate, which subsequently precipitates as zinc oxide. This, however is true, only when the solubility limit of zinc oxide is attained. Any further production of  $\text{Zn}(\text{OH})_4^{2-}$  at the electrode will result in the precipitation of ZnO from the solution. Problems associated with these solid

particles of ZnO are manifold. They not only affect the shape of the electrode, but also

This Page Left Blank Intentionally

the thermal and electrical conductivity adversely. Their high specific gravity settles them down causing an uneven distribution of ZnO and hence a non-uniform current distribution during charge. There is another dimension to this problem. During discharge, the concentration of  $\text{OH}^-$ , decreases in the anode and increases in the cathode and this may influence the solubility of ZnO in KOH. In fact, local depletion of  $\text{OH}^-$  is the main reason for the loss in capacity (i.e. end of discharge) at very high rates as observed by us. This is because, the solution phase conductivity becomes so low, that the resistance to the passage of current becomes extremely high. However, any investigation into this phenomenon of ZnO precipitation and its shape change-effects, is out of the scope of the present work and effects of ZnO precipitation have been neglected. Also, it has been assumed that the solution is saturated with the zincate ion  $\text{Zn}(\text{OH})_4^{2-}$  always and does not have a role to play in the dynamics. A model based on the effects of precipitation and influence of zincate ion had already been proposed by Podlaha et al [26] for the  $\text{MnO}_2$  / Zn batteries. Thus  $\text{Zn}(\text{OH})_4^{2-}$  is not considered in the present model which also is supported by the fact that the  $K_{\text{eq}}$  is moderate for the precipitation reaction [26]. Future developments of the present model would incorporate the same as applicable. The simple model is obtained by combining equation (4) and equation (5) into one equation which is (3).

Hence we are left only with three reactions for consideration: two at the cathode and one at the anode. Newman's macro-homogenous model of porous electrodes along with the constitutive laws of dilute solution theory, are used to predict the profiles of various variables. The ions in the solution are  $\text{K}^+$ ,  $\text{OH}^-$  and  $\text{Zn}(\text{OH})_4^{2-}$ . The electrolyte is highly concentrated in  $\text{K}^+$  and  $\text{OH}^-$ , relative to the zincate ion and hence its contribution

is neglected. The interaction between the ions has been neglected which is another way of stating the usage of dilute solution theory. A more complete and rigorous approach would be to use concentrated solution theory [Appendix B], which could find place in the future work.

The macroscopic approach views the entire porous electrode as a superposition of two continua – the matrix that holds the active material and the solution residing in the pores. The species present mainly in the solution are  $K^+$ ,  $OH^-$  and  $Zn(OH)_4^{2-}$ . But as stated earlier, the zincate ion interference will be discarded and the solution be considered to be composed mainly of  $K^+$  and  $OH^-$  and treated as a binary electrolyte. Hence the respective flux equations are:

$$N_{K^+} = -\frac{\epsilon}{\tau}(D_{K^+}\nabla C_{K^+} - \frac{D_{K^+}Fz_{K^+}C_{K^+}}{RT}\nabla\phi_2) + C_{K^+}\mathbf{v} \quad (6)$$

$$N_{OH^-} = -\frac{\epsilon}{\tau}(D_{OH^-}\nabla C_{OH^-} - \frac{D_{OH^-}Fz_{OH^-}C_{OH^-}}{RT}\nabla\phi_2) + C_{OH^-}\mathbf{v} \quad (7)$$

The above two equations follow from dilute solution theory. Any convection inside the cell is considered negligible due mainly to the tight packing and hence the last term on the RHS is discarded (i.e.  $\mathbf{v} = 0$ ). Only the diffusion and migration fluxes contribute to the movement of species in the cell. The condition of electro-neutrality yields:

$$\sum z_i C_i = 0 \quad (8)$$

The binary electrolyte approximation along with electro-neutrality yields:

$$C_{K^+} = C_{OH^-} = C \quad (9)$$

This leads to a single concentration equation, which is devoid of the potential term [Appendix A].



$$\frac{\partial(\epsilon C)}{\partial t} = -\nabla \cdot \left( -\frac{\epsilon}{\tau} D_{eff} \nabla C \right) + \left( \frac{D_{eff}}{2D_{OH^-}} \right) R_{OH^-} \quad (10)$$

where

$$D_{eff} = \frac{2D_{K^+} D_{OH^-}}{D_{K^+} + D_{OH^-}} \quad (11)$$

In the equation (10),  $R_{OH^-,i}$  would account for the source term of  $OH^-$  in the  $i^{th}$  reaction.

For the discharge, the source term for  $OH^-$  is positive in the cathode, null in the separator and negative in the anode. The source term depends on the number of independent reactions occurring at the electrodes. In the positive electrode, there are two independent reactions (reactions 1 and 2) and hence two independent source terms for the production of  $OH^-$ . In the negative electrode, only one reaction (reaction 3) is considered important.

Hence:

$$R_{OH^-,Ag} = R_{OH^-,1} + R_{OH^-,2} \quad (12)$$

$$R_{OH^-,sep} = 0 \quad (13)$$

$$R_{OH^-,Zn} = R_{OH^-,3} \quad (14)$$

The individual source terms are given by:

$$R_{OH^-,1} = -\frac{a_{Ag} i_1 s_{OH^-,1}}{n_1 F} \quad (15)$$

$$R_{OH^-,2} = -\frac{a_{Ag} i_2 s_{OH^-,2}}{n_2 F} \quad (16)$$

$$R_{OH^-,3} = -\frac{a_{Zn} i_3 s_{OH^-,3}}{n_3 F} \quad (17)$$

where  $i_1, i_2$  and  $i_3$  are the local current densities for the electrode reactions 1,2 and 3;  
 $a_{Ag}$  and  $a_{Zn}$  are the surface area per unit volume of the silver and zinc electrodes;  $F$  is the faraday constant ;  $n_1, n_2$  and  $n_3$  are the number of electrons transferred in the reactions 1,2 and 3;  $s_{OH^-,1}, s_{OH^-,2}$  and  $s_{OH^-,3}$  are the stoichiometric coefficients of  $OH^-$  in the reactions 1,2 and 3;

For the silver electrode, the local current densities can be related by a Butler-Volmer type expression:

$$i_1 = i_{01} \left\{ \left( \frac{C_{OH^-}}{C_{OH^-}^b} \right)^2 \left( \frac{M_{Ag_2O}}{0.5 M_{Ag}^{tot}} \right) \exp\left( \frac{F\alpha_{a1}}{RT} \eta_1 \right) - \left( \frac{M_{AgO}}{M_{Ag}^{tot}} \right)^2 \exp\left( -\frac{F\alpha_{c1}}{RT} \eta_1 \right) \right\} \quad (18)$$

$$i_2 = i_{02} \left\{ \left( \frac{C_{OH^-}}{C_{OH^-}^b} \right)^2 \left( \frac{M_{Ag}}{M_{Ag}^{tot}} \right)^2 \exp\left( \frac{F\alpha_{a2}}{RT} \eta_2 \right) - \left( \frac{M_{Ag_2O}}{0.5 M_{Ag}^{tot}} \right) \exp\left( -\frac{F\alpha_{c2}}{RT} \eta_2 \right) \right\} \quad (19)$$

For the zinc electrode a similar expression is used:

$$i_3 = i_{03} \left\{ \left( \frac{C_{OH^-}}{C_{OH^-}^b} \right)^2 \left( \frac{M_{Zn}}{M_{Zn}^{tot}} \right) \exp\left( \frac{F\alpha_{a3}}{RT} \eta_3 \right) - \left( \frac{M_{ZnO}}{M_{Zn}^{tot}} \right) \exp\left( -\frac{F\alpha_{c3}}{RT} \eta_3 \right) \right\} \quad (20)$$

where

$$\eta_1 = \phi_1 - \phi_2 - U_1^0 \quad (21)$$

$$\eta_2 = \phi_1 - \phi_2 - U_2^0 \quad (22)$$

$$\eta_3 = \phi_1 - \phi_2 - U_3^0 \quad (23)$$

Here,  $i_{0i}$  is the equilibrium exchange current density,  $\alpha_{ai}$  and  $\alpha_{ci}$  are the anodic and cathodic transfer coefficients,  $\eta_i$  is the overpotential of the  $i^{th}$  electrodic reaction ;

$M_a$  - local molar density of the species 'a' ;  $M_{Zn}^{tot}$  is the molar density of total zinc

content (i.e. present as Zn and ZnO) ;  $M_{Ag}^{tot}$  is the molar density of total silver content (i.e. present as Ag, AgO and Ag<sub>2</sub>O) ;  $\phi_1$  - the matrix potential ;  $\phi_2$  - solution potential;  $R$  is the gas constant and  $T$  is the temperature of operation.

For the silver electrode, the normalization and the correction for the capacity are done against the total silver content of the electrode  $M_{Ag}^{tot}$ . This takes into account the decline in capacity as the discharge progresses. It is worth noting that the amount of silver in Ag<sub>2</sub>O is twice that of in Ag or AgO. Hence the normalization for Ag<sub>2</sub>O includes a 0.5 in the denominator. In case of zinc electrode, the normalization is relative to  $M_{Zn}^{tot}$ . Similar expressions for nickel electrode [11] and silver electrode [15] have been reported in literature. The  $(\frac{M_a}{M_a^{tot}})$  is a capacity term which takes into account the decline or increase of capacity during charge and discharge respectively where 'a' is the solid species involved in the reaction. The main difference between the above Butler-Volmer expressions and those already reported in the literature [11,15] is that, in our expression, the forward and backward reactions have two different capacity terms which are proportional to the reactants involved in the forward and backward reactions. As a result, the same model can be used to study both the charge and discharge behavior with only the sign of the cell current ( $i_{cell}$ ) reversed.

The superficial current density in the solution phase is the sum of the currents contributed by the individual ions.

$$i_2 = F \sum z_i N_i \quad (24)$$

This leads us to the following expression [Appendix B].

$$\mathbf{i}_2 = -\kappa \nabla \phi_2 - \frac{\varepsilon}{\tau} \mathbf{F} \sum z_i D_i \nabla C_i \quad (25)$$

where

$$\kappa = \frac{\varepsilon}{\tau} \frac{\mathbf{F}^2}{RT} \sum z_i^2 D_i C_i \quad (26)$$

is the effective conductivity of the solution phase. There is no contribution by convection and dispersion is negligible. The diffusion potential term in the expression for  $\mathbf{i}_2$  would vanish if the diffusion coefficients are equal. In our case they are not.

The extent of reaction is related to the superficial current density through the following expression:

$$\nabla \cdot \mathbf{i}_2 = ai \quad (27)$$

where  $i$  is the sum of the current densities of all the independent reactions in a particular region. In the silver electrode,

$$i = i_1 + i_2 \quad (28)$$

In the separator there is no reaction and hence  $i$  is zero. In the zinc electrode,

$$i = i_3 \quad (29)$$

For the matrix, the current density is related to the potential as follows:

$$\mathbf{i}_1 = -\sigma_{avg} \nabla \phi_1 \quad (30)$$

where  $\sigma$  is the effective electrical conductivity of the matrix and  $\phi_1$  is the potential in the matrix. The effective electrical conductivity of the matrix is obtained by considering parallel conduction paths and is given as:

$$\sigma = \sum \sigma_a m_a^\xi \quad (31)$$

where  $m_a$  is the mass fraction (defined over solid phase only) of the solid species 'a' and  $\xi$  being a empirical constant. It has been assumed that  $\xi=1.5$ , as has been conventional in the literature [26]. A current balance yields:

$$\mathbf{i}_1 + \mathbf{i}_2 = \mathbf{i}_{\text{cell}} \quad (32)$$

Divergence of the cell current is equal to zero and this yields the familiar relation :

$$\nabla \cdot \mathbf{i}_2 = -\nabla \cdot \mathbf{i}_1 = ai \quad (33)$$

The change of electrode porosity due to the electrode reaction is expressed as:

$$\frac{\partial \varepsilon}{\partial t} = \left( \sum_{\substack{\text{solid} \\ \text{phases}}} \frac{s_a M_a^w}{\rho_a n F} \right) \nabla \cdot \mathbf{i}_2 \quad (34)$$

The complete set of the equations with the boundary and initial conditions is provided in the tables (1-5). The parameters used in the simulation are given in table 6. A short discussion on the boundary conditions follows.

In our studies the electrode discharge behavior has been investigated. All were galvanostatic discharge studies and hence a constant cell current was used. But the model is flexible enough to pursue other studies like constant voltage and pulse discharge/charge. At the start of the simulation the porosity of the electrode and concentrations of the species in the solution are assumed to be uniform. Active material is also assumed uniformly distributed.

$$@t = 0, \text{ any } x, C_{\text{OH}^-} = C_{\text{OH}^-}^0 = C_0 \text{ and } \varepsilon = \varepsilon_0 \quad (35)$$

where  $C_{\text{OH}^-}^0$  or  $C_0$  is the initial concentration of  $\text{OH}^-$  and  $\varepsilon_0$  is the initial electrode porosity. At the back of the electrode the flux of the species is set to zero.

$$\nabla C_i = 0 \quad (36)$$

The potential in the solution is arbitrarily set to zero at the anode current collector.

Along with the current conservation it yields,

$$@x=0, \quad -\sigma \nabla \phi_1 = i_{\text{cell}} \quad (37)$$

$$@x=l_{Ag}+l_{sep}+l_{Zn}, \quad -\sigma \nabla \phi_1 = i_{\text{cell}} \quad (38)$$

$$@x=0, \quad \nabla \phi_2 = 0 \quad (39)$$

$$@x=l_{Ag}+l_{sep}+l_{Zn}, \quad \phi_2 = 0 \quad (40)$$

Continuity of fluxes along the interfaces is assumed as is conventional. The densities of the solid phases vary with state of discharge. The solid phases involved in our model are : Ag, Ag<sub>2</sub>O and AgO in the cathode and ZnO and Zn in the anode. At any point of time, mole balance shows:

$$2M_{Ag_2O} + M_{AgO} + M_{Ag} = M_{Ag}^{tot} \quad (41)$$

$$M_{ZnO} + M_{Zn} = M_{Zn}^{tot} \quad (42)$$

Since these relations apply, there are only two 3 independent variables and the variables we chose to work with are  $M_{AgO}$  and  $M_{Ag}$  for the silver electrode and  $M_{Zn}$  for the zinc electrode. The equations read:

$$\frac{\partial M_{AgO}}{\partial t} = \frac{-a_{AgO} i_1 s_{AgO,1}}{n_1 F} \quad (43)$$

$$\frac{\partial M_{Ag}}{\partial t} = \frac{-a_{Ag} i_2 s_{Ag,2}}{n_2 F} \quad (44)$$

$$\frac{\partial M_{Zn}}{\partial t} = \frac{-a_{Zn} i_3 s_{Zn,3}}{n_3 F} \quad (45)$$

A mass ratio  $\theta_1$ , of total zinc content to total silver content is defined since it is one of the factors that control the limiting capacity of the system. It is preferable to make

the cell ,silver limited and hence there is usually excess zinc in the system . The ratio  $\theta_1$  has been set to be 0.866 in accordance with Himy [24]. It is notable that the limiting capacity in such a case will be that of silver's. There is also another ratio  $\theta_2$  which characterizes the amount of silver in  $\text{Ag}_2\text{O}$  to amount of silver in  $\text{AgO}$ .  $\theta_2$  is set as  $\frac{1}{3}$  for the present simulation [25]. It is notable that  $\theta_2$  affects the open circuit potential of the system.

The only equation that is yet to be formulated is the energy equation. It can be written as:

$$(\rho c_p)_{avg} \frac{\partial T}{\partial t} = -\nabla \cdot (-k_{avg} \nabla T) + Q \quad (46)$$

In the above equation,  $\rho, c_p$  and  $k_{avg}$  are instantaneous values averaged on the composite material. They are given as ::

$$(\rho c_p)_{avg} = c_{p,l} \rho_l \varepsilon + (1-\varepsilon) \sum c_{p,s} \rho_s M_s^w M_s \quad (47)$$

$$k_{avg} = \sum_{all\ solids} k_s [(1-\varepsilon)w_s]^\xi + \sum_{all\ liquids} k_l [\varepsilon w_l]^\xi \quad (48)$$

where 's' corresponds to the solid species and  $l$  corresponds to the electrolyte. The thermal conductivity of the composite is also given by an expression similar to the electrical conductivity where  $w_s$  is the mass fraction (defined over all phases) of the solid species 's' and liquid species 'l' and  $\xi$  being an empirical constant set equal to 1.5.

The source term  $Q$ , comprises of the resistive heating from ohmic and kinetic phenomena. The ohmic heating is given by the following expression:

$$Q_{ohm} = \left( \frac{\mathbf{i}_1 \cdot \mathbf{i}_1}{\sigma} \right) + \left( \frac{\mathbf{i}_2 \cdot \mathbf{i}_2}{\kappa} \right) \quad (49)$$

The first term corresponds to the heat generated due to the passage of current in the matrix and the second, in the solution. The kinetic source term is given as [Appendix C]:

$$Q_{kin} = \sum_{\substack{i=local \\ reactions}} a_i (\eta_i - T \left( \frac{\partial U_{i,ref}}{\partial T} \right)_p) \quad (50)$$

The reversible part of the  $Q_{kin}$  is the one associated with the variation of  $U_{i,ref}$  with temperature. Since the data on variation of  $U_{i,ref}$  with temperature is not known, it is assumed that, the kinetic heat source term is mainly contributed by, the product of local overpotential and local reaction rate. A similar approach has been adopted by Pals and Newman [22] for the simulation of  $TiS_2$  cells. Hence

$$Q_{kin} = \sum_{\substack{i=local \\ reactions}} a_i \eta_i \quad (51)$$

We now have the complete system of equations to predict the temperature rise associated with the cell. Tables (1-5) list all equations solved for the simulation with appropriate boundary and initial conditions.

The second part of the model is the prediction of the temperature profiles in a stack of 5 cells. A typical cell stack is given in Fig 2. The model for a single cell is solved and the numerical values for the energy equation are obtained. These values are exported to FIDAP<sup>TM</sup> and equation (46) is solved once again for a stack of five cells. But unlike the single cell model, the stack model is non-adiabatic. A convective boundary



condition is employed on the outside of casing and continuity of heat flux is assumed between the cell interfaces. Thus the boundary condition becomes:

$$-k\nabla T = h(T - T_0) \text{ @ casing/air interface} \quad (52)$$

assuming that the cell starts discharge at ambient temperature.

Thus it essentially uses the one-dimensional adiabatic source term obtained from the single cell model as the source term for solution. This approach is rather a heavy approximation since it neglects the (y, z) spatial dependence of the source term. We consider this as a first step to predict the hotspot in a stack of cells. More complex and complete models will be built later taking into account the comprehensive dependency of the source terms.

#### **Method of solution:**

Numerical solution of the above system of equations (single cell model) presented in tables (1-5) was obtained through the finite element software FEMLAB™ (version 2.1). The FEMLAB™ 2.1 engine is designed to solve a set of coupled differential-algebraic equations of second order in a specific format. Its flexibility allows the user to define equations at ease. The convergence criterion was that the difference between two successive solutions at all mesh points be less than 0.001 %. The values for the parameters are listed in the table 7.

The second part of the model is the prediction of the 3-D temperature profiles in a stack of 5 cells. This was accomplished by using the commercial finite-element code FIDAP™ (version 8.0). One of the shortcomings of FIDAP™ 8.0 is that it cannot handle the potential in the matrix and the solution together. This is because of the following reasons:

- (1) The solver is not capable of handling a set of equations, which has time derivatives and another set which does not. The model equations for matrix and solution potentials are devoid of time derivatives (since the model neglects the effects of double layer charging).
- (2) There was no way to allow the two potentials to be "present" at the same point. This would require a user-defined scalar with a user-defined flux term for which there is no provision in FIDAP™ 8.0. The only possible work around is to consider the potentials as two individually reacting species. This once again was unacceptable once the model equations became too complex and appropriate "reactions" could not be formulated.

The same equations for a two and three-dimensional models were tried with FEMLAB™ 2.1 but the problem would not start, for even the two-dimensional model of a single cell. The reason is that the model is very non-linear and the number of equations to be solved is high. Presently the memory requirements and computational time with FEMLAB™ 2.1 are very high. The experience with FEMLAB™ 2.1 shows that it is presently not good at handling three-dimensional models which have more than four highly non-linear equations per node and the mesh, fine. Another major disadvantage of FEMLAB™ 2.1 is that the meshing is not fully user-controlled. It has the option of only a paved mesh and this may affect the convergence in highly non-linear problems.

Since both softwares have limitations, it was decided to use FEMLAB™ 2.1 to solve the one-dimensional model to obtain the performance characteristics of a single cell. The numerical values for the energy equation were then obtained from FEMLAB™ 2.1, averaged over the domains, regressed and then used for predicting the temperature

profiles in the cell-stack using FIDAP™ 8.0. Fig 3 shows the grid used for a stack of 5 cells for the computation. This grid was prepared by the post-processor GAMBIT™ 1.0.

Table 1 – Equations for the positive (i.e Silver ) region (  $0 < x < l_{Ag}$  )

Equation	S.No
$\frac{\partial(\varepsilon C)}{\partial t} = -\nabla \cdot \left( -\frac{\varepsilon}{\tau} D_{eff} \nabla C \right) + \left( \frac{D_{eff}}{2D_{OH^-}} \right) R_{OH^-, Ag}$	[A.1.1]
$\frac{\partial M_{AgO}}{\partial t} = \frac{-a_{Ag} j_1 s_{AgO,1}}{n_1 F}$	[A.1.2]
$\frac{\partial M_{Ag}}{\partial t} = \frac{-a_{Ag} j_2 s_{Ag,1}}{n_2 F}$	[A.1.3]
$2M_{Ag_2O} + M_{AgO} + M_{Ag} = M_{Ag}^{tot}$	[A.1.4]
$\nabla \cdot \mathbf{i}_1 = -a_{Ag} j$	[A.1.5]
$\nabla \cdot \mathbf{i}_2 = a_{Ag} j$	[A.1.6]
$j = j_1 + j_2$	[A.1.7]
$j_1 = j_{01} \left\{ \left( \frac{C_{OH^-}}{C_{OH^-}^b} \right)^2 \left( \frac{M_{Ag_2O}}{0.5M_{Ag}^{tot}} \right) \exp\left( \frac{F\alpha_{a1}}{RT} \eta_1 \right) - \left( \frac{M_{AgO}}{M_{Ag}^{tot}} \right)^2 \exp\left( -\frac{F\alpha_{c1}}{RT} \eta_1 \right) \right\}$	[A.1.8]
$j_2 = j_{02} \left\{ \left( \frac{C_{OH^-}}{C_{OH^-}^b} \right)^2 \left( \frac{M_{Ag}}{M_{Ag}^{tot}} \right)^2 \exp\left( \frac{F\alpha_{a2}}{RT} \eta_2 \right) - \left( \frac{M_{Ag_2O}}{0.5M_{Ag}^{tot}} \right) \exp\left( -\frac{F\alpha_{c2}}{RT} \eta_2 \right) \right\}$	[A.1.9]
$\mathbf{i}_1 = -\sigma_{avg, Ag} \nabla \phi_1$	[A.1.10]
$\mathbf{i}_2 = -\kappa_{Ag} \nabla \phi_2 - \varepsilon_{Ag} \mathbf{F} (D_{K^+} - D_{OH^-}) \nabla C$	[A.1.11]
$\frac{\partial \varepsilon_{Ag}}{\partial t} = \left( \frac{s_{Ag_2O,1} M_{Ag_2O}^w}{\rho_{Ag_2O} n_1 F} + \frac{s_{AgO,1} M_{AgO}^w}{\rho_{AgO} n_1 F} \right) a_{Ag} j_1 + \left( \frac{s_{Ag,2} M_{Ag}^w}{\rho_{Ag} n_2 F} + \frac{s_{Ag_2O,2} M_{Ag_2O}^w}{\rho_{Ag_2O} n_2 F} \right) a_{Ag} j_2$	[A.1.12]
$(\rho_{cp})_{avg, Ag}^* \frac{\partial T}{\partial t} = -\nabla \cdot (-k_{avg, Ag} \nabla T) + \left( \frac{\mathbf{i}_1 \cdot \mathbf{i}_1}{\sigma_{avg, Ag}} + \frac{\mathbf{i}_2 \cdot \mathbf{i}_2}{\kappa_{Ag}} \right) + (a_{Ag} j_1 \eta_1 + a_{Ag} j_2 \eta_2)$	[A.1.13]

where

$D_{eff} = \frac{2D_{K^+}D_{OH^-}}{D_{K^+} + D_{OH^-}}$	[A.1.14]
$R_{OH^-,Ag} = R_{OH^-,1} + R_{OH^-,2} = -\frac{a_{Ag}j_1^{S_1,OH^-}}{n_1F} - \frac{a_{Ag}j_2^{S_2,OH^-}}{n_2F}$	[A.1.15]
$\eta_1 = \phi_1 - \phi_2 - U_1^0$	[A.1.16]
$\eta_2 = \phi_1 - \phi_2 - U_2^0$	[A.1.17]
$\sigma_{avg,Ag} = \sum \sigma_a m_a^k = \sigma_{Ag} \left[ \frac{M_{Ag}^w M_{Ag}}{(M_{Ag}^w M_{Ag} + M_{Ag_2O}^w M_{Ag_2O} + M_{AgO}^w M_{AgO})} \right]^{1.5} +$ $\sigma_{Ag_2O} \left[ \frac{M_{Ag_2O}^w M_{Ag_2O}}{(M_{Ag}^w M_{Ag} + M_{Ag_2O}^w M_{Ag_2O} + M_{AgO}^w M_{AgO})} \right]^{1.5} +$ $\sigma_{AgO} \left[ \frac{M_{AgO}^w M_{AgO}}{(M_{Ag}^w M_{Ag} + M_{Ag_2O}^w M_{Ag_2O} + M_{AgO}^w M_{AgO})} \right]^{1.5}$	[A.1.18]
$\kappa_{Ag} = \frac{\epsilon_{Ag} F^2}{RT} \sum z_i^2 D_i C_i = \frac{\epsilon_{Ag} F^2}{RT} (D_{K^+} + D_{OH^-}) C$	[A.1.19]
$(\rho c_p)_{avg,Ag} = (1-\epsilon) \left[ \frac{(\rho_{AgO} c_{p,AgO} M_{AgO}^w M_{AgO} + \rho_{Ag_2O} c_{p,Ag_2O} M_{Ag_2O}^w M_{Ag_2O} + \rho_{Ag} c_{p,Ag} M_{Ag}^w M_{Ag})}{M_{AgO}^w M_{AgO} + M_{Ag_2O}^w M_{Ag_2O} + M_{Ag}^w M_{Ag}} \right] + \epsilon \rho_l c_{p,l}$	[A.1.20]
$k_{avg,Ag} = \sum k_a w_a^k = k_{Ag} \left[ \frac{(1-\epsilon_{Ag}) M_{Ag}^w M_{Ag}}{((1-\epsilon_{Ag})(M_{Ag}^w M_{Ag} + M_{Ag_2O}^w M_{Ag_2O} + M_{AgO}^w M_{AgO}) + \epsilon_{Ag} \rho_l)} \right]^{1.5} +$ $k_{Ag_2O} \left[ \frac{(1-\epsilon_{Ag}) M_{Ag_2O}^w M_{Ag_2O}}{((1-\epsilon_{Ag})(M_{Ag}^w M_{Ag} + M_{Ag_2O}^w M_{Ag_2O} + M_{AgO}^w M_{AgO}) + \epsilon_{Ag} \rho_l)} \right]^{1.5} +$ $k_{AgO} \left[ \frac{(1-\epsilon_{Ag}) M_{AgO}^w M_{AgO}}{((1-\epsilon_{Ag})(M_{Ag}^w M_{Ag} + M_{Ag_2O}^w M_{Ag_2O} + M_{AgO}^w M_{AgO}) + \epsilon_{Ag} \rho_l)} \right]^{1.5} +$ $k_l \left[ \frac{\epsilon_{Ag} \rho_l}{((1-\epsilon_{Ag})(M_{Ag}^w M_{Ag} + M_{Ag_2O}^w M_{Ag_2O} + M_{AgO}^w M_{AgO}) + \epsilon_{Ag} \rho_l)} \right]^{1.5}$	[A.1.21]
$M_{Ag_2O} = \frac{(M_{Ag}^{tot} - M_{AgO} - M_{Ag})}{2}$ (same as [A.1.4])	[A.1.22]

Table 2 – Equations for the Separator region(  $l_{Ag} < x < (l_{Ag} + l_{sep})$  )

Equation	S.No
$\frac{\partial(\epsilon C)}{\partial t} = -\nabla \cdot \left( -\frac{\epsilon}{\tau} D_{eff} \nabla C \right)$	[A.2.1]
$\nabla \cdot \mathbf{i}_2 = 0$	[A.2.2]
$\mathbf{i}_2 = -\kappa_{sep} \nabla \phi_2 - \epsilon_{sep} \mathbf{F} (D_{K^+} - D_{OH^-}) \nabla C$	[A.2.3]
$(\rho c_p)_{avg, sep} \frac{\partial T}{\partial t} = -\nabla \cdot (-k_{avg, sep} \nabla T) + \left( \frac{\mathbf{i}_2 \cdot \mathbf{i}_2}{\kappa_{sep}} \right)$	[A.2.4]

where:

$D_{eff} = \frac{2D_{K^+}D_{OH^-}}{D_{K^+} + D_{OH^-}}$ (same as [A.1.14] )	[A.2.5]
$\kappa_{sep} = \frac{\epsilon_{sep} \mathbf{F}^2}{RT} \sum z_i^2 D_i C_i = \frac{\epsilon_{sep} \mathbf{F}^2}{RT} (D_{K^+} + D_{OH^-}) C$	[A.2.6]
$(\rho c_p)_{avg, sep} = (1 - \epsilon_{sep}) \rho_{sep} c_{p, sep} + \epsilon_l \rho_l c_{p, l}$	[A.2.7]
$k_{avg, sep} = \sum k_a w_a^{\frac{1}{2}} = k_{sep} \left[ \frac{(1 - \epsilon_{sep}) \rho_{sep}}{(1 - \epsilon_{sep}) \rho_{sep} + \epsilon_{sep} \rho_l} \right]^{1.5} + k_l \left[ \frac{\epsilon_{sep} \rho_l}{(1 - \epsilon_{sep}) \rho_{sep} + \epsilon_{sep} \rho_l} \right]^{1.5}$	[A.2.8]

**Table 3 – Equations for the negative (i.e. Zinc) Region**

$$(l_{Ag} + l_{sep}) < x < (l_{Ag} + l_{sep} + l_{Zn})$$

Equation	S.No
$\frac{\partial(\varepsilon C)}{\partial t} = -\nabla \cdot \left( -\frac{\varepsilon}{\tau} D_{eff} \nabla C \right) + \left( \frac{D_{eff}}{2D_{OH^-}} \right) R_{OH^-, Ag}$	[A.3.1]
$\frac{\partial M_{Zn}}{\partial t} = \frac{-a_{Zn} j_3 s_{Zn,3}}{n_3 F}$	[A.3.2]
$M_{ZnO} + M_{Zn} = M_{Zn}^{tot}$	[A.3.3]
$\nabla \cdot \mathbf{i}_1 = -a_{Zn} j$	[A.3.4]
$\nabla \cdot \mathbf{i}_2 = a_{Zn} j$	[A.3.5]
$j = j_3$	[A.3.6]
$j_3 = j_{03} \left\{ \left( \frac{C_{OH^-}}{C_{OH^-}^b} \right)^2 \left( \frac{M_{Zn}}{M_{Zn}^{tot}} \right) \exp\left( \frac{F\alpha_{a3}}{RT} \eta_3 \right) - \left( \frac{M_{ZnO}}{M_{ZnO}^{tot}} \right) \exp\left( -\frac{F\alpha_{c3}}{RT} \eta_3 \right) \right\}$	[A.3.7]
$\mathbf{i}_1 = -\sigma_{avg,Zn} \nabla \phi_1$	[A.3.8]
$\mathbf{i}_2 = -\kappa_{Zn} \nabla \phi_2 - \varepsilon_{Zn} F (D_{K^+} - D_{OH^-}) \nabla C$	[A.3.9]
$\frac{\partial \varepsilon_{Zn}}{\partial t} = \left( \frac{s_{Zn,3} M_{Zn}^w}{\rho_{Zn} n_3 F} + \frac{s_{ZnO,3} M_{ZnO}^w}{\rho_{ZnO} n_3 F} \right) a_{Zn} j_3$	[A.3.10]
$(\rho c_p)_{avg,Zn} \frac{\partial T}{\partial t} = -\nabla \cdot (-k_{avg,Zn} \nabla T) + \left( \frac{\mathbf{i}_1 \cdot \mathbf{i}_1}{\sigma_{avg,Zn}} + \frac{\mathbf{i}_2 \cdot \mathbf{i}_2}{\kappa_{Zn}} \right) + (a_{Zn} j_3 \eta_3)$	[A.3.11]

where:

$D_{eff} = \frac{2D_K \cdot D_{OH^-}}{D_K + D_{OH^-}}$ (same as [A.1.14])	[A.3.12]
$R_{OH^-, Zn} = R_{OH^-, 3} = -\frac{a_{Zn} j_3 s_{OH^-, 3}}{n_3 F}$	[A.3.13]
$\eta_3 = \phi_1 - \phi_2 - U_3^0$	[A.3.14]
$\sigma_{avg, Zn} = \sum \sigma_a m_a^{\xi} = \sigma_{Zn} \left[ \frac{M_{Zn}^w M_{Zn}}{(M_{Zn}^w M_{Zn} + M_{ZnO}^w M_{ZnO})} \right]^{1.5} + \left[ \frac{M_{ZnO}^w M_{ZnO}}{(M_{Zn}^w M_{Zn} + M_{ZnO}^w M_{ZnO})} \right]^{1.5}$	[A.3.15]
$\kappa_{Zn} = \frac{\varepsilon_{Ag} F^2}{RT} \sum z_i^2 D_i C_i = \frac{\varepsilon_{Ag} F^2}{RT} (D_K + D_{OH^-}) C$	[A.3.16]
$(\rho c_p)_{avg, Zn} = (1 - \varepsilon) \left[ \frac{(\rho_{Zn} c_{p, Zn} M_{Zn}^w M_{Zn} + \rho_{ZnO} c_{p, ZnO} M_{ZnO}^w M_{ZnO})}{M_{Zn}^w M_{Zn} + M_{ZnO}^w M_{ZnO}} \right] + \varepsilon \rho_l c_{p, l}$	[A.3.17]
$k_{avg, Zn} = \sum k_a w_a^{\xi} = k_{Zn} \left[ \frac{(1 - \varepsilon_{Zn}) M_{Zn}^w M_{Zn}}{(1 - \varepsilon_{Zn})(M_{Zn}^w M_{Zn} + M_{ZnO}^w M_{ZnO}) + \varepsilon_{Zn} \rho_l} \right]^{1.5} +$ $k_{ZnO} \left[ \frac{(1 - \varepsilon_{Zn}) M_{ZnO}^w M_{ZnO}}{(1 - \varepsilon_{Zn})(M_{Zn}^w M_{Zn} + M_{ZnO}^w M_{ZnO}) + \varepsilon_{Zn} \rho_l} \right]^{1.5} +$ $k_l \left[ \frac{\varepsilon_{Zn} \rho_l}{(1 - \varepsilon_{Zn})(M_{Zn}^w M_{Zn} + M_{ZnO}^w M_{ZnO}) + \varepsilon_{Zn} \rho_l} \right]^{1.5}$	[A.3.18]
$M_{ZnO} = M_{Zn}^{tot} - M_{Zn}$ (same as [A.3.3])	[A.3.19]



Table 4 - Boundary Conditions

Centre of the silver electrode ( $x=0$ )	S.No	Silver-Separator interface ( $x=l_{Ag}$ )	S.No
$\nabla C = 0$	[B.1.1]	$\frac{\epsilon_{Ag}}{\tau_{Ag}} \nabla C _{Ag} = \frac{\epsilon_{sep}}{\tau_{sep}} \nabla C _{sep}$	[B.2.1]
$i_1 = i_{cell}$	[B.1.2]	$i_1 = 0$	[B.2.2]
$i_2 = 0$	[B.1.3]	$i_2 = i_{cell}$	[B.2.3]
$\nabla T = 0$	[B.1.4]	$-k_{avg, Ag} \nabla T _{Ag} = -k_{avg, sep} \nabla T _{sep}$ (see [A.2.8] & [A.1.21] )	[B.2.4]

Zinc-Separator interface ( $x=l_{Ag}+l_{sep}$ )	S.No	Centre of the zinc electrode ( $x=l_{Ag}+l_{sep}+l_{Zn}$ )	S.No
$\frac{\epsilon_{sep}}{\tau_{sep}} \nabla C _{sep} = \frac{\epsilon_{Zn}}{\tau_{Zn}} \nabla C _{Zn}$	[B.3.1]	$\nabla C = 0$	[B.4.1]
$i_1 = 0$	[B.3.2]	$i_1 = i_{cell}$	[B.4.2]
$i_2 = i_{cell}$	[B.3.3]	$i_2 = 0, \phi_2 = 0$	[B.4.3]
$-k_{avg, sep} \nabla T _{sep} = -k_{avg, Zn} \nabla T _{Zn}$ (see [A.2.8] & [A.1.21] )	[B.3.4]	$\nabla T = 0$	[B.4.4]

Table 5 - Initial Conditions (@  $t = 0$ )

Variable	Silver region	Separator	Zinc region
$C$	$C_0$	$C_0$	$C_0$
$M_{AgO}$	$M_{AgO}^0$	-	-
$M_{Ag}$	$M_{Ag}^0$	-	-
$M_{Zn}$	-	-	$M_{Zn}^0$
$\epsilon_{Ag}$	$\epsilon_{Ag}^0$	-	-
$\epsilon_{Zn}$	-	-	$\epsilon_{Zn}^0$
$T$	$T_0$	$T_0$	$T_0$

## Results and discussion

There are many parameters in the model equations that affect the discharge characteristics of the cell. In this section the effects of exchange current density ( $i_{01}, i_{03}$ ), initial electrolyte concentration ( $C_0$ ) and electrolyte diffusion coefficient ( $D_{OH^-}$ ) are presented. Various discharge rates ranging from 0.1C to 8C rate were studied. Since we are concerned primarily with high discharge rates, we exclude any rate less than 1C to be mentioned in the following studies. The rates 1C and 2C have been elaborated with figures in detail. 4C and 8C rates had little information different from 1C and 2C rates and hence just appropriately mentioned without much detail.

### Cell voltage:

A cell's primary variable of importance is the cell voltage. We discuss the various parameters and their influence on the cell voltage. Figs 4-7 show how the cell voltage varies with various discharge rates. Higher the discharge rate, lower is the cell voltage.

#### *Effect of $i_{01}$*

$i_{01}$  has a pronounced effect on the cell voltage. Three values:  $2 \times 10^{-3}$ ,  $2 \times 10^{-4}$  and  $2 \times 10^{-5}$  A/cm<sup>2</sup> were used to study the behavior of the cell. As shown in fig.4 the cell voltage drops by approx. 0.05 volts for every order of magnitude of the exchange current density of the reaction 1. It also explains the drastic reduction in the cell voltage as we go for higher rates of discharge. This agrees well with the experimentally measured values reported by Moden et al [25]. In the low rate studies, a stable potential of 1.55 V was obtained which once again agrees very well with the experimental studies. So silver oxide materials with a good

exchange current density for reaction 1 are bound to yield higher cell voltage and also stand higher rates of discharge. It is also notable that for an exchange current density of  $2 \times 10^{-3} \text{ A/cm}^2$  there is a considerable decrease in the slope for both 1C and 2C rates between (800-900s) and (300-400s) respectively (fig 4). A suitable explanation is presented in the **Reaction profiles** section to follow.

#### *Effect of $i_{03}$*

The exchange current density of reaction 3 influences the cell voltage in the way similar to  $i_{01}$ . A study of fig 5 tells us that the cell voltage drops by 0.05 volts for an order of magnitude of  $i_{03}$ . A higher exchange current density thus would lead to a higher cell voltage.

#### *Effect of $C_0$ (initial concentration)*

Three concentrations were studied: 25, 35 and 45 % KOH. The results are shown in fig 6 for a particular set of values of other parameters. As is evident, the cell voltage for a higher concentration of KOH, is higher. For every 10% rise in KOH concentration, cell voltage increases by approximately 0.02V. The effect of concentration is high in high discharge rates since it strongly affects the capacity utilization, which clearly indicates that discharge is mass transfer limited at high rates. Typical concentration profiles as a function of time are given in fig 7 and fig 8 for 1C and 2C discharge rates respectively. They clearly show that as the concentration of  $\text{OH}^-$  ions in the negative electrode goes to zero, the discharge ends implying that the discharge process is mass transfer controlled at high discharge rates. The diffusion is not fast enough to replenish and compensate the continuous consumption of  $\text{OH}^-$  in the anode, which leads to the eventual end

of discharge. A higher initial concentration ( $C_0$ ) of KOH thus has more  $\text{OH}^-$  to sustain the reaction and leads to a higher utilization of capacity. With 25% KOH, the state of discharge (SOD) is 56 %, with 35 % KOH it is 83 % and with 45 % KOH it is 94 % for 2C rate (fig 6). This essentially means that if a silver zinc cell be subjected to high discharge rates from an incompletely charged battery, the concentration of KOH be as high as possible, to obtain maximum utilization of capacity.

#### *Effect of $D_{\text{OH}^-}$*

The values of diffusivity of  $\text{OH}^-$  ion used in the literature vary by an order of magnitude. Hence it was decided to use two values for  $D_{\text{OH}^-}$  ( $8.4 \times 10^{-5} \text{ cm}^2/\text{s}$  and  $8.4 \times 10^{-6} \text{ cm}^2/\text{s}$ ) and verify the dependence of the cell performance. A look at fig 9 shows that, the cell voltage is easily higher by a good margin (0.02 V for 1C rate and 0.04 V for 2C rate) in the beginning of discharge, for higher  $D_{\text{OH}^-}$ . It is notable that despite the higher diffusivity, the discharge ends quicker though at a higher value of end voltage, which implies that at 2C rate, even the higher value of diffusivity used in the study, is insufficient to check on the mass transfer limitations.

#### *Effect of C rate (rate of discharge)*

From figs 4,5,6 and 9 it is evident that higher the rate of discharge lower the cell voltage. Approximately the 1C rate and 2C rate differ by 0.07 V. The trend is clear in the figs.

## Maximum state of discharge (MSOD)

The extent to which a cell discharges depends on various parameters.

### *Effect of $i_{01}$ and $i_{03}$*

Both the exchange current densities have almost no effect on MSOD as is evident from the figs 4 and 5. This is because the discharge is mass-transfer controlled. It is the local non-availability of the  $\text{OH}^-$  ions that leads to the abrupt end of discharge thereby lowering MSOD.

### *Effect of $C_0$*

Concentration of  $\text{OH}^-$  ions is easily one major factor that influences MSOD. As was observed previously (fig 6), higher the initial concentration, higher the percent discharge of the active material. This is because higher  $C_0$  delays the local depletion of  $\text{OH}^-$  ions. The effect of concentration on MSOD is insignificant in 1C rate (all close to 97%) but very pronounced in 2C rates. As observed earlier, with 25% KOH, the MSOD is 56 %, with 35 % KOH it is 83 % and with 45 % KOH it is 94 % for 2C rate (fig 6).

### *Effect of $D_{\text{OH}^-}$*

The explanation offered earlier in the cell voltage section is applicable here.

### *Zinc to Ag content ratio ( $\theta_1$ )*

There are two more parameters which deserve mention while we investigate MSOD - the mass ratio of Zinc to Ag ( $\theta_1$ ) and the ratio of  $\text{Ag}_2\text{O}$  to  $\text{AgO}$  ( $\theta_2$ ), in the cell at the beginning of discharge. Himy [24] recommends a

value of 0.866 for  $\theta_1$  and advocates that a silver-zinc cell be intentionally made silver limiting.  $\theta_2$  on the other hand is a design parameter of choice and an indicator of the state of the system. By state of the system, we mean a cell being subjected to number of cycles and then allowed to rest for enough time to let the concentration gradients be nullified by diffusion.  $\theta_2$  is usually zero in the first cycle since the first cycle starts after the complete oxidation of Ag to AgO. In the successive cycles, due to various irreversibilities associated with the system (eg. shape change), AgO may not be completely restored and a portion of it remains as Ag<sub>2</sub>O. A value of 1/3 has been used in all the simulations according to Moden [24]. Though  $\theta_2$  is 1/3, the amount of silver ( $M_{Ag}^0$ ) assumed to be present in the system at the start of simulation as Ag is zero.

## Reaction profiles

### *Zinc electrode*

Fig.10 (1C rate) and fig.11 (2C rate) show the typical reaction distribution in the anode as the discharge progresses. There is clearly a front that moves from the separator ( $x = l_{Ag} + l_{sep} = 0.1567$  cm) towards the anode current collector ( $x = l_{Ag} + l_{sep} + l_{Zn} = 0.5567$  cm). As the zinc in the anode is consumed during discharge, more and more of interior zinc is used up until the end of discharge. At the start of discharge there is more reaction at the separator end. The reaction in the interior regions is not high. The curves at 500s (fig 10) and 200s (fig 11) show the same. Since the reaction is high, the reactants get consumed faster and this results in the depletion of zinc at the site of the reaction (i.e. at the separator end). This leads to a reduction in the local rate of reaction 3, which is the cause

for the development of the front. The curves at 1000s and 1500s for 1C rate (fig 10) and at 400s and 600s for 2C rate (fig 11) show the evolution of the front. At 2000s for 1C rate (fig 10) and at 800s for 2C rate (fig 11), the development of front is practically complete. Once fully formed, the front moves more to the interior of the zinc electrode consuming more active material. The movement of the front stops with the end of discharge which is due to the local depletion of  $\text{OH}^-$  ions.

Fig 12 and fig 13 show the distribution of the active material (Zn) left in the negative electrode for 1C and 2C rates respectively. As explained afore, the zinc in the anode is consumed as the front progresses into the interior. A new quantity, *penetration depth* ( $l_p$ ), is defined as the distance from the separator at which the local fraction of zinc left is 0.01 at the end of discharge. For 1C rate it is close to 0.15 cm and for 2C rate it is 0.07 cm. The penetration depth gives an idea of how much of the electrode space is "completely" utilized for discharge or the "dead" region of the cell for discharge.

Another parameter, *reaction depth* ( $l_r$ ), is defined to facilitate better understanding of the state of electrode after discharge. It is defined as the distance from the separator, where the ratio of the fraction of Zn left, to the fraction of Zn left at the anode current collector end ( $x = l_{\text{Ag}} + l_{\text{sep}} + l_{\text{Zn}} = 0.5567$ ), is 0.99. For 1C rate the reaction depth is 0.34 cm and for 2C rate it is 0.2 cm. The reaction depth gives an idea about how much of the electrode has been "practically active" during discharge. A ratio of reaction depth ( $l_r$ ) to the length of the zinc electrode ( $l_{\text{Zn}}$ ) gives the fraction of area of the electrode active during



discharge. It is 85% for 1C rate and 50% for 2C rate. It is worth noting that the region of reaction depth sans the penetration depth (figs 12 and 13) shows a profile of Zn – the active material- after discharge. This profile influences the charge/discharge cycles that would follow this discharge.

It is however important to note that both these quantities are highly influenced by operating conditions and parameters. These quantities can be used only as “status indicators” (along with  $\theta_1$  and  $\theta_2$ ) of the electrode. Towards the end of discharge a numerical instability develops due to the fact that the operating conditions now favor the reverse reactions (charging), but the current ( $i_{cell}$ ) is forcibly in the opposite direction. Hence the cell stops discharging abruptly.

#### *Silver electrode*

A reaction front is not observed in the silver electrode (figs 14 and 15) because two parallel reactions occur for discharge. But the reaction rate is high at the start near the separator ( $x = l_{Ag} = 0.1067$  cm), similar to anode, and is shown in fig 14 and fig 15 for 1C and 2C rates respectively. For the 1C rate, towards the end of discharge the rate of reaction is high at the current collector end ( $x=0$ ) and low at the separator end ( $x = l_{Ag} = 0.1067$  cm). This behavior is not observed in 2C rate where the rate is almost uniform over the entire electrode towards the end of discharge. The reason is the difference in SOD between the two rates of discharge. The MSOD for 1C rate is approximately 97 % and is less than 56% for 2C rate. A comparison between the two graphs (figs 14 and 15) tells us that around 56% SOD (2000s for 1C rate and 1000s for 2C rate) the rate profile is uniform and the rate of 2C is approximately twice that of 1C. To facilitate the

discussion on the rates of reactions 1 and 2 we define two fractions  $f_1$  and  $f_2$  as follows:

$$f_1(x,t) = \frac{\text{Rate of reaction 1 in silver electrode at } (x,t)}{\text{Total reaction rate in silver electrode at } (x,t)} = \frac{i_1}{i_1 + i_2} \quad (53)$$

$$f_2(t) = \text{Spatial average of } f_1 = \frac{1}{l_{Ag}} \int_0^{l_{Ag}} \left( \frac{i_1}{i_1 + i_2} \right) dx \quad (54)$$

The cell voltage vs time curve (Fig 4) indicates that for  $i_{01} = 2 \times 10^{-3} \text{ A/cm}^2$  there is a change in curve behavior for both 1C and 2C rates between (800-900s) and (300-400s) respectively. Fig 16 shows that at the same interval  $f_2$  approaches 0.5. Initially reaction 1 is much faster but later it slows down and becomes equal to reaction 2. Though the rate of reaction 1 is high in the start, it gets progressively slow and becomes equal to the rate of reaction 2. This was observed experimentally by Dirkse [2] who has attributed this to the partial reversibility of reaction 1. The reason for the reversibility in our case, is the increase in concentration of  $\text{OH}^-$  at the cathode, which drives the reaction 1 back according to Le chatelier's principle. An idea about how the rates of reactions 1 and 2 compare, can be obtained from Fig 16.  $f_2$  represents the fraction of total current contributed by reaction 1 and hence  $(1-f_2)$  would represent the corresponding quantity for reaction 2.  $f_2$  is close to 1 in the start and approaches 0.5 eventually. As  $f_2$  approaches 0.5, the net rate of production of  $\text{Ag}_2\text{O}$  approaches zero (fig 17) and the cathode can be viewed as having just one overall reaction namely  $\text{AgO}$  going to  $\text{Ag}$ . This observation is important since it may help remove unnecessary usage of a complex model, when a simpler one substitutes it in the same league.

Later, when the three-dimensional model for a stack of such cells is sought after, the observations made here will be used to simplify and lessen the intensity of the computational task.

Not only does the net rate of production of  $\text{Ag}_2\text{O}$  go to zero (Fig 17), but the  $\text{Ag}_2\text{O}$  itself gets locally completely depleted after 2000s for 1C rate (Fig 18) and after 700s for 2C rate (Fig 19). This is because the rate of the reaction 1 decreases with time progressively and after sometime becomes lower than the rate of reaction 2. But the rate of reaction 2 is dependent on reaction 1. As a result, the over-all rate, is determined by the reaction 1 and it thus becomes the rate determining step (RDS). Hence, as soon as  $\text{Ag}_2\text{O}$  is produced by the first reaction, the second reaction consumes it immediately, which leads to the local depletion of  $\text{Ag}_2\text{O}$  much earlier than the end of discharge.

### **Porosity**

Fig 20 shows the typical variation of porosity for 1C rate during discharge. The plot shows the variation of the ratio of instantaneous porosity to the initial porosity in the respective regions. It can be seen that the porosity of anode and cathode do not vary appreciably during discharge. The separator porosity is a constant since no reaction takes place in that region. This is another important observation since this discards the necessity to include the porosity equations (A.1.12 and A.3.10) for three-dimensional problems. It also lowers the difficulty in solving the concentration equations (A.1.1 and A.3.1) since the porosity term in the time derivative becomes a constant and reduces the non-linearity to a good extent.

## Temperature rise and profiles

The prediction of temperature rise is one of the important features of this model. The energy equation (A.1.13, A.2.4 and A.3.11) appears complicated with all the specific heats and thermal conductivities averaged rigorously. It is worth mentioning here that since the conductivities of the materials in a silver-zinc cell are high, a low rate discharge does not produce a local temperature rise. Fig 21 and 22 show the typical distribution profiles of temperature rise in the cell at 1C and 2C rates. Since it is evident that the temperature rise at a given instant of time does not vary appreciably over  $x$ , an average temperature rise ( $T_{avg-rise}$ ) plot for the cell would make just as much sense. We provide here a study of the influence of parameters on the average temperature rise in the cell. By average temperature rise, we mean:

$$T_{avg-rise}(t) = \frac{1}{(l_{Ag} + l_{sep} + l_{Zn})} \int_0^{(l_{Ag} + l_{sep} + l_{Zn})} (T(x,t) - T_0) dx \quad (54)$$

Moden et al [25] have reported 0.395 °F/min (0.22 K/min) and 0.974 °F/min (0.54 K/min) rise for the discharge. An inspection of fig 23 shows that the average temperature reaches approximately 14 K at 1C rate at end of discharge, which is approximately 0.23 K/min and thus agrees excellently with Moden et al [25]. Similarly for the 2C rate, the temperature rise from the fig 23 is 0.48 K/min, which is a little less than the reported value.

Figs 23 through 26 show how the average temperature is influenced by various parameters. Fig 23 shows that the effect of  $i_{01}$  on the average temperature rise is insignificant since even for orders of magnitude difference in the exchange current density the temperature rise is approximately the same. However higher the anodic

current density ( $i_{03}$ ), lower the average temperature rise in the cell. Fig 24 shows how the  $i_{03}$  influences the average temperature rise in the cell.

At low diffusivity values, the discharge ends early (fig 25). For 1C rate the difference is pronounced and a higher diffusivity value ( $8 \times 10^{-5} \text{ cm}^2/\text{s}$ ) results in a higher utilization of capacity (fig 9). But for 2C rate, even a higher value of diffusivity is unable to check the depletion of  $\text{OH}^-$  ions and hence makes no difference in the discharge time. As a result, the effect on the average temperature rise is more apparent with the 2C rates than on the 1C rates. Fig 23 shows that the difference is approximately 2K.

Finally the effect of initial concentration ( $C_0$ ) on the average temperature rise in the cell is shown in Fig 26. Like diffusivity, concentration affects the discharge time considerably i.e. a higher utilization of capacity at higher concentration (fig 6). The average temperature rise in the cell is lower for a higher value of concentration at a given instant of time though not very significant. Nevertheless the studies have revealed that the heating primarily is due to the kinetic resistance term and not joule.

#### *The stack model*

The results for 5-cell stack model are given in figs 27-32. Fig 27 shows the temperature contours on the entire stack. The highest temperature rise in the cell is 7K as is the case for the 2C rate shown in fig. Sectional views of the temperature profiles are also provided in figs fidap2-6. These indicate clearly the hotspot is towards the center of the stack as expected. The energy equation when solved simultaneously with the Butler-Volmer and continuity equations, can provide more realistic results for three-dimensional problems. Efforts are due in that direction.

## Conclusions

In this paper, a mathematical model has been developed to study the performance and thermal behavior of the silver-zinc cell during discharge. The model could explain the abrupt end of discharge because of mass transfer limitations and also was able to predict the temperature rise associated with the discharge. We could also predict the drastic change of slope in the cell-voltage – time curve and the influence of parameters on the cell-voltage. The reaction distribution profiles in the anode and cathode along with distribution of the active materials were predicted. The cell stack model was outlined and future efforts to develop a full three-dimensional model have been mentioned.

## Appendix A

### Derivation of equation (10)

The species continuity equations for  $K^+$  and  $OH^-$  are:

$$\frac{\partial(\epsilon C_{K^+})}{\partial t} = -\nabla \cdot \mathbf{N}_{K^+} \quad (55)$$

$$\frac{\partial(\epsilon C_{OH^-})}{\partial t} = -\nabla \cdot \mathbf{N}_{OH^-} + R_{OH^-} \quad (56)$$

$K^+$  does not participate in the reaction and hence no source term is associated with it.

The flux expressions for  $K^+$  and  $OH^-$  are given by dilute solution theory.

$$\mathbf{N}_{K^+} = -\frac{\epsilon}{\tau} (D_{K^+} \nabla C_{K^+} - \frac{D_{K^+} \mathbf{F} z_{K^+} C_{K^+}}{RT} \nabla \phi_2) + C_{K^+} \mathbf{v} \quad \text{from (6)}$$

$$\mathbf{N}_{OH^-} = -\frac{\epsilon}{\tau} (D_{OH^-} \nabla C_{OH^-} - \frac{D_{OH^-} \mathbf{F} z_{OH^-} C_{OH^-}}{RT} \nabla \phi_2) + C_{OH^-} \mathbf{v} \quad \text{from (7)}$$

Since there is no flow,  $\mathbf{v}=0$  and the last term in the flux expression drops out.

From electroneutrality

$$\sum z_i C_i = 0 \quad \text{from (8)}$$

Since  $z_{K^+}=1$  and  $z_{OH^-}=-1$ ,

$$C_{K^+} = C_{OH^-} = C \quad \text{from (9)}$$

The eqn (55), (56), (6) and (7) can be combined with (8) and (9) and can be written as :

$$\frac{\partial(\epsilon C)}{\partial t} = -\nabla \cdot \left( -\frac{\epsilon}{\tau} (D_{K^+} \nabla C - \frac{D_{K^+} \mathbf{F} C}{RT} \nabla \phi_2) \right) \quad (57)$$

$$\frac{\partial(\epsilon C)}{\partial t} = -\nabla \cdot \left( -\frac{\epsilon}{\tau} (D_{OH^-} \nabla C + \frac{D_{OH^-} \mathbf{F} C}{RT} \nabla \phi_2) \right) + R_{OH^-} \quad (58)$$

Multiplying (57) by  $D_{OH^-}$  and (58) by  $D_{K^+}$  and adding them together gets rid of the term

with the  $\phi_2$  in the equations.

$$(D_{OH^-} + D_{K^+}) \frac{\partial(\epsilon C)}{\partial t} = -\nabla \cdot \left( -\frac{\epsilon}{\tau} (2D_{OH^-} D_{K^+} \nabla C) + D_{K^+} R_{OH^-} \right) \quad (59)$$

which leads to

$$\frac{\partial(\epsilon C)}{\partial t} = -\nabla \cdot \left( -\frac{\epsilon}{\tau} \frac{2D_{K^+} D_{OH^-}}{D_{K^+} + D_{OH^-}} \nabla C \right) + \left( \frac{D_{K^+}}{D_{K^+} + D_{OH^-}} \right) R_{OH^-} \quad (60)$$

or

$$\frac{\partial(\epsilon C)}{\partial t} = -\nabla \cdot \left( -\frac{\epsilon}{\tau} D_{eff} \nabla C \right) + \left( \frac{D_{eff}}{2D_{OH^-}} \right) R_{OH^-} \quad \text{which is equation (10)}$$

where

$$D_{eff} = \frac{2D_{K^+} D_{OH^-}}{D_{K^+} + D_{OH^-}} \quad \text{which is equation (11)}$$



## Appendix B

### *Derivation of equation (25)*

The expression for  $\mathbf{i}_2$  is derived as follows:

$$\mathbf{i}_2 = F \sum z_i \mathbf{N}_i \quad \text{from (24)}$$

From (55),(56),(9) and (24) we have,

$$\mathbf{i}_2 = F \left[ \left( -\frac{\varepsilon}{\tau} (D_{K^+} \nabla C - \frac{D_{K^+} F C}{RT} \nabla \phi_2) \right) - \left( -\frac{\varepsilon}{\tau} (D_{OH^-} \nabla C_{OH^-} + \frac{D_{OH^-} F C}{RT} \nabla \phi_2) \right) \right] \quad (61)$$

which reduces to

$$\mathbf{i}_2 = \frac{F^2}{RT} \frac{\varepsilon}{\tau} (D_{K^+} + D_{OH^-}) C \nabla \phi_2 - \frac{F \varepsilon}{\tau} (D_{K^+} - D_{OH^-}) \nabla C \quad (62)$$

which is an expanded form of equation (25)

### *Concentrated solution theory*

In case of concentrated solution theory, the equations (6) and (7) will be replaced

by:

$$\mathbf{N}_{K^+} = (-D_{K^+} \varepsilon^{(1+\tau)} \nabla C_{K^+} + \frac{t_{K^+}}{z_{K^+} F} \mathbf{i}_2) + C_{K^+} \mathbf{v} \quad (63)$$

$$\mathbf{N}_{OH^-} = (-D_{OH^-} \varepsilon^{(1+\tau)} \nabla C_{OH^-} + \frac{t_{OH^-}}{z_{OH^-} F} \mathbf{i}_2) + C_{OH^-} \mathbf{v} \quad (64)$$

where  $t_{K^+}$  and  $t_{OH^-}$  are the transference numbers of the respective ions. Since  $\mathbf{v}=0$ , these equations when combined with (55) and (56) and electroneutrality (24),

$$\frac{\partial(\varepsilon C)}{\partial t} = -\nabla \cdot \left( -D_{K^+} \varepsilon^{(1+\tau)} \nabla C + \frac{t_{K^+}}{z_{K^+} F} \mathbf{i}_2 \right) \quad (65)$$

$$\frac{\partial(\varepsilon C)}{\partial t} = -\nabla \cdot \left( -D_{OH^-} \varepsilon^{(1+\tau)} \nabla C + \frac{t_{OH^-}}{z_{OH^-} F} \mathbf{i}_2 \right) + R_{OH^-} \quad (66)$$

Eliminating the term containing  $\mathbf{i}_2$  in both the expressions, we obtain

$$\frac{\partial(\epsilon C)}{\partial t} = \left( \frac{1}{\frac{t_{OH^-}}{z_{OH^-}} - \frac{t_{K^+}}{z_{K^+}}} \right) \left[ \nabla \cdot (\epsilon^{(1+\tau)} (\frac{D_{OH^-} t_{K^+}}{z_{K^+}} - \frac{D_{K^+} t_{OH^-}}{z_{OH^-}}) \nabla C) - \frac{t_{K^+}}{z_{K^+}} R_{OH^-} \right] \quad (67)$$

The solution current  $i_2$  is given by:

$$i_2 = -\kappa \nabla \phi_2 - \kappa \frac{RT}{F} \left( \frac{t_{OH^-}}{z_{OH^-}} + \frac{t_{K^+}}{z_{K^+}} \right) \nabla (\ln C) \quad (68)$$

where

$$\kappa = \kappa_0 \epsilon^{(1+\tau)} \quad (69)$$

The equations (67), (68) and (69) would replace (10), (25) and (26).

## Appendix C

### *Formulation of the energy equation*

In a half cell the reaction enthalpy has two components. A portion of it goes to heat up the system and the rest goes out as the electric power of the system [19]. Hence the energy balance of a half cell is given as:

$$Q = \sum_k r_k (-\Delta H_k) - P \quad (70)$$

where the first term on the RHS refers to the reaction enthalpy of all the reactions in the electrode. The second term is the electric power given by:

$$P = \underbrace{\sum_k r_k (-\Delta G_k)}_{\text{ideal work}} - \underbrace{\sum_k a |i_k| \eta_k}_{\text{kinetic losses}} - \underbrace{\left( \frac{\mathbf{i}_1 \cdot \mathbf{i}_1}{\sigma_{avg}} + \frac{\mathbf{i}_2 \cdot \mathbf{i}_2}{\kappa} \right)}_{\text{joule heating}} \quad (71)$$

The first term in the expression for  $P$  is the reversible component of power. The second term accounts for the losses due to kinetic phenomena and the third term accounts for the ohmic losses. Since by our conventions anodic overpotential and anodic currents are positive and corresponding cathodic are negative,  $Q$  reduces to

$$Q = \sum_k r_k (-\Delta H_k + \Delta G_k) + \sum_k a i_k \eta_k + \left( \frac{\mathbf{i}_1 \cdot \mathbf{i}_1}{\sigma_{avg}} + \frac{\mathbf{i}_2 \cdot \mathbf{i}_2}{\kappa} \right) \quad (72)$$

which further reduces to :

$$Q = \sum_k r_k (-T \Delta S_k) + \sum_k a i_k \eta_k + \left( \frac{\mathbf{i}_1 \cdot \mathbf{i}_1}{\sigma_{avg}} + \frac{\mathbf{i}_2 \cdot \mathbf{i}_2}{\kappa} \right) \quad (73)$$

The entropy change is related to the free energy by:

$$\Delta S_k = - \left( \frac{\partial (\Delta G_k)}{\partial T} \right)_p \quad (74)$$

And for an electrochemical reaction, the free energy is related to the potential as:

$$\Delta G_k = -n_k \mathbf{F} U_{k,ref} \quad (75)$$

Also

$$r_k = \frac{ai_k}{n_k \mathbf{F}} \quad (76)$$

Thus equation (72) simplifies to equation (50)

$$Q = \sum_k ai_k \left( -T \frac{\partial U_{k,ref}}{\partial T} \right) + \sum_k ai_k \eta_k + \left( \frac{\mathbf{i}_1 \cdot \mathbf{i}_1}{\sigma_{avg}} + \frac{\mathbf{i}_2 \cdot \mathbf{i}_2}{\kappa} \right) \quad (77)$$

which after rearrangement leads to:

$$Q = \sum_k ai_k \left( \eta_k - T \frac{\partial U_{k,ref}}{\partial T} \right) + \left( \frac{\mathbf{i}_1 \cdot \mathbf{i}_1}{\sigma_{avg}} + \frac{\mathbf{i}_2 \cdot \mathbf{i}_2}{\kappa} \right) \quad (78)$$

which is the source term for the energy equation.

Fig 1. Schematic of a silver zinc-cell

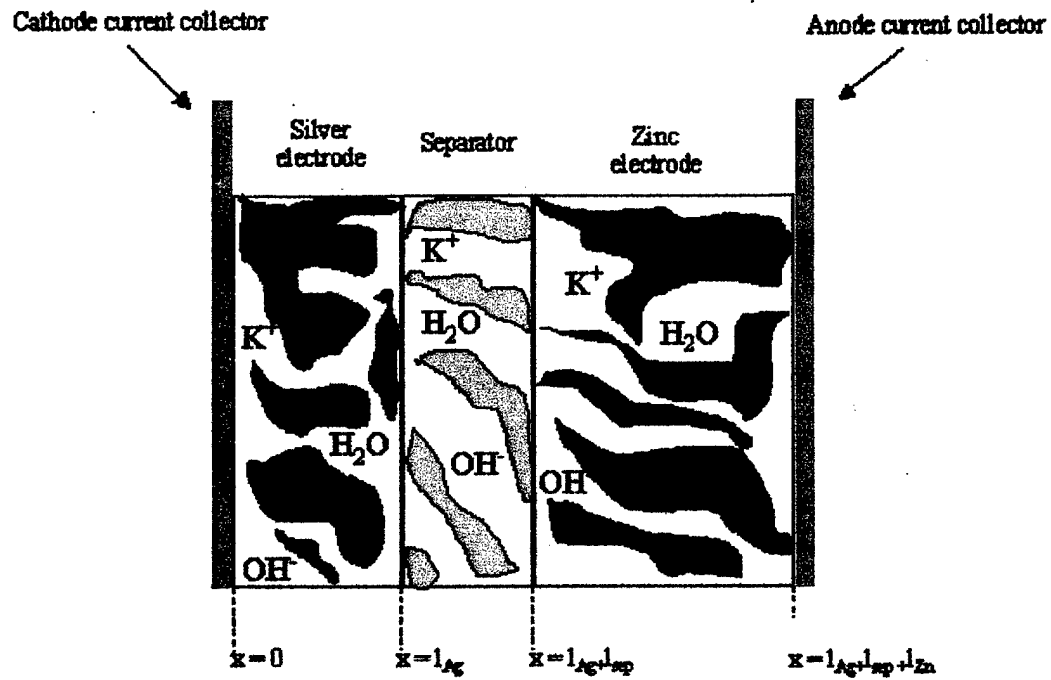


Fig 2. Stack of silver-zinc cells

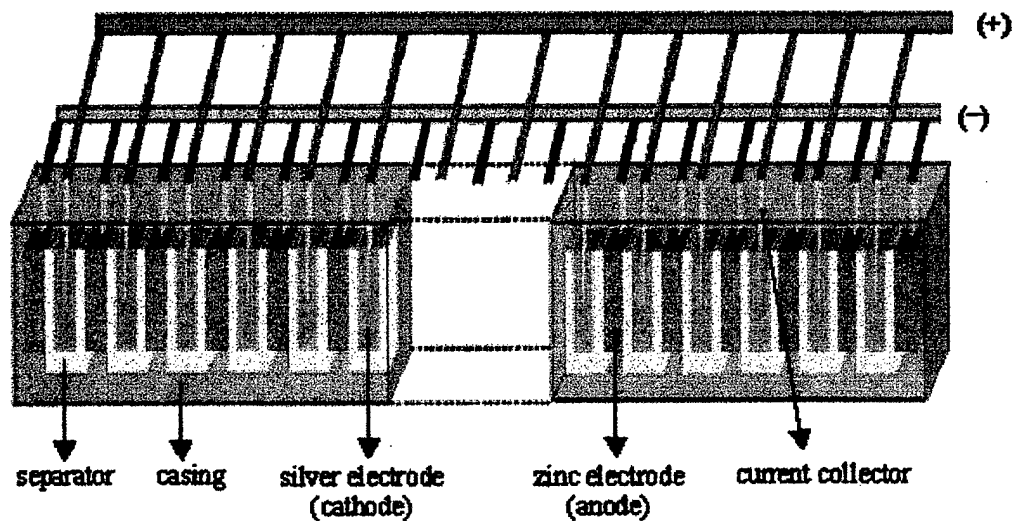


Fig 3. Five-cell stack grid

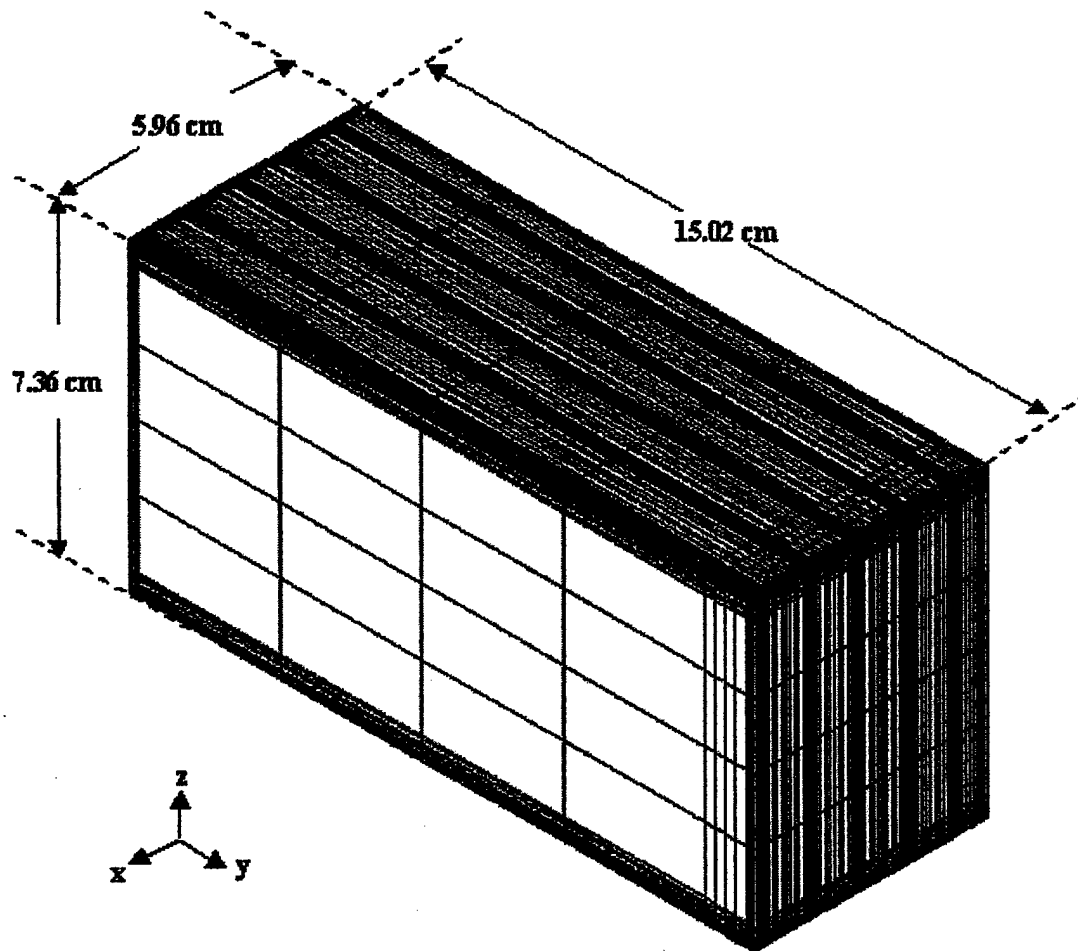


Fig 4. Effect of  $i_{01}$  on cell voltage for 1C and 2C discharge rates

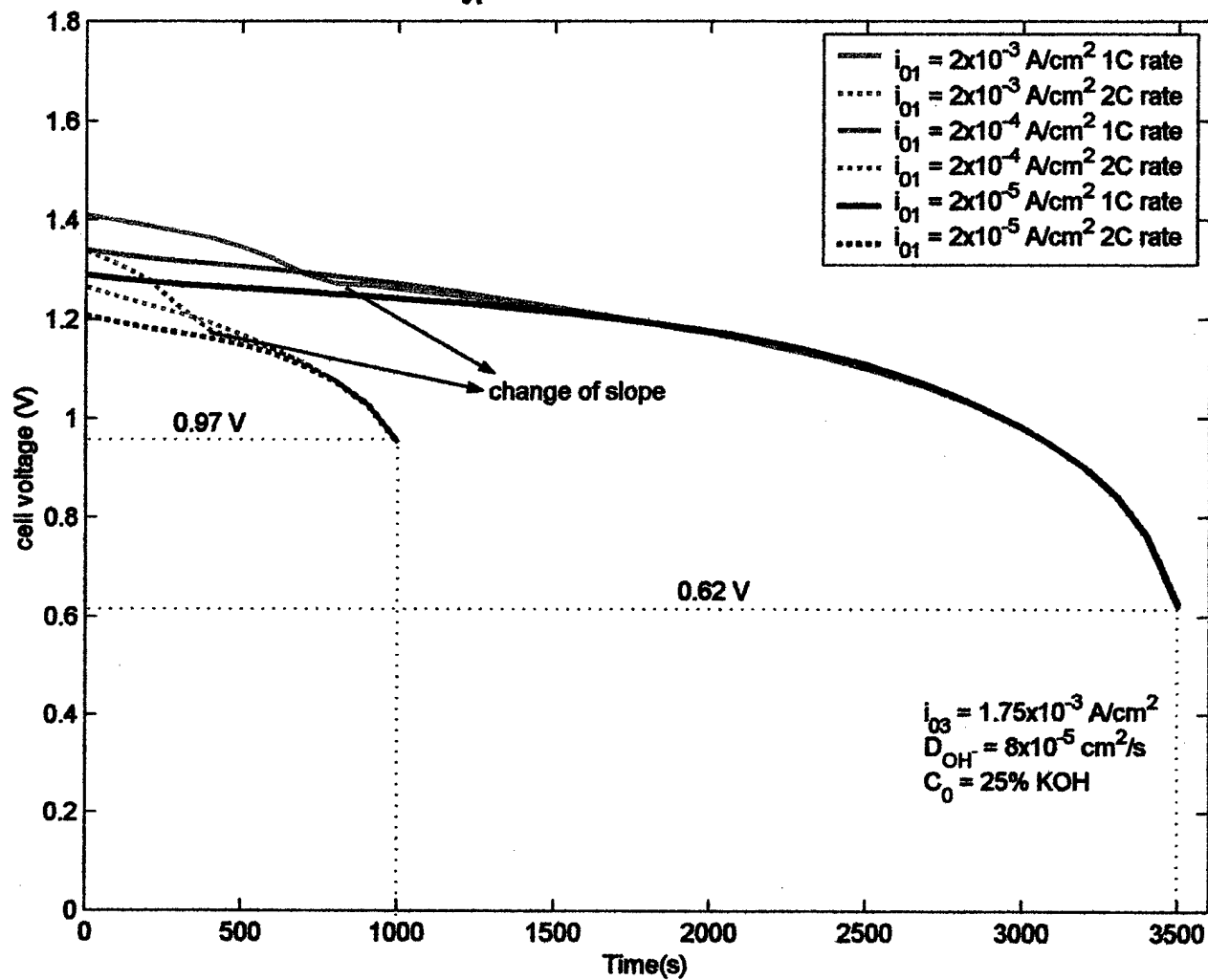


Fig 5. Effect of  $i_{O_2}$  on cell voltage for 1C and 2C discharge rates

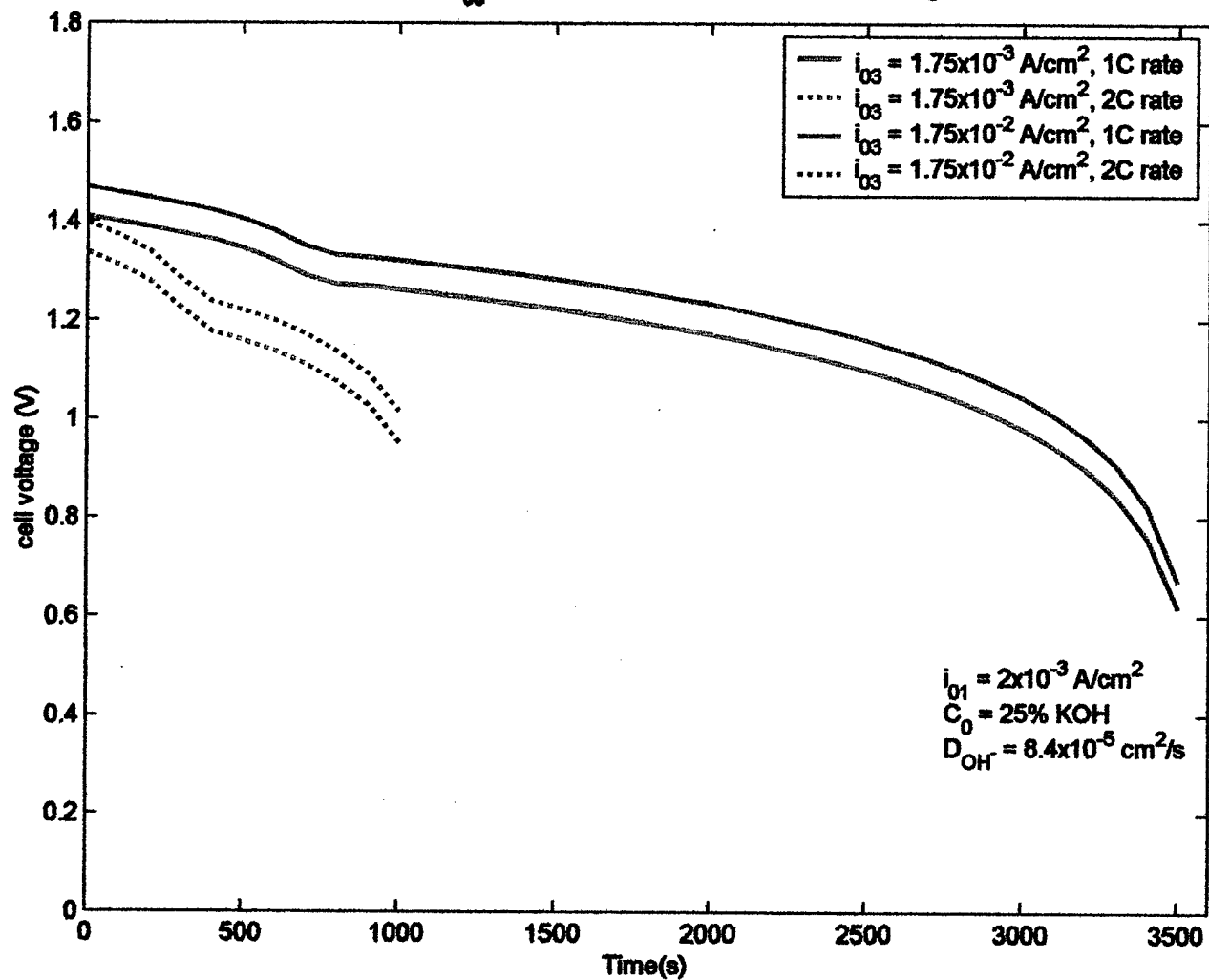




Fig 6. Effect of Initial concentration ( $C_0$ ) of  $\text{OH}^-$  on cell voltage for 1C and 2C discharge rates

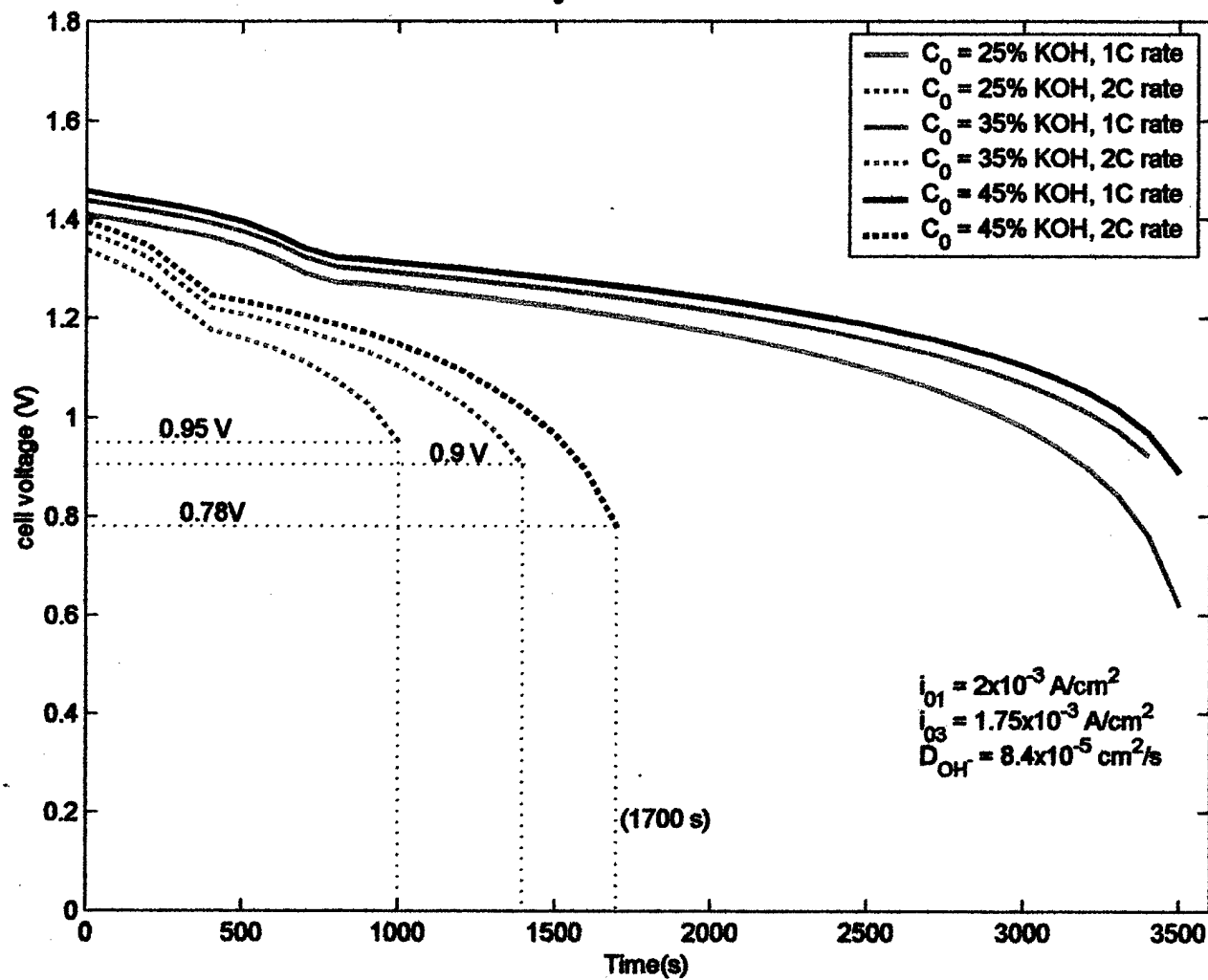


Fig 7. Typical concentration profile during discharge (1C rate)

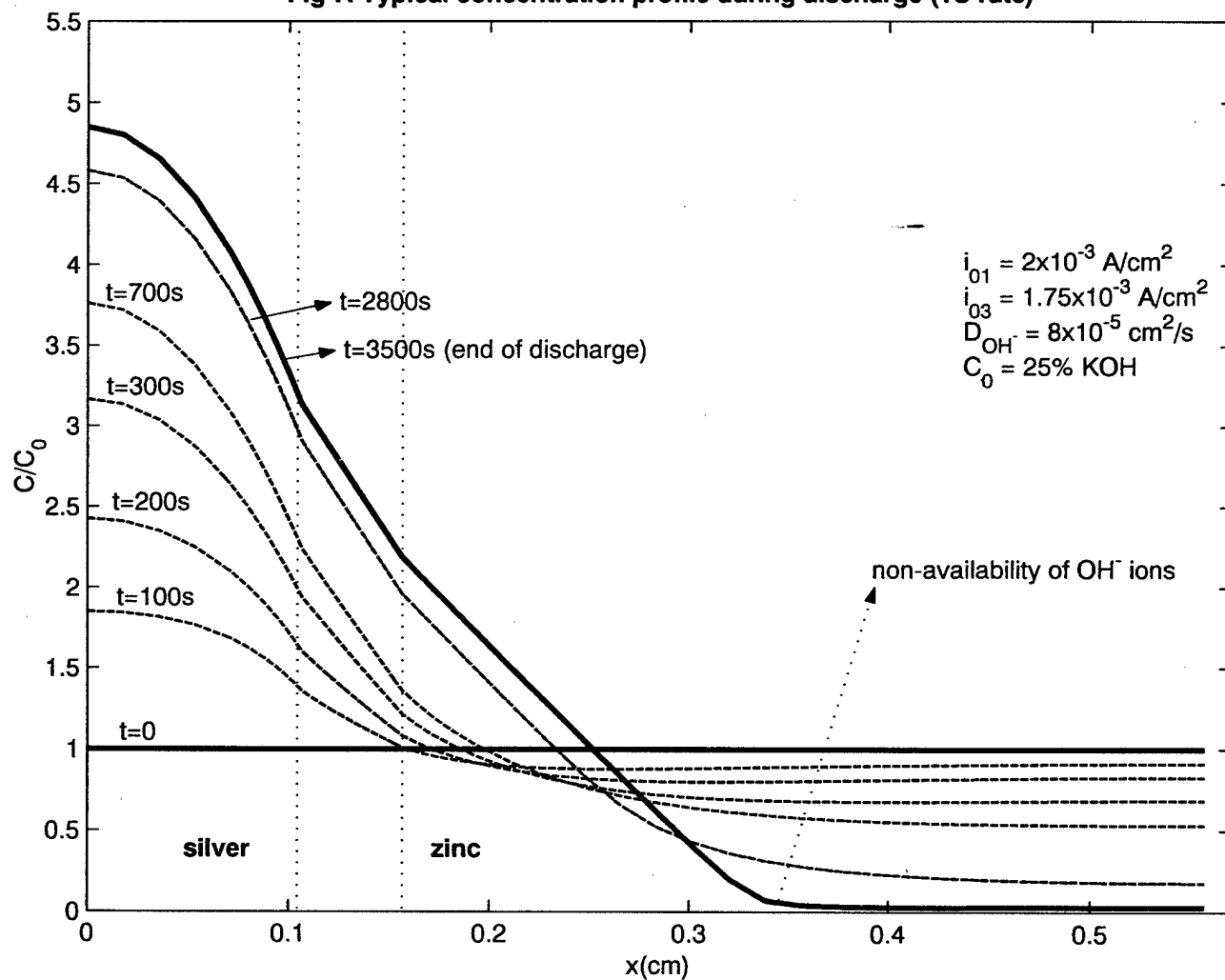


Fig 8. Typical concentration profile during discharge (2C rate)

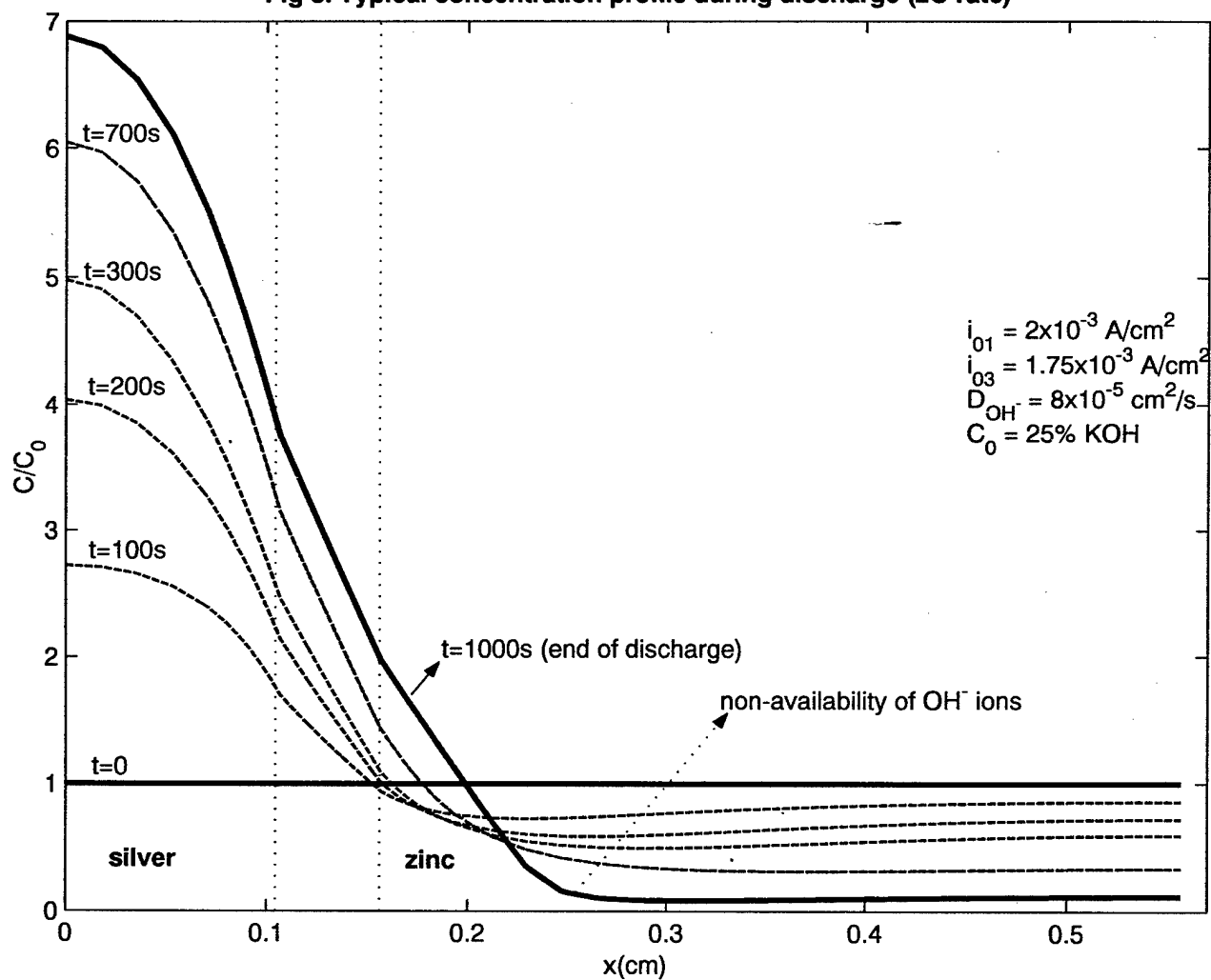


Fig 9. Effect of  $D_{OH^-}$  on cell voltage for 1C and 2C discharge rates

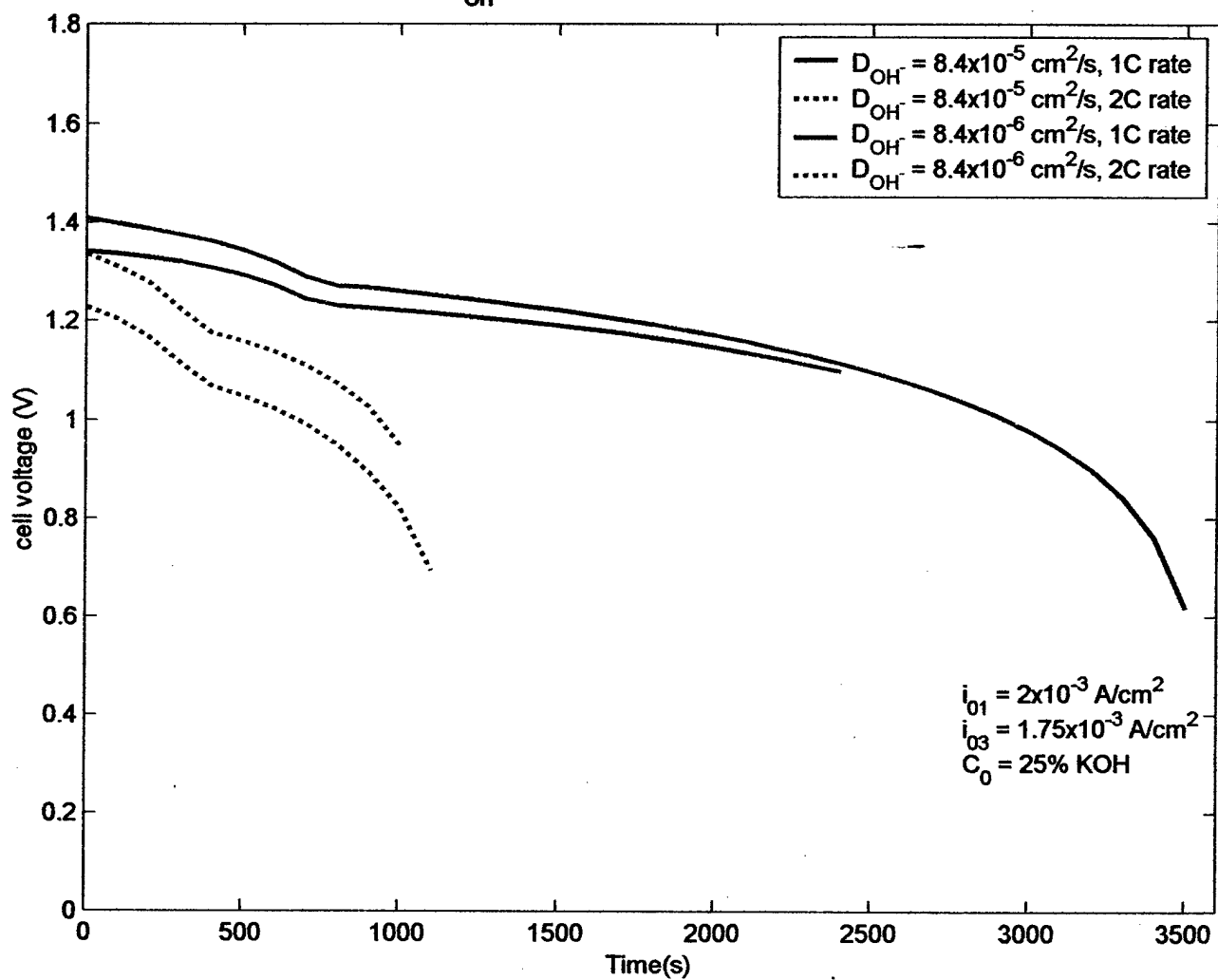


Fig 10. Typical reaction distribution in zinc electrode (1Crate)

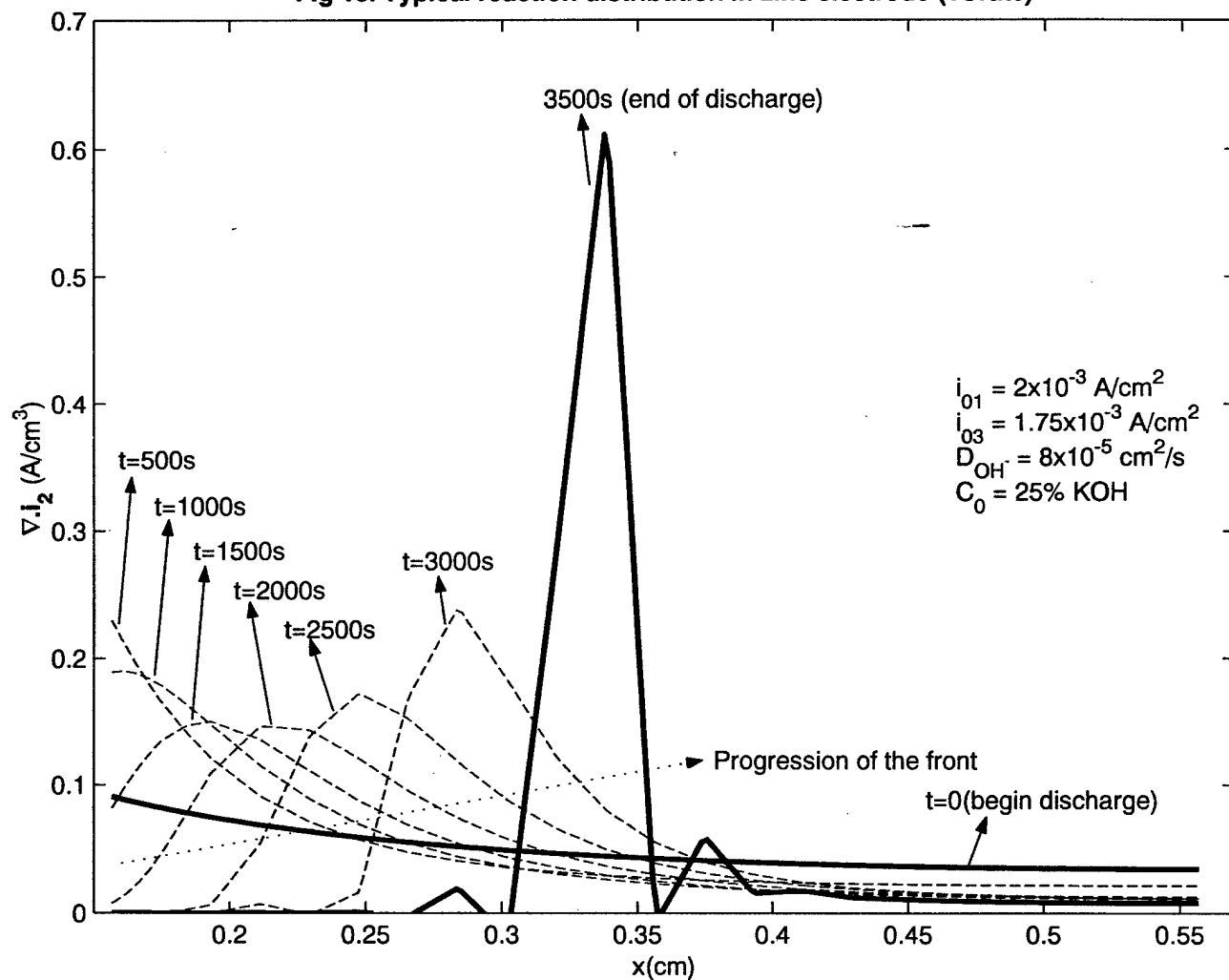


Fig 11. Typical reaction distribution in zinc electrode (2Crate)

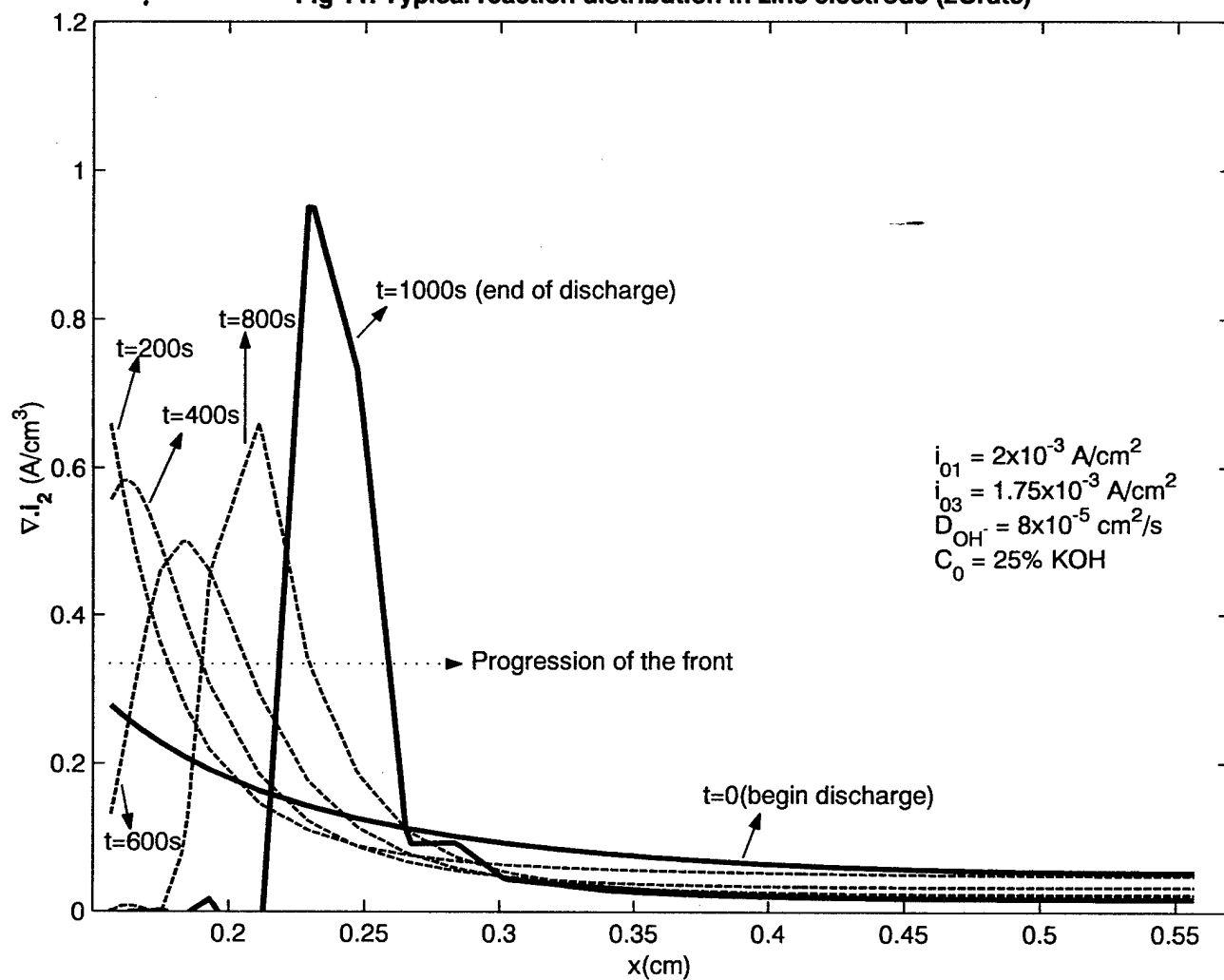


Fig 12. Typical distribution of Zn in zinc electrode (1C rate)

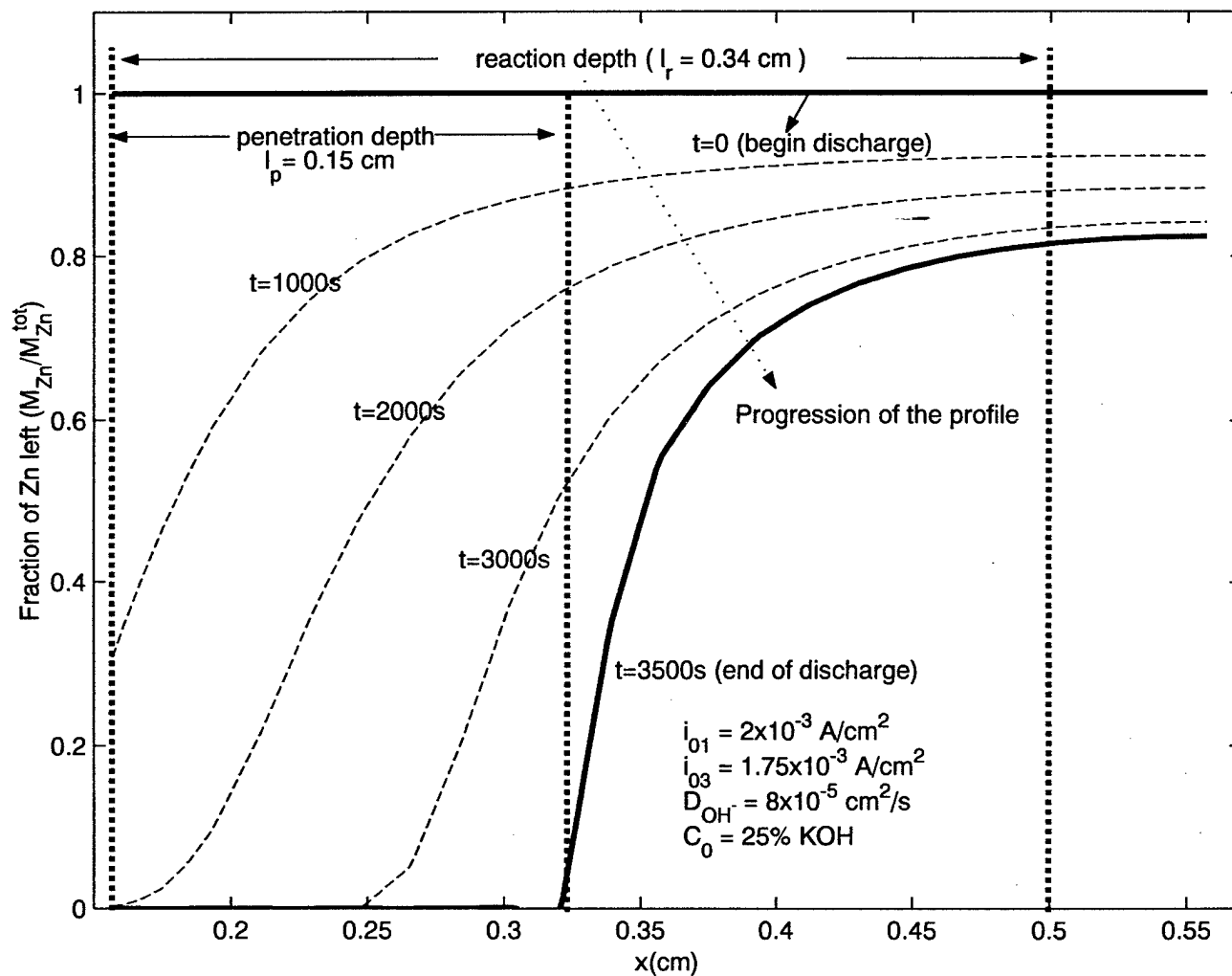


Fig 13. Typical distribution of Zn in zinc electrode (2C rate)

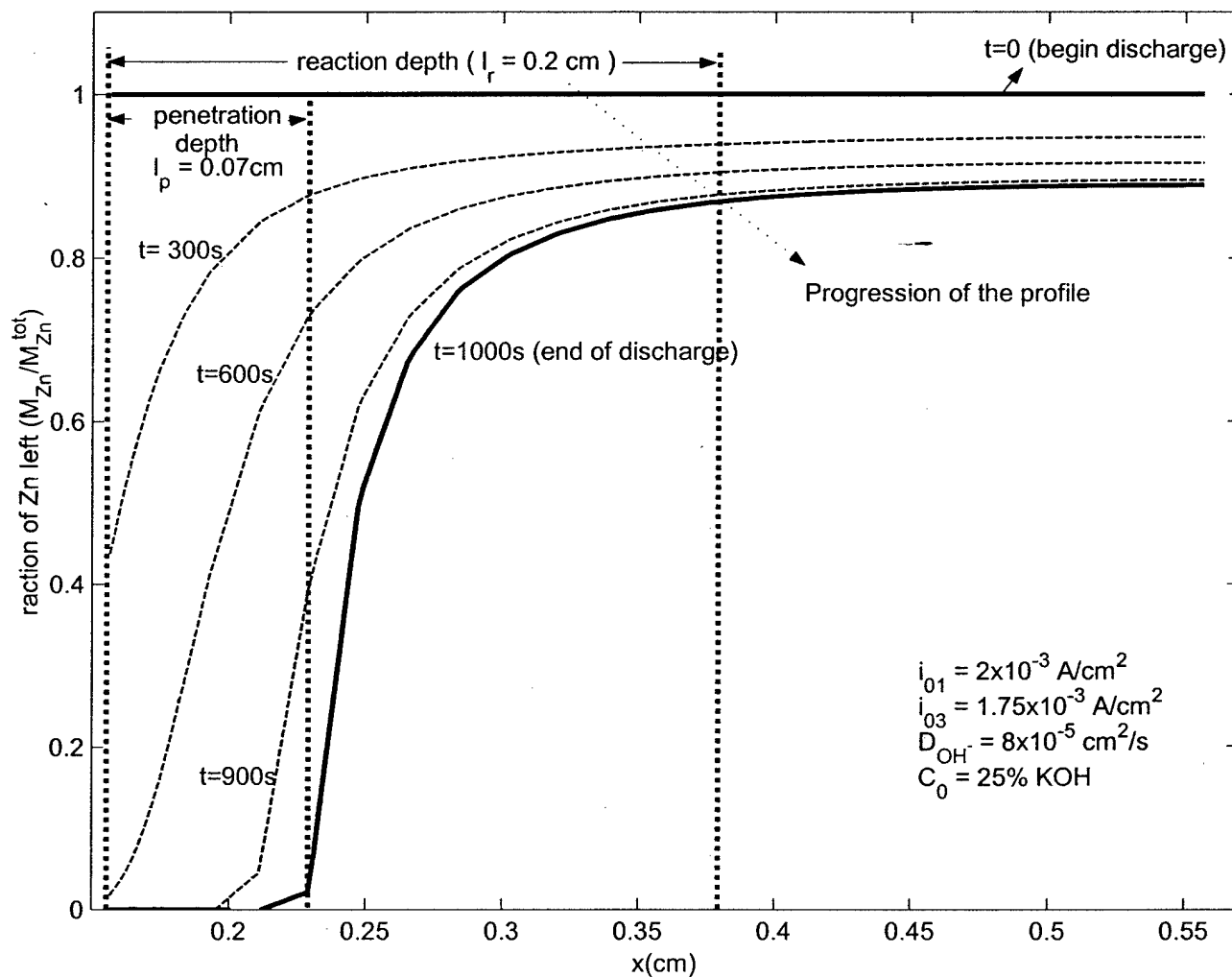




Fig 14. Typical reaction distribution in silver electrode (1C rate)

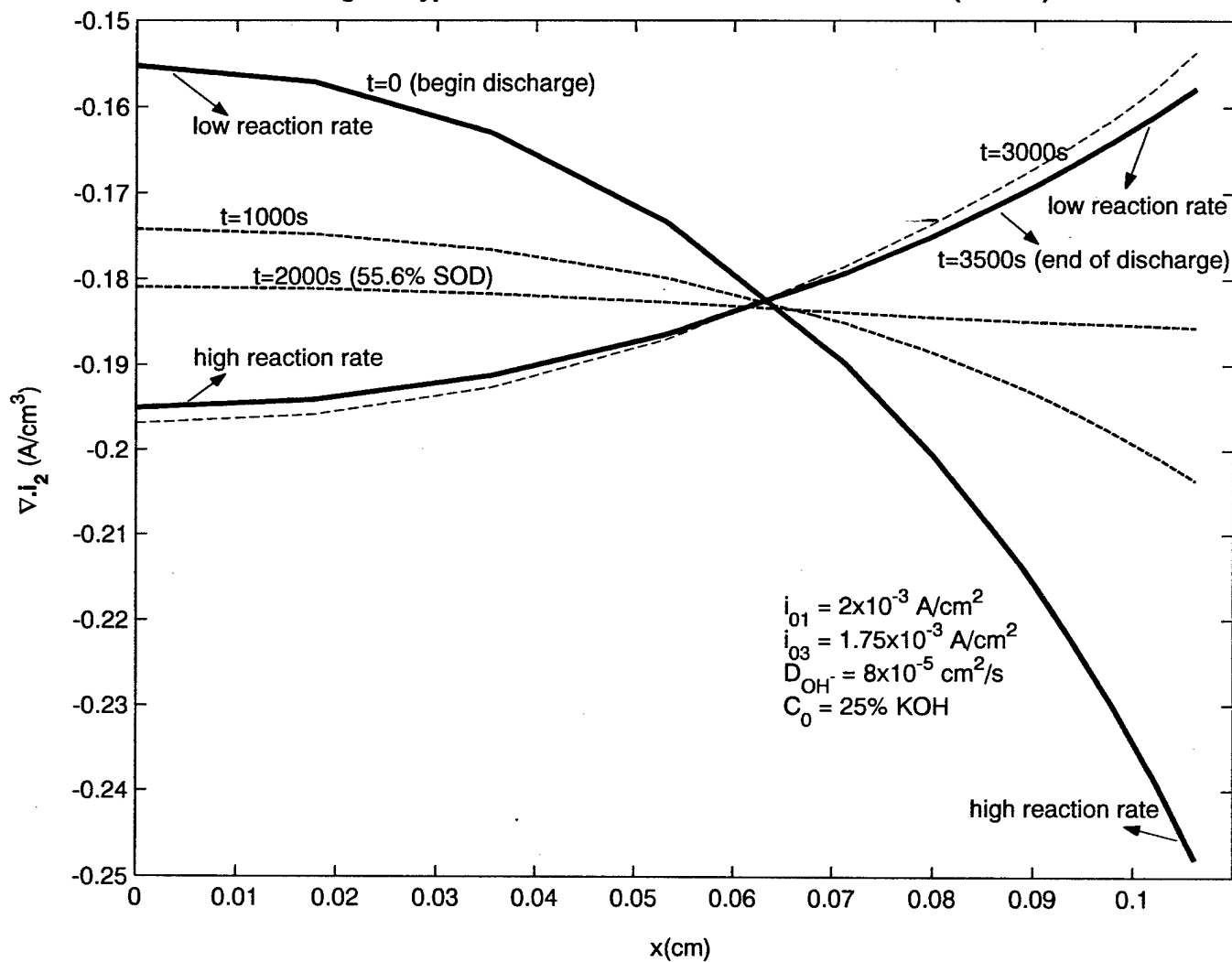


Fig 15. Typical reaction distribution in silver electrode (2C rate)

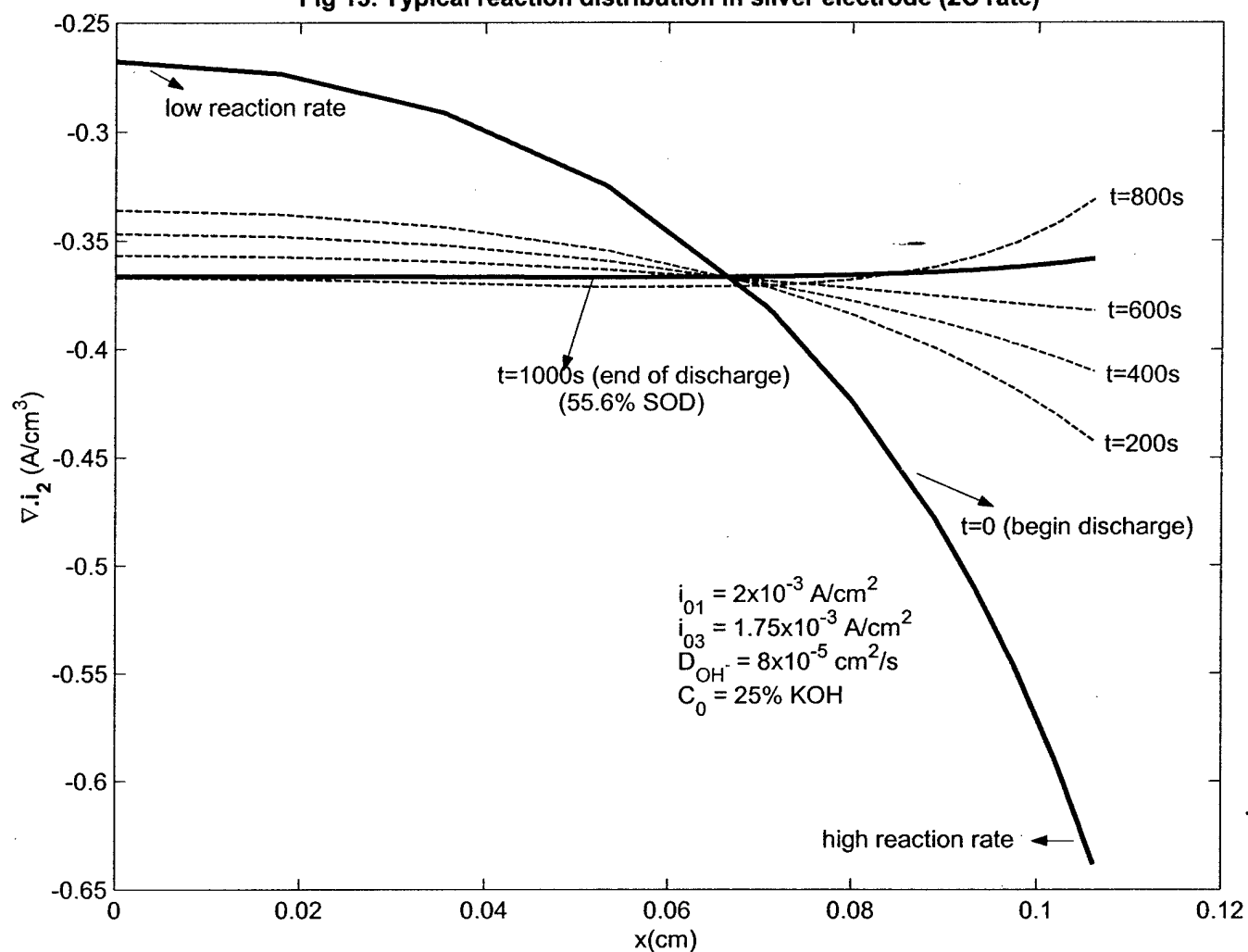


Fig 16. Variation of (normalized) rate of reaction 1 ( $f_2$ ) with time

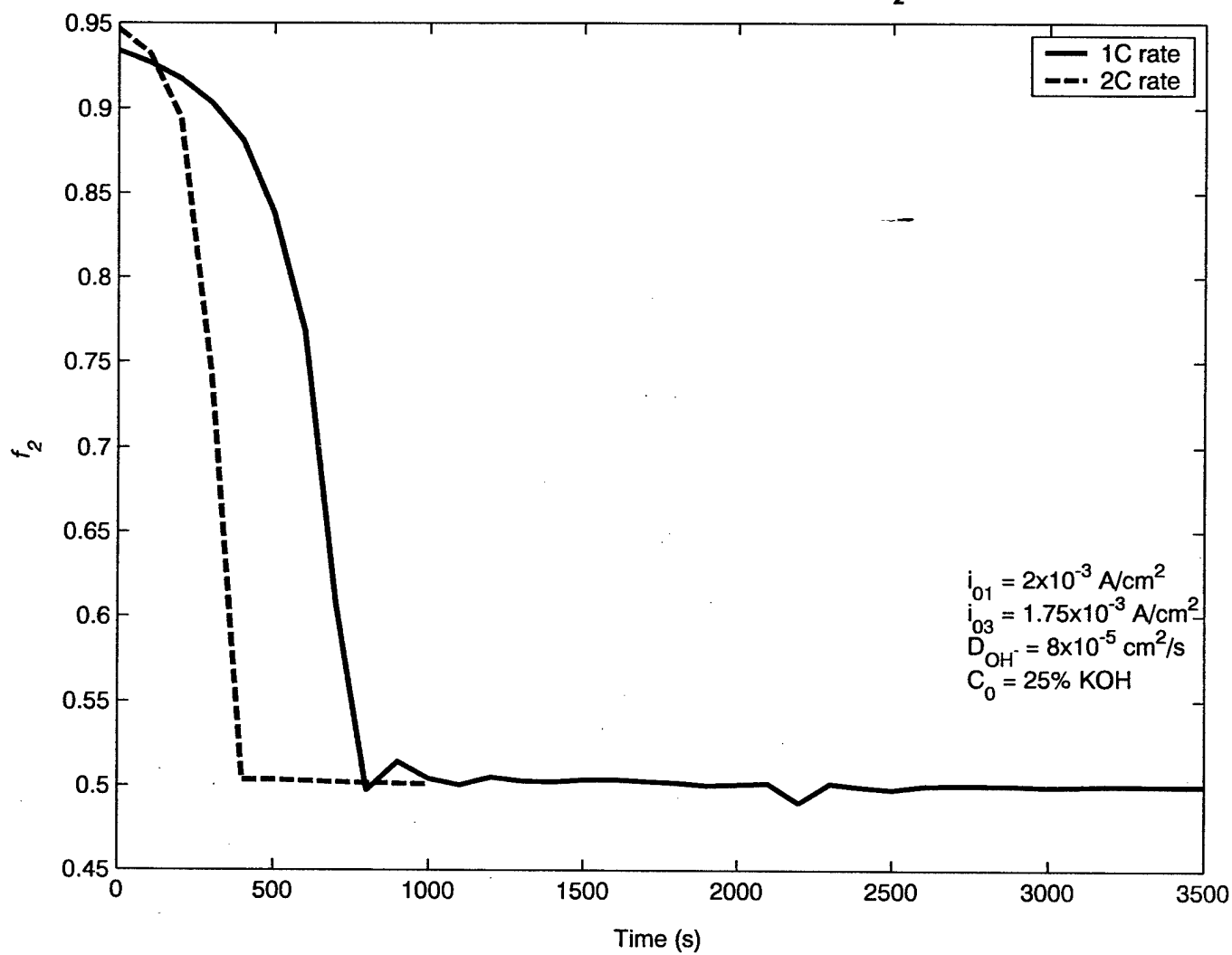


Fig 17. Net rate of production of  $\text{Ag}_2\text{O}$  vs time

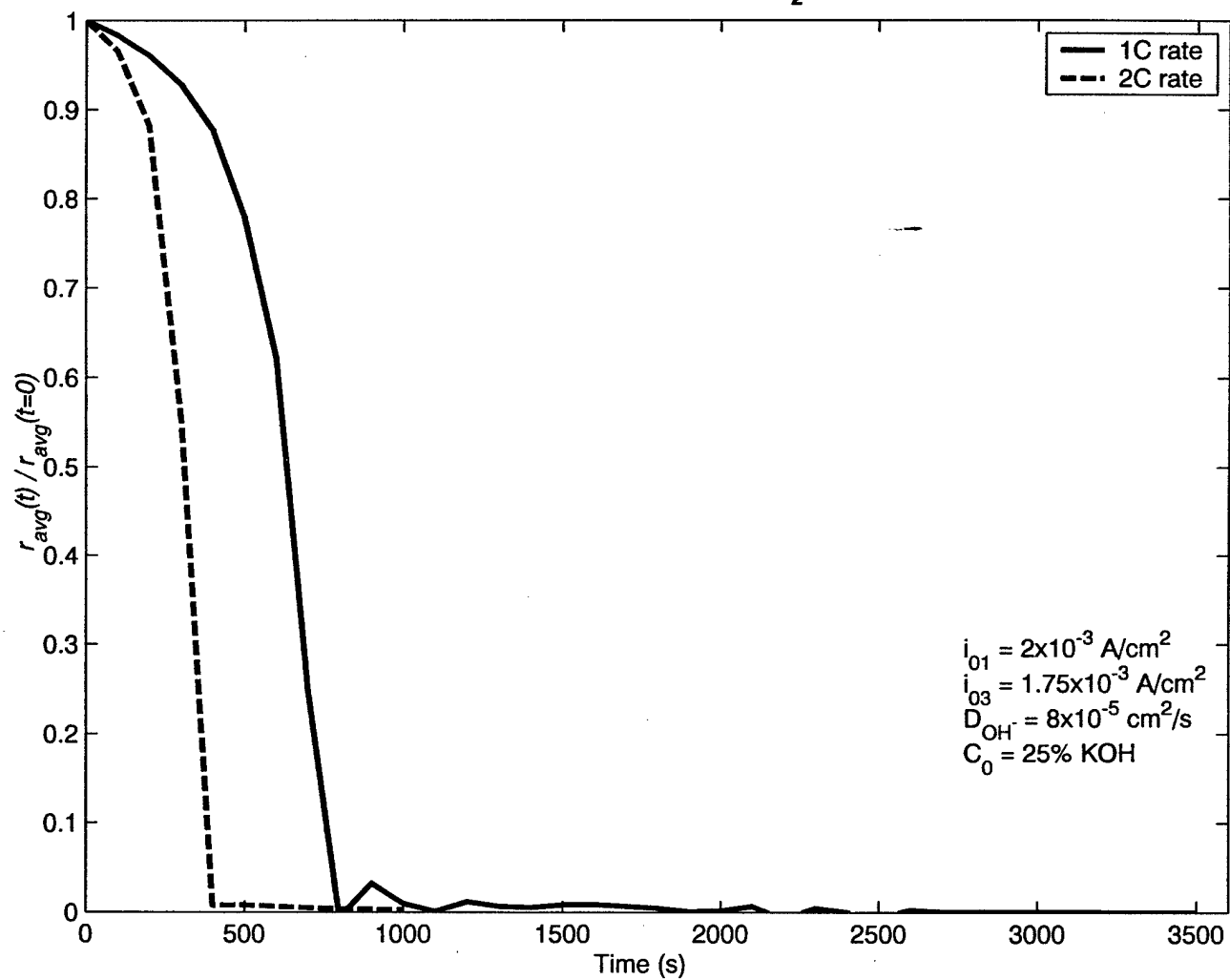


Fig 18. Distribution of  $\text{Ag}_2\text{O}$  over the silver electrode vs time (1C rate)

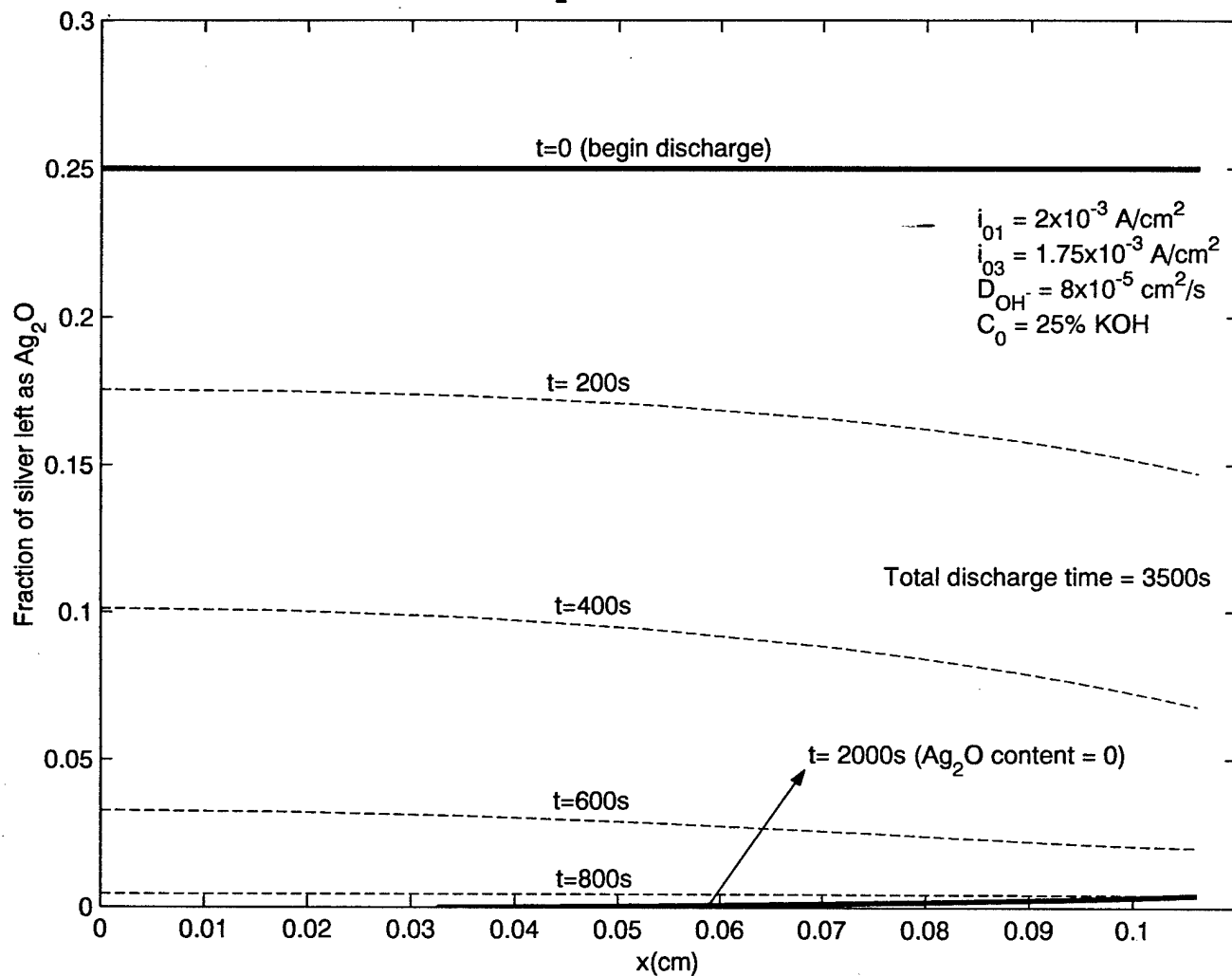


Fig 19. Distribution of  $\text{Ag}_2\text{O}$  over the silver electrode vs time (2C rate)

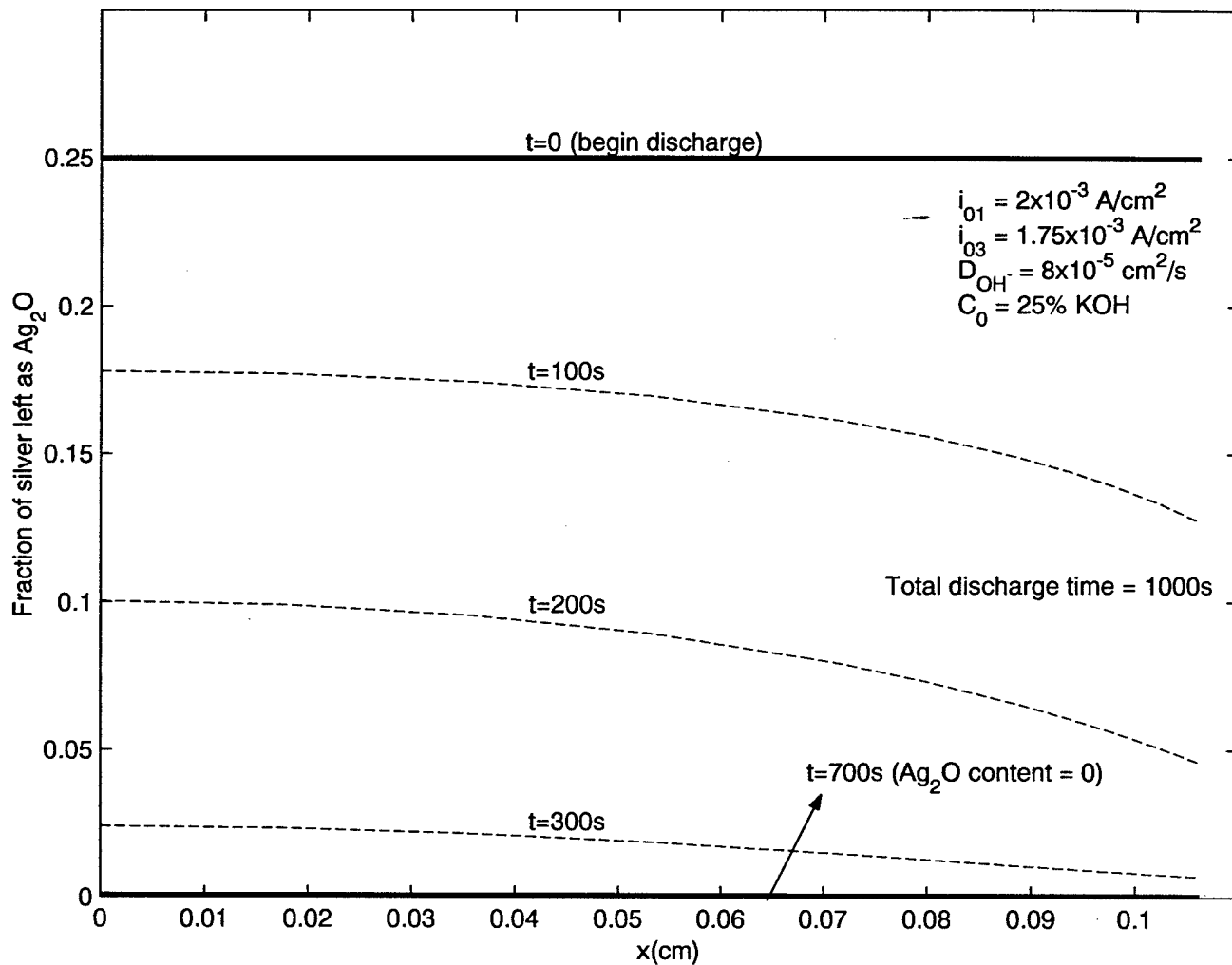


Fig 20. Typical porosity distribution profiles (1C rate)

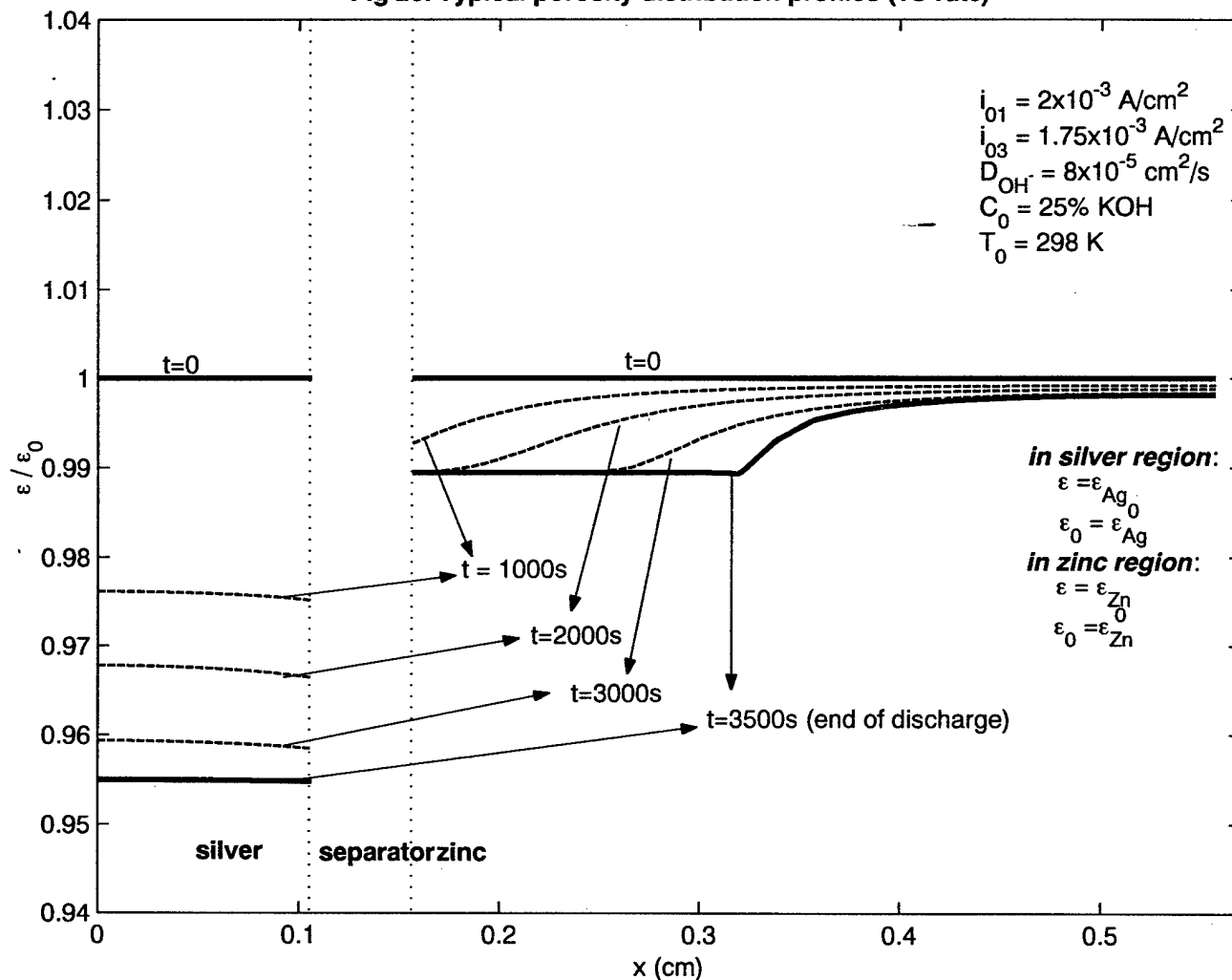


Fig 21. Typical temperature rise profiles in silver-zinc cell (1C rate)

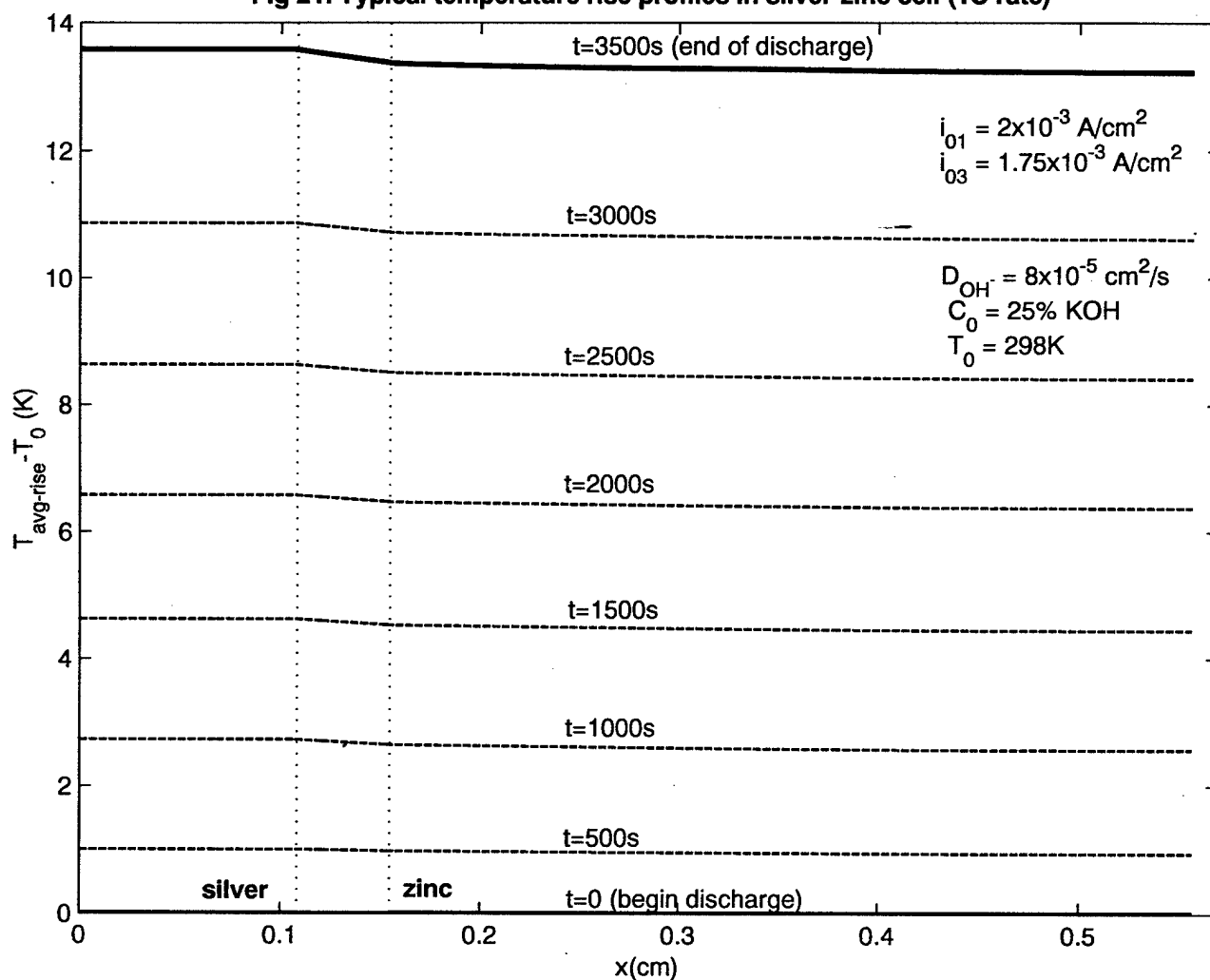




Fig 22. Typical temperature rise profiles in a silver-zinc cell (2C rate)

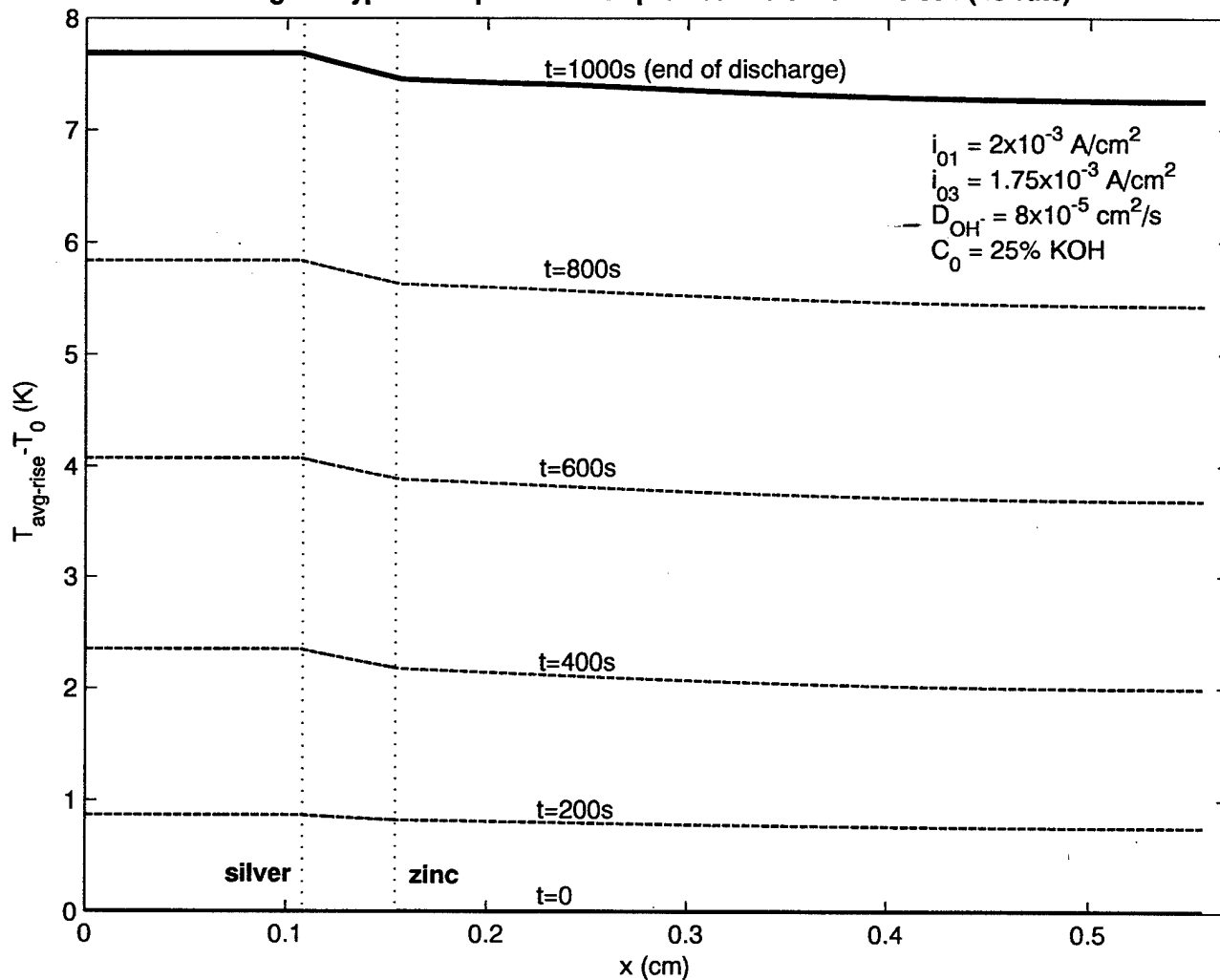


Fig 23. Effect of  $i_{01}$  on the average temperature rise of the cell

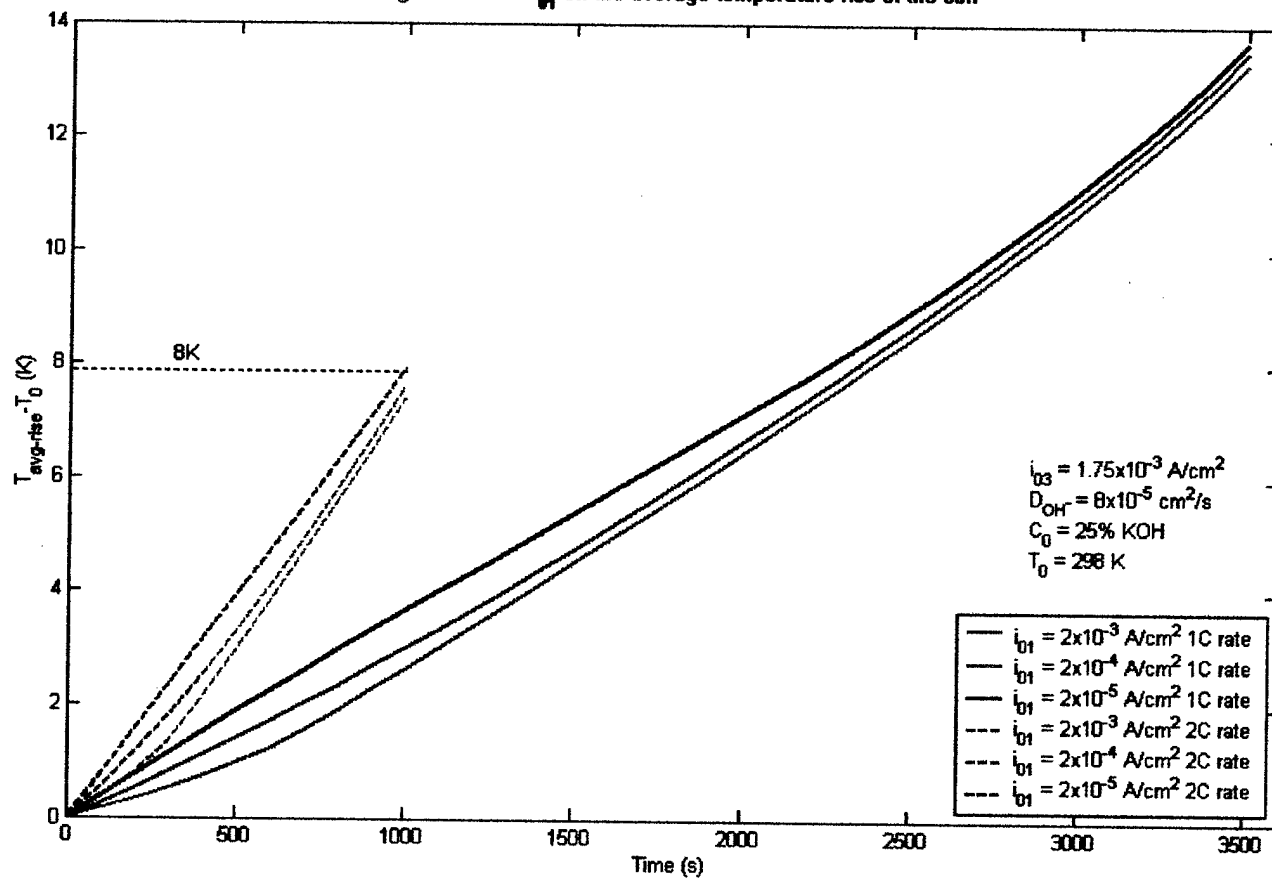


Fig 24. Effect of  $i_{03}$  on the average temperature rise of the cell

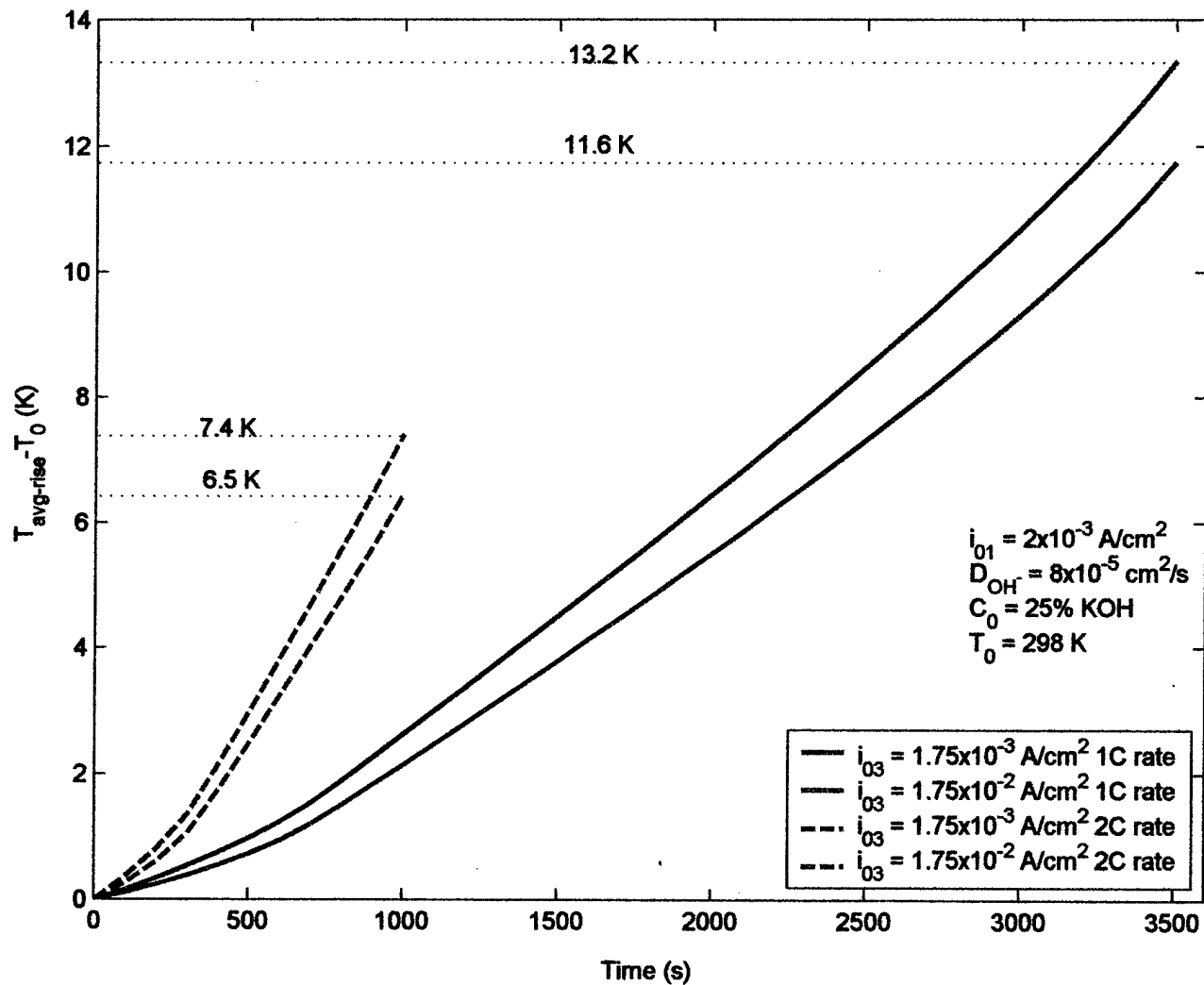


Fig 25. Effect of  $D_{OH^-}$  on the average temperature rise of the cell

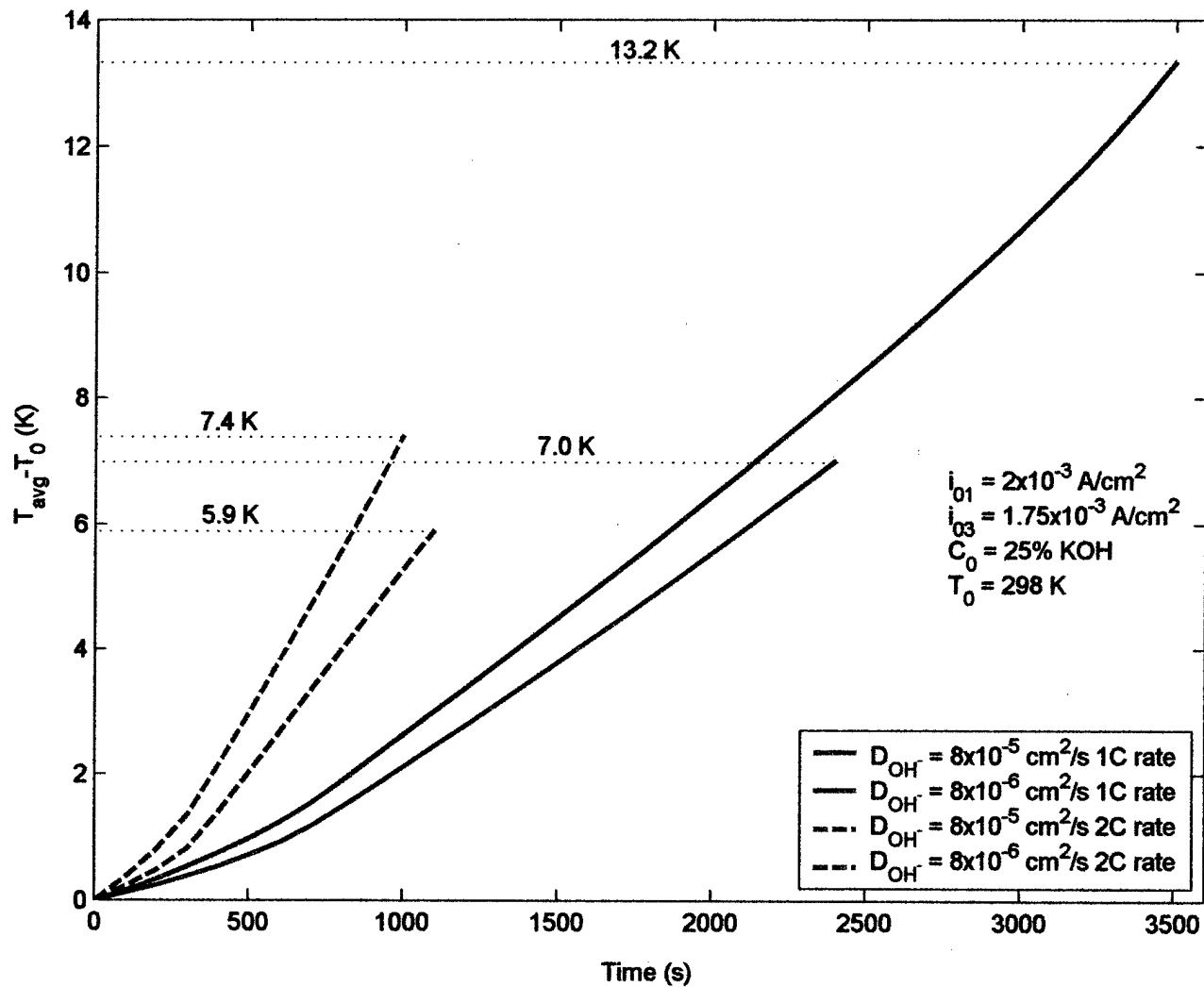
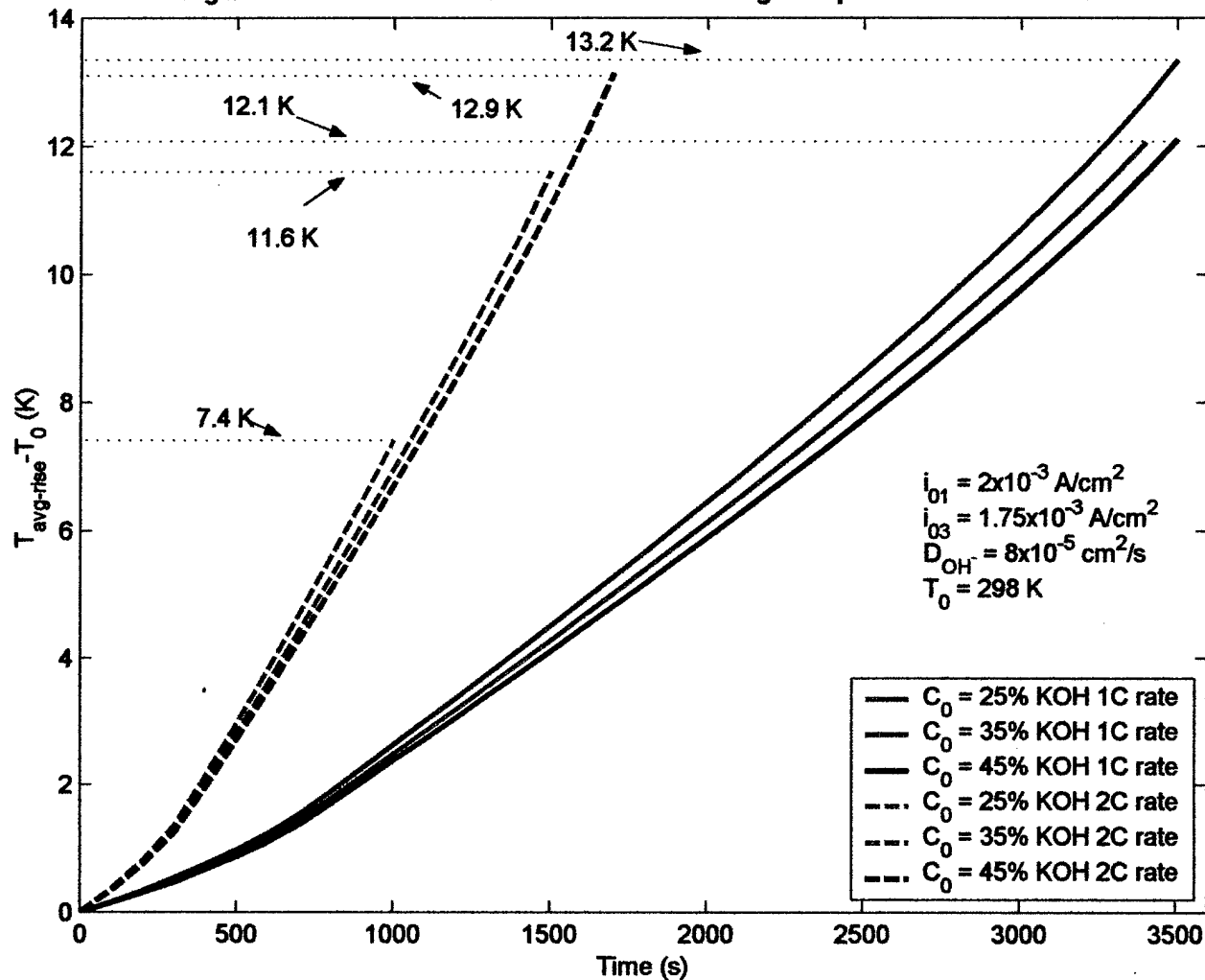


Fig 26. Effect of initial concentration on the average temperature rise in the cell



**This Page is Left Blank Intentionally**

Fig 27. Temperature profiles in 5-cell stack (full body view)

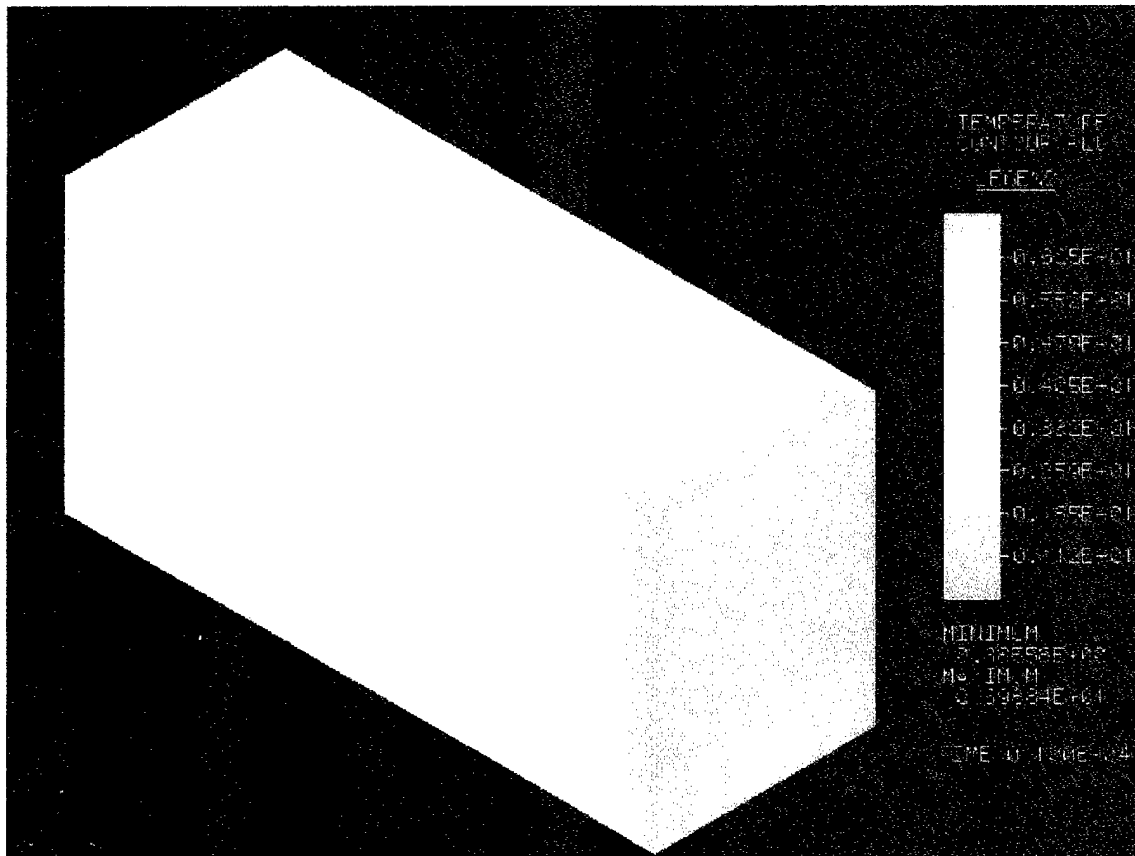
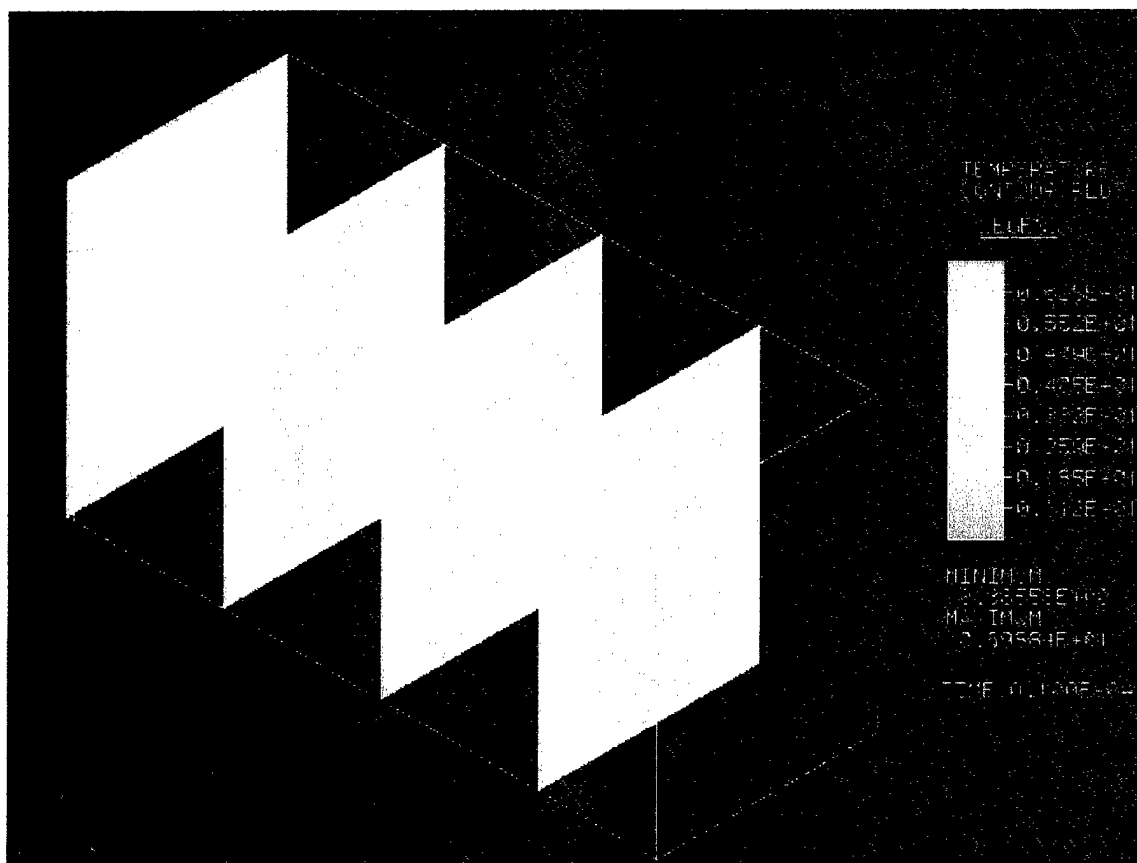
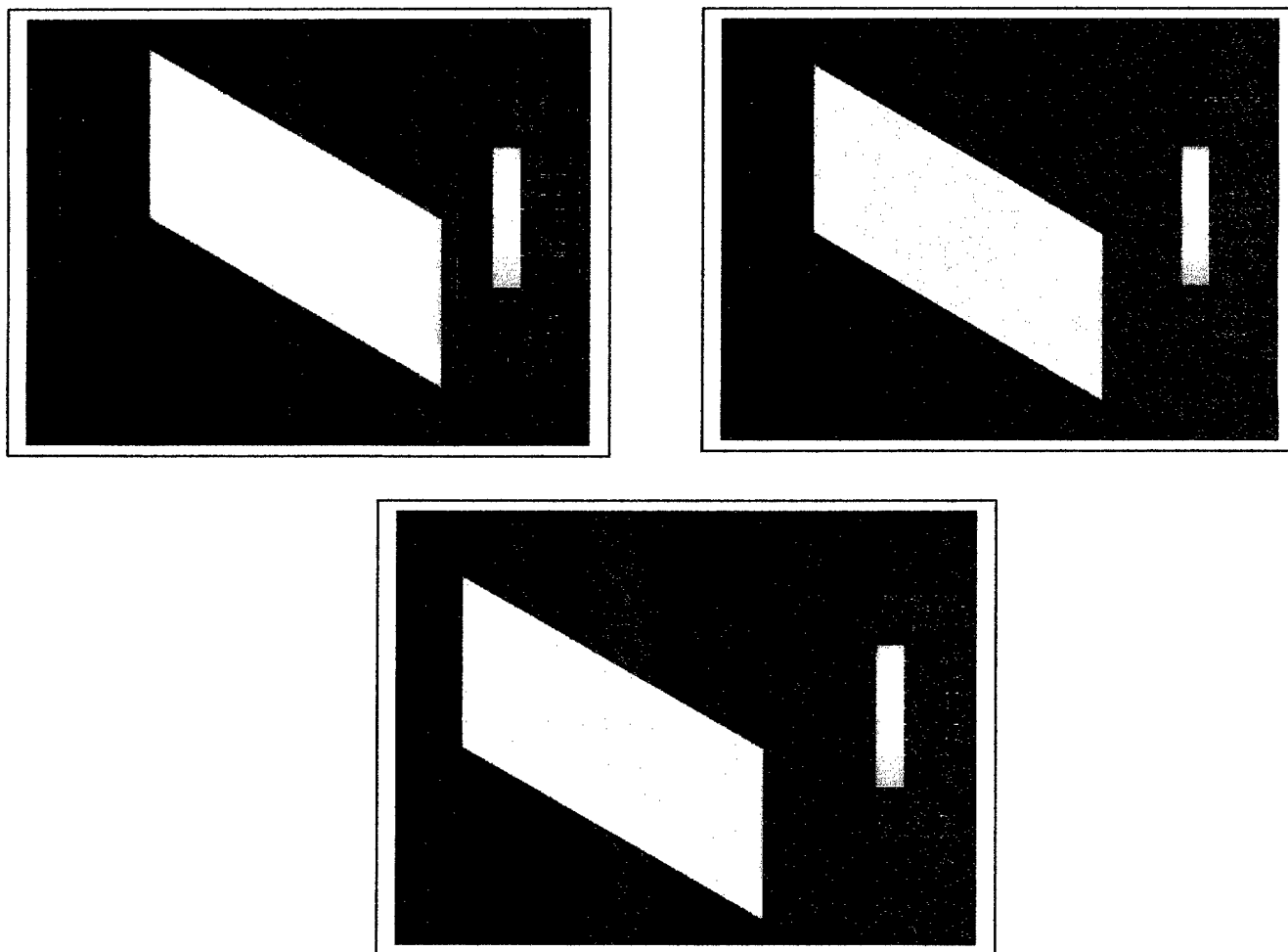


Fig 28. Temperature profiles in 5-cell stack (x-z planes)





**Fig 29. Temperature profiles in 5-cell stack (*y-z* planes)**



**Table 6 - Parameters**

$a_{Ag}$	50 (cm <sup>2</sup> /cm <sup>3</sup> )
$a_{Zn}$	50 (cm <sup>2</sup> /cm <sup>3</sup> )
$C_{OH^-}^b$	8x10 <sup>-3</sup> (mol/cm <sup>3</sup> )
$c_{p,Ag}$	0.234 (J/K/g)
$c_{p,AgO}$	0.343 (J/K/g)
$c_{p,Ag_2O}$	0.343 (J/K/g)
$c_{p,l}$	2.52 (J/K/g)
$c_{p,sep}$	1.339 (J/K/g)
$c_{p,Zn}$	0.389 (J/K/g)
$c_{p,ZnO}$	2.91 (J/K/g)
$D_{K^+}$	0.84x10 <sup>-5</sup> (cm <sup>2</sup> /s)
<b>F</b>	96487 C
$i_{02}$	2.52x10 <sup>-5</sup> (A/cm <sup>2</sup> )
$k_{Ag}$	4.3 (W /cm /K)

$k_{AgO}$	0.207 (W /cm /K)
$k_{Ag_2O}$	0.207 (W /cm /K)
$k_l$	0.02 (W /cm /K)
$k_{sep}$	0.0024 (W /cm /K)
$k_{Zn}$	1.2 (W /cm /K)
$k_{ZnO}$	0.207 (W /cm /K)
$l_{Ag}$	0.1067 cm
$l_{sep}$	0.05 cm
$l_{Zn}$	0.4 cm
$M_{Ag}^0$	0
$M_{AgO}^0$	0.003 mol/cm <sup>3</sup>
$M_{Ag}^{tot}$	0.004 mol/cm <sup>3</sup>
$M_{Zn}^0$	0.0015 mol/cm <sup>3</sup>
$M_{Zn}^{tot}$	0.0015 mol/cm <sup>3</sup>

$M_{Ag}^w$	108
$M_{AgO}^w$	124
$M_{Ag_2O}^w$	232
$M_{Zn}^w$	65
$M_{ZnO}^w$	81
$n_1$	2
$n_2$	2
$n_3$	2
<b>R</b>	8.314 (J/mol/K)
$s_{OH^-,1}$	2
$s_{OH^-,2}$	2
$s_{OH^-,3}$	2
$s_{Ag,2}$	2
$s_{AgO,1}$	-2
$s_{Zn,3}$	2

$T_0$	298 K
$U_1^0$	0.604 V
$U_2^0$	0.342 V
$U_3^0$	-1.305 V
$V_{Ag}$	7.3 cm <sup>3</sup>
$V_{Zn}$	27.5 cm <sup>3</sup>
$z_{K^+}$	1
$z_{OH^-}$	-1
$\alpha_{a1}$	1.3
$\alpha_{c1}$	0.7
$\alpha_{a2}$	1.5
$\alpha_{c2}$	0.5
$\alpha_{a3}$	1
$\alpha_{c3}$	1

$\epsilon_{Ag}^0$	0.322
$\epsilon_{sep}$	0.5
$\epsilon_{Zn}^0$	0.731
$\theta_1$	0.866
$\theta_2$	0.333
$\tau$	1
$\xi$	1.5

S.No	Reference
1.	Walter J.Hammer and D.Norman Craig, in "A reproducible and stable Silver-Silver oxide electrode," <i>J. Electrochem. Soc.</i> , <b>104</b> , 206 (1957)
2.	Dirkse, in "The Silver Oxide Electrode" Technical Review, <i>J. Electrochem. Soc.</i> , <b>454</b> (1959)
3.	Charles P. Wales and Jeanne Burbank, in "Oxides on the silver electrode", <i>J. Electrochem. Soc.</i> , <b>106</b> , 885(1959)
4.	Dirkse in "The AgO-Ag <sub>2</sub> O electrode in the alkaline solution", <i>J. Electrochem. Soc.</i> , <b>109</b> , 173(1962)
5.	E.G.Gagnon and L.G.Austin, <i>J. Electrochem. Soc.</i> , <b>119</b> , 807-811 (1972)
6.	Frank R. McLarnon and Elton J. Carins in "The secondary alkaline zinc electrode", <i>J. Electrochem. Soc.</i> , <b>138</b> , 645 (1991)
7.	King Wai Choi and Douglas N.Bennion and John Newman in "Engineering analysis of shape change in zinc secondary electrode", <i>J. Electrochem. Soc.</i> , <b>123</b> , 1616 (1976)
8.	Drannan Hamby and Jeffrey Wirkkala in "Further experimental tests of the convective flow theory of Zn secondary electrode shape change", <i>J. Electrochem. Soc.</i> , <b>125</b> , 1020 (1978)
9.	John S. Newman and Charles W. Tobias in "Theoretical analysis of current distribution in porous electrodes" <i>J. Electrochem. Soc.</i> , <b>109</b> , 1181 (1962)
10.	John Newman and William Tidemann in "Porous Electrode theory with battery applications", <i>AIChE journal</i> , Vol <b>21</b> , 25 ( Jan 1975)
11.	K.W.Choi and N.P.Yao in " A mathematical model for porous nickel electrodes in zinc.nickel oxide cells"
12.	W.G.Sunu, Ph.D thesis, University of California, Los Angeles, CA (1978)
13	W.G.Sunu and D.N.Bennion in "Transient amd failure analyses of the porous zinc electrode – Part 1", <i>J. Electrochem. Soc.</i> , <b>127</b> , 2007(1980)
14	W.G.Sunu and D.N.Bennion in "Transient amd failure analyses of the porous zinc electrode – Part 2", <i>J. Electrochem. Soc.</i> , <b>127</b> , 2017(1980)
15	S.L.Blanton, J.W.Weidner and J.W.Vanzee, in the Proceedings of the Douglas N. Bennion Memorial Symposium on Topics in Electrochemical Engineering, J.Newman and R.E.White, Eds, Proceedings Vol.94-22, The Electrochemical Society Inc., Pennington,NJ, 208-228 (1994)
16	K.W.Choi and N.P.Yao in "", <i>J. Electrochem. Soc.</i> , <b>125</b> , 1011-1019, (1978)
17	K.W.Choi and N.P.Yao in "", <i>J. Electrochem. Soc.</i> , <b>126</b> , 1321-1328, (1979)

18	H.F.Gibbard, <i>J. Electrochem. Soc.</i> , <b>125</b> , 353-358(1978)
19	Markku J. Lampinen and Marina Fomino in "Analysis of free energy and entropy changes for half-cell reactions", <i>J. Electrochem. Soc.</i> , <b>140</b> , 3537-3546 (1993)
20	D.Bernardi, E.Pawlikowski and J.Newman in "A general energy balance for battery systems", <i>J. Electrochem. Soc.</i> , <b>132</b> , 5-12 (1985)
21	J.Lee, K.Choi, N.Yao and C.Christianson in "Three dimensional thermal modeling of electric vehicle batteries", <i>J. Electrochem. Soc.</i> , <b>133</b> , 1286-1291 (1986)
22	C.Pals and J.Newman in "Thermal modeling of Litium/polymer batery – I. Discharge behavior of a single cell", <i>J. Electrochem. Soc.</i> , <b>142</b> , 3274-3281 (1995)
23	C.Pals and J.Newman in "Thermal modeling of Litium/polymer batery – II. Temperature profiles in a cell stack", <i>J. Electrochem. Soc.</i> , <b>142</b> , 3282-3288 (1995)
24	Albert Himy in "Silver-Zinc battery – Phenomena and Design principles", Vantage Press, First edition (1986)
25	Moden's work in navy
26	E.J.Podlaha and H.Y.Cheh in "Modeling of cylindrical alkaline cells – V. High discharge rates", <i>J. Electrochem. Soc.</i> , <b>141</b> , 15-27(1994)



## Part II: Models and Predictions for the Fuel Cells

**PREDICTING THE ENERGY TRANSPORT INSIDE  
A SERPENTINE FLOW-FIELD PEM FUEL CELL**

by

**S. Shimpalee,<sup>1</sup> and J. W. Van Zee<sup>1,\*</sup>**  
University of South Carolina  
Columbia, SC 29208

**Van Zee Group Technical Memorandum # 10**

**March 2002**

---

<sup>1</sup> Department of Chemical Engineering

\* To whom correspondence should be addressed, Corresponding Author, FAX: (803)-777-8142, e-mail: [vanzee@engr.sc.edu](mailto:vanzee@engr.sc.edu).

## **PREDICTING THE ENERGY TRANSPORT INSIDE A SERPENTINE FLOW-FIELD PEM FUEL CELL**

**S. Shimpalee and J. W. Van Zee\***  
Department of Chemical Engineering  
University of South Carolina  
Columbia, SC 29208

### **Abstract**

In addition to the generation of direct current from a PEM fuel cell (PEMFC), water and heat are also produced. The water inside a PEMFC can be condensed or evaporated depending on the local partial pressures and temperature. These local three-dimensional distributions and the phase change of water in a PEMFC with a serpentine flow field (SFF) are predicted by using Computational Fluid Dynamics (CFD) software modified to include a model that describes the electrochemical reactions, transport through the membrane, and water film formation. The simulations and the resulting energy flows can predict the experimentally observed optimum in current at a fixed voltage and how this optimum depends on inlet humidity. Analysis of the energy flows reveals how water phase-change is coupled with local temperature changes, membrane humidity levels, and variations in the local current density. The predictions also show how the temperature distribution is coupled with the heat of reaction, mass and energy flows, and water evaporation and condensation.

---

\* Corresponding author

## Nomenclature

$a_k$	=	activity of water in stream $k$ , dimensionless
$A_{cv}$	=	specific surface area of the control volume (c.v.), $m^{-1}$
$Area_{cv}$	=	Surface area of control volume, $m^2$
$C_{wk}$	=	concentration of water vapor at $k^{th}$ interface of the membrane, $mol\ m^{-3}$
$C_{wlk}$	=	concentration of water liquid at $k^{th}$ interface of the membrane, $mol\ m^{-3}$
$D_h$	=	hydraulic diameter of flow channel, $m$
$D_{H_2,l}$	=	Diffusion coefficient of $H_2$ in liquid water film, $6.3 \times 10^{-9}\ m^2\ s^{-1}$
$D_{O_2,l}$	=	Diffusion coefficient of $O_2$ in liquid water film, $2.4 \times 10^{-9}\ m^2\ s^{-1}$
$D_{nj}$	=	binary diffusion coefficient of species $n$ in mixture $j$ , $m^2\ s^{-1}$
$D_w$	=	diffusion coefficient of water, $m^2\ s^{-1}$
$F$	=	Faraday constant, $96487\ C\ mole\ of\ electrons^{-1}$
$H_{H_2,l}$	=	Henry's law constant for Hydrogen in liquid water film, $8.9 \times 10^9\ Pa$
$H_{O_2,l}$	=	Henry's law constant for Oxygen in liquid water film, $2.12 \times 10^{10}\ Pa$
$h_{rxn}$	=	enthalpy of water formation, $kJ\ kmol^{-1}$
$h_{fg}$	=	enthalpy of vaporization for water, $kJ\ kg^{-1}$
$I$	=	local current density, $A\ m^{-2}$
$I_o$	=	exchange current density $A\ m^{-2}$
$m_{n,k}$	=	mass fraction of the species $n$ in stream $k$ , dimensionless
$M_{m,dry}$	=	equivalent weight of a dry membrane, $kg\ mol^{-1}$
$M_n$	=	molecular weight of species $n$ , $kg\ mol^{-1}$
$mass_n$	=	mass of species $n$ , $kg$
$m_{w,l}$	=	mass fraction of liquid water
$n_d$	=	electro-osmotic drag coefficient (number of water molecules carried per proton)
$P_{w,k}^{sat}$	=	vapor pressure of water in stream $k$ , $Pa$
$P$	=	pressure, $Pa$
$P_n$	=	partial pressure of species $n$ , $Pa$
$Q$	=	volume flow rate, $m^3\ s^{-1}$
$R$	=	universal gas constant, $8.314\ J\ mol^{-1}\ ^\circ K^{-1}$
$r$	=	condensation rate, $s^{-1}$
$S$	=	source term
$S_{he}$	=	heat source term from electrochemical losses for energy equations
$S_{hp}$	=	heat source term from water phase change for energy equations
$t_m$	=	membrane thickness, $m$
$t_{f,a}$	=	Liquid water film on the anode, $m$
$t_{f,c}$	=	Liquid water film on the cathode, $m$
$T$	=	temperature, $^\circ K$
$u, v, w$	=	velocities in $x, y$ , and $z$ directions respectively, $m\ s^{-1}$
$V_{oc}$	=	cell open-circuit voltage, $V$
$V_{cell}$	=	cell voltage, $V$
$X_L$	=	channel length measured from anode inlet, $m$
$X_{i,k}$	=	mole fraction of species $i$ in stream $k$

### Greek symbols

$\alpha(x,y)$	=	net water flux per proton flux
$\alpha_K$	=	kinetic transfer coefficient for reaction $K$ , $\alpha_c=0.5$ and $\alpha_a=1.0$ here
$\beta_\xi$	=	permeability in the $\xi$ direction
$\varepsilon$	=	Porosity of gas diffusion layer, 0.5 for the calculations here
$\eta(x,y)$	=	overpotential for the electrochemical reactions, V
$\lambda$	=	water content in the membrane
$\mu$	=	dynamic viscosity, kg-s m <sup>-2</sup>
$\rho_{m, dry}$	=	density of a dry membrane, kg m <sup>-3</sup>
$\rho$	=	density of the mixture, kg m <sup>-3</sup>
$\rho_n$	=	Density of species $n$ , kg m <sup>-3</sup>
$\sigma_m$	=	membrane conductivity, ohm <sup>-1</sup> m <sup>-1</sup>

### Subscripts and superscripts

$a$	=	anode
$c$	=	cathode
$CO_2$	=	carbon dioxide
$e$	=	electrochemical reaction
$H_2$	=	hydrogen
$K$	=	anode or cathode
$l$	=	liquid
$N_2$	=	nitrogen
$O_2$	=	oxygen
$p$	=	phase change
$v$	=	water vapor
$w$	=	liquid water
$sat$	=	saturated
$\xi$	=	dummy variable for direction $x$ , $y$ , or $z$ .

### Introduction

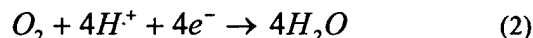
There are different types of fuel cells available to transform chemical energy directly to electrical energy without significantly polluting the environment. One of these, the Proton Exchange Membrane Fuel Cell (PEMFC), operates at a lower temperature than other types of fuel cells and it may be a power source for future automobiles and stationary power generators. Under conditions of excess inlet humidity, a three-dimensional (3-D) multi-species flow simulation with water phase change is necessary to understand the heat and mass transfer inside an experimental 10-

cm<sup>2</sup> PEMFC shown in Fig. 1 of Dutta et al. [1] because there is transport in the axial direction, in the direction perpendicular to bulk flow, and in the direction parallel with the membrane and electrode assembly (MEA). Thus, the complete 3-D Navier-Stokes equations should be solved to obtain the velocity and pressure distributions along the serpentine flow channels. Moreover, the temperature distribution of the MEA, the entire flow channel, and the graphite current collector should be computed by a 3-D energy equation because the mass flow conditions, with temperature details and corresponding water activities in both the cathode and the anode, are coupled to the net water flux per proton, the electroosmotic drag coefficient, and the membrane conductivity. Consequently, they affect the prediction of the local current density in a PEMFC and their accurate prediction is critical for analysis of MEA performance data from SFF cells. In this work, the electrochemical reactions of hydrogen and oxygen are modeled at the interface, and bulk flow is computed based on a control volume approach. The spatial source terms including species and heat sources created by electrochemical reactions and the phase-change model are developed and these terms are included in the 3-D flow solver.

The general concept of fuel cell operation is characterized as gas-mixture transport, water phase change, and the transformation of species by electrochemical reactions. The hydrogen from the anode flow channel is transported through the diffusion layer toward the MEA surface. Hydrogen molecules are dissociated to protons and electrons in the catalyst as:



The liquid water that impregnates the MEA hydrates the protons. Electroosmosis and diffusion transport the water in the MEA. The air mixture in cathode channel is transported through the diffusion layer toward the MEA where oxygen reacts with protons as:



The products of this process are direct current, water, and heat. The water can be in both liquid and vapor phases depending on the partial pressure of water vapor and water-saturated pressure. Too much water at any location causes a blockage of electrochemical reaction site (i.e., flooding) and too little water causes the membrane to be very resistive. Therefore, water management is significantly important in optimizing fuel cell performance.

In numerical studies of PEMFCs, most models focused on one-dimensional (1-D) and two-dimensional (2-D) flow with transport of the reactants and products in the flow channels and across the membrane. There are some models that emphasize 3-D fuel cell simulation [2-7], but only a few of these concentrate on two-phase behavior of water [2-4]. On the other hands, Refs. 8-10 show a 2-D two-phase model without the energy balance. Note that Refs. 9 and 10 are for interdigitated flow fields. To date, a discussion of the spatially dependent heats of reactions and phase change and the effect of these effects on energy transport has not been presented and this discussion is the purpose of this paper.

Some history of the recent advances in the prediction of PEMFC performance may be useful to put the work presented here in perspective. Most of 1-D, 2-D, and 3-D PEMFC models have been reviewed recently in Shimpalee et al. [11]. In recent

numerical predictions of PEMFCs, Wang et al. [12] demonstrated the transport and two-phase flow of reactants and products for the air cathode only. They showed that in their half-cell 2-D model, the capillary action could affect water transport inside a fuel cell. However, their work did not consider the effect of heat generated inside the PEMFC and this heat can significantly reduce the liquid water saturation by evaporation. Refs. 7, 10, and 12 account for the distribution of water in the membrane by integrating the flux expression that includes diffusion electroosmotic drag coefficients but Ref. 7 used constant properties rather than those that are dependent on the concentration of water between the anode and cathode. On the other hand, Refs. 2 and 3 assumed that the flux of water through the membrane was controlled by the activity of water at the anode and that average diffusion and electroosmotic drag coefficients, dependent on local anode activities, could be used to predict the local current distribution for a 3-D straight channel. These equations were applied to a SSF laboratory cell geometry and the predictions were shown to agree with experimental data where water condensation was moderate [4, 13].

Here, we extend the straight channel work of by Shimpalee and Dutta [3] by emphasizing the inlet humidity effect on the performance, energy transfer, and water transport inside a 3-D 10-cm<sup>2</sup> PEMFC with a 20-channel SSF. For this steady state 3-D multi-species PEMFC simulation, the energy balance includes spatially dependent source terms to account for the heat created by electrical losses, electrochemical formation of water, and the phase change of the water. We now account, as discussed below, for the condensation of water to form a film that restricts the transport of O<sub>2</sub> or H<sub>2</sub> according to a Henry's law solubility. In a recent paper [14] we exercised the model



described here and verified that the constitutive equations discussed below give predictions that agree with the measured flux of water through the membrane obtained from water balance data at 101 kPa. That procedure allows one to verify constitutive equations used for the electrochemical kinetics, the diffusion coefficient of water, and the electroosmotic drag.

### **Model development**

A typical PEMFC has SFF blocks separated by gas diffusion layers (GDLs) and the MEA; one block is for the anode gas mixture and the other is for the cathode gas mixture. The reacting gases in the blocks may flow in a parallel direction (co-flow), a counter-flow configuration, or a cross flow configuration depending on the orientation of the inlet and outlet. The reacting gases are transported from the main flow channel to the electrode surface through the GDLs. The model converts the electrochemical aspects of the governing differential equations to source terms that are usable for the control volume analysis. Also the source terms that simulate the exothermal electrochemical reaction and the phase change of the water are included in the 3-D energy equation as shown in Ref. 3. We extend these previous models by including here the thickness of a local water film formed by water condensation and we include the solubility of the hydrogen and oxygen in that film so that the flux of the reacting species through the liquid film is properly included. (This Henry's law solubility was also used in Ref. 12). We use the model to predict the effect of inlet humidity on the temperature distribution, local and averaged current densities, water transport, and energy transfer in the SFF PEMCF. The average quantities are compared with

experimental data at 202 kPa and they give an indication of the effects of drying and flooding of the MEA.

The computation domain, as shown in Fig. 1, is composed of the anode flow channel, anode diffusion layer, MEA, cathode diffusion layer, and cathode flow channel. This figure also shows the grid arrangement used. Four chemical species are considered: hydrogen, oxygen, nitrogen, and water. The water can exist in either the liquid or the gas phase. The conservation of mass equation (Table 1a, Equation 1) in the 3-D flow solver software, STAR-CD, was modified to include the electrochemical aspects of a fuel cell. The phase change of water is simulated with the source terms,  $S_m$ , shown by Equations 8 and 10-15 of Table 1b. These electrochemical reaction terms correspond to the consumption of hydrogen and water vapor in the anode, and the consumption of oxygen and production of water vapor in the cathode. Equation 11 accounts for the phase change in water by comparing the partial pressure of water vapor to the saturation pressure at the local temperature. If the partial pressure of water vapor is greater than the saturation pressure, water vapor condenses to form liquid water. On the other hand, if the partial pressure of water vapor is lower than saturation pressure, the liquid water evaporates to form water vapor. The amount evaporated is limited by the amount of liquid water available in each control volume. Equations 12 and 13 present the source terms of water vapor produced and consumed by electrochemical effects on the membrane surface of both the anode and cathode. The flux of water through the MEA is included as source terms at the anode and cathode by accounting for net water flux per proton, water content in the membrane, and water diffusion coefficient as defined by Equations 20, 21, and 23 of Table 2, respectively.

The momentum transport equation (Equation 2 of Table 1a) has a source term for the porous media ( $z_3 \leq z \leq z_4$  and  $z_2 \leq z \leq z_1$ ) used to model flows through the diffusion layer based on Darcy's law or the Ergun equation (see e.g., Bird et al. [15]). Some CFD codes such as STAR-CD do not need source terms when one uses the porous media equations. Other codes may require the addition of a source term that effectively converts the momentum equation in the x-direction to  $\frac{\partial P}{\partial x} = -\frac{\mu}{\beta_x} u$  in the porous layer because  $\beta_x$  is very small and thus the other terms become negligible. In essence, a pressure drop is created in the porous diffusion layer that is proportional to the mixture velocity in the cell.

The species transport equations (Equations 3-6 of Table 1a) are solved for the mass flow rates of hydrogen, water vapor, liquid water, and oxygen species based on the bulk-mixture velocities,  $u$ ,  $v$ , and  $w$ , and the diffusion mass fluxes  $J_{\xi n}$ . We assume that the liquid water is in the form of small freely suspended droplets in the gas flow and thus we use a Laplacian form of the Navier Stokes equation. We therefore consider that the two phases flow together and this assumption holds for normal operating conditions of a PEMFC because high liquid loadings will not allow for steady state operation. The species binary diffusion coefficients are calculated as shown by Equation 19 in Table 2. The diffusion coefficient of each species in the mixture is reduced by 50 percent in the diffusion layer to account for the effect of porosity and pore-tortuosity as discussed in Dutta et al. [16]. The flux of water through the membrane is critical to the predictions and we have used the same equation for water content in the membrane as that given in Springer et al. [17]. Equation 22 gives the

relationship between the electro-osmotic drag coefficient and water content in the membrane. This equation is obtained by our curve-fitting of the data of Ref. 17. Our functionality for the diffusion coefficient, given in Equation 23 of Table 2, uses the corrected diffusion coefficient ( $D_{\lambda}$ ) and it depends on cell temperature and water content of the membrane surface.

The expressions for water concentration in liquid and gaseous phases at the anode and cathode sides are presented in Equations 24 and 25. The local current density equation given in Equation 26 is a function of membrane properties, cell voltage, and cell over-potential as in our previous publications [e.g., 1, 16]. The equation of local membrane conductivity or membrane ionic resistance is also provided as Equation 27. This equation was developed from the data of Springer et al. [17] and is a function of water content on the anode membrane surface and local temperature. Equation 28 shows the expression of local cell overpotential which includes the effect of polarization due to dilution of the hydrogen as well as the previously used oxygen overpotential expression [e.g., Refs. 1, 3, 16].

It is important to note that the source terms in Table 1b correspond to the control volume and not the boundary conditions at the anode or cathode interfaces. For the correct determination of the concentrations and activities at the membrane-diffusion layer interface, the mole fraction for each species used in these equations must be extrapolated to the membrane surface. A linear extrapolation was used with the grid shown in Fig. 1 and this achieved satisfactory grid-independent solutions. The exception to this is when there is a liquid film of sufficient thickness. In that case, we include the solubility for the reacting gases at the gas/water film interface and we

therefore account for mass transfer resistance of the gas diffusing through the film (if it exists) more accurately. We use Henry's law to calculate the solubility of hydrogen and oxygen in the liquid water film if it is present on MEA surface. The diffusion length of this soluble gas is determined by the thickness of the film of water on the MEA corrected for the porosity of the GDL. Thus we account for the average pore flooding by considering an average film thickness. The equations for these effects are shown as Equations 29-33 in Table 2.

The heat sources used in this model combine the electrochemical energy losses,  $S_{h_e}$ , and the thermal effects produced by the phase change of water,  $S_{h_p}$ . The heat source created by electrochemical energy losses occurs inside the MEA ( $z_8$  in Fig. 1). This electrochemical heat source is given by the difference of the total energy released by the electrochemical reaction at cathode membrane surface ( $z_2$  in Fig. 1) and the electrical energy extracted out of the fuel cell as shown in Equation 16 of Table 1b. A second heat source,  $S_{h_p}$ , is produced by the phase change effects of water and it can take place anywhere in the flow channels and diffusion layers. It is given by Equation 17 of Table 1b.

A control volume technique based on a commercial flow solver, STAR-CD (version 3.151), was used to solve the coupled governing equations. As discussed above, this software requires specification of the source terms for species transport equations, the phase change equations for water, and heat generation equations created by electrochemical reactions as shown in Table 1b. Since the source terms are functions of dependent variables and parameters, active and passive scalars were used in addition to subroutines in STAR-CD. Specifically in STAR-CD, we used POSDAT

for the output control and for the electrochemical equations, FLUINJ for the mass source terms, SORSCA for the scalar control, SORENT for the enthalpies.

As mentioned earlier, Fig. 1 illustrates the geometry of the laboratory PEMFC used in our experiments [18] and thus this geometry is used for the predictions presented below. There are two flow channels (the upper is the anode and the lower is the cathode) separated by two diffusion layers and one MEA. There are twenty serpentine passes in the flow path, so that the flow path is sixty-six centimeters long in the axial direction with a 0.1 (height) x 0.08 (width)  $\text{cm}^2$  cross-section flow area. Each diffusion layer has dimensions of 0.025 (height) x 3.20 (width) x 3.20 (length)  $\text{cm}^3$ . The total grid size of this fuel cell simulation is 34 x 200 x 28 uniform grid cells. The transport of water and protons is simulated by source terms in control volumes in contact with the membrane. The three momentum equations corresponding to the x, y, and z directions are solved first, then, a pressure correction equation is used to adjust the mass balance (i.e., the SIMPLE algorithm of Patankar [19]). Next, a 3-D enthalpy equation computes temperature for the entire geometry, which is coupled with the heat generation created by electrochemical reactions and the phase change calculation. Species transport equations are solved after these bulk flow and temperature calculations, and the mixture properties for conductivity, viscosity, density, and diffusivity in each control volume are updated based on the local species mass fractions. The anode side gas mixture contains hydrogen, water vapor, and liquid water; whereas, the cathode side gas mixture contains oxygen, water vapor, liquid water, and nitrogen. Therefore, density and viscosity of the two flow channels are entirely different and they vary from one location to another.

## Results and discussion

The goal of this paper is to compare distributions of the temperature, the heat sources, and the condensation and evaporation rates and to show how they correlate with the current density. We discuss these distributions and correlations for various inlet humidity conditions. Specifically, we use three of the four inlet humidity conditions reported in the experimental study of Lee et al. [18] and shown in Fig. 2. For Fig. 2, the cell temperature and the operating pressure were held constant at 343 °K and 202 kPa and the inlet humidity conditions were varied by changing the gas humidifier temperature of both the anode and the cathode. The cell current was measured for approximately 10 hours and the results indicate that the best performance was obtained at  $T_{A/C} = 85/75$  °C and that oscillations occur at  $T_{A/C} = 65/55$  °C indicating insufficient water content in the membrane. The performance at  $T_{A/C} = 95/85$  °C is lower than at  $T_{A/C} = 85/75$  °C because the inlet humidity is too high and this causes part of the electrode to be blocked by condensed water. Note that Ref. 18 describes the experimental conditions in more detail and that the dew points for these conditions are approximately 5 °C lower than the humidifier temperatures. The model was exercised using the inlet, boundary conditions, and parameters of Table 3 and the results are discussed below. The thermal boundary conditions at the current collectors (i.e., locations  $Z_0$ ,  $Z_5$ ,  $Z_6$ , and  $Z_7$ ) were fixed at 343 °K because our experimental PEMFC has a large thermal mass for these current collectors. The model calculates the current density on the surface of the MEA and Table 4 shows the comparison between the data and the predictions. Note that we cannot model the oscillations observed for the 65/55

°C condition but the average of these oscillations agrees well with the predictions with the parameters of Table 3.

Figure 3a shows the local current density distribution on the membrane surface for the 65/55 °C humidity condition. Note that this figure could not be presented with a 1-D or 2-D model. This figure reveals a spatial variation of the current density and the highest current density is found at the outlet region and the lowest is shown at the inlet. For this humidity condition, membrane dehydration is observed (as discussed below with Figs. 7 and 8) and this decreases the local membrane conductivity. Thus the local current density is low around the first four channels. After about 0.006 m on the width, the current density starts to increase as the water content of the membrane at the anode side begins to enhance the membrane conductivity. The water content is discussed below for this condition. The local current density for this condition varies from 0.282 A/cm<sup>2</sup> to 0.620 A/cm<sup>2</sup>.

Figure 3b presents the local current density distribution on the membrane surface for the 85/75 °C humidity condition. Here, in contrast to Fig. 3a, the spatial variation of the current density is such that the highest current density is at the inlet region and the lowest is shown at the outlet. The current density decreases along the flow path toward the outlet due to the decrease of anode water activity and the depletion of reacting gases (oxygen and hydrogen) that are not shown. For this particular condition, the current density varies from 0.80 A/cm<sup>2</sup> to 0.34 A/cm<sup>2</sup>. Therefore, there is non-uniformity in electrochemical reaction on the catalyst layers of the MEA and this will affect the temperature distribution inside a PEMFC.



Figure 3c shows the local current density distribution on the membrane surface for the 95/85 °C humidity condition. For this condition the local current density also decreases from the inlet toward the outlet but the values are lower than for the humidity condition shown in Fig. 3b. The maximum current density in Fig 3c is about 0.68 A/cm<sup>2</sup> and the minimum is 0.28 A/cm<sup>2</sup> compared to about 0.80 and 0.34 in Fig 3b. This is because higher humidity generates a film of water (i.e., flooding) on the cathode side and also in the first channel of the anode. The flooding creates higher resistance for access of the oxygen and hydrogen to the catalyst on the membrane surface as already explained.

Figure 4 illustrates the temperature contours for the 85/75 °C humidity condition at a cross-section plane in width and height (i.e., y-z plane) at a length of  $x = 0.016$  m in Fig. 3b. There are two locations presented in this figure, locations (a) and (c). Location (a) corresponds to coordinates near the entrance region ( $0.003 \text{ m} < y < 0.008 \text{ m}$ ,  $0.0005 \text{ m} < z < 0.0031 \text{ m}$ , and  $x = 0.016 \text{ m}$ ) and location (c) corresponds to coordinates near the outlet of the fuel cell ( $0.027 \text{ m} < y < 0.032 \text{ m}$ ,  $0.0005 \text{ m} < z < 0.0031 \text{ m}$ , and  $x = 0.016 \text{ m}$ ). For both locations, the upper channel includes a graphite current collector, anode flow channel, and a diffusion layer and the lower channel is for the cathode side. At location (a) the temperature decreases in a semi circular pattern from the center of each cross-flow width towards the center of the rib spacing (i.e., the land in contact with the GDL) and it also decreases from the membrane surface toward the flow channel surfaces of both the anode and the cathode. The temperature difference between the membrane and surfaces of both sides is about 6 °K. For this condition, there is more heat generated by energy losses ( $S_{h_e}$ ) than by condensation and evaporation ( $S_{h_p}$ ) as discussed below with

Figs. 6-9. The temperature distribution in the graphite current collector is more uniform than in the flow channels and diffusion layers because of a higher thermal conductivity. The local temperature decreases also along the flow path from the inlet toward the outlet as shown by comparing (a) and (c). In (c) the temperature difference between the membrane and both the anode and the cathode surfaces is only around 2 °K. The change from 6 °K to 2 °K is due to the decrease in local current density and the heat produced by electrochemical reactions. Similar cross-section temperature profiles were also obtained for the other humidity conditions but the x-y distribution tends to give a better understanding of the effect of humidity as shown in Fig. 5. —

Figure 5 shows the temperature distributions on the anode membrane surface, where  $z = 0.00185$  m (i.e.,  $z = z_3$  in Fig. 1) for all three humidity conditions. The temperature distribution for the humidity condition of 65/55 °C shown in Fig. 5a is consistent with the current distribution given in Fig. 3a, where the minimum temperature is 345.6 °K at the inlet region and the maximum temperature is 348.9 °K around the outlet. This variation in temperature corresponds to the variation of local current density and the temperature values are created by heat generation from energy losses ( $S_{h_e}$ ) and by the heat adsorbed during water evaporation ( $S_{h_p}$ ). Figure 5b presents the temperature distribution for the 85/75 °C humidity condition. This temperature variation is between 352 °K and 346 °K, it decreases along the flow path, and it follows Fig. 3b where the highest current density is at the inlet. The local temperature for the 95/85 °C humidity, shown in Fig. 5c, is similar to the temperature distribution of Fig. 5b, even though the local current density of the inlet humidity is about 15% lower. For this highest humidity condition, the higher temperature is still a result of a higher

current density at the inlet even though there is some condensation at the cathode and in the cathode gas diffusion layer and flow channel as discussed below with Fig. 9. Note that the heat of condensation can transfer easily from the cathode to the anode side of the MEA because the MEA is thin and because a well humidified MEA has a thermal conductivity closer to water than a plastic.

Figure 6 shows the volumetric heat source by energy loss or electrochemical reaction for all humidity conditions. Fig. 6a presents the heat source caused by energy loss ( $S_{h_e}$ ) for the 65/55 °C humidity condition. This distribution of the heat source distribution is consistent with the distribution of local current density and temperature in Figs. 3a and 5a, respectively. The value varies between  $3.82 \times 10^7$  W/m<sup>3</sup> and  $6.84 \times 10^7$  W/m<sup>3</sup> from inlet toward outlet due to the increase in local current density. The total heat source has a contribution from both this heat due to energy loss and the heat of condensation which for this case is negative, as discussed with respect to Fig. 7a below, since water is evaporating. Figure 6b illustrates the distribution of volumetric heat source created by energy loss for the humidity condition of 85/75 °C. Again, this distribution is in contrast to that shown in Fig. 6a, and it corresponds to the contours of local current density given in Fig. 3b with the maximum heat source occurring at the inlet with the value of  $6.32 \times 10^7$  W/m<sup>3</sup> and the minimum value of  $2.72 \times 10^7$  W/m<sup>3</sup> occurring at the exit. The heat source for the humidity of 95/85 °C is given in Fig. 6c and it shows a similar distribution as in Fig. 6b but the value is slightly lower due to the lower the local current densities shown in Fig. 3c.

Figs. 7 and 8 show the volumetric condensation rates on the anode and cathode membrane surfaces, respectively, for the three inlet humidity conditions. Note that the

negative sign indicates evaporation and in these figures there is only evaporation on the anode for all three humidity conditions. The evaporation rate decreases from the inlet to the outlet for the 65/55 °C condition (Fig. 7a) because the partial pressure of water in the anode increases from the inlet toward the outlet. However in Figs. 7b and 7c, the evaporation rates increase from the inlet toward the outlet because there is more water in the anode at the inlet, because the electroosmotic drag carries water from the anode to the cathode, and because the partial pressure of water in the anode decreases along the length. On the cathode in Fig. 8a, the evaporation appears from the inlet towards two-thirds of the MEA surface due to the dry inlet humidity condition of both anode and cathode. In the last one-third of the MEA surface, water vapor starts to condense because the production rate upstream was sufficient to allow the water activity to be greater than one. For Figs. 8b and 8c, only condensation occurs on the cathode membrane surface. The value increases from the inlet to the outlet in both Figs. 8b and 8c. Figure 8c shows a higher value consistent with the higher inlet humidity and it verifies the hypothesis that flooding has occurred for the 95/85 °C humidity condition.

Figure 9 can be used to discuss the mass fraction of liquid water. Our experience is that a mass fraction of liquid water equal to 3% creates a liquid film of sufficient thickness to hinder an electrochemical reaction and that a value of 5% indicates a locally flooded electrode. Figure 9a illustrates the liquid water mass fraction at the cathode side for a condition of 65/55 °C humidity at different locations (a), (b), and (c) where location (b) is located at the center of the fuel cell width ( $0.019 \text{ m} < y < 0.024 \text{ m}$  and  $x = 0.016 \text{ m}$ ) and locations (a) and (c) are the same as for Fig. 4. From these three locations, it can be verified that no liquid water is present on the MEA

surface for the condition of 65/55 °C humidity condition. Also the mass fraction decreases from the MEA surface toward the flow channel and this is a result of the low inlet humidity, the back-diffusion of cathode water to hydrate the anode membrane surface, and the higher temperature at the MEA which leads to evaporation of any liquid water.

Figure 9b shows the liquid water mass fraction at the cathode side for the 85/75 °C humidity condition at the same locations as those in Fig. 9a. At the inlet location (a) there is very little liquid water (mass fraction  $< 0.3\%$ ) present in the diffusion layer and the third cathode channel. The high temperature at this location creates evaporation rather than condensation. Then further down the channel at location (b), the liquid water mass fraction on the cathode side increases to about 3%. This mass fraction indicates sufficient condensation and the thickness of the film starts to increase resistance to oxygen transport and lowers the concentration of oxygen at the MEA surface. This lower oxygen causes the local current density to decrease from about  $0.6 \text{ A/cm}^2$  at  $y = 0.016 \text{ m}$  to about  $0.34 \text{ A/cm}^2$  at  $y = 0.024 \text{ m}$ . Here, the liquid water present in this area is approximately 2.5%, below what we consider to be membrane flooding. At the location (c), the liquid water concentration has increased to 4.3%, indicating significant liquid water accumulation. Flooding of the membrane creates higher oxygen resistance and decreases local performance. Consequently, the non-uniformity in local current density shown in Fig. 3a and the lower current in the final three channels are not only attributed to lower anode water activity and the decrease in the partial pressure of oxygen in the flow channels, but also the water flooding of the cathode at the exit section.

Figure 9c shows the cathode liquid water mass fraction for the 95/85 °C humidity condition at the same three locations as Figs. 9a and 9b. Here the predictions indicate that the liquid water mass fraction is significantly larger in the last three channels than for the case of the 85/75 °C humidity condition. The numerical values vary from 0.46% at the inlet to almost 11% at the outlet. At these mass fractions, liquid water present in the cathode does not block a significant volume of pores in the cathode GDL and thus the electrochemical reaction is not completely blocked. This lack of complete blockage is a result of the density difference between the gas and the liquid. This is, since the density of the liquid is  $10^3$  times larger than the density of the gas, the volume occupied (and the average projected surface area for the flux) by the liquid water at 10% mass fraction is small. Note however that blockage of even a few of the GDL pores at the flow channel/GDL interface can create high oxygen overpotentials and thus dramatically lower the local electrochemical reaction.

## Conclusions

The 3-D simulation of a SSF PEMFC was achieved during drying and flooding of the MEA with the addition of the heat transfer equation and a water phase change model. This study included the necessary electrochemical phenomena and the source terms for the 3-D Navier-Stokes equations to account for the hydrogen and oxygen reactions on either side of the MEA. The effects of the gases inlet humidity on the local current density, the temperature, and the water activity were studied in this work. The present results compare well with the experimental data.

The main result of heat generation inside the fuel cell by electrochemical losses and water phase changes is a major decrease in the local current density created by an increase in local temperature which leads to evaporation and subsequent dehydration of the MEA. The main result of the phase change model is the ability to account for condensation of water which leads to MEA flooding and the subsequent formation of a liquid film. The result of this film, if it is thick enough, is to increase the resistance to the electrochemical reaction by restricting the flux of either hydrogen or oxygen. Therefore, the current density of the fuel cell is decreased. This paper also showed that fuel cell performance depends not merely on the external temperature imposed at the current collectors but also on the temperature rise created by electrical losses and water phase changes inside the PEMFC.

The model was able to predict how the PEMFC performance changes with different inlet humidity condition. Membrane dehydration is observed at very low inlet humidity conditions; and diffusion layer and membrane flooding are detected at very high inlet humidity conditions. The predicted current densities agree with those observed experimentally for all of these conditions with the same parameters that were used previously and were shown to predict water balance data [14]. It was also shown that local mass fractions of water on the order of 10% at the MEA surface do not completely block the electrochemical reaction. The simulations predict the maximum in current density as a function of inlet humidity. We suggest that this model can be used to determine optimum flow field designs as a function of inlet humidity.

## Acknowledgment

This project was supported by the DOE through Cooperative Agreement Number DE-FG02-91ER75666, ONR Grant # N00014-98-1-0554, and University Transportation Center/ South Carolina State University.

## References

- [1] S. Dutta, S. Shimpalee, and J. W. Van Zee, "Numerical Prediction Of Mass-Exchange Between Cathode And Anode Channels In A PEM Fuel Cell," *Intl. J. of Heat and Mass Transfer*, **44** (2001), 2029-2042.
- [2] S. Shimpalee, "Numerical Prediction Of Gas-Humidification Effects On Energy Transfer In PEM Fuel Cell," Ph.D. dissertation, Dept. of Mechanical Engineering, University of South Carolina, Columbia, SC (2001).
- [3] S. Shimpalee and S. Dutta, "Numerical Prediction Of Temperature Distribution In PEM Fuel Cells," *Numerical Heat Transfer, Part A*, **38** (2000), 111-128.
- [4] S. Shimpalee, S. Dutta, and J. W. Van Zee, "Numerical Prediction Of Local Temperature And Current Density In A PEM Fuel Cell," Proc. of ASME IMECE, Orlando, FL. **HTD 366-1** (2000) 1-12.
- [5] S. Um and C. Y. Wang, "Three-Dimensional Analysis Of Transport And Reaction In Proton Exchange Membrane Fuel Cells," Proc. of ASME IMECE, Orlando, FL., **HTD 366-1** (2000), 19.
- [6] T. Zhou and H. Liu, "3-D Model Of Proton Exchange Membrane Fuel Cells," Proc. of ASME IMECE, Orlando, FL. **HTD 366-1** (2000) 43 -49.
- [7] T. Berning, D. M. Lu, and N. Djilali, "Three-Dimensional Computational Analysis Of Transport Phenomena In A PEM Fuel Cell," *J. Power Sources*, **106** (2002) 284-294.
- [8] S. Um, C. Y. Wang, and K. S. Chen, "Computational Fluid Dynamics Of Proton Exchange Membrane Fuel Cells," *J. of Electrochemical Soc.*, **147** (2000), 4485-4493.
- [9] J. Yi and T.V. Nguyen, "Multicomponent Transport In Porous Electrodes Of Proton Exchange Membrane Fuel Cells Using The Interdigitated Gas Distributors," *J. of Electrochemical Soc.*, **146** (1999) 38-45.



- [10] T.V. Nguyen, "Modeling Two-Phase Flow in the Porous Electrodes of Proton Exchange Fuel Cells Using Interdigitated Flow Fields," *Proceedings of the Tutorial in Electrochemical Engineering and Mathematical Modeling*, The Electrochemical Society, Pennington, NJ, **PV-99-14** (1999) 222-232.
- [11] S. Shimpalee, W. K. Lee, J. W. Van Zee, and H. Naseri-Neshat, "Advances In Computational Fluid Dynamics Modeling For PEM Fuel Cells," *Proceedings of 36th Intersociety Energy Conversion Engineering Conference in Savannah, GA, IECEC2001-ET-10* (2001) 959-965.
- [12] Z. H. Wang, C. Y. Wang, and K. S. Chen, "Two-Phase Flow And Transport In The Air Cathode Of Proton Exchange Membrane Fuel Cells," *J. of Power Sources*, **94** (2001), 40-50.
- [13] S. Shimpalee, S. Dutta, W. K. Lee, and J. W. Van Zee, "Effect Of Humidity On PEM Fuel Cell Performance Part II: Numerical Simulation," *Proc. of ASME IMECE*, Nashville, TN., **HTD 364-1** (1999), 367-374.
- [14] W-k. Lee, S. Shimpalee, and J. W. Van Zee, "Verifying Predictions of Water and Current Distributions in a Serpentine Flow-Field PEMFC," *Journal of the Electrochemical Society*, **150** (2003) A341-A348.
- [15] R. Bird, W. Stewart, and E. Lightfoot, *Transport Phenomena*, John Wiley & Sons, New York, NY (1960).
- [16] S. Dutta, S. Shimpalee, and J. W. Van Zee, "Three-Dimensional Numerical Simulation Of Straight Channel PEM Fuel Cells," *J. of Applied Electrochemistry*, **30** (2000), 135-146.
- [17] T. Springer, T. Zawodzinski, and S. Gottesfeld, "Polymer Electrolyte Fuel Cell Model," *J of Electrochemical Society*, **138** (1991), 2334-2342.
- [18] W-k. Lee, J. W. Van Zee, S. Shimpalee, and S. Dutta, "Effect Of Inlet Humidity On PEM Fuel Cell Performance Part I: Experiments," *Proc. of ASME IMECE*, Nashville, TN., **HTD 364-1** (1999) 359-366.
- [19] S. Patankar, *Numerical Heat Transfer and Fluid Flow*, Hemisphere Publishing Corporation, New York, NY (1980).

**This Page is Left Blank Intentionally**

Table 1a: Governing equations.

Governing equations	Mathematical expressions
Conservation of mass	$\frac{\partial(\rho u)}{\partial x} + \frac{\partial(\rho v)}{\partial y} + \frac{\partial(\rho w)}{\partial z} = S_m \quad (1)$
Momentum transport	$u \frac{\partial(\rho u)}{\partial x} + v \frac{\partial(\rho u)}{\partial y} + w \frac{\partial(\rho u)}{\partial z} = -\frac{\partial p}{\partial x} + \frac{\partial}{\partial x} \left( \mu \frac{\partial u}{\partial x} \right) + \frac{\partial}{\partial y} \left( \mu \frac{\partial u}{\partial y} \right) + \frac{\partial}{\partial z} \left( \mu \frac{\partial u}{\partial z} \right) + S_{px} \quad (2)$ $u \frac{\partial(\rho v)}{\partial x} + v \frac{\partial(\rho v)}{\partial y} + w \frac{\partial(\rho v)}{\partial z} = -\frac{\partial p}{\partial y} + \frac{\partial}{\partial x} \left( \mu \frac{\partial v}{\partial x} \right) + \frac{\partial}{\partial y} \left( \mu \frac{\partial v}{\partial y} \right) + \frac{\partial}{\partial z} \left( \mu \frac{\partial v}{\partial z} \right) + S_{py}$ $u \frac{\partial(\rho w)}{\partial x} + v \frac{\partial(\rho w)}{\partial y} + w \frac{\partial(\rho w)}{\partial z} = -\frac{\partial p}{\partial z} + \frac{\partial}{\partial x} \left( \mu \frac{\partial w}{\partial x} \right) + \frac{\partial}{\partial y} \left( \mu \frac{\partial w}{\partial y} \right) + \frac{\partial}{\partial z} \left( \mu \frac{\partial w}{\partial z} \right) + S_{pz}$
Hydrogen transport (anode side)	$u \frac{\partial(\rho m_{H_2})}{\partial x} + v \frac{\partial(\rho m_{H_2})}{\partial y} + w \frac{\partial(\rho m_{H_2})}{\partial z} = \frac{\partial(J_{x,H_2})}{\partial x} + \frac{\partial(J_{y,H_2})}{\partial y} + \frac{\partial(J_{z,H_2})}{\partial z} + S_{H_2} \quad (3)$
Water vapor transport	$u \frac{\partial(\rho m_{wv})}{\partial x} + v \frac{\partial(\rho m_{wv})}{\partial y} + w \frac{\partial(\rho m_{wv})}{\partial z} = \frac{\partial(J_{x,wv})}{\partial x} + \frac{\partial(J_{y,wv})}{\partial y} + \frac{\partial(J_{z,wv})}{\partial z} + S_{wv} + S_{awv} + S_{cwv} \quad (4)$
Water liquid transport	$u \frac{\partial(\rho m_{wl})}{\partial x} + v \frac{\partial(\rho m_{wl})}{\partial y} + w \frac{\partial(\rho m_{wl})}{\partial z} = \frac{\partial(J_{x,wl})}{\partial x} + \frac{\partial(J_{y,wl})}{\partial y} + \frac{\partial(J_{z,wl})}{\partial z} + S_{wl} \quad (5)$
Oxygen transport (cathode side)	$u \frac{\partial(\rho m_{O_2})}{\partial x} + v \frac{\partial(\rho m_{O_2})}{\partial y} + w \frac{\partial(\rho m_{O_2})}{\partial z} = \frac{\partial(J_{x,O_2})}{\partial x} + \frac{\partial(J_{y,O_2})}{\partial y} + \frac{\partial(J_{z,O_2})}{\partial z} + S_{O_2} \quad (6)$
Energy equation	$\frac{\partial(\rho u h)}{\partial x} + \frac{\partial(\rho v h)}{\partial y} + \frac{\partial(\rho w h)}{\partial z} = \frac{\partial}{\partial x} \left( k \frac{\partial T}{\partial x} \right) + \frac{\partial}{\partial y} \left( k \frac{\partial T}{\partial y} \right) + \frac{\partial}{\partial z} \left( k \frac{\partial T}{\partial z} \right) + S_{hp} + S_{he} \quad (7)$

Table 1b: Source terms for governing equation of Table 1a.

Governing equations	Non-zero volumetric source terms and Location of application according Fig. 1.
Conservation of mass	$S_m = S_{H_2} + S_{wv_p} + S_{wl_p} + S_{awv_e} \text{ at } z = z_3$ $S_m = S_{O_2} + S_{wv_p} + S_{wl_p} + S_{cww_e} \text{ at } z = z_2$ <span style="float: right;">(8)</span>
Momentum transport	$S_{px} = -\frac{\mu}{\beta_x}, S_{py} = -\frac{\mu}{\beta_y}, S_{pz} = -\frac{\mu}{\beta_z} \text{ at } z_1 \leq z \leq z_2 \text{ and } z_3 \leq z \leq z_4$ <span style="float: right;">(9)</span>
Hydrogen transport (anode side)	$S_{H_2} = -\frac{I(x,y)}{2F} M_{H_2} A_{cv} \text{ at } z = z_3$ <span style="float: right;">(10)</span>
Water vapor transport	$S_{wv_p} = \frac{M_{H_2O} \sum_{n \text{ of } v} \frac{\text{mass } n \text{ of } v}{M_{n \text{ of } v}} \left[ \frac{P_{wv}^{sat} - P_{wv}}{P} \right] * r}{\left( 1 - \frac{P_{wv}^{sat}}{P} \right)} \text{ at } z_0 \leq z \leq z_5$ <span style="float: right;">(11)</span>
	$S_{awv_e} = -\frac{\alpha(x,y)}{F} I(x,y) M_{H_2O} A_{cv} \text{ at } z = z_3$ <span style="float: right;">(12)</span>
	$S_{cww_e} = \frac{I + 2\alpha(x,y)}{2F} I(x,y) M_{H_2O} A_{cv} \text{ at } z = z_2$ <span style="float: right;">(13)</span>
Water liquid transport	$S_{wl_p} = -S_{wv_p} \text{ at } z_0 \leq z \leq z_5$ <span style="float: right;">(14)</span>
Oxygen transport (cathode side)	$S_{O_2} = -\frac{I(x,y)}{4F} M_{O_2} A_{cv} \text{ at } z = z_2$ <span style="float: right;">(15)</span>
Energy equation	<p><u>Heat source by energy losses</u></p> $S_{h_e} = h_{rxn} * \left[ \frac{1}{2F} I(x,y) * A_{cv} \right]_{z=z_2} - (I(x,y) V_{cell} A_{cv})_{z=z_2} \text{ at } z = z_8$ <span style="float: right;">(16)</span> <p><u>Heat source by phase change</u></p> $S_{h_p} = S_{wl_p} * h_{fg} \text{ at } z_0 \leq z \leq z_5$ <span style="float: right;">(17)</span>

Table 2: Constitutive equations for modeling electrochemical effects.

Diffusion mass flux of species $n$ in $\xi$ direction	$J_{\xi,n} = -\rho D_{\xi,n} \frac{\partial m_{K,n}}{\partial \xi}$	(18)
Binary diffusion coefficient [15]	$\frac{PD_{n,j}(x,y)}{(P_{c-n} * P_{c-j})^{1/3} \cdot (T_{c-n} T_{c-j})^{5/12} \cdot (\frac{1}{M_n} + \frac{1}{M_j})^{1/2}} = 3.64 \times 10^{-8} \left( \frac{T(x,y)}{\sqrt{T_{c-n} T_{c-j}}} \right)^{2.334}$	(19)
Net water transfer coefficient per proton	$\alpha(x,y) = n_d(x,y) - \frac{F}{I(x,y)} D_W(x,y) \frac{(C_{we}(x,y) - C_{wa}(x,y))}{t_m}$	(20)
Water content in the membrane	$\lambda = 0.043 + 17.8Ia_a - 39.85a_a^2 + 36.0a_a^3, 0 < a_a \leq 1$ $= 14 + 1.4(a_a - 1); 1 < a_a \leq 3$	(21)
Electro-osmotic drag coefficient	$n_d = 0.0029\lambda^2 + 0.05\lambda - 3.4 \times 10^{-19}$	(22)
Water diffusion coefficient	$D_W = D_\lambda \exp(2416(\frac{1}{303} - \frac{1}{T(x,y)})); D_\lambda = 10^{-10}, \lambda < 2; D_\lambda = 10^{-10}(1 + 2(\lambda - 2)), 2 \leq \lambda \leq 3;$ $D_\lambda = 10^{-10}(3 - 1.67(\lambda - 3)), 3 < \lambda < 4.5; D_\lambda = 1.25 \times 10^{-10}, \lambda \geq 4.5$	(23)
Water vapor concentration for anode and cathode surfaces of the MEA	$C_{wK}(x,y) = \frac{\rho_{m,dry}}{M_{m,dry}} (0.043 + 17.8a_K - 39.8a_K^2 + 36.0a_K^3); a_K \leq 1$ $= \frac{\rho_{m,dry}}{M_{m,dry}} (14 + 1.4(a_K - 1)); \text{ for } a_K > 1, \text{ where } K = a \text{ or } c$	(24)
Water activity	$a_K = \frac{X_{w,K} P(x,y)}{P_{w,K}^{sat}}$	(25)
Local current density	$I(x,y) = \frac{\sigma_m(x,y)}{t_m} \{V_{oc} - V_{cell} - \eta(x,y)\}$	(26)
Local membrane conductivity	$\sigma_m(x,y) = \left( 0.514 \frac{M_{m,dry}}{\rho_{m,dry}} C_{wa}(x,y) - 0.326 \right) \exp \left( \frac{1}{303} \left( \frac{1}{T(x,y)} - \frac{1}{T(x,y)} \right) \right)$	(27)
Local overpotential	$\eta(x,y) = \frac{RT(x,y,z_2)}{\alpha_c F} \ln \left[ \frac{I(x,y)P(x,y,z_2)}{I_{O_2} P_{O_2}(x,y,z_2)} \right] + \frac{RT(x,y,z_3)}{\alpha_a F} \ln \left[ \frac{I(x,y)P(x,y,z_3)}{I_{O_{H_2}} P_{H_2}(x,y,z_3)} \right]$	(28)

Water film thickness	$t_{f,k} = \frac{m_{w,l}(\sum mass_n)}{\varepsilon \rho_{wl} Area_{cv}} \quad (29)$
Gas Solubility	$P_{O_2}(x,y,z_2) = X_{O_2}(x,y,z_2)P(x,y,z_2) \quad (30)$ $-\frac{I(x,y)}{4F}M_{O_2} = \rho_{O_2}D_{O_2,l} \left[ \frac{X_{O_2}(x,y,z_2 - t_{f,c})P(x,y,z_2 - t_{f,c})H_{O_2,l}^{-1} - X_{O_2}(x,y,z_2)}{t_{f,c}} \right] \quad (31)$ $P_{H_2}(x,y,z_3) = X_{H_2}(x,y,z_3)P(x,y,z_3) \quad (32)$ $-\frac{I(x,y)}{2F}M_{H_2} = \rho_{H_2}D_{H_2,l} \left[ \frac{X_{H_2}(x,y,z_3 + t_{f,a})P(x,y,z_3 + t_{f,a})H_{H_2,l}^{-1} - X_{H_2}(x,y,z_3)}{t_{f,a}} \right] \quad (33)$

**Table 3: Inlet and boundary conditions for predictions.**

Humidifier Temperature $T_{A/C}$ , °C		65/55	85/75	95/85
Inlet Humidity Description		Very low	High	Very high
Anode channel inlet conditions	Velocity (m/s)	1.735	2.21	2.56
	Mole fraction of $H_2$	0.96	0.86	0.79
	Mole fraction of water vapor	0.04	0.14	0.21
	Mole fraction of water liquid	0	0	0
	$I_{OH2}$ (A/m <sup>2</sup> )	1000	1000	1000
Cathode channel inlet conditions	Inlet temperature (°K)	343	343	343
	Velocity (m/s)	7.33	9.05	12.9
	Mole fraction of $O_2$	0.20	0.18	0.15
	Mole fraction of $N_2$	0.763	0.69	0.56
	Mole fraction of water vapor	0.037	0.13	0.29
Operating conditions	Mole fraction of water liquid	0	0	0
	$I_{O2}$ (A/m <sup>2</sup> )	100	100	100
	Inlet temperature (°K)	343	343	343
	Permeability of diffusion layer ( $\times 10^{-12}$ m <sup>2</sup> )	1.0 (porosity ~ 70%)	1.0 (porosity ~ 70%)	1.0 (porosity ~ 70%)
	Condensation rate (1/s)	1.0	1.0	1.0
	Cell voltage (V)	0.6	0.6	0.6
	Membrane thickness ( $\mu$ m)	50	50	50
	Graphite collector conductivity (W/m-°K)	5.7	5.7	5.7
	Operating pressure (kPa)	202	202	202

**Table 4: Comparison of observed and predicted values for average current density.**

	Very low inlet humidity	High inlet humidity	Very high inlet humidity
Experimental average (A/cm <sup>2</sup> )	0.37	0.62	0.42
Numerical average (A/cm <sup>2</sup> )	0.39	0.59	0.44

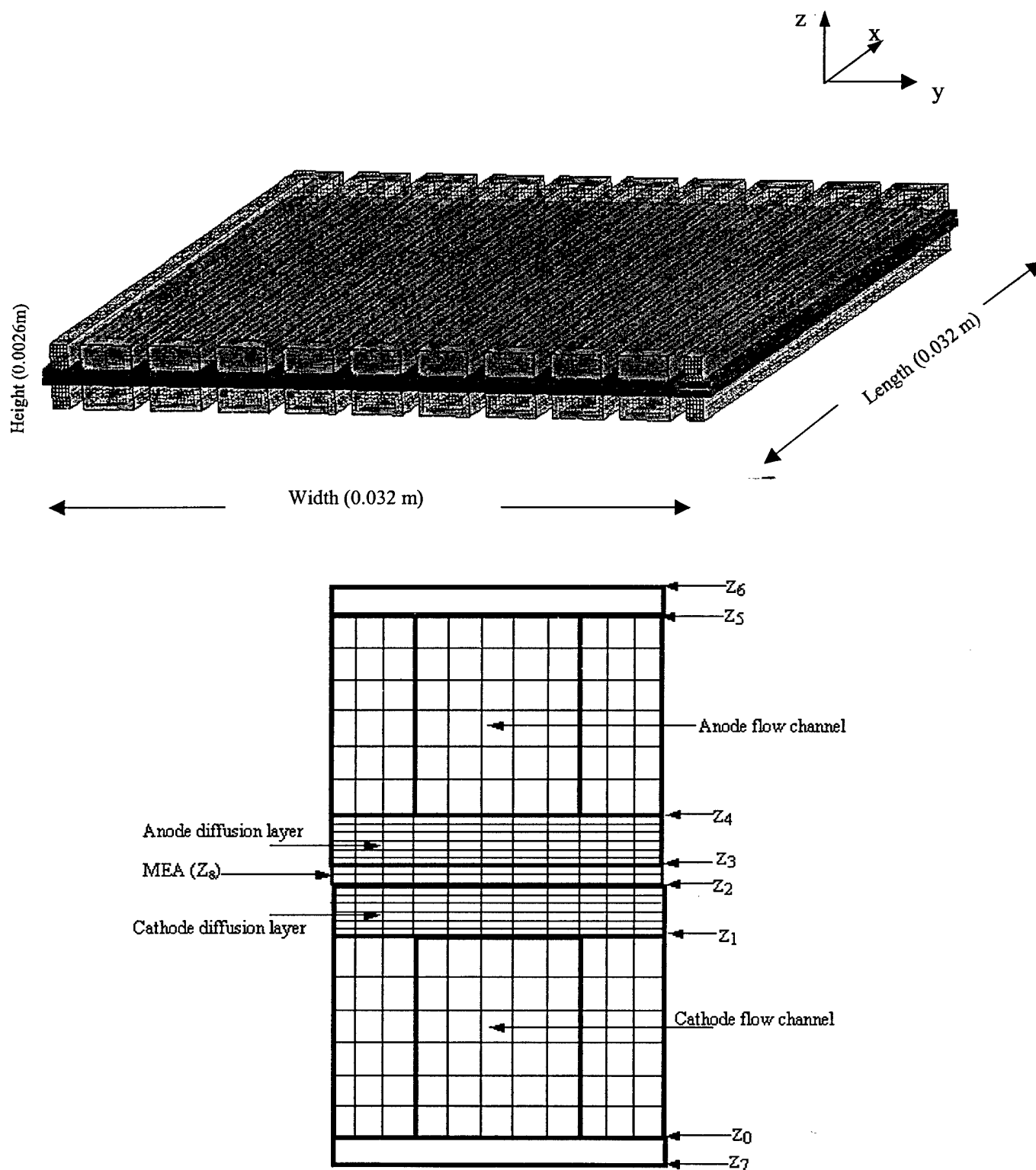


Fig. 1. The geometrical model of the SSF fuel cell (with graphite current collector removed for clarity) and the detail of the computational domain and grid arrangement used for the predictions. The origin for  $z$  is at  $z_7$ .



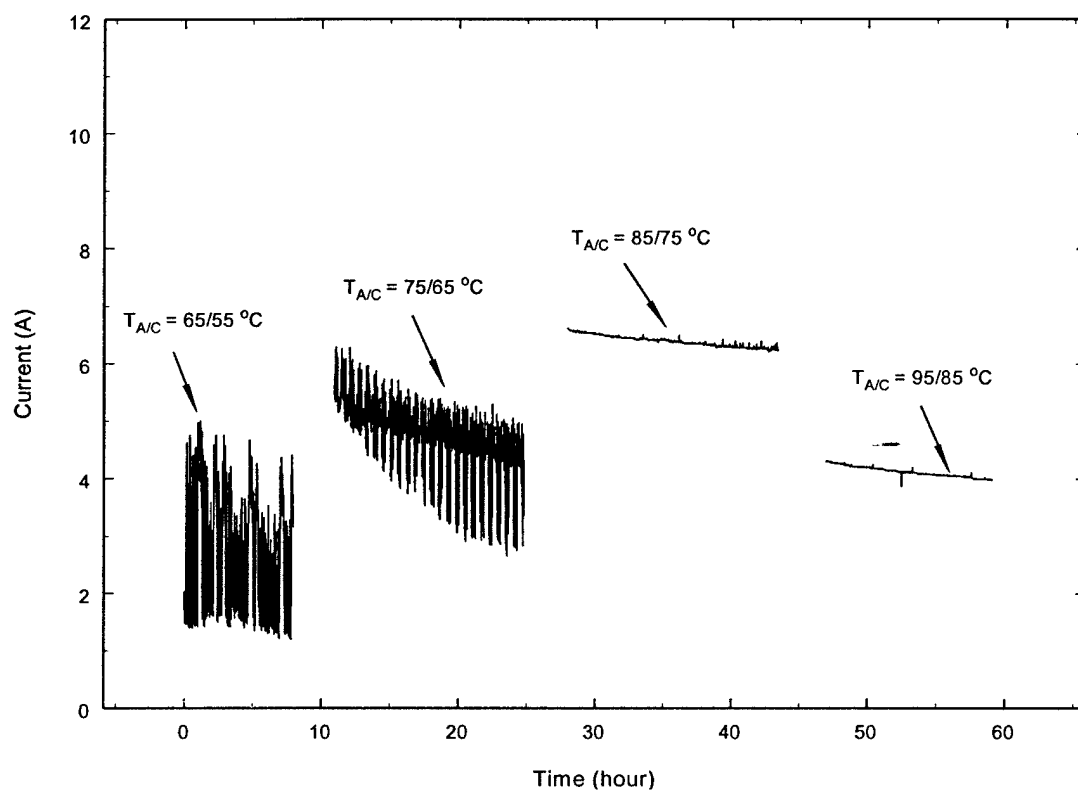


Fig. 2. The effect of inlet humidity on the PEM fuel cell current at 70 °C cell temperature, 0.6 V,  $P(A/C) = 202/202$  kPa, and flow rate  $(A/C) = 76/319$  cm<sup>3</sup> min<sup>-1</sup>. From Lee et al. [18].

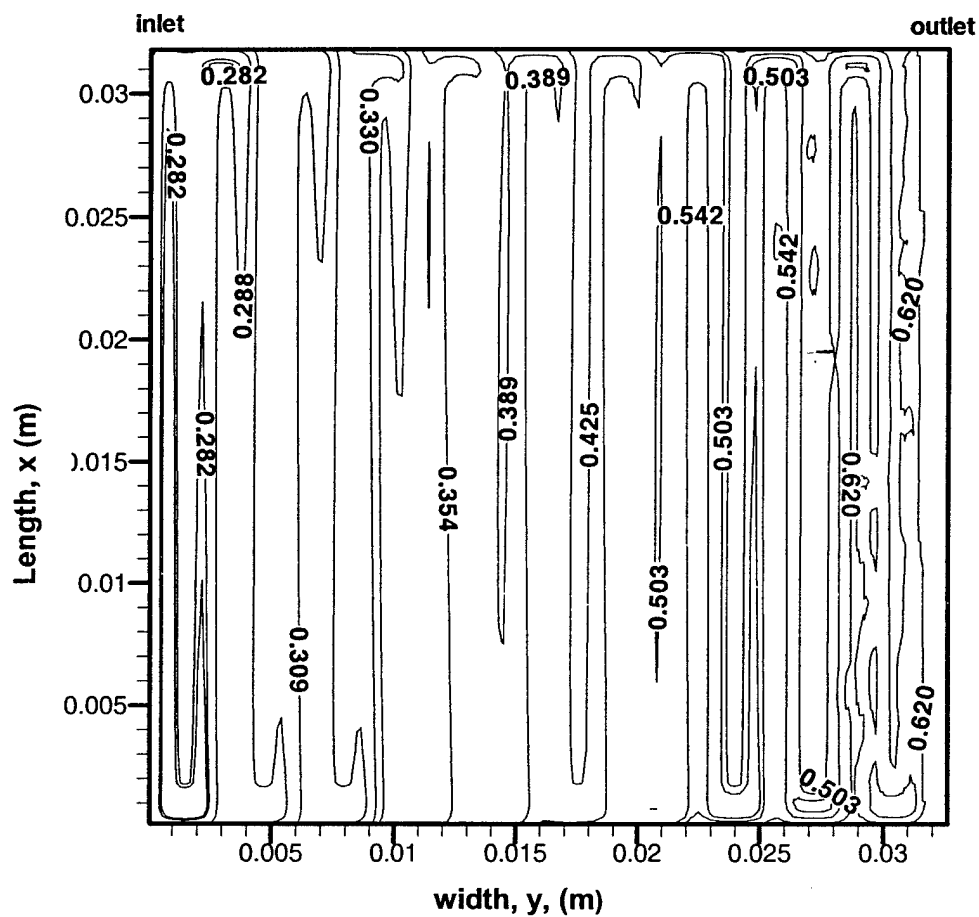


Fig. 3a. Current density ( $\text{A cm}^{-2}$ ) distribution on the membrane surface for the 65/55  $^{\circ}\text{C}$  humidity condition.

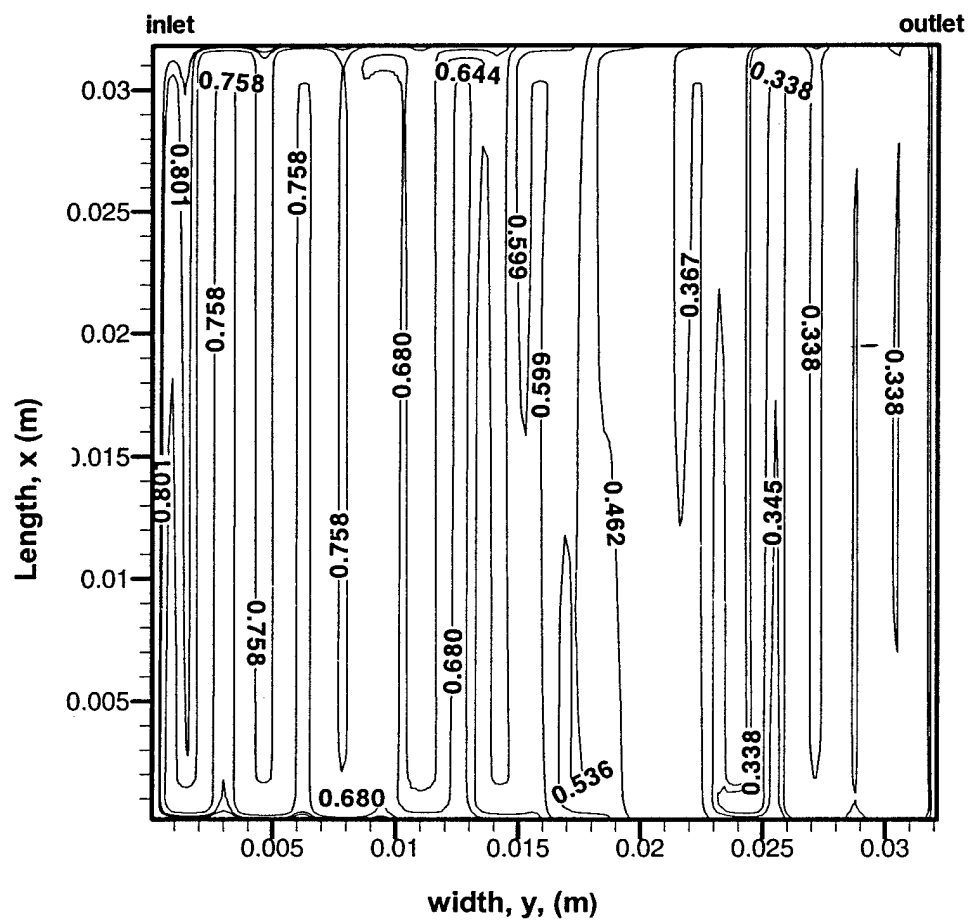


Fig. 3b. Current density ( $\text{A cm}^{-2}$ ) distribution on the membrane surface for the 85/75 °C humidity condition.

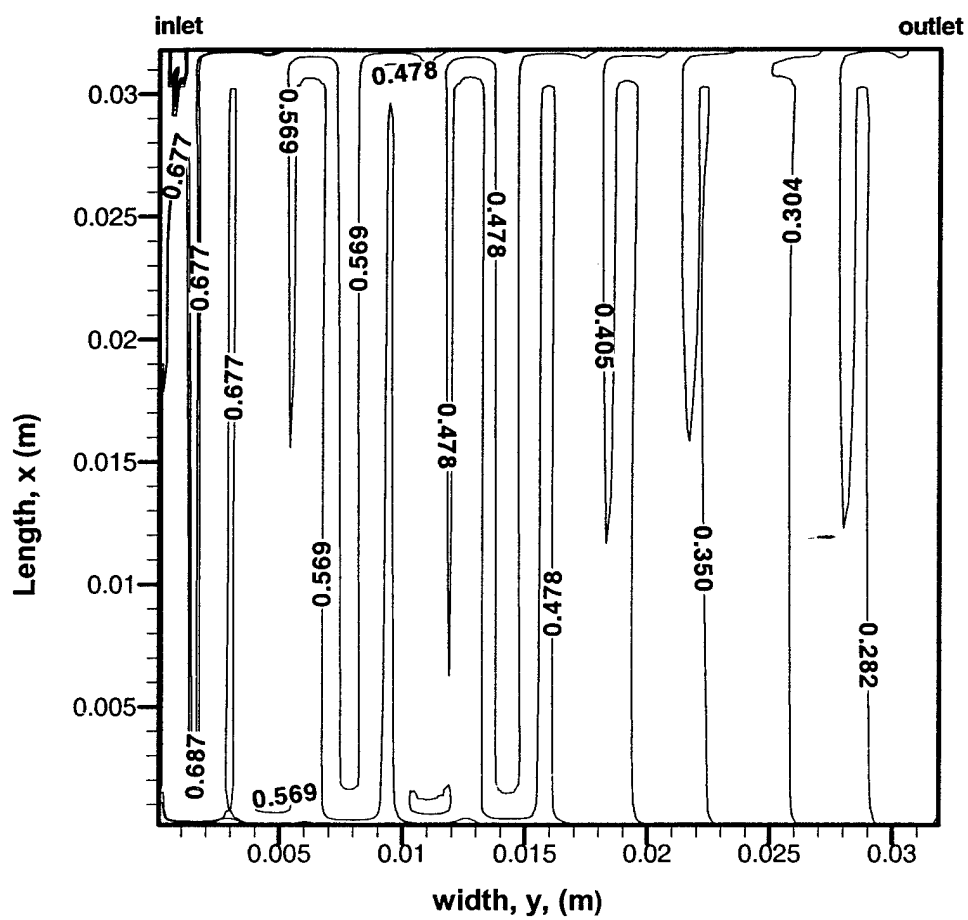
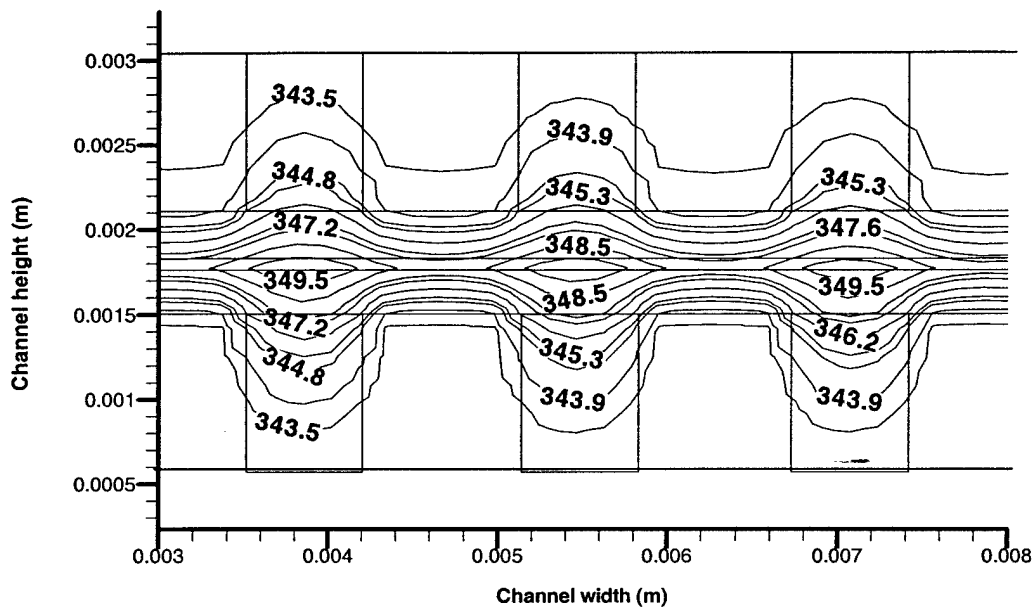


Fig. 3c. Current density ( $\text{A cm}^{-2}$ ) distribution on the membrane surface for the 95/85 °C humidity condition.

(a)



(c)

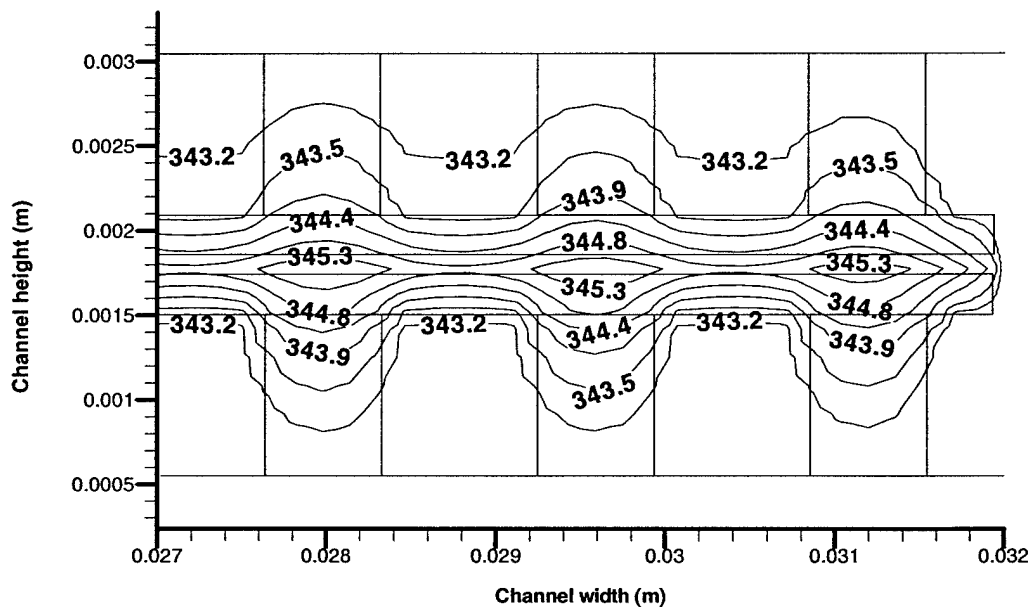


Fig. 4. Temperature ( $^{\circ}\text{K}$ ) distribution at locations (a) and (c) for the 85/75  $^{\circ}\text{C}$  humidity condition.

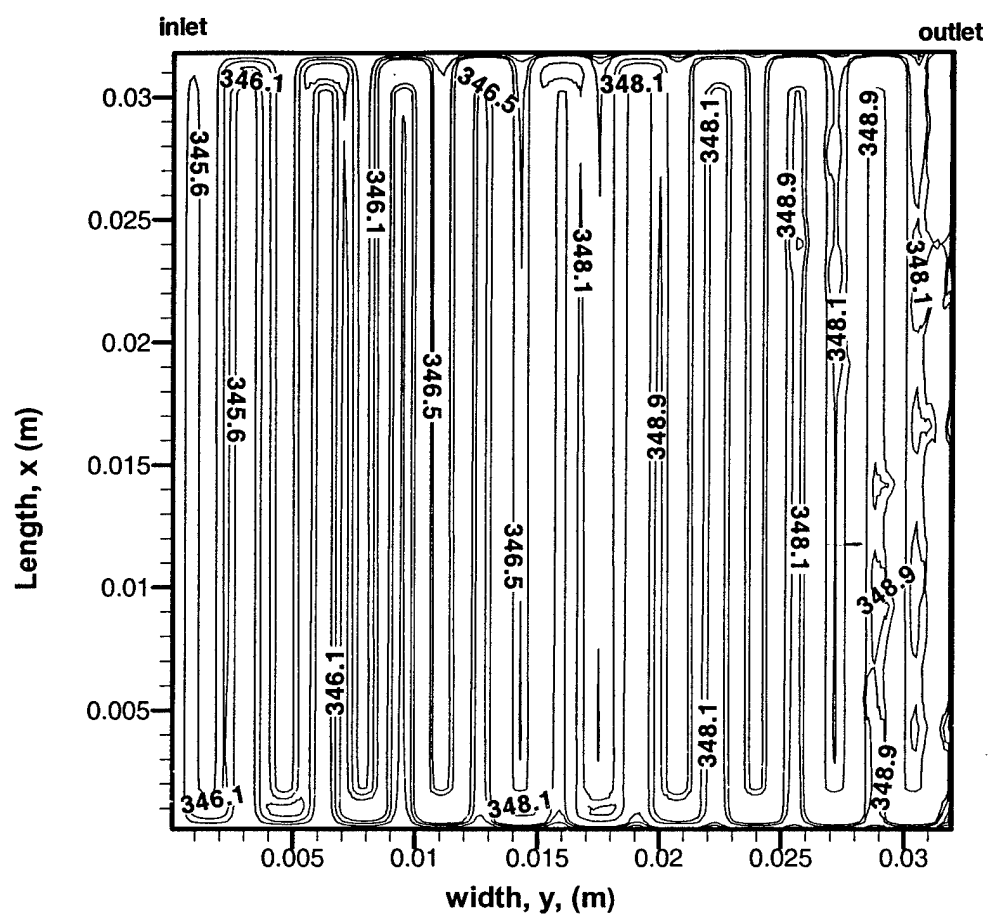


Fig. 5a. Temperature ( $^{\circ}\text{K}$ ) distribution on the anode membrane surface for the 65/55  $^{\circ}\text{C}$  humidity condition.



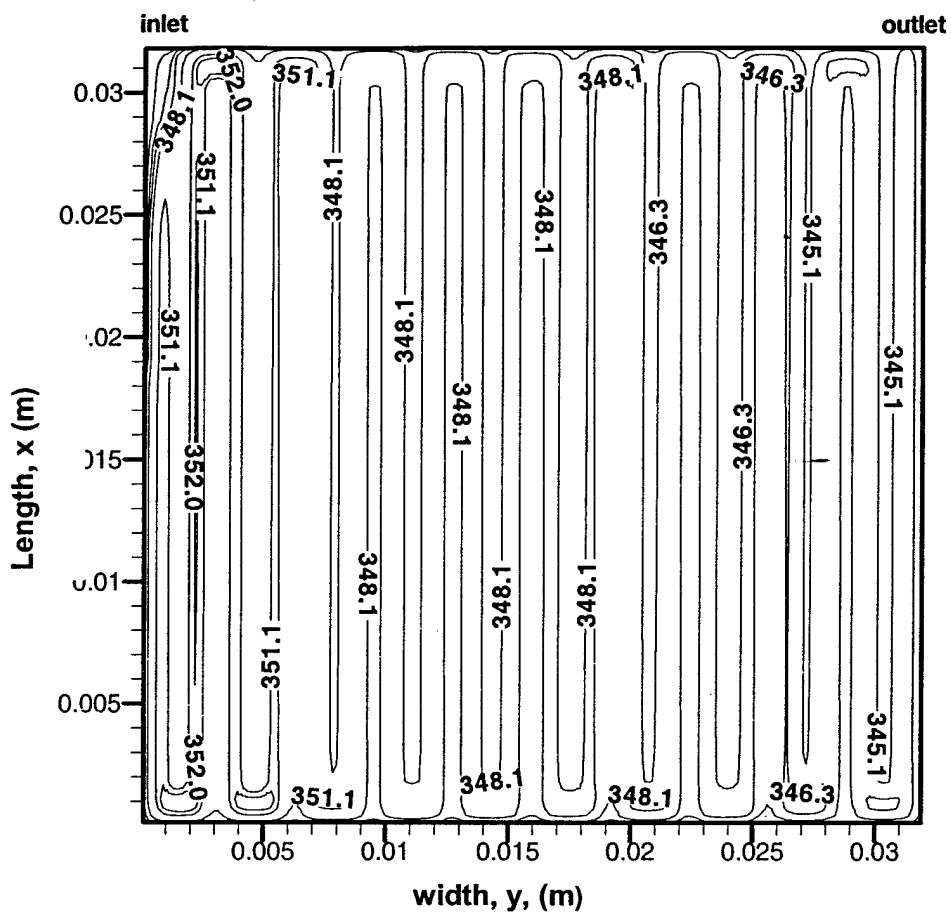


Fig. 5c. Temperature ( $^{\circ}\text{K}$ ) distribution on the anode membrane surface for the 95/85  $^{\circ}\text{C}$  humidity condition.



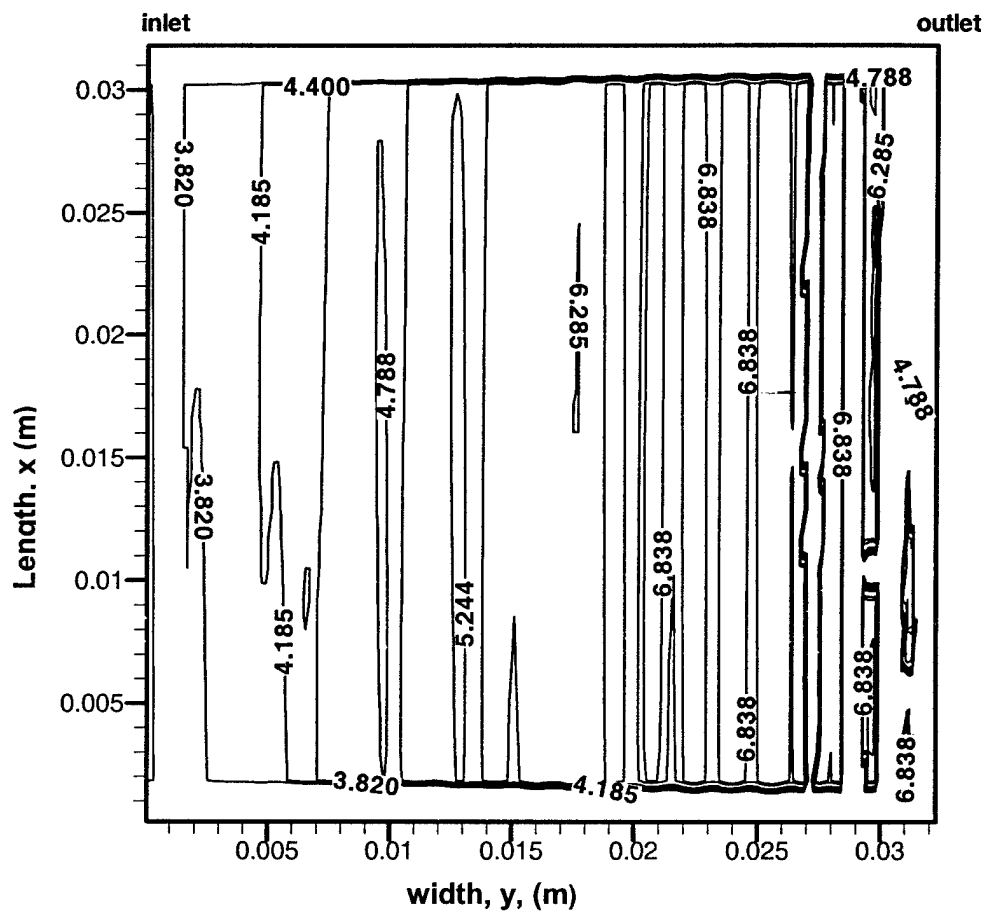


Fig. 6a. Distribution of the heat source,  $S_h \times 10^{-7}$  ( $\text{W m}^{-3}$ ), from electrochemical losses for the 65/55 °C humidity condition.

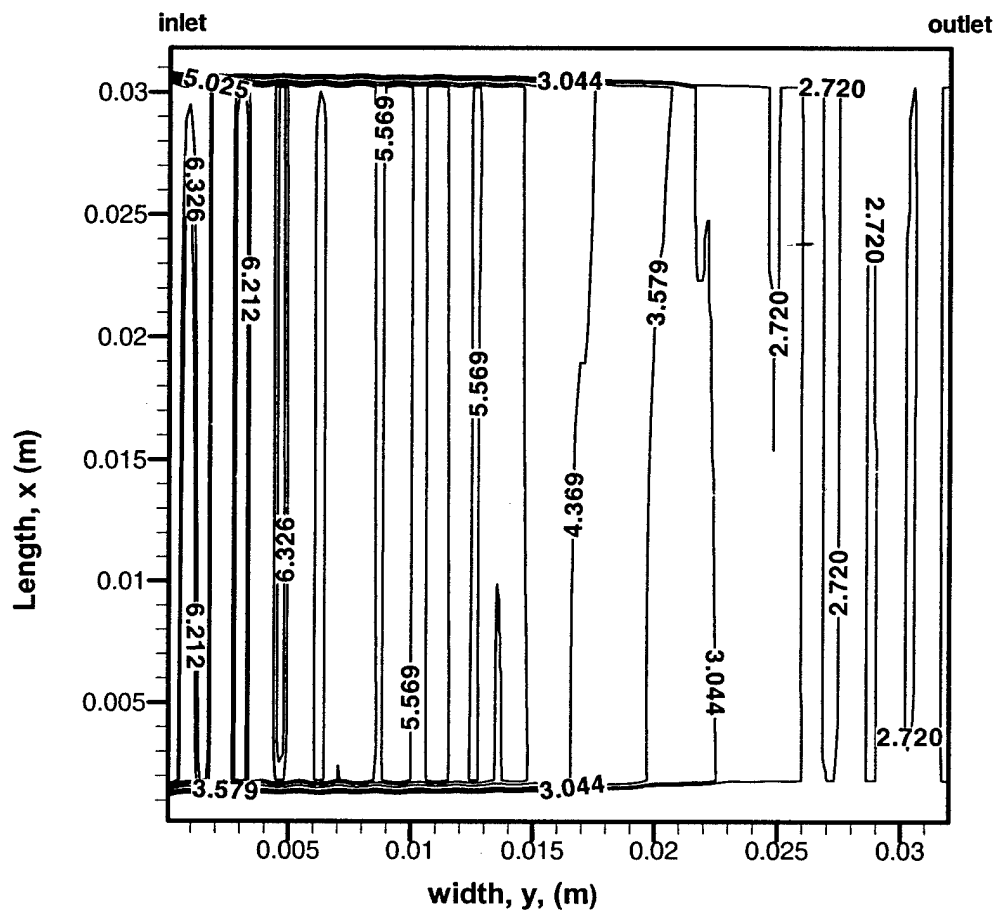


Fig. 6b. Distribution of the heat source,  $S_{h_e} \times 10^{-7}$  ( $\text{W m}^{-3}$ ), from electrochemical losses for the 85/75 °C humidity condition.

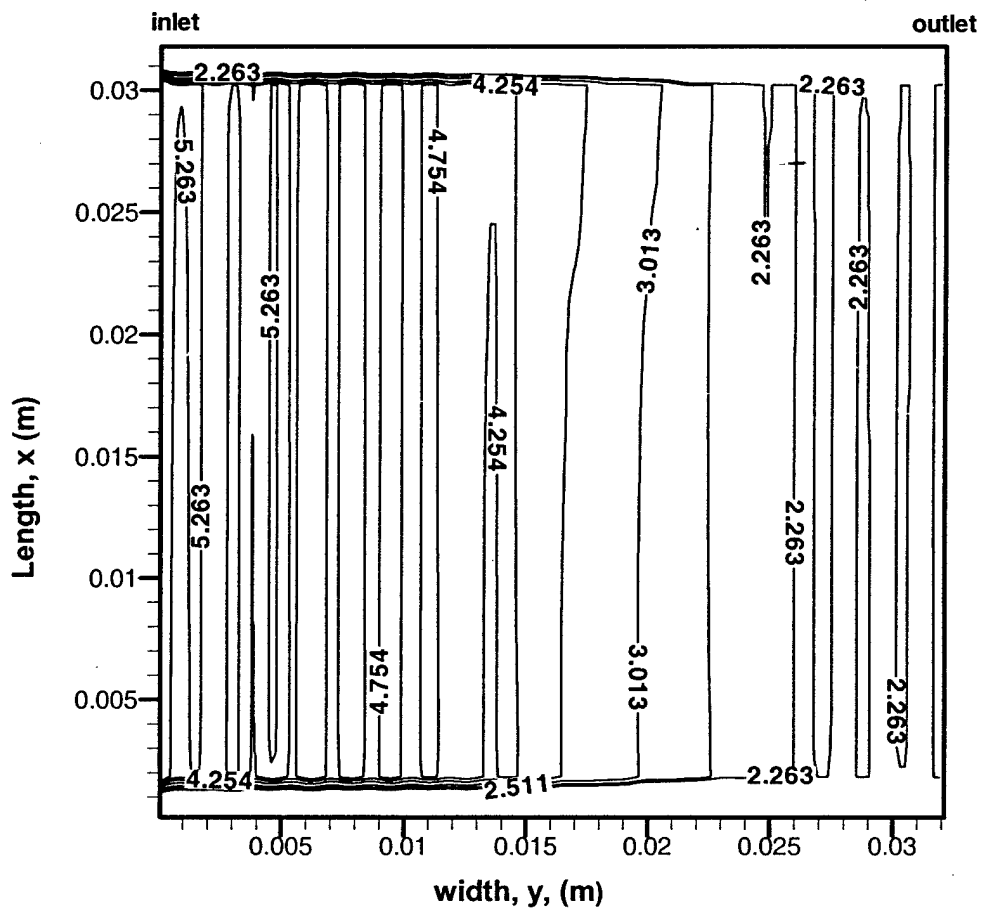


Fig. 6c. Distribution of the heat source,  $S_h \times 10^{-7} \text{ (W m}^{-3}\text{)}$ , from electrochemical losses for the 95/85 °C humidity condition.

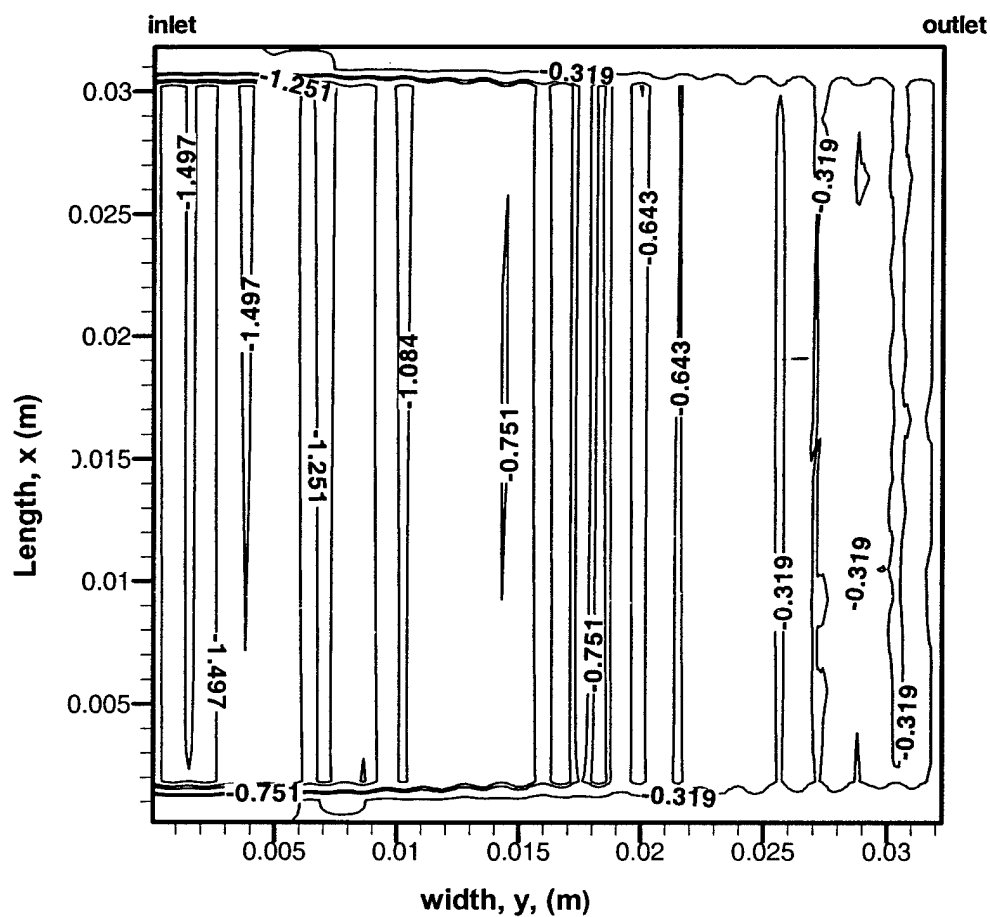
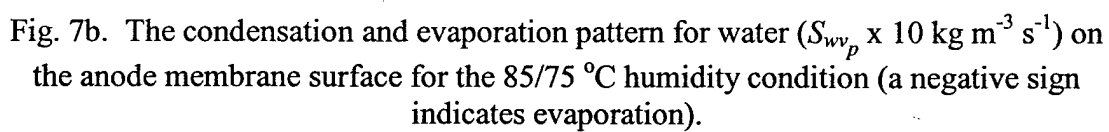


Fig. 7a. The condensation and evaporation pattern for water ( $S_{wv} \times 10 \text{ kg m}^{-3} \text{ s}^{-1}$ ) on the anode membrane surface for the 65/55 °C humidity condition (a negative sign indicates evaporation).



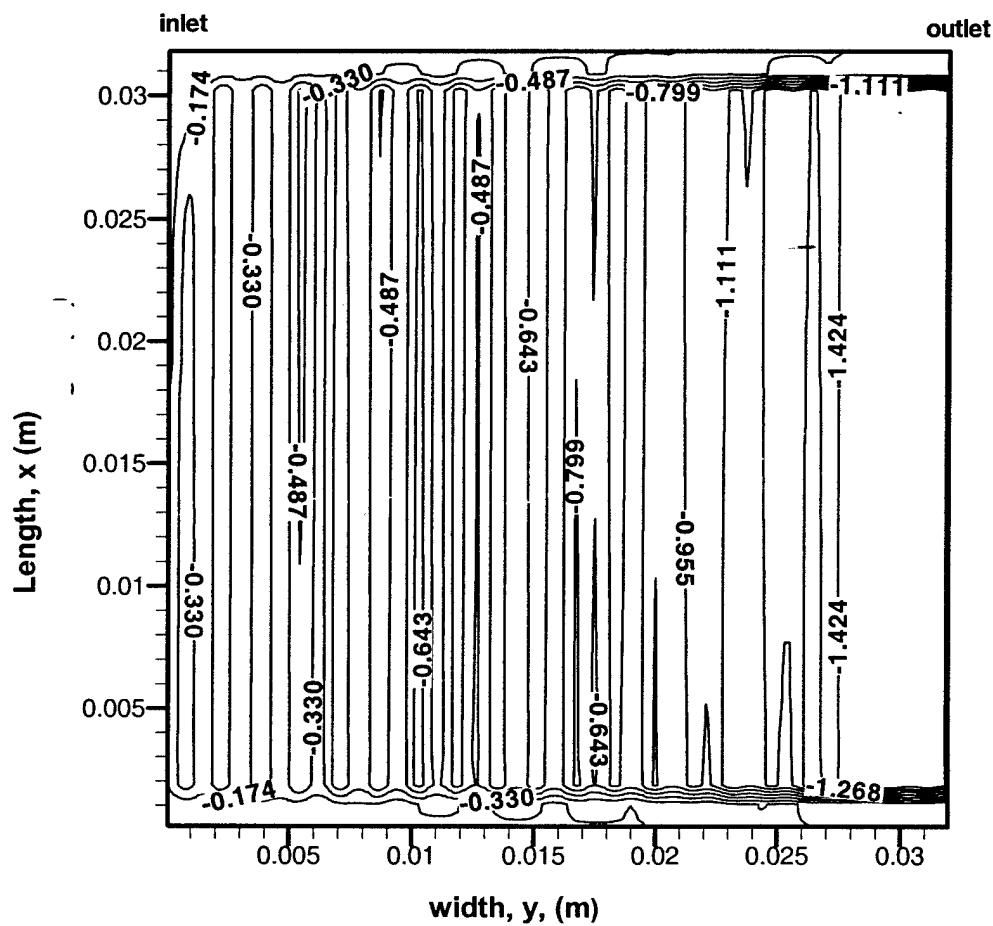


Fig. 7c. The condensation and evaporation pattern for water ( $S_{wv} \times 10 \text{ kg m}^{-3} \text{ s}^{-1}$ ) on the anode membrane surface for the 95/85 °C humidity condition (a negative sign indicates evaporation).

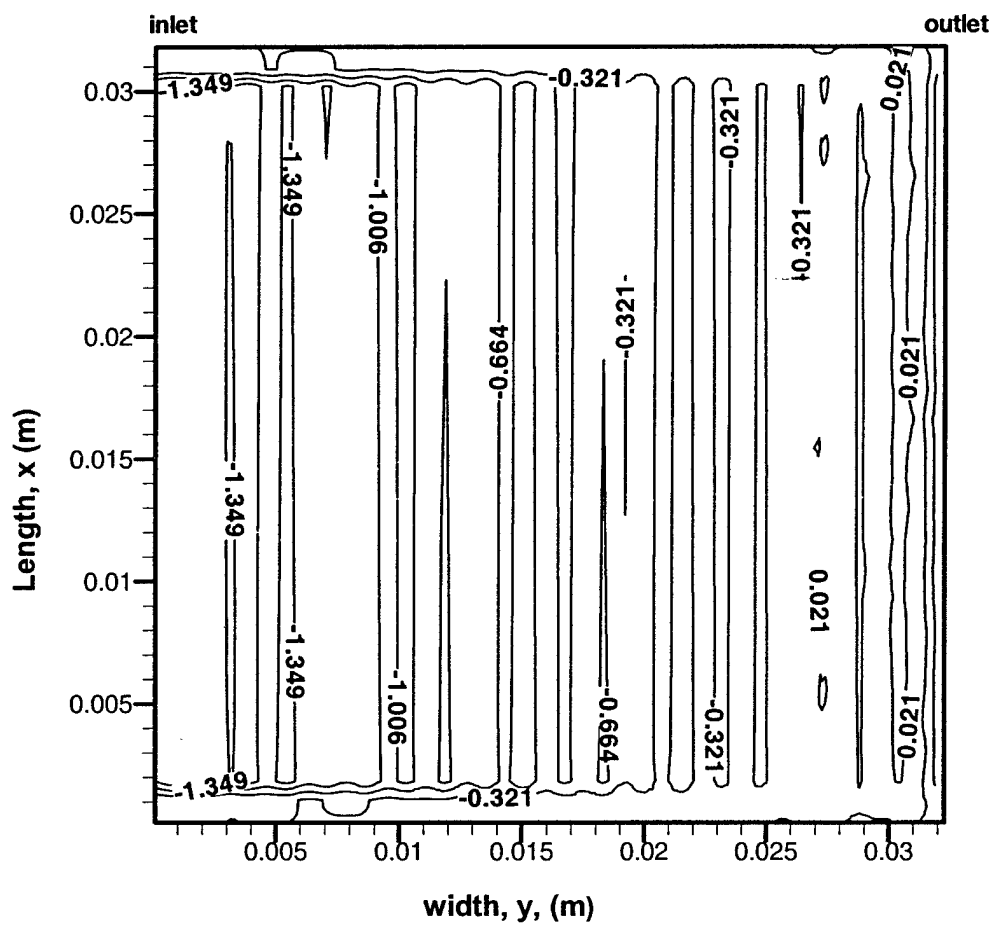


Fig. 8a. The condensation and evaporation pattern for water ( $S_{wvp} \times 10 \text{ kg m}^{-3} \text{ s}^{-1}$ ) on the cathode membrane surface for the 65/55 °C humidity condition (a negative sign indicates evaporation).

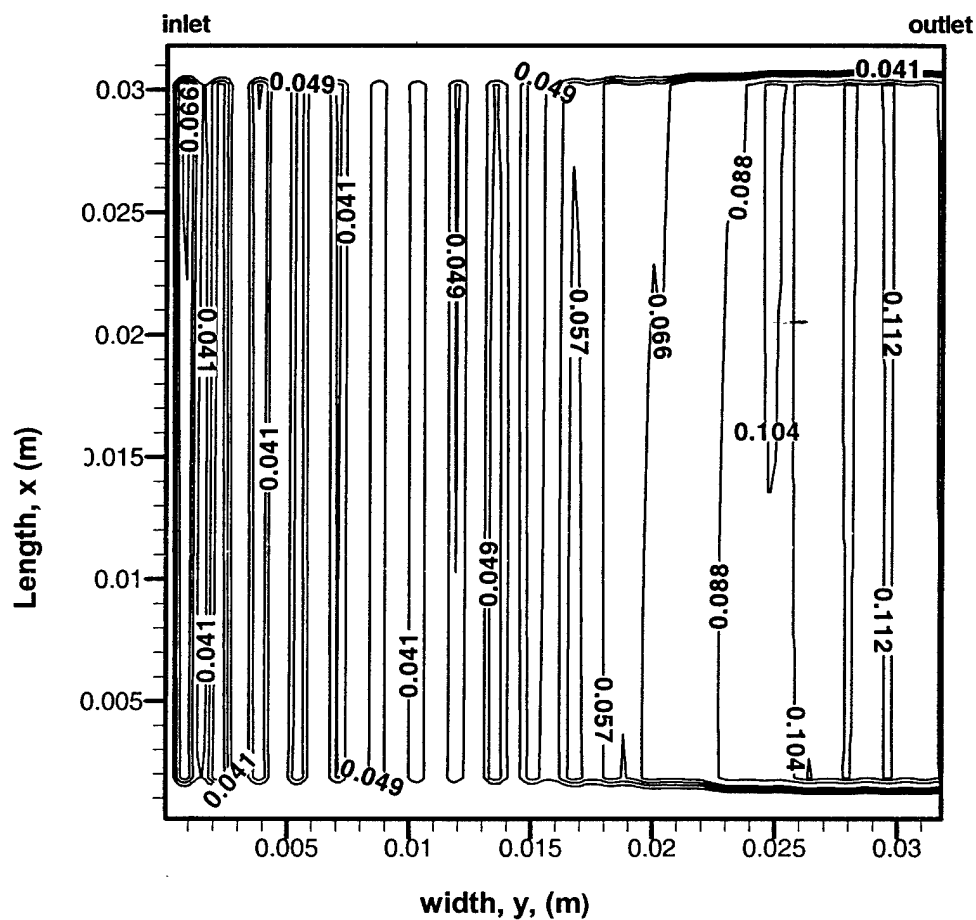


Fig. 8b. The condensation and evaporation pattern for water ( $S_{wv_p} \times 10 \text{ kg m}^{-3} \text{ s}^{-1}$ ) on the cathode membrane surface for the 85/75 °C humidity condition (a negative sign indicates evaporation).



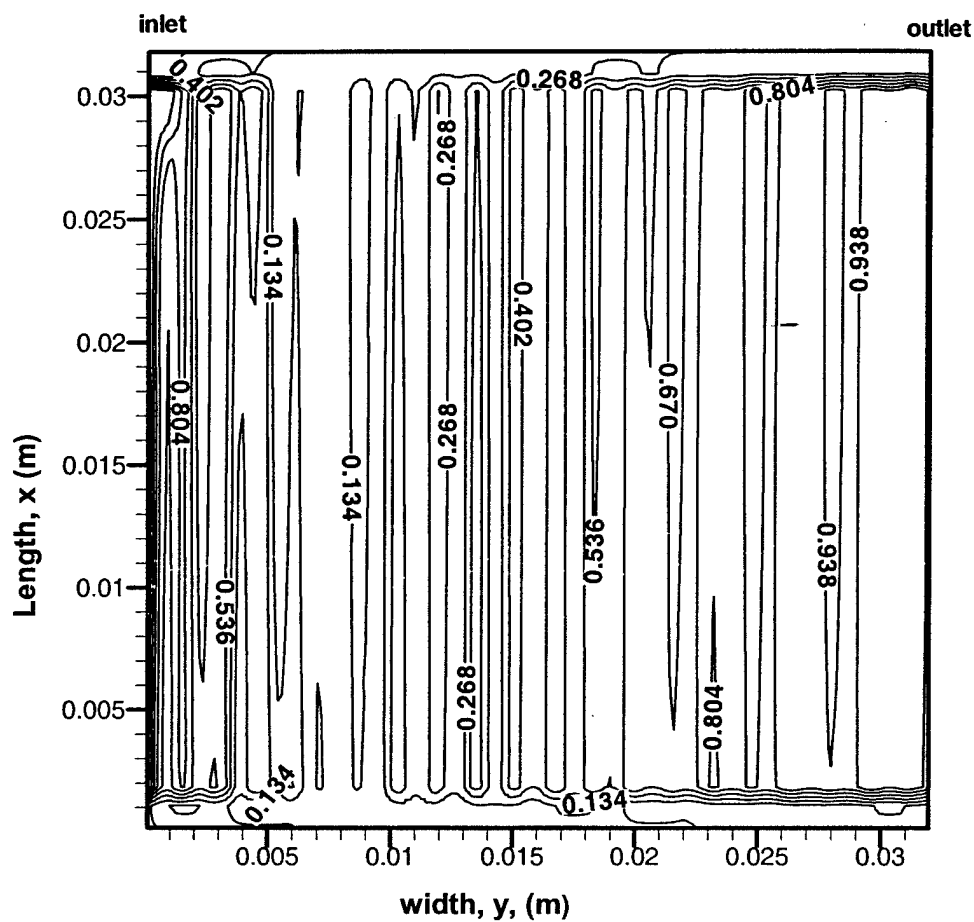


Fig. 8c. The condensation and evaporation pattern for water ( $S_{wvp} \times 10 \text{ kg m}^{-3} \text{ s}^{-1}$ ) on the cathode membrane surface for the 95/85 °C humidity condition (a negative sign indicates evaporation).

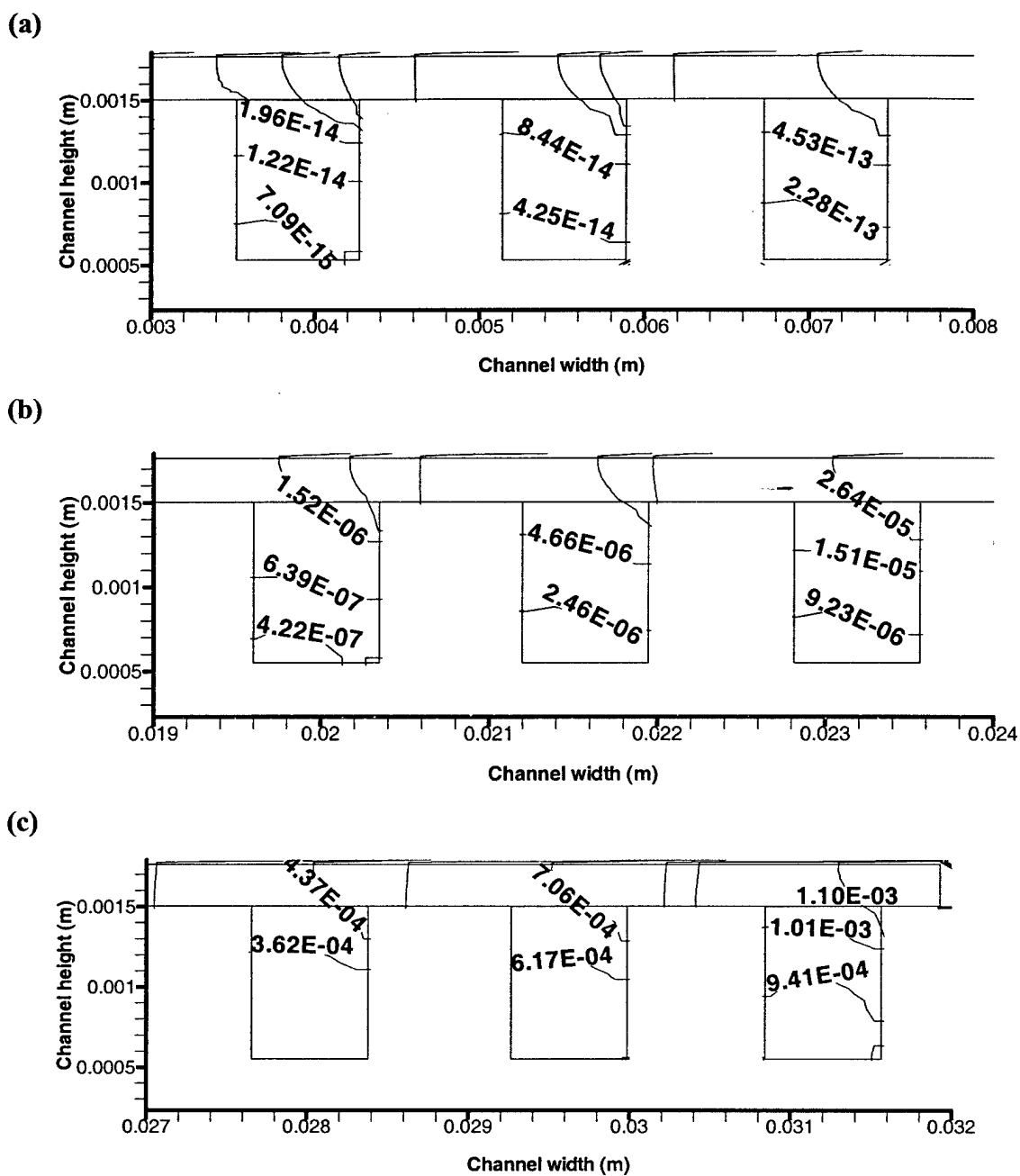
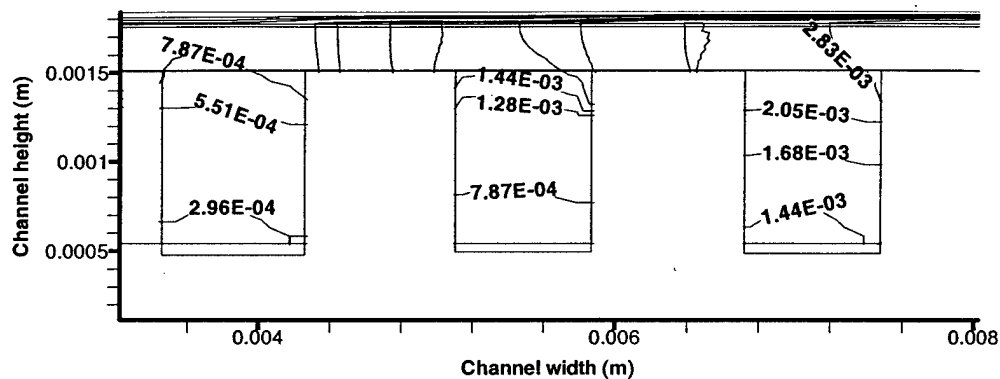
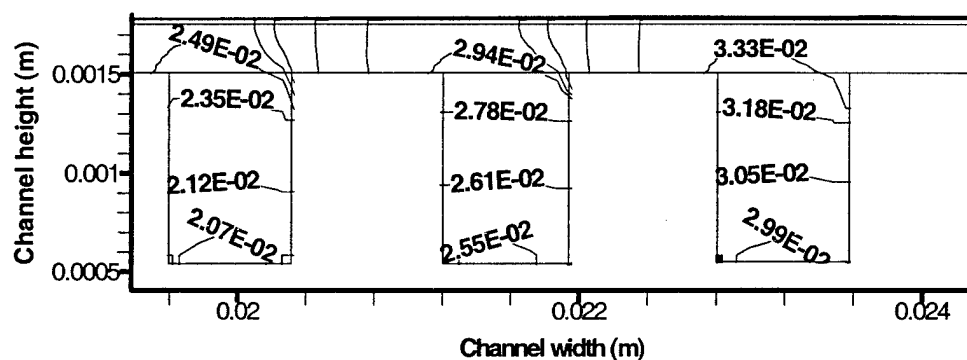


Fig. 9a. Liquid water mass fraction on the cathode side at locations (a), (b), and (c) for the 65/55 °C humidity condition.

(a)



(b)



(c)

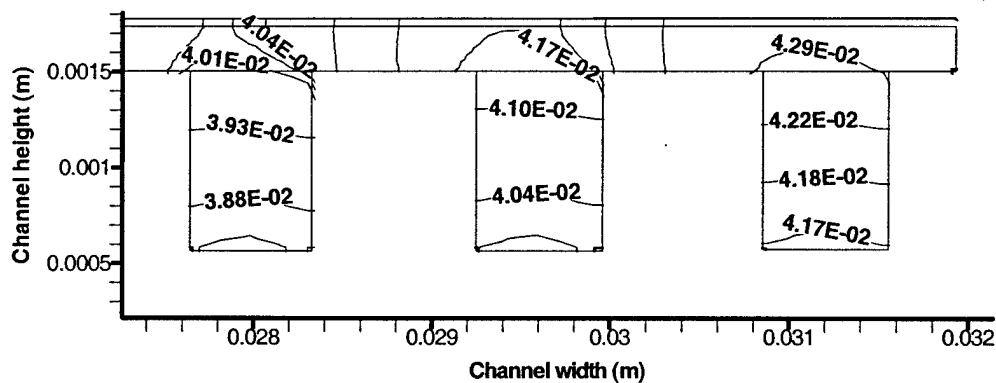
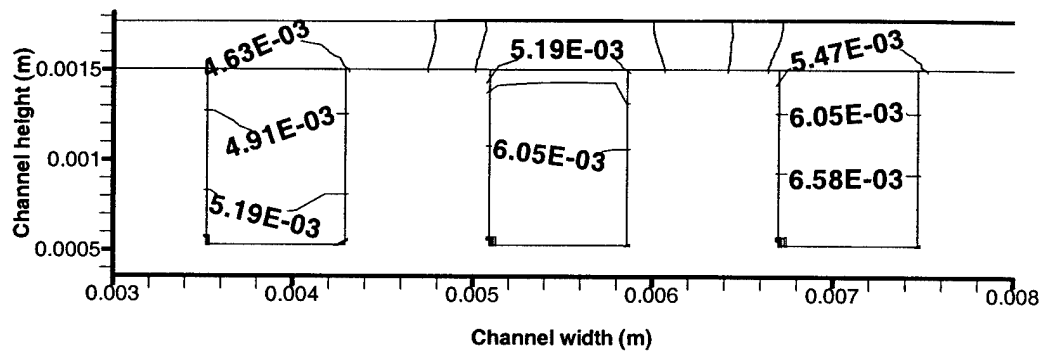
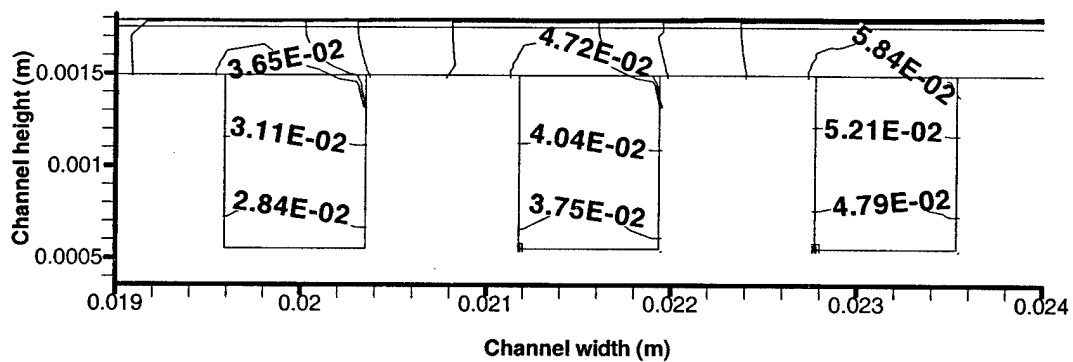


Fig. 9b. Liquid water mass fraction on the cathode side at locations (a), (b), and (c) for the 85/75 °C humidity condition.

(a)



(b)



(c)

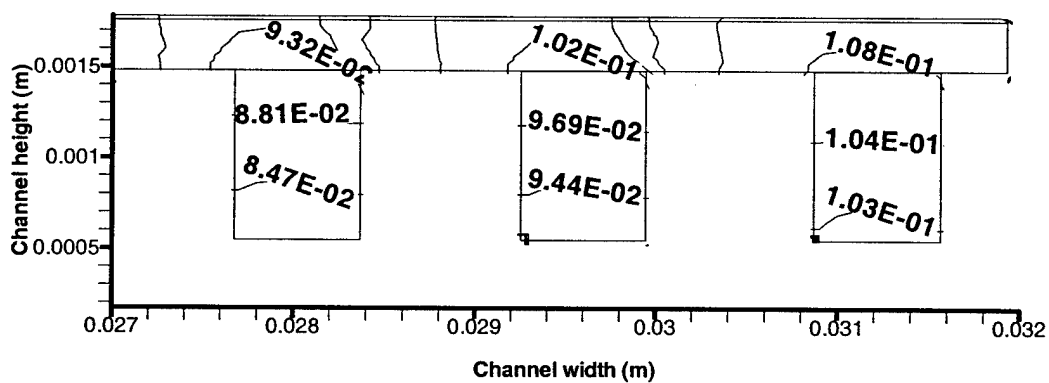


Fig. 9c. Liquid water mass fraction on the cathode side at locations (a), (b), and (c) for the 95/85 °C humidity condition.

**PREDICTING THE TRANSIENT RESPONSE OF A SERPENTINE  
FLOW-FIELD PEMFC.**

**I: EXCESS TO NORMAL FUEL AND AIR**

**S. Shimpalee (shimpale@engr.sc.edu), W-k. Lee (leew@engr.sc.edu),  
and J. W. Van Zee<sup>1</sup> (vanzee@engr.sc.edu)**

Department of Chemical Engineering, University of South Carolina, Columbia, SC 29208

**H. Naseri-Neshat (hnaseri@hotmail.com)**

Department of Mechanical Engineering Technology, South Carolina State University,  
Orangeburg, SC 29117

**Van Zee Group Technical Memorandum # 11**

**February 2002**

Submitted as a *Technical Paper*  
to

Prof. Ulrich Stimming  
*Fuel Cells-From Fundamentals to System*  
Fuelcells.paper@ph.tum.de

October 18, 2002

---

<sup>1</sup> - Corresponding author: Phone: (803) 777-2285; FAX: (803)-777-8265, e-mail: vanzee@engr.sc.edu

Keywords: PEM, fuel cells, Membrane Electrode Assembly, Electric vehicle

## Abstract

A three-dimensional numerical simulation of the transient response of a Polymer Electrolyte Membrane Fuel Cell (PEMFC) subjected to a variable load is presented. The model parameters are typical for a laboratory-scale cell with a serpentine flow path and a  $10\text{-cm}^2$  reactive area. The simulation uses a commercial computational fluid dynamics solver modified to include the electrochemical behavior. The predictions are based on an isothermal set of equations and include transient responses of the cell in terms of local distributions of the current density and gas mole fractions. The predictions show transients in the current density that overshoot the final state value when the cell voltage is abruptly changed from 0.7 V to 0.5 V for fixed excess initial stoichiometric flowrates. The fixed flowrates are excess because they correspond to stoichiometries of 2.6 and 4.4 at 0.7 V for the  $0.35\text{ A/cm}^2$  predicted initial current density. The percent overshoot decreases with the rate of voltage change and it is shown to change with anode gas flow rates. Also the magnitude of this overshoot and undershoot can be adjusted by changing the rate of voltage change and the operating conditions. The overshoot behavior for these excess stoichiometric flowrates is shown to depend on changes in the oxygen mole fraction distributions.

## Introduction

The control, design, and optimum operation of PEMFCs will require an understanding of its dynamics when there are changes in either the current, voltage, or power. These dynamics would be important for power conditioning in residential applications and for automotive systems performing in a Federal Urban Driving Scenario. While some of these dynamics could be determined from experiments, a model capable of predicting the transient response would be useful in the design flow fields and for optimization of control schemes. We are particularly interested in overshoot behavior because recent experiments in our laboratory [1] indicated the possibility of overshoot behavior dependent on the rate of voltage change.

As a guide for simple one-dimensional (1-D) and two-dimensional (2-D) models that may be developed in the future, we present here a three-dimensional (3-D) solution to the isothermal time-dependent Navier-Stokes equations for the flow channel and diffusion layers of a serpentine flow field. To obtain this solution, the 3-D model of Shimpalee et al. [2] was extended by including the time dependent analysis of a 10-cm<sup>2</sup> reactive area. This set of equations, as shown below, does not account explicitly for the condensation of water vapor resulting from the local partial pressure exceeding the saturation pressure of water, but rather it calculates the activity of water in the gas phase and allows the analyst to manually turn off the reaction in the cells where the thickness of condensed liquid restricts mass transfer to the catalyst. Recent steady-state versions of this model (Shimpalee et al. [4] and Shimpalee and Dutta [5]) account for this water phase change and include the energy balance to predict temperature changes, but under some operational conditions liquid water does not significantly affect the

performance of the cell and computational time can be saved by neglecting these phase changes. Hence, an isothermal single phase approximation is used here.

The equations of this paper and the results discussed below can be related to previous works. For example, Um and Wang [6, 7] presented similar equations for their 3-D model and applied those to a double straight channel (approximately 7 cm long). They used their own code and the equation solver was not specified. In the results presented below we used a commercially available computational fluid dynamics (CFD) solver and we had to supply subroutines to account for the electrochemical reactions of hydrogen and oxygen for source terms in the transport equations. The complete equations are solved with a control volume based discretization of the computational domain to obtain the velocity and pressure distribution in the flow channels and the gas diffusion layers for every time interval.

In contrast to the transient analysis presented here and the one figure of transient predictions shown in Ref. 7, preceding modeling studies have focused on the steady state behavior of the fuel cell. Some models considered only 1-D simulations [8-10], several models concentrated on 2-D flow with transport of the reactants and products in the flow channels and across the membranes [11-18], and recent models put emphasis on the 3-D simulations [2-7, 19-22]. These works have been reviewed by Shimpalee et al. [23].

### **Model development**

In this study, the 3-D model of Shimpalee et al. [2, 3] is extended by including the accumulation (time dependent) term. Thus, this is a transient, 3-D, isothermal,



single phase, and multi-species investigation of a single PEM fuel cell with twenty serpentine channels. Again, an isothermal set of equations is used to increase computational speed and to provide a basis of comparison for future work. The flow path consists of a serpentine gas channel and the details of the computational domain have been shown previously, [2-4, 21]. Figure 1 also shows the channel geometry and associated coordinate system. A thin membrane-electrode-assembly (MEA) is sandwiched between anode and cathode diffusion layers. Figure 2 shows more details of the computational domain, which consists of the anode flow channel, the anode diffusion layer, the MEA, the cathode diffusion layer, and the cathode flow channel. Figure 2 further shows different z-locations that are used in defining source terms (see Table 1 for a list of symbols and Tables 2 and 3 for the equations used in this paper). The species considered are hydrogen, oxygen, nitrogen, and water vapor. The fuel cell operation is characterized as gas transport and transformation of one species to the other. The hydrogen from the anode flow channel is transported through the diffusion layer toward the membrane. Hydrogen molecules are dissociated to protons and electrons in the catalyst. The water that impregnates the MEA hydrates the protons and it is transported by both electro-osmosis and diffusion according to Equation 15 of Table 3. The air mixture in the cathode channel is transported through the diffusion layer toward the membrane where oxygen reacts with protons. The water activity in the membrane is simulated by surface-based source terms in the control volumes in contact with the membrane.

Table 2 shows the model equations. The steady state aspects of these equations have been discussed elsewhere [3, 21]. It may be important to note that the time

dependent conservation of mass equation (Table 2, Equation 1) in the 3-D flow domain is modified to include the electrochemical reactions of a fuel cell by using the respective source terms,  $S_m$ , specified through Equations 7 and 9-12 of Table 2. Note that the source terms are zero in most of the computational domain. These terms corresponds to the consumption of hydrogen in the anode, and the consumption of oxygen and production of water in the cathode. The flux of water is also included as a source term at the anode and cathode (i.e., Equations 10 and 12) by accounting for the diffusion, water content in the membrane, and electro-osmotic drag coefficient as defined by Equations 15, 16, and 17 of Table 3.

The species transport equations (Equations 3-6 of Table 2) are solved for the mass flow rates of the hydrogen, water, and oxygen species based on the mixture component velocities,  $u$ ,  $v$ , and  $w$ , and the diffusion mass fluxes  $J_{\xi l}$  for every time step. The species binary diffusion coefficients are calculated as shown by Equation 14 in Table 3. Fuller and Newman [11] integrate the flux expression for the diffusion of water through the membrane whereas Refs. 10, 12, and 14 assumed a linear gradient as shown by Equation 15. In this study, the diffusion coefficient of each species in the diffusion layer was reduced arbitrarily by 50 percent to account for the effect of porosity and pore-tortuosity. The flux of water through the membrane is critical to the predictions and here we have used the same equation for water content in the membrane as given in Springer et al. [8]. Equation 17 gives relationship between the electro-osmotic drag coefficient and water content in the membrane. This equation is arrived at by curve-fitting the values of water content in the membrane and electro-osmotic drag

coefficient presented in Springer et al. [8]. The diffusion coefficient given in Equation 18 in Table 3 is taken from Nguyen and White [12].

The expressions for water concentration at the anode and cathode sides,  $C_{w,a}$  and  $C_{w,c}$ , are calculated according to Equation 19, and the activity of water is also defined in Table 3. Moreover, the effects of local hydrogen and oxygen overpotentials are accounted as shown in Equation 23. It is important to note that the source terms in Table 2 correspond to the control volume and not the boundary conditions at the anode or cathode interfaces. For the correct determination of the concentrations and activities at the membrane-diffusion layer interface, the mole fraction for each species used in these equations is extrapolated to the membrane surface.

It is important to note that here the transient predictions below assume negligible capacitance per unit area. That is the transient current is the sum of a Faraday current density as described by Equation 21 of Table 3 and a charging current density,  $I_c(x,y)$ . This charging current is related to the change in overpotential,  $\eta(x,y)$ :

$$I_c(x,y) = C \frac{d\eta(x,y)}{dt}$$

#### *Numerical procedure*

A control volume technique based on FLUENT (version 4.56) commercial flow solver was used to solve the coupled time dependent governing equations. Since we neglect  $I_c(x,y)$  the predictions shown below would apply to *Pt* electrode by not a *Pt/Ru* electrode since *Ru* has a large  $C$ . Several subroutines were added to calculate and account for the source terms, permeability, electrochemical reactions, and flux of protons and water across the membrane according to the equations of Tables 2-3.

Figures 1 and 2 show the geometry of fuel cell modeled in this work, which consists of two flow channels separated by diffusion layers and MEA. There are twenty serpentine passes in the flow path, so that the flow is approximately sixty centimeters long in the axial direction with  $0.1 \text{ (height)} \times 0.08 \text{ (width)} \text{ cm}^2$  cross-section flow area. Each diffusion layer has dimension of  $0.025 \text{ (height)} \times 3.20 \text{ (width)} \times 3.20 \text{ (length)} \text{ cm}^3$ . A total of  $34 \times 200 \times 28$  cells (elements) were used to model the fuel cell. That is, we use  $34 \times 200 \times 6$  cells for both anode and cathode diffusion layers and  $34 \times 200 \times 6$  cells for both anode and cathode flow channels,  $34 \times 200 \times 2$  cells for the MEA, and  $34 \times 200 \times 2$  cells for caps on the flow channels corresponding to the graphite current collectors.

The solution procedure used in this commercial flow solver is based on a SIMPLE algorithm [24]. For every time step, three momentum equations corresponding to three spatial coordinates are solved, followed by a pressure correction equation that corrects the mass balance. Species transport equations are solved after the bulk flow calculation. The mixture properties at each control volume are calculated based on the local species content. The anode side gas mixture contains hydrogen and water vapor. On the other hand, the cathode side gas mixture contains oxygen, water vapor, and nitrogen. Therefore, the density and viscosity of the two flow channels are different and vary from one location to the other. Note that the solution procedure for the time-dependent predictions is a fully implicit scheme [24]. Therefore, the newly calculated values of the variables prevail throughout the time step  $\Delta t$ . We tested the results to be sure that they were independent of time step size. That is for example we stepped from 0.02 s to 0.04 s first with a  $\Delta t$  of 0.001 s and then with a  $\Delta t$  of 0.005 s and the results were the same to within 5%. Also, during steady state simulations, a separate grid

independence test was performed by increasing and decreasing the number of the grid cells on a straight channel. The number of grid cell was decreased and increased by 50 percent of the base case, and predicted results were compared with the base result. The results were less than 2 percent different from each other.

## Results and discussion

The effects of the rate of change in cell voltage on cell performance are studied for three different rates shown in Figure 3. Condition #1 is a step change, and conditions #2 and #3 correspond to incremental changes with the time profiles detailed in Table 4. For most of predictions, operating flow rates for this study corresponded to flow rates that were 1.2 times greater than that required (by the measured current) for hydrogen (i.e., 20% excess hydrogen) and 2.0 time greater than that required for air (i.e., 100% excess air) at the cell voltage of 0.5 V. Thus we call this a stoichiometric flow (stoic) of 1.2/2.0 (i.e., 1.2 for anode and 2.0 for the cathode). The anode and cathode flows were co-current and constant. The initial conditions correspond to steady state concentrations and velocity and pressure distributions at 0.5 V with a feed velocity of 2.6 m/s. This corresponds to an initial stoic of 2.6/4.4 at 0.7 V and a final stoic of ~1.2/2.0 at 0.5 V. Thus we have an excess amount of fuel and air at time equal zero and a stoic of 1.2/2.0 at time equal to infinity. Other inlet conditions and physical properties are shown in Table 5. The operating pressure is 101 kPa and cell temperature is constant at 70°C. The membrane thickness used in this simulation is 50 microns.

Figure 4 shows the response in the average current density when the changes in

cell voltages are step and incremental as shown in Figure 3. The cell voltage incremental change in this figure is for condition #2 of Figure 3. Results are shown for two anode flow rates for the cell voltage change of condition #2, corresponding to stoics of 1.2 and 2.4 at 0.5 V. In this figure when the cell voltage is changed in one time step from 0.7 V to 0.5 V, the average current density rapidly increases from 0.35 A/cm<sup>2</sup> to 1.15 A/cm<sup>2</sup>. Then the current density decreases with time and reaches steady state at  $t = 0.17$  s with the current density of 0.90 A/cm<sup>2</sup>. When the rate of voltage change is slower as for condition #2 with an anode stoic of 1.2, the current density increases initially and reaches the maximum average current density of 1.10 A/cm<sup>2</sup> at  $t = 0.18$  s. Again, the current density decreases until  $t = 0.35$  s when it reaches the steady state value of 0.90 A/cm<sup>2</sup>. When the anode stoic is increased to 2.4, the maximum current reaches 1.21 A/cm<sup>2</sup> at  $t = 0.18$  s and the final steady state is 0.92 A/cm<sup>2</sup>. Figure 4 shows that the average current density overshoots its final steady state value for conditions #1 and #2 and that the peak of current overshoot depends on the rate of change of the voltage and the amount of gas flow rate. Higher gas flow rates result in greater current overshoot and a longer time to reach steady state.

Figure 5 illustrates the transient current response with the voltage changes of conditions #2 and #3 of Figure 3. This figure confirms that the magnitude of current overshoot is affected by the rate of change of cell voltage. For the rate of change of cell voltage corresponding to condition #3 in Figure 3, the maximum average current density reaches 0.92 A/cm<sup>2</sup> at  $t = 0.8$  s and cell voltage of 0.52 V. The current density reached steady state value of 0.90 A/cm<sup>2</sup> at  $t = 1.0$  s. Additional computations not shown here verified that the overshoot could be eliminated completely if a proper

function for the cell voltage change is implemented. This function can have a high rate of voltage change initially as long as the voltage change is small as the voltage approaches 0.5 V. The reasons for the overshoot are discussed below.

Figure 6 shows the local current density on the membrane surface for four time steps and cell voltages for the step change. These figures show the spatial variations of local current density, which cannot be provided in 1-D and 2-D models. At the steady state corresponding to the cell voltage of 0.7 V and  $t = 0.0$  s, the local current density is higher in the inlet region and decreases along the flow channel towards the outlet due to the lowering of anode activity of water by electroosmotic transport. The maximum and minimum local densities are  $0.43 \text{ A/cm}^2$  and  $0.30 \text{ A/cm}^2$  respectively. The variation of current density is relatively small over the entire cell area. There are also current density variations at the channel bends and the higher current density is larger on the outside edges of the bends. This is because the sharp turns of the bends produce re-circulation zones around the outward corners (edges), resulting in larger velocities and hence higher gas concentrations at the inner corners than the outer corners. When the cell voltage is lowered to 0.5 V in 0.01 s, the local current density significantly increases over the membrane surface but the contour pattern is similar to the  $t = 0.0$  s result. The highest local current density is  $1.624 \text{ A/cm}^2$  and the lowest value is  $0.970 \text{ A/cm}^2$ . As time increases, there is more non-uniformity of local current density distribution. At 0.08 s, the local current reduces considerably from the center of the membrane surface toward the outlet due to decreasing of oxygen concentration. The highest local current density is located around the inlet with a value of  $1.74 \text{ A/cm}^2$  and the lowest local current density is at the outlet with a value of  $0.63 \text{ A/cm}^2$ . The figure for 10.0 s shows

that at the final state the local current density varies from  $1.71 \text{ A/cm}^2$  to  $0.27 \text{ A/cm}^2$  and that it decreases from the center region of the membrane surface towards the outlet region. This is because the high reaction rate regions consume the hydrogen and oxygen at the beginning of the channel and the down stream regions are depleted in reactants.

Figure 7 shows the transient local oxygen mole fraction contours on the membrane surface corresponding to the current density of Fig. 6. These figures reveal that the local oxygen mole fraction patterns are consistent with the local current density contours. When the cell voltage is changed to 0.5 V with a time step of 0.01 s, the distribution of oxygen mole fraction becomes quite non-uniform and shows a rapid depletion towards the outlet regions of the membrane surface. The decrease of oxygen mole fraction in the inlet region of the membrane cell is about 18%, whereas the decrease is about 30% for the outlet region. Comparison of the four time step contours shows that the oxygen mole fraction in the inlet area of the membrane surface reaches its steady state value of 0.09 (a 38% reduction) in a time span of 0.08 s and that it reaches the steady value of 0.002 (a 98% reduction) over the last 50% of the membrane in 10 s. Under these conditions, there is not enough oxygen for reactions in the last section of the cell even though the over all stoich is 2.0 for the cathode.

There is a marked difference in transient local current density contours for the incremental change of cell voltage corresponding to conditions #2 and #3 of Figure 3. These differences are discussed by comparing Figs. 8 and 9 with Fig. 6. At time  $t=0.0$  s the current density contour plot is the same for all three conditions. Then for each time step each figure shows, in general, that the current density contours for gradually decrease from the inlet to the outlet. The major difference for the three conditions



occurs at the time step at which the maximum overshoot occurs. The magnitude of the current density for all three conditions is comparable in the immediate inlet region of the cell but a slower rate of voltage changes allows the current density towards the outlet region to approach the final value at the time of the peak current. At this peak current, the current density distribution is more uniform for conditions with more rapid cell voltage change. The current density distribution is most non-uniform at the peak current for condition #3 (i.e., the slower rate of cell voltage change). As a result, the amount of overshoot for the average current density is lower for condition #3. These local current densities are a result of the concentration of the reacting gases, particularly oxygen under these operating conditions. The final contours of both Figures 8 and 9 represent the local current density contours at the steady state. These contours are similar to the condition #1 (i.e., a step change in voltage).

Figures 10 and 11 show the transient local oxygen mole fraction for incremental voltage change of conditions #2 and #3, respectively. The time steps and cell voltages shown in Figures 10 and 11 correspond to the currents of Figures 8 and 9 respectively. These figures verify that the variation of local current density for the specified stoichiometry, cell voltage and time step change is due to the local oxygen concentration. The oxygen decreases from the center of membrane surface and is almost depleted toward the outlet when cell voltage is decreased to its steady state value.

## **Conclusions**

A 3-D time-dependent simulation of a PEMFC was shown for different rates of load change. Contours of local current density and oxygen concentration were presented

and discussed. For the particular operating conditions and properties used in this study, the results indicate that there can be current overshoot of the final cell current with the cell voltage is changed at 1 V/s from 0.7 V to 0.5 V. The peak of this overshoot depends on the rate of voltage change and anode stoichiometry and the peak of current overshoot can be reduced or eliminated by decreasing the rate at which the cell voltage is changed. Similar behavior could be expected for changes in current. This overshoot behavior is a result of local non-uniformity in the current density distributions. The non-uniformity of local current density distribution depends on anode water activity and local concentration of the reacting gases, especially the oxygen concentration for the conditions of this study. These results can help our on-going studies of flow-field configuration. Design changes in these flow-fields should improve the undesirable fuel cell performance such as the current overshoot as a result of load change, and will increase the performance dramatically.

### **Acknowledgements**

The authors gratefully acknowledge the financial support of this work by the South Carolina State University/University Transportation Center (Grant # 2000-013), the Department of Energy-EPSCoR (Cooperative Agreement # DE-FG02-91ER75666), and the Office of Naval Research (Grant # N00014-98-1-0554).

### **References**

- [1] unpublished data of M. C. Mathews, 2001, and N. Shah and R. Hobden, 2000, Department of Chemical Engineering, University of South Carolina, Columbia, SC.
- [2] S. Shimpalee, S. Dutta, W.K. Lee, and J. W. Van Zee, *Proceedings of ASME IMECE*, Nashville, TN. 5, 1999, 464.

- [3] S. Dutta, S. Shimpalee, and J.W. Van Zee, *J. Applied Electrochemistry*, **2000**, 30, 135-146.
- [4] S. Shimpalee and S. Dutta, *Numerical Heat Transfer, Part A*, **2000**, 38, 111-128.
- [5] S. Shimpalee, S. Dutta, and J. W. Van Zee, *Proceedings of ASME IMECE*, Orlando, FL. **2000**, 1, 1.
- [6] S. Um and C. Y. Wang, *Proceedings of ASME IMECE*, Orlando, FL. **2000**, 1, 19.
- [7] S. Um, C. Y. Wang, and K. S. Chen, 2000, *J. of Electrochem. Soc.* **2000**, 147, 4485-4493.
- [8] T. E. Springer, T. A. Zawodzinski, and S. Gottesfeld, *J. of Electrochem. Soc.* **1991**, 138, 2334-2342.
- [9] D. M. Bernardi and M. W. Verbrugge, *AIChE J.* **1991**, 37, 1151-1163.
- [10] D. M. Bernardi and M. W. Verbrugge, 1992, *J. Electrochem. Soc.* **1992**, 139, 2477-2491.
- [11] T. Fuller and J. Newman, *J. of Electrochem. Soc.* **1993**, 140, 1218-1225.
- [12] T. Nguyen and R. White, *J. of Electrochem. Soc.* **1993**, 140, 2178-2186.
- [13] A. West and T. Fuller, *J. of Applied Electrochemistry*, **1996**, 26, 557-565.
- [14] J. Yi and T. Nguyen, *J. of Electrochem. Soc.* **1998**, 145, 1149-1159.
- [15] J. Yi and Y. Nguyen, *J. of Electrochem. Soc.* **1999**, 146, 38-45.
- [16] V. Garua, H. Liu, S. Kakac, *J. of AIChE* 1998, 44, 2410-2422.
- [17] A. Kazim, H. Liu, and P. Forges, *J. of Applied Electrochemistry* **1999**, 29, 1409-1416.
- [18] A. Kulikovskiy, J. Divisek, and A. Kornyshev, *J. of Electrochem. Soc.* **1999**, 146, 3981-3991.
- [19] S. Shimpalee, *Ph.D. dissertation*, Dept. of Mechanical Engineering, University of South Carolina, SC. **2001**.
- [20] H. Naseri-Neshat, S. Shimpalee, S. Dutta, W.K. Lee, and J. W. Van Zee, *Proceedings of ASME IMECE*, Nashville, TN. **1999**, 4, 341.
- [21] S. Dutta, S. Shimpalee, and J. W. Van Zee, *Intl. J. of Heat and Mass Transfer* **2001**, 44/11, 2029-2042.
- [22] T. Zhou and H. Liu, in *Proceeding of ASME IMECE*, Orlando, FL. 1 (2000) 43.
- [23] S. Shimpalee, W.K. Lee, H. Naseri-Neshat, & J.W. Van Zee, *Proceedings of 36th Intersociety Energy Conversion Engineering Conference in Savannah, GA, ECEC2001-ET-10*, p 959 - 965, 2001.
- [24] S. V. Patankar, *Numerical Heat Transfer and Fluid Flow*, Hemisphere, New York **1980**.
- [25] R. Bird, W. Stewart, and E. Lightfoot, 'Transport Phenomena', John Wiley & Sons, Inc., NY **1960**.

**Table 1. List of Symbols**

$a_K$	=	activity of water in stream K, dimensionless
$A_{cv}$	=	specific surface area of the control volume (c.v.), $m^{-1}$
$C$	=	condensation rate ( $s^{-1}$ )
$C_{wK}$	=	concentration of water vapor at K interface of the membrane, $mol\ m^{-3}$
$D_{n,j}$	=	binary diffusion coefficient of species n in mixture j, $m^2s^{-1}$
$D_w$	=	diffusion coefficient of water, $m^2s^{-1}$
$F$	=	Faraday constant, 96487 C mole-of-electrons $^{-1}$
$I$	=	local current density, $A\ m^{-2}$
$I_o$	=	exchange current density $A\ m^{-2}$
$m_{n,K}$	=	mass fraction of the species n in stream K, dimensionless
$M_{n,dry}$	=	equivalent weight of a dry membrane, $kg\ mol^{-1}$
$M_n$	=	molecular weight of species n, $kg\ mol^{-1}$
$mass_n$	=	mass of species n, kg
$n_d$	=	electro-osmotic drag coefficient (number of water molecules carried per proton)
$P_{w,K}^{sat}$	=	vapor pressure of water in stream K, Pa
$P$	=	pressure, Pa
$P_n$	=	partial pressure of species n, Pa
$Q$	=	volume flow rate, $m^3/s$
$R$	=	universal gas constant, $8.314\ J\ mol^{-1}\ K^{-1}$
$S$	=	source term
$t$	=	time (s)
$t_m$	=	membrane thickness, m
$T$	=	temperature, K
$u, v, w$	=	velocities in x, y, and z directions respectively, $m\ s^{-1}$
$V_{oc}$	=	cell open-circuit voltage, V
$V_{cell}$	=	cell voltage, V
$x$	=	channel length measured from anode inlet, m
$X_{w,K}$	=	mole fraction of water in stream K
<i>Greek symbols</i>		
$\alpha$	=	net water flux per proton flux
$\beta_\xi$	=	permeability in the $\xi$ direction
$\eta$	=	total overpotential for oxygen and hydrogen reactions, V
$\lambda$	=	water content in the membrane
$\mu$	=	dynamic viscosity, $kg\ s\ m^{-2}$
$\rho_{m,dry}$	=	density of a dry membrane, $kg\ m^{-3}$
$\rho$	=	density of the mixture, $kg\ m^{-3}$
$\sigma_m$	=	membrane conductivity, $ohm^{-1}\ m^{-1}$
<i>Subscripts and superscripts</i>		
$a$	=	anode
$c$	=	cathode
$CO_2$	=	carbon dioxide
$e$	=	electrochemical reaction
$H_2$	=	hydrogen
$K$	=	anode or cathode streams
$N_2$	=	nitrogen
$O_2$	=	oxygen
$v$	=	vapor
$w$	=	water
$sat$	=	saturated
$\xi$	=	dummy variable for direction x, y, or z.

**Table 2: Governing equations and source terms.**

Governing Equations	Mathematical expressions	Non-zero volumetric source terms and location of application (see Figure 2)
Conservation of mass	$\frac{\partial \rho}{\partial t} + \frac{\partial(\rho u)}{\partial x} + \frac{\partial(\rho v)}{\partial y} + \frac{\partial(\rho w)}{\partial z} = S_m$	(1) $S_m = S_{H_2} + S_{aw} \text{ at } z = z_3$ $S_m = S_{O_2} + S_{cw} \text{ at } z = z_2$ (7)
Momentum transport	$\begin{aligned} \frac{\partial(\rho u)}{\partial t} + u \frac{\partial(\rho u)}{\partial x} + v \frac{\partial(\rho u)}{\partial y} + w \frac{\partial(\rho u)}{\partial z} &= -\frac{\partial p}{\partial x} + \frac{\partial}{\partial x} \left( \mu \frac{\partial u}{\partial x} \right) + \frac{\partial}{\partial y} \left( \mu \frac{\partial u}{\partial y} \right) + \frac{\partial}{\partial z} \left( \mu \frac{\partial u}{\partial z} \right) + S_{px} \\ \frac{\partial(\rho v)}{\partial t} + u \frac{\partial(\rho v)}{\partial x} + v \frac{\partial(\rho v)}{\partial y} + w \frac{\partial(\rho v)}{\partial z} &= -\frac{\partial p}{\partial y} + \frac{\partial}{\partial x} \left( \mu \frac{\partial v}{\partial x} \right) + \frac{\partial}{\partial y} \left( \mu \frac{\partial v}{\partial y} \right) + \frac{\partial}{\partial z} \left( \mu \frac{\partial v}{\partial z} \right) + S_{py} \\ \frac{\partial(\rho w)}{\partial t} + u \frac{\partial(\rho w)}{\partial x} + v \frac{\partial(\rho w)}{\partial y} + w \frac{\partial(\rho w)}{\partial z} &= -\frac{\partial p}{\partial z} + \frac{\partial}{\partial x} \left( \mu \frac{\partial w}{\partial x} \right) + \frac{\partial}{\partial y} \left( \mu \frac{\partial w}{\partial y} \right) + \frac{\partial}{\partial z} \left( \mu \frac{\partial w}{\partial z} \right) + S_{pz} \end{aligned}$	(2) $S_{px} = -\frac{\mu u}{\beta_x};$ $S_{py} = -\frac{\mu v}{\beta_y};$ $S_{pz} = -\frac{\mu w}{\beta_z}$ (8) $\text{at } z_1 \leq z \leq z_4$
Hydrogen transport (anode side)	$\frac{\partial(\rho m_{H_2})}{\partial t} + u \frac{\partial(\rho m_{H_2})}{\partial x} + v \frac{\partial(\rho m_{H_2})}{\partial y} + w \frac{\partial(\rho m_{H_2})}{\partial z} = \frac{\partial(J_{x,H_2})}{\partial x} + \frac{\partial(J_{y,H_2})}{\partial y} + \frac{\partial(J_{z,H_2})}{\partial z} + S_{H_2}$	(3) $S_{H_2} = -\frac{I(x,y)}{2F} M_{H_2} A_{cv} \text{ at } z = z_3$ (9)
Water transport (anode side)	$\frac{\partial(\rho m_{aw})}{\partial t} + u \frac{\partial(\rho m_{aw})}{\partial x} + v \frac{\partial(\rho m_{aw})}{\partial y} + w \frac{\partial(\rho m_{aw})}{\partial z} = \frac{\partial(J_{x,aw})}{\partial x} + \frac{\partial(J_{y,aw})}{\partial y} + \frac{\partial(J_{z,aw})}{\partial z} + S_{aw}$	(4) $S_{aw} = -\frac{\alpha(x,y)}{F} I(x,y) M_{H_2O} A_{cv}$ $\text{at } z = z_3$ (10)
Oxygen transport (cathode side)	$\frac{\partial(\rho m_{O_2})}{\partial t} + u \frac{\partial(\rho m_{O_2})}{\partial x} + v \frac{\partial(\rho m_{O_2})}{\partial y} + w \frac{\partial(\rho m_{O_2})}{\partial z} = \frac{\partial(J_{x,O_2})}{\partial x} + \frac{\partial(J_{y,O_2})}{\partial y} + \frac{\partial(J_{z,O_2})}{\partial z} + S_{O_2}$	(5) $S_{O_2} = -\frac{I(x,y)}{4F} M_{O_2} A_{cv}$ $\text{at } z = z_2$ (11)
Water transport (cathode side)	$\frac{\partial(\rho m_{cw})}{\partial t} + u \frac{\partial(\rho m_{cw})}{\partial x} + v \frac{\partial(\rho m_{cw})}{\partial y} + w \frac{\partial(\rho m_{cw})}{\partial z} = \frac{\partial(J_{x,cw})}{\partial x} + \frac{\partial(J_{y,cw})}{\partial y} + \frac{\partial(J_{z,cw})}{\partial z} + S_{cw}$	(6) $S_{cw} = \frac{I + 2\alpha(x,y)}{2F} I(x,y) M_{H_2O} A_{cv}$ $\text{at } z = z_2$ (12)

Table 3. Equations for modeling electrochemical effects.

Diffusion mass flux of species $l$ in $\xi$ direction	$J_{l,l} = -\rho D_{l,l} \frac{\partial m_{K,l}}{\partial \xi}$ (13)
Binary diffusion coefficient [25]	$\frac{PD_{i,j}(x,y)}{(P_{c-i} * P_{c-j})^{1/3} (T_{c-i} T_{c-j})^{5/12} \cdot (\frac{1}{M_i} + \frac{1}{M_j})^{1/2}} = 3.64 \times 10^{-8} \left( \frac{T_{cell}}{\sqrt{T_{c-i} T_{c-j}}} \right)^{2.334}$ (14)
Net water transfer coefficient per proton	$\alpha(x,y) = n_d(x,y) - \frac{F}{I(x,y)} D_W(x,y) \frac{(C_{wc}(x,y) - C_{wa}(x,y))}{t_m}$ (15)
Water content in the membrane	$\lambda = 0.043 + 17.81a_a - 39.85a_a^2 + 36.0a_a^3; 0 < a_a \leq 1$ $= 14 + 1.4(a_a - 1); 1 < a_a \leq 3$ (16)
Electro-osmotic drag coefficient	$n_d = 0.0029\lambda^2 + 0.05\lambda - 3.4 \times 10^{-19}$ (17)
Water diffusion coefficient	$D_W = n_d 5.5 \times 10^{-11} \exp \left[ \frac{1}{303} \left( \frac{1}{T} - \frac{1}{T} \right) \right]$ (18)
Water concentration for anode and cathode surfaces of the MEA	$C_{wK}(x,y) = \frac{\rho_{m,dry}}{M_{m,dry}} (0.043 + 17.8a_K - 39.8a_K^2 + 36.0a_K^3); a_K \leq 1$ $= \frac{\rho_{m,dry}}{M_{m,dry}} (14 + 1.4(a_K - 1)); \text{ for } a_K > 1, \text{ where } K = a \text{ or } c$ (19)
Water activity	$a_K = \frac{X_{w,K} P(x,y)}{P_{w,K}^{sat}}$ (20)
Local current density	$I(x,y) = \frac{\sigma_m(x,y)}{t_m} \{V_{oc} - V_{cell} - \eta(x,y)\}$ (21)
Local membrane conductivity	$\sigma_m(x,y) = \left( 0.00514 \frac{M_{m,dry}}{\rho_{m,dry}} C_{wa}(x,y) - 0.00326 \right) \cdot \exp \left( 1268 \left( \frac{1}{303} - \frac{1}{T} \right) \right) \times 10^2$ (22)
Local overpotential	$\eta(x,y) = \frac{RT}{0.5F} \ln \left[ \frac{I(x,y)P(x,y)}{I_{o_{O_2}} P_{O_2}(x,y)} \right] + \frac{RT}{0.5F} \ln \left[ \frac{I(x,y)P(x,y)}{I_{o_{H_2}} P_{H_2}} \right]$ (23)
Viscosity of mixture	$\mu = \sum_i m_i \mu_i$ (24)

Table 4: Voltage changes profiles

Condition #1	Time (s)	-0.10	0.00	0.01	0.05	0.10	0.20	0.30	0.40	0.50	0.60	0.70	0.80	0.90	1.00	1.10
	Voltage (V)	0.70	0.70	0.50	0.50	0.50	0.50	0.50	0.50	0.50	0.50	0.50	0.50	0.50	0.50	0.50
Condition #2	Time (s)	-0.10	0.00	0.07	0.08	0.09	0.10	0.11	0.12	0.13	0.14	0.15	0.16	0.17	0.18	1.10
	Voltage (V)	0.70	0.70	0.70	0.69	0.68	0.67	0.66	0.63	0.60	0.57	0.54	0.52	0.50	0.50	0.50
Condition #3	Time (s)	-0.1	0	0.05	0.1	0.15	0.2	0.25	0.35	0.45	0.55	0.7	0.8	0.9	1	1.1
	Voltage (V)	0.7	0.7	0.695	0.69	0.68	0.67	0.66	0.63	0.6	0.57	0.54	0.52	0.51	0.5	0.5

**Table 5. Inlet conditions, physical properties, and model parameters.**

Cell voltage	Volts	0.5
Anode channel inlet conditions for stoich of 1.2	Velocity ( $\text{m s}^{-1}$ )	2.6
	Mole fraction of $\text{H}_2$	0.729
	Mole fraction of $\text{H}_2\text{O}$	0.271
	Dew point temperature ( $^{\circ}\text{C}$ )	~65
Cathode channel inlet conditions for stoich of 2.0	Velocity ( $\text{m s}^{-1}$ )	9.9
	Mole fraction of $\text{O}_2$	0.165
	Mole fraction of $\text{N}_2$	0.622
	Mole fraction of $\text{H}_2\text{O}$	0.213
	Dew point temperature ( $^{\circ}\text{C}$ )	~57
Operating conditions	Operating Pressure (kPa)	101
	Cell Voltage (V)	0.5
	Permeability of diffusion layer ( $\text{m}^2$ )	$3.3 \times 10^{-15}$
Membrane thickness ( $\mu\text{m}$ )	50	
Density of dry membrane ( $\text{kg m}^{-3}$ )	2000	
Equivalent weight of a dry membrane ( $\text{kg mol}^{-1}$ )	1.1	
Oxygen exchange current density ( $\text{A m}^{-2}$ )	140	
Hydrogen exchange current density ( $\text{A m}^{-2}$ )	1000	



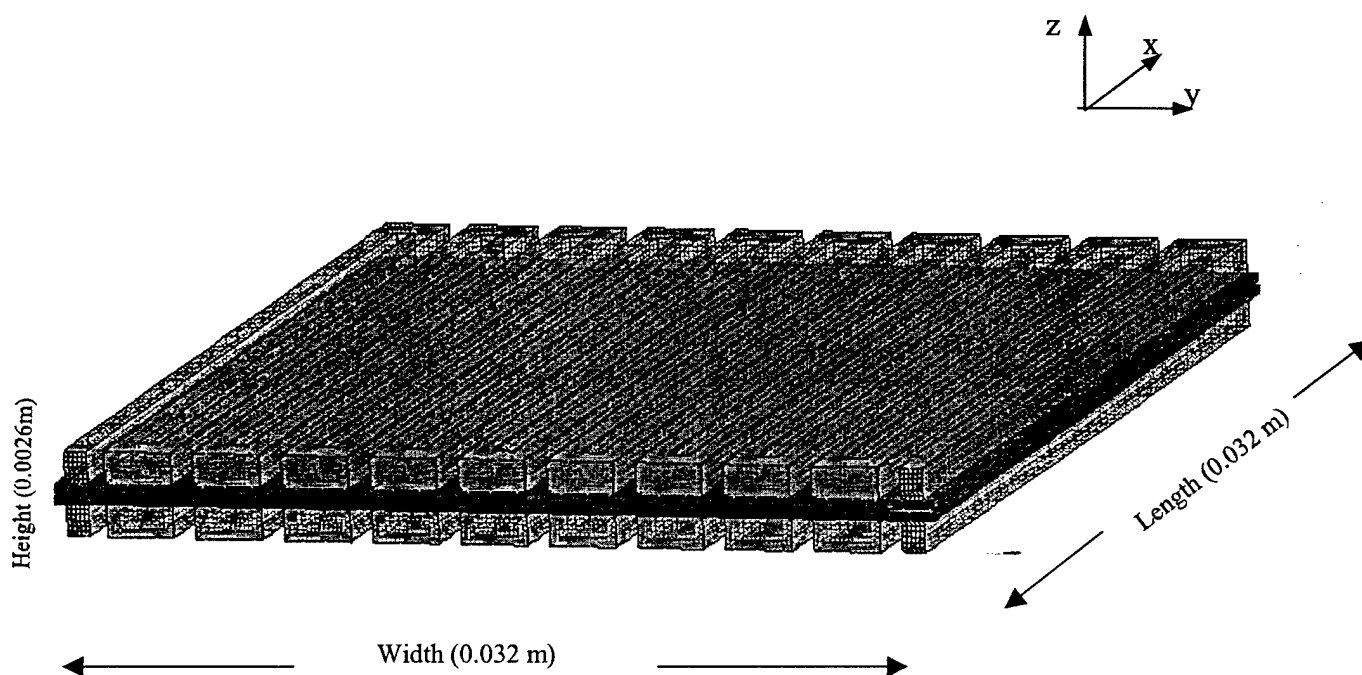
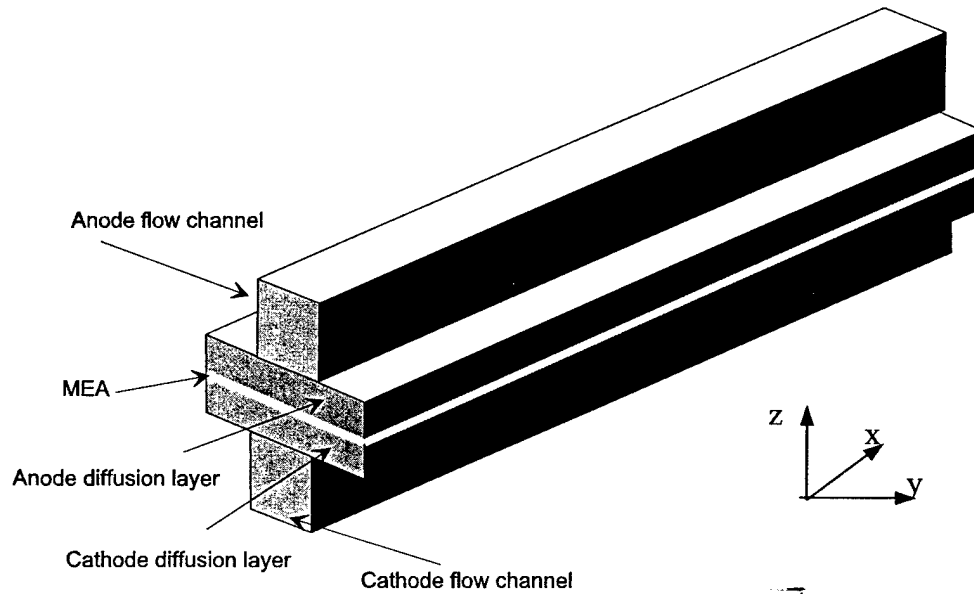


Figure 1. The picture shows actual flow-field plate with the gas channel and its geometry model. There are twenty straight channels connected in a serpentine fashion. Anode and cathode side flow channels are symmetric and placed properly aligned on top of each other [2, 3].

**A straight section  
of a flow channel**



**Typical cross-section of a flow channel**

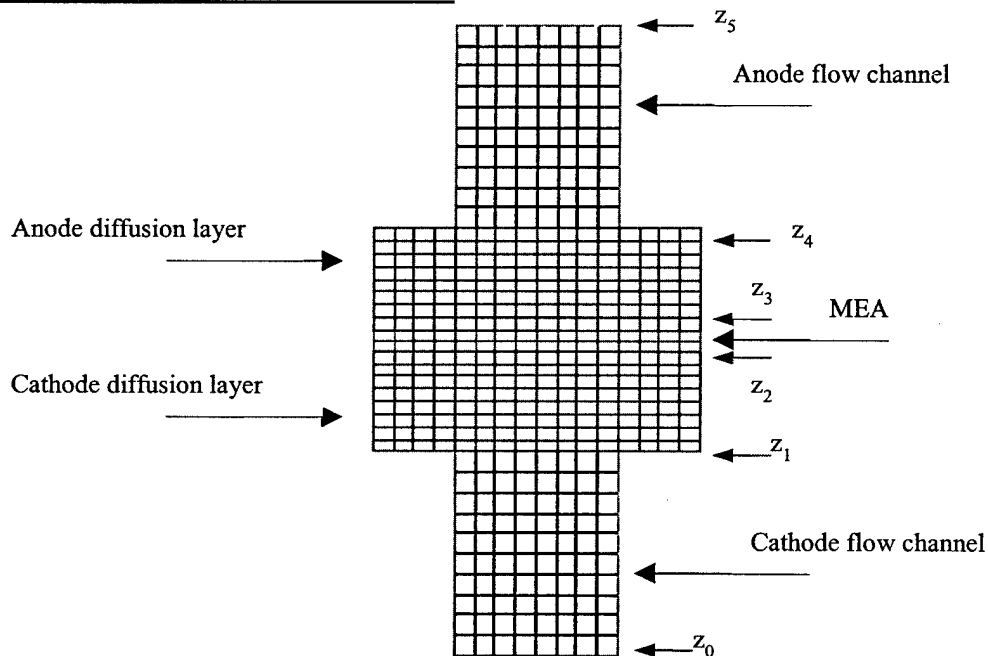


Figure 2. The detail of computational domain and grid arrangement used in this model [2, 3]. Note the number of volume elements used in Refs. [2] and [3] and shown in this figure is greater in the z-direction than the number used here as discussed in the text.

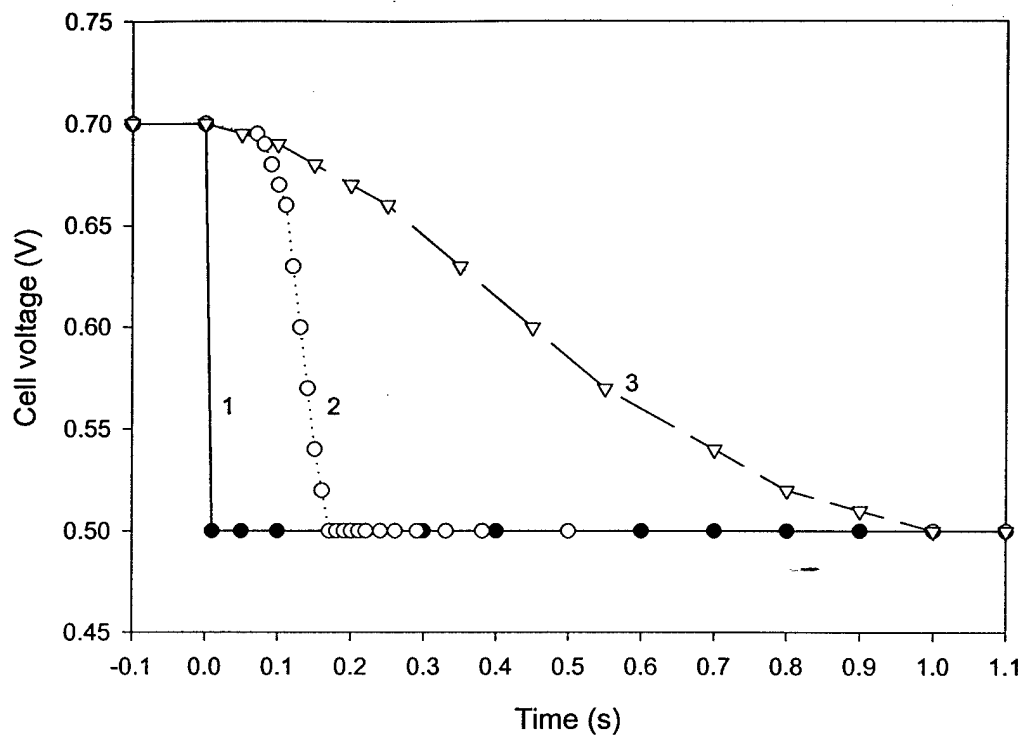


Figure 3. Cell voltage changes with time used in this study. Condition 1 (●), a step change; condition 2 (○), an increment change 1; condition 3 (▽), a slower increment change.

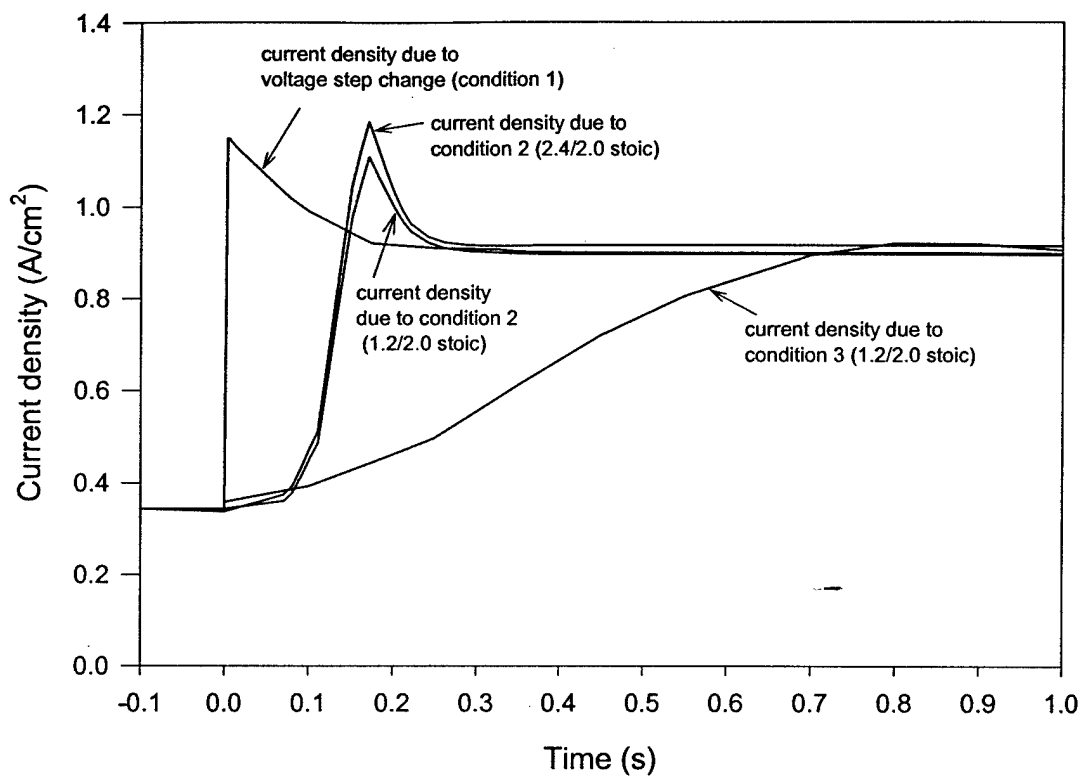


Figure 4. Transient response of average current density for three rates of voltage change from 0.7V to 0.5V.

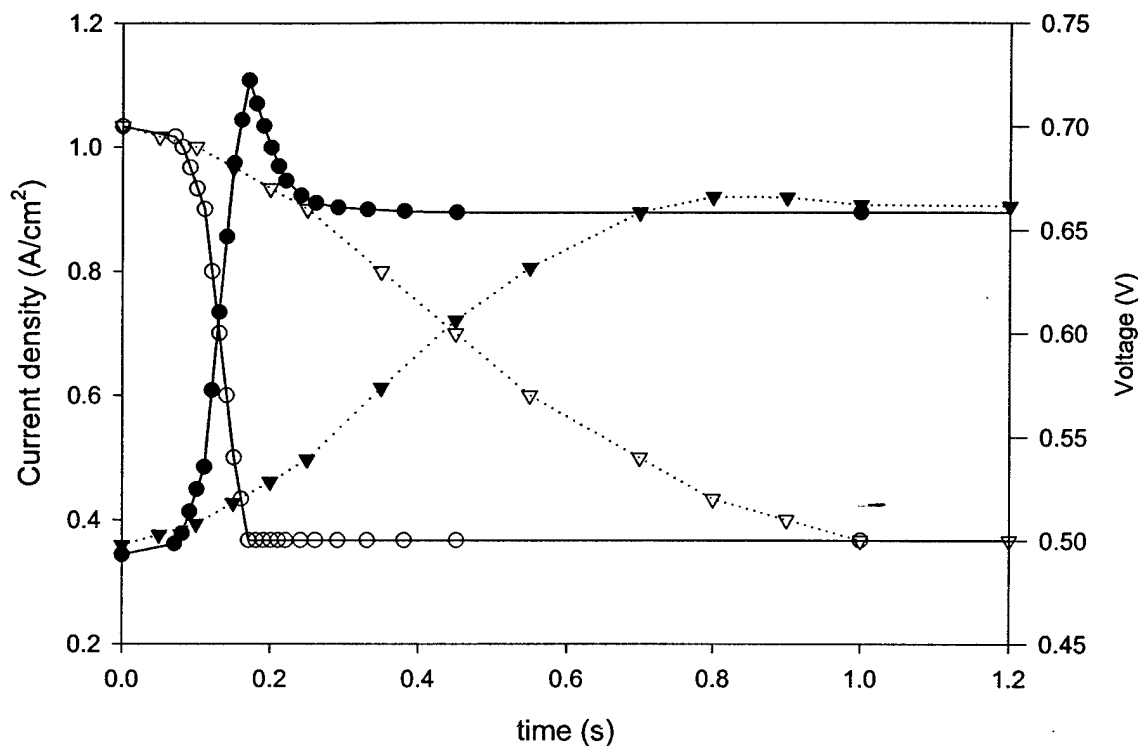
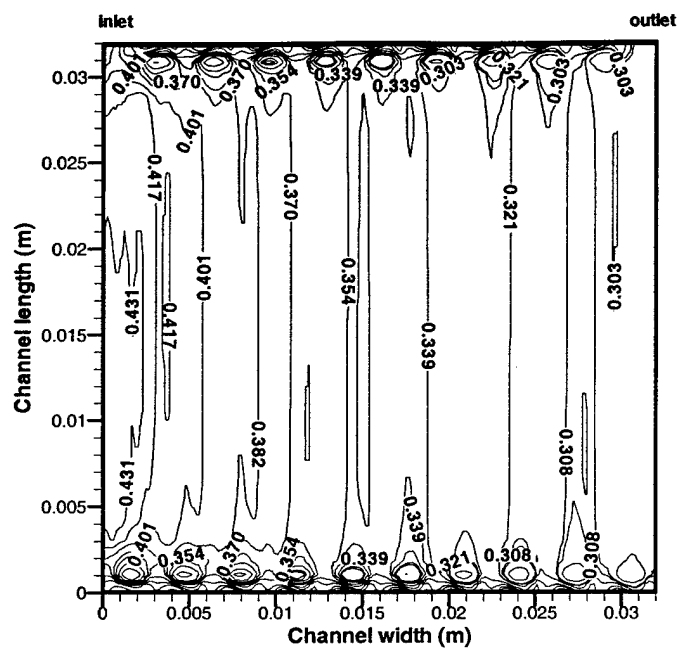
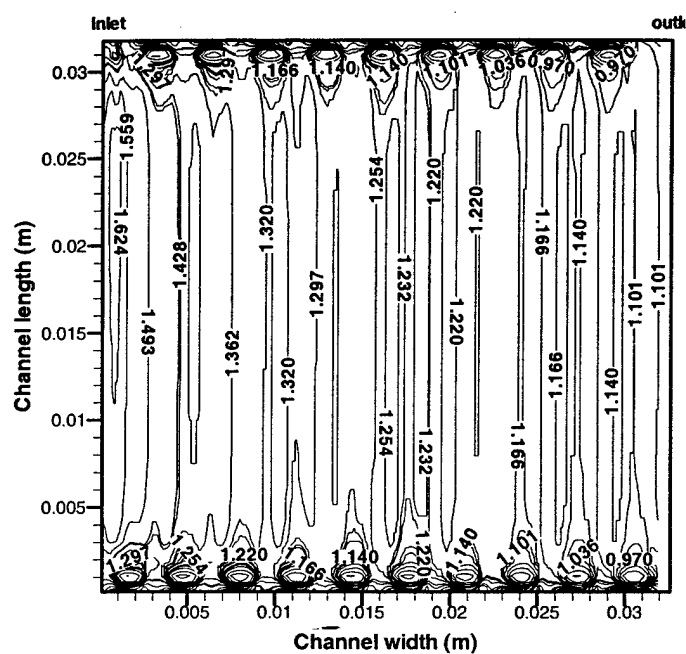


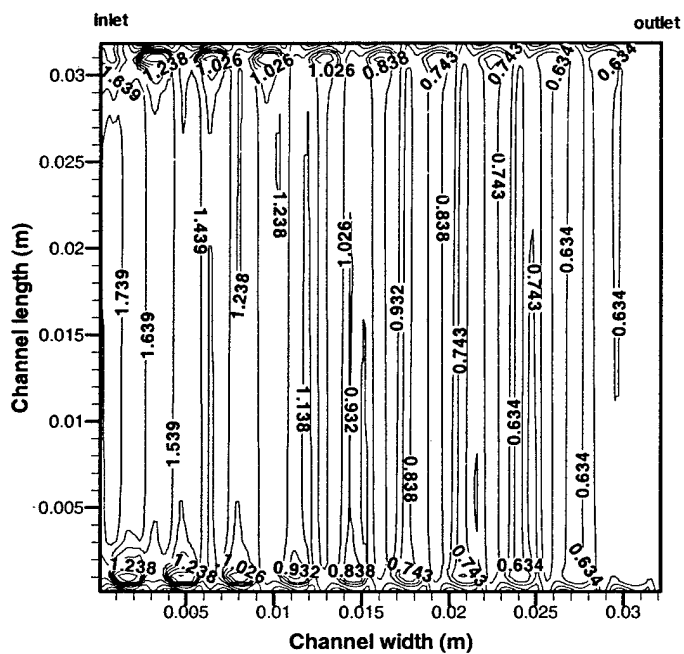
Figure 5. Transient response of average current density with different voltage increment change from 0.7V to 0.5V (● condition # 2 current density; ○ condition # 2 voltage; ▼ condition # 3 current density; ▽ condition # 3 voltage).



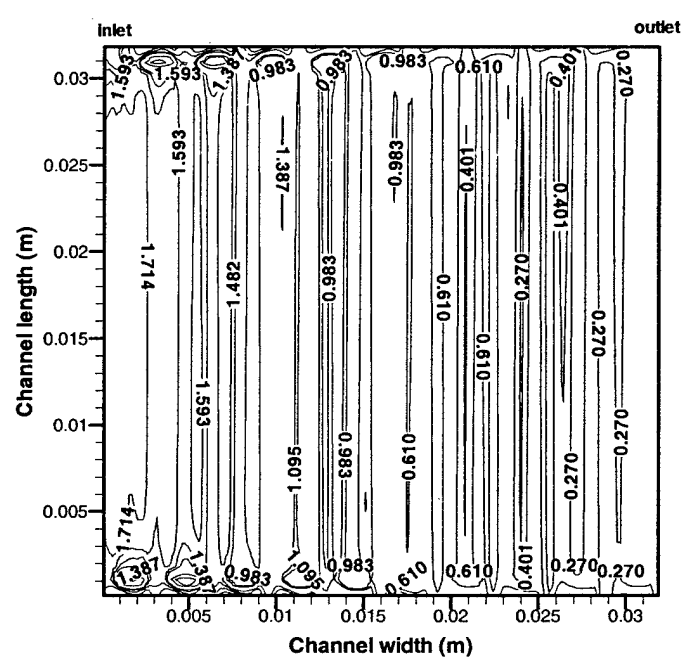
$t = 0.0s, 0.7V$



$t = 0.01s, 0.5V$



$t = 0.08s, 0.5V$



$t = 10.0s, 0.5V$

Figure 6. Local transient current density ( $A/cm^2$ ) contours at different times and cell voltages for step voltage change condition (Condition #1).

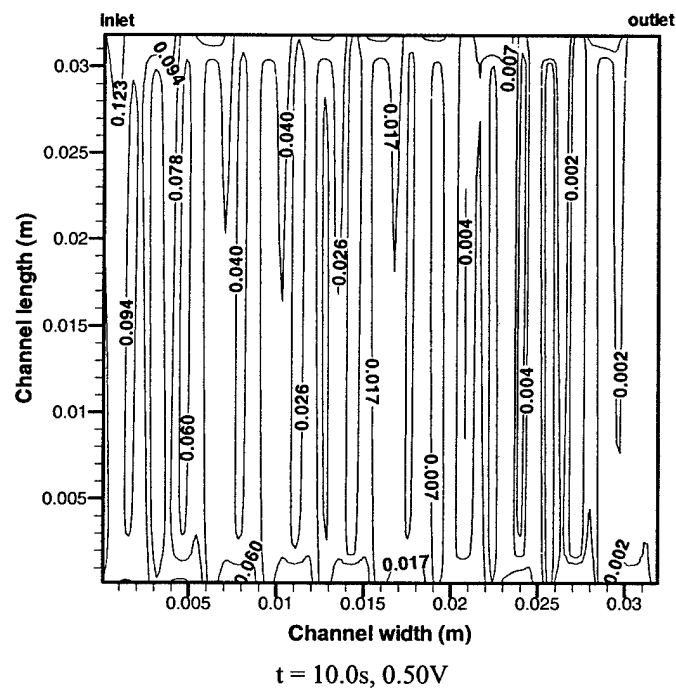
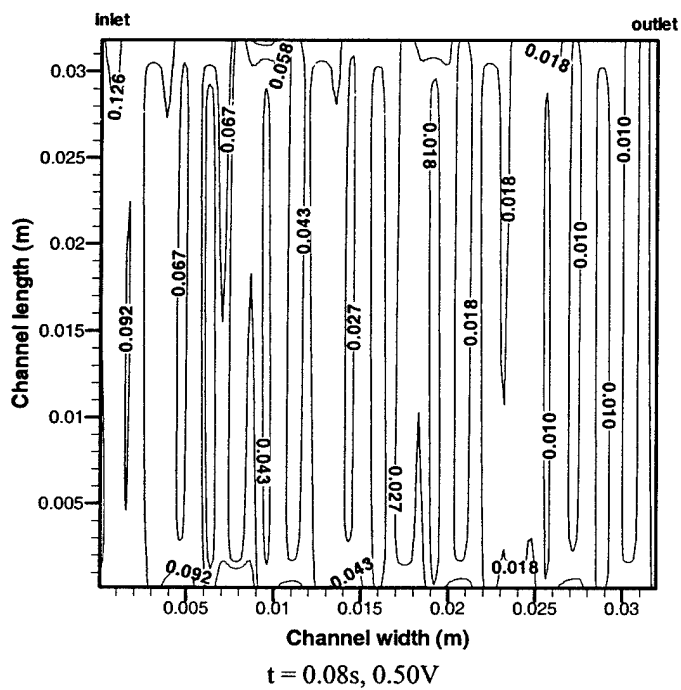
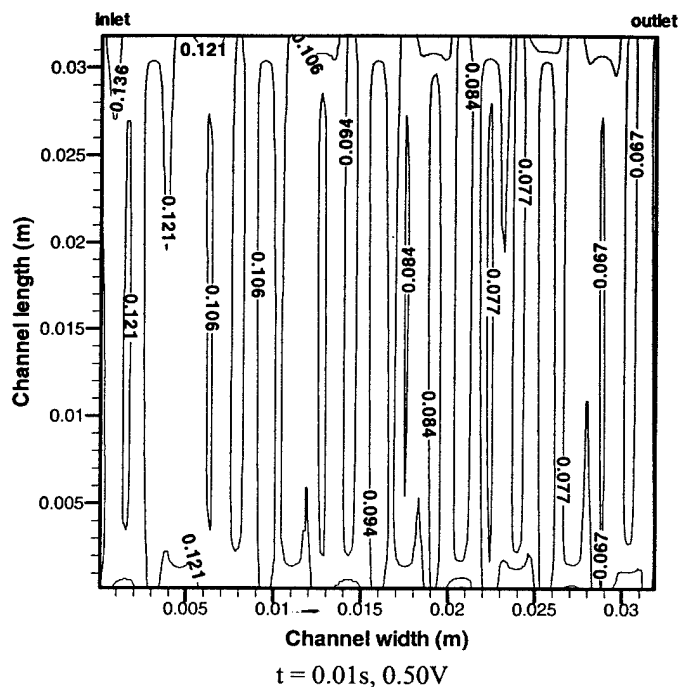
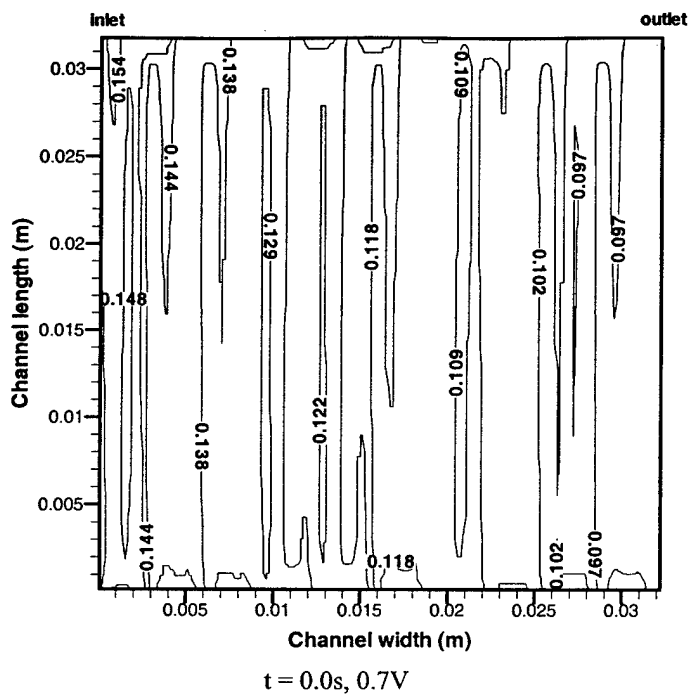
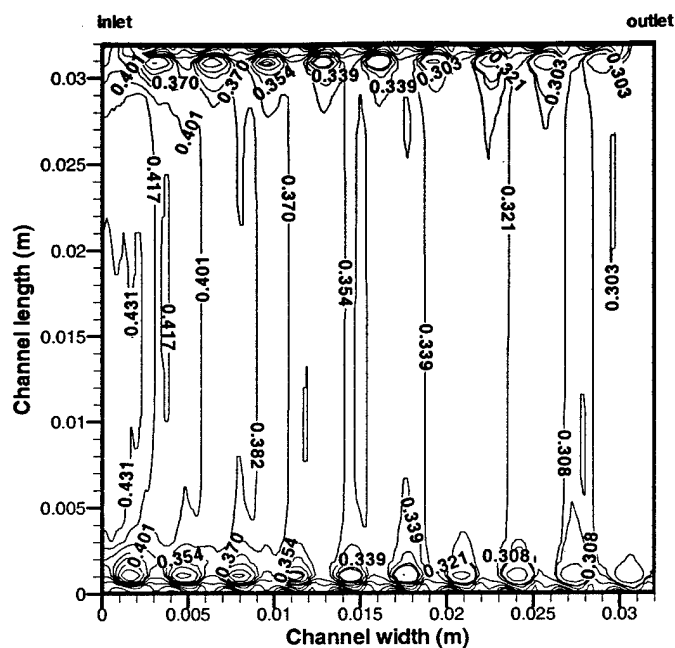
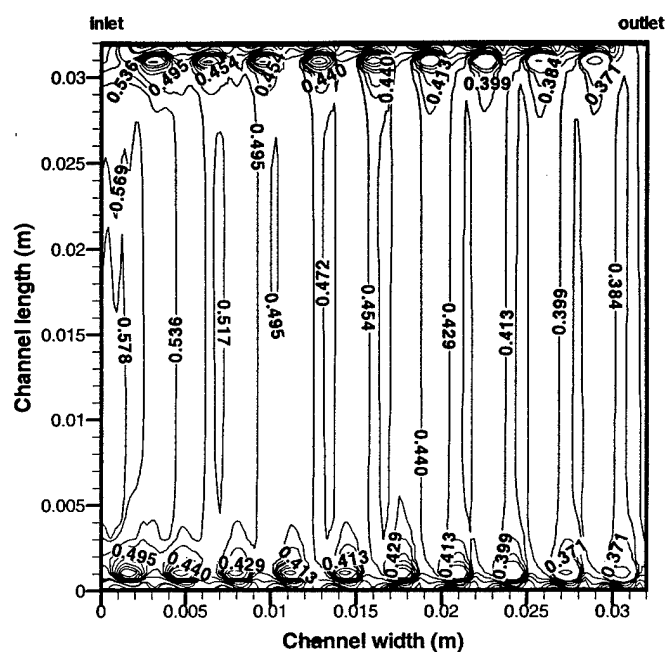


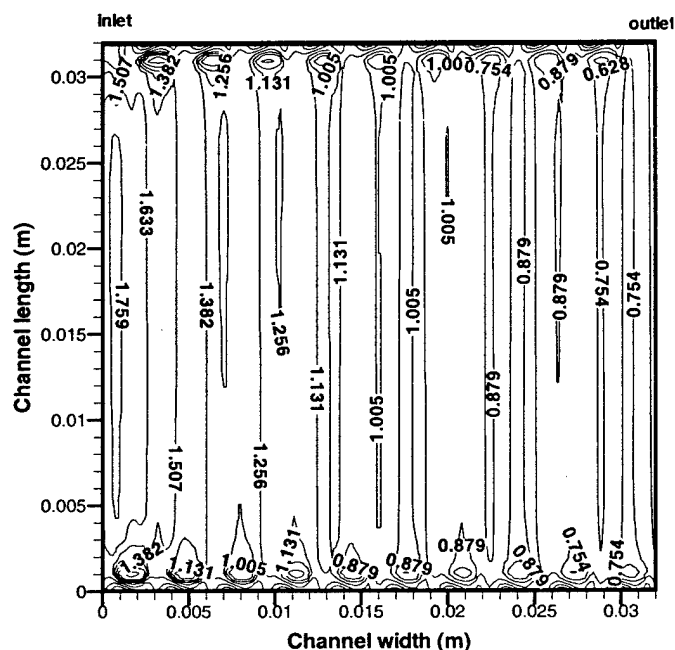
Figure 7. Local transient oxygen mole fraction contours at different times and cell voltages for step voltage change condition # 1.



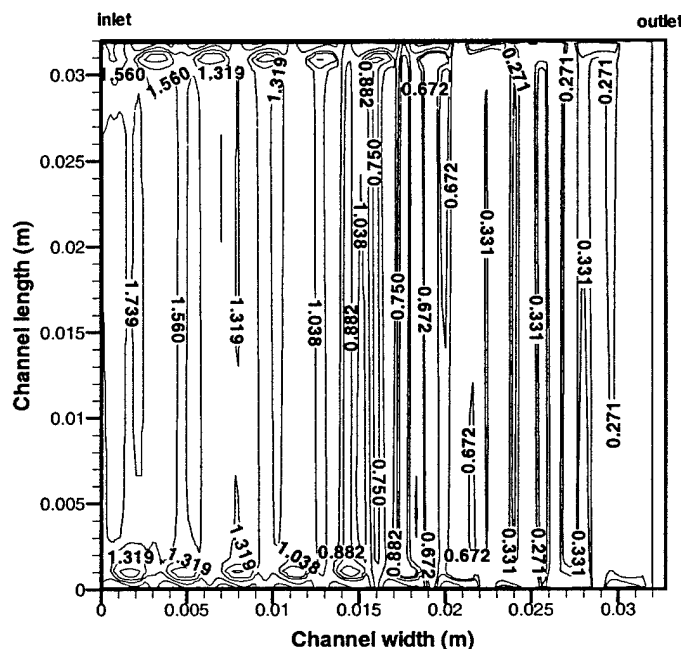
$t = 0.0s, 0.7V$



$t = 0.10s, 0.67V$



$t = 0.18s, 0.50V$



$t = 0.50s, 0.50V$

Figure 8. Local transient current density ( $A/cm^2$ ) contours at different times and cell voltage for increment voltage change condition #2. Here the maximum current occurs at  $t = 0.18s$ .



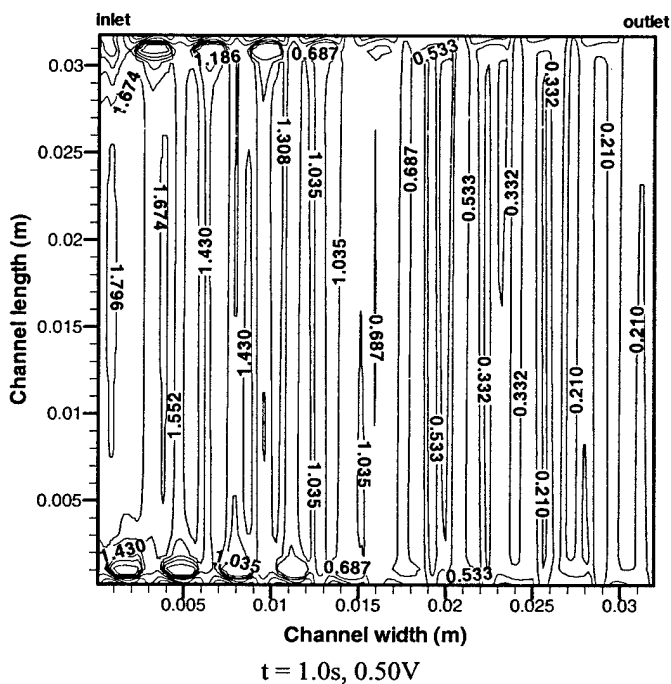
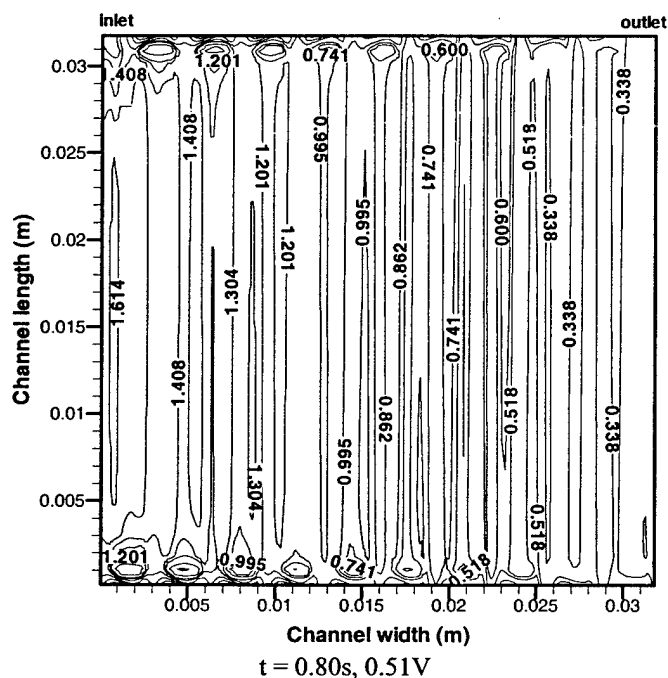
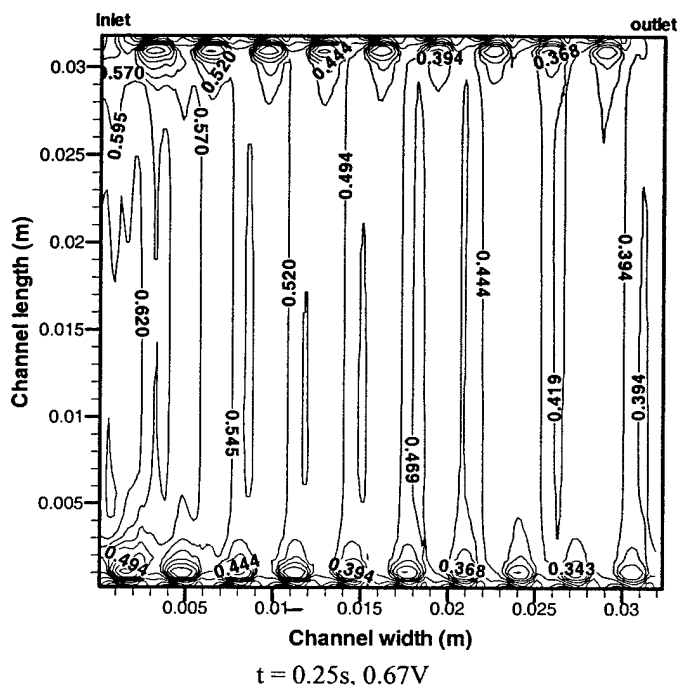
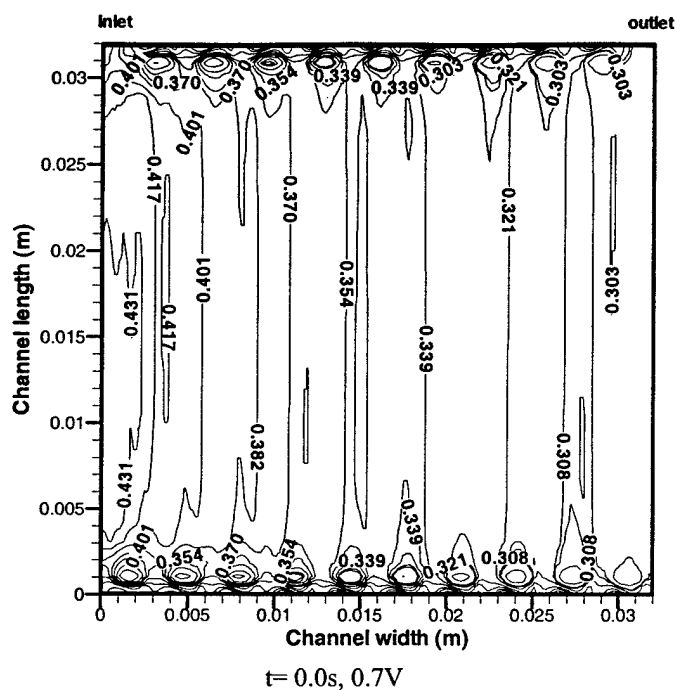


Figure 9. Local transient current density ( $A/cm^2$ ) contours at different times and cell voltages for increment voltage change condition #3. Here the maximum current occurs at  $t = 0.8s$ .



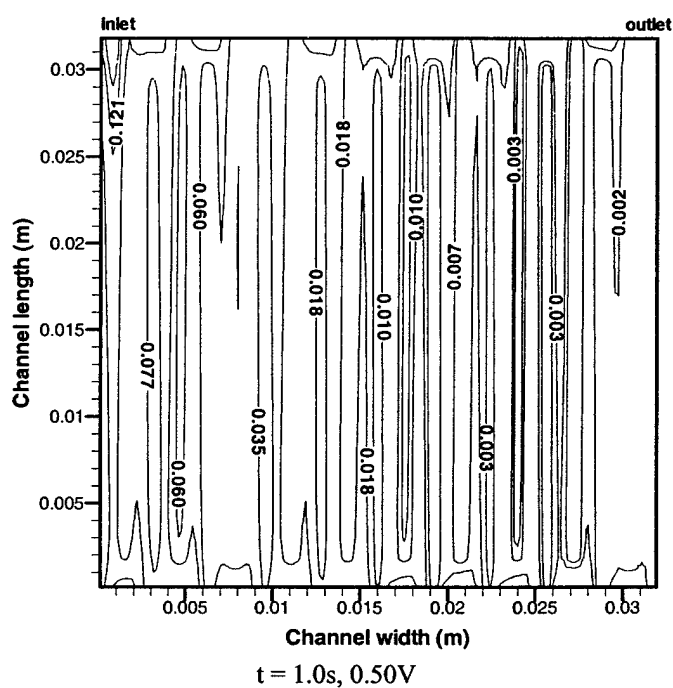
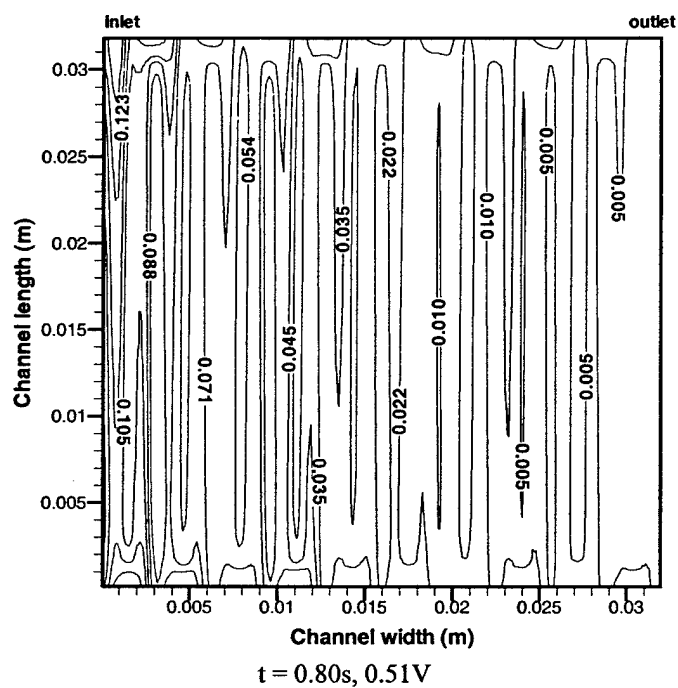
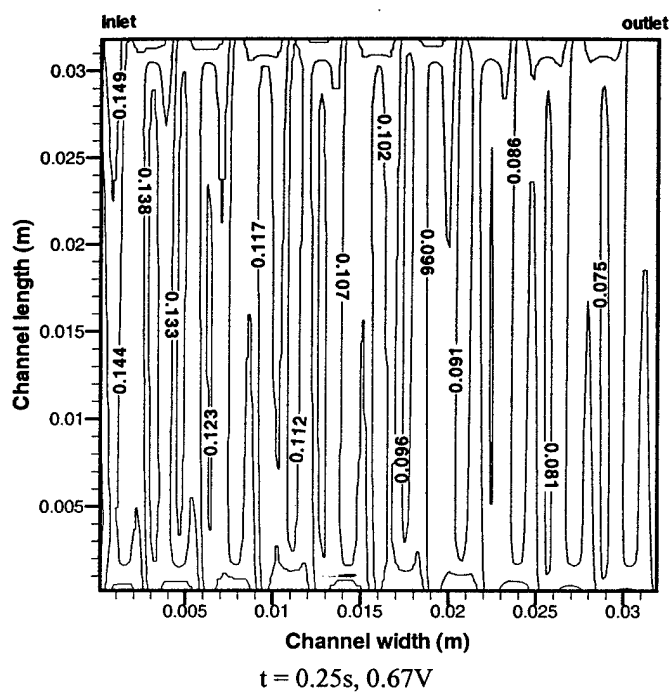
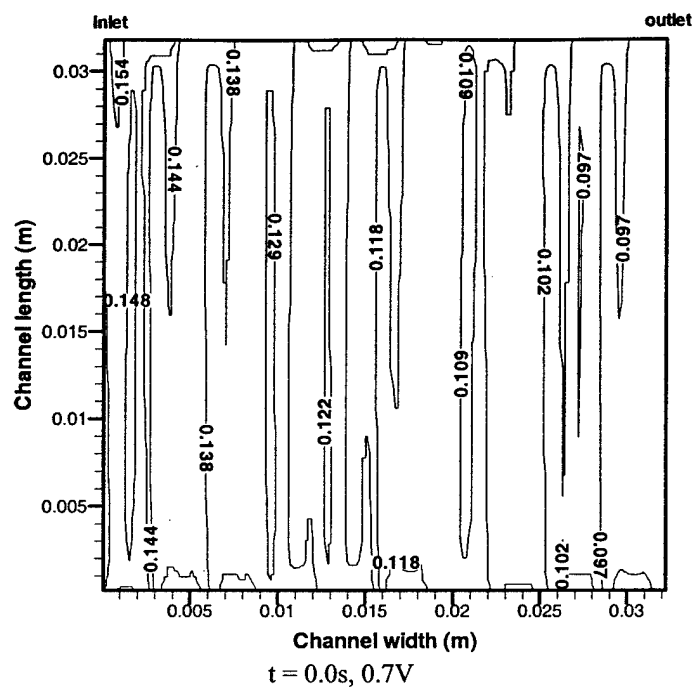


Figure 11. Local transient oxygen mole fraction contours at different times and cell voltages for increment voltage change condition #3.

**PREDICTING THE TRANSIENT RESPONSE OF A SERPENTINE  
FLOW-FIELD PEMFC.**

**II: NORMAL TO MINIMAL FUEL AND AIR**

**S. Shimpalee (shimpale@engr.sc.edu), W-k. Lee (leew@engr.sc.edu),  
and J. W. Van Zee<sup>1</sup> (vanzee@engr.sc.edu)**

Department of Chemical Engineering, University of South Carolina, Columbia, SC 29208

**H. Naseri-Neshat (hnaseri@hotmail.com)**

Department of Mechanical Engineering Technology, South Carolina State University,  
Orangeburg, SC 29117

**Van Zee Group Technical Memorandum # 12**

**February 2002**

Submitted as a *Technical Paper*  
to

Prof. Ulrich Stimming  
*Fuel Cells-From Fundamentals to System*  
Fuelcells.paper@ph.tum.de

October 27, 2002

---

<sup>1</sup> - Corresponding author: Phone: (803) 777-2285; FAX: (803)-777-8142, e-mail: vanzee@engr.sc.edu

Keywords: PEM, fuel cells, Membrane Electrode Assembly, Electric vehicle

## Abstract

The 3-D transient model presented in Part I is used to study the overshoot and undershoot behavior observed in a PEMFC during operation with fixed normal stoichiometric flowrates of hydrogen and air for a 1.0 V/s change in the load. In contrast to the behavior with excess flow shown in part I, the predictions show second order responses for both decreases and increases in the load. That is, there is current overshoot when the load cell is decreased from 0.7 V to 0.5 V and there is current undershoot when the cell voltage is increased from 0.5 V to 0.7 V. The simulation of a  $10\text{-cm}^2$  reactive area with a serpentine flow path is used to explain this behavior in terms of the reacting gas concentrations, the flow through the gas diffusion media, the movement of water through the MEA by electroosmotic and back diffusion forces, and the variation in the distributions of current density. The operating conditions correspond to 101 kPa, 70 °C cell temperature, anode and cathode dewpoints and stoichiometries of 65 °C and 57 °C and 1.45 and 2.42 at an initial operating voltage of 0.7 V and current density of  $0.33\text{ A/cm}^2$ . The fixed flowrates correspond to stoichiometries of 1.05 and 1.73 at 0.5 V for the  $0.46\text{ A/cm}^2$  predicted current density. The predictions illustrate regions where the MEA may alternate between wet and dry conditions and this may be useful to explain stability and durability of the MEA during transient operation.

## Introduction

Transient load changes during operation of PEMFCs with fixed gas flowrates may expose the MEA to various degrees of stoichiometry for either stationary or automotive applications. This transient operation may be a result of a sudden demand as an appliance starts or as a vehicle is accelerated or decelerated. Further these transients may be of sufficient magnitude and speed that gas flowrates cannot be adjusted by feedback control or that the capacitors in the system cannot accommodate the demand. Thus, the fuel cell by default or design may need to act as a capacitor during the power demand surge. The use of a mathematical model and a time-dependent three dimensional (3-D) equation solver is presented here to illustrate situations where the current does not change in a typical first-order manner between steady states. In fact we have observed experimentally [1] and through our predictions that the current can exhibit pseudo second-order behavior with overshoots and undershoots of the current.

In part I of this series [2], we presented a time-dependent 3-D model and the corresponding simulation results that showed the effect of anode stoichiometry and rate of voltage change on the transient response of a 10-cm<sup>2</sup> PEMFC with a serpentine flow field. That paper considered the response when the flow of gas was large, exceeding a stoichiometry of 2.6/4.4<sup>a</sup> for 0.7 V and 1.2/2.0 for 0.5 V (i.e. a constant flow rate of 90 cm<sup>3</sup>/s and 355 cm<sup>3</sup>/s for the anode/cathode respectively at 101 kPa and 70 °C for 0.33 A/cm<sup>2</sup> at 0.7 V). The simulation used a commercial computational fluid dynamics (CFD) solver, FLUENT, with modified subroutines to account for the electrochemical reactions of hydrogen and oxygen and the transport of water through the membrane and catalysts layer. The complete 3-D Navier-Stokes equations were solved with a control-volume-based discretization of the computational domain and the velocity and pressure distribution in the flow channels and the gas diffusion layer were obtained for every time step.

In contract to part I, we present here predictions to discuss the behavior when the fixed flowrates correspond to normal and maximum utilization (i.e., changes in stoichiometry from 1.45/2.42 to 1.05/1.73). That is, in an effort to expand the understanding the behavior of a PEMFC, we present here a study that focuses on changes in the cell voltage between 0.7 V and 0.5 V for a stoichiometry of 1.45/2.42 for the 0.7 V conditions (i.e., 0.33 A/cm<sup>2</sup>). The operation at 0.5 V results in almost complete utilization of the hydrogen and perhaps a mass transfer limitation of the oxygen. We call this 1.05/1.73 stoichiometry a “minimal” stoichiometric condition because the cell operated a fixed voltage cannot exhibit truly starved condition (i.e., the current will adjust to the supply of fuel).

This numerical simulation uses the same transient, isothermal, 3-D mass transfer model and serpentine gas-flow-channel geometry as part I. The operating conditions and model parameters of this work are shown in Table 1. The transient load profile consists of changing the cell voltage from 0.7 V at steady state to 0.5 V and from 0.5 V at steady state to 0.7 V at an average rate of 1 V/s. This rate was not linear as shown in Table 2 because we followed the output from an experimental load. As discussed in part I, the predictions were grid and time-step independent.

## Results and Discussion

Figure 1 shows how the averaged current density changes when the cell voltages are changed from 0.5 V to 0.7 V and from 0.7 V to 0.5 V. The average is obtained by multiplying the current in each grid cell by the surface area of each cell, summing the resulting current, and then dividing this current by 10-cm<sup>2</sup>. Figure 1a shows undershoot in the current density when the cell voltage is increased. The lowest averaged current density is 0.23 A/cm<sup>2</sup> when the cell voltage reaches 0.685 V, and then it increases and reaches a steady state value at 0.33 A/cm<sup>2</sup>. Note that the flow condition at 0.7 V

---

<sup>a</sup> Our notation for specifying operating conditions is to list the anode conditions first followed by the cathode. Thus, the stoic

corresponds to stoichiometries of 1.45/2.42 at 0.33 A/cm<sup>2</sup> and that at 0.5 V these conditions correspond to stoichiometries of 1.05/1.73 for 0.46 A/cm<sup>2</sup>. Figure 1b shows overshoot behavior. The averaged current density increases from 0.33 A/cm<sup>2</sup> to 0.96 A/cm<sup>2</sup> when the cell voltage is 0.52 V and then the current density decreases and reaches the steady state at 0.46 A/cm<sup>2</sup>. This is the same current density as that shown at 0.5 V in Figure 1a. Note that the symbols shown in Figure 1 and subsequent figures are for convenience and that they are not related to the true stepping of the numerical integration. The height of the overshoot and undershoot can be changed by the rate of cell voltage change and by the flow rates (See the discussion by Shimpalee et al. [2] for the case of excess stoichiometry), but those changes are not the focus of our work here. Instead, here we fix the rate of voltage change and flowrate and study the dependent variables in order to understand their interactions during current overshoot/undershoot behavior.

Figure 2 shows the variation of the averaged values of variables to be studied in this paper. These variables are net water flux per proton (Alpha), oxygen mole fraction, and hydrogen mole fraction. As discussed above, the equations for these variables are shown in Tables 1 and 2 of Ref. 2. Consider the change from a "minimal O<sub>2</sub>" condition to a "typical O<sub>2</sub>" concentration when the cell voltage is increased from 0.5 V to 0.7 V as shown in Figure 2a. Here, the averaged net water flux per proton decreases until the cell voltage reaches 0.57 V and then it shows its own overshoot behavior before it reaches a steady state value after the cell voltage reaches 0.7 V. During this change, the oxygen mole fraction and the hydrogen mole fraction increase and also reach steady state values substantially after the voltage has reached 0.7 V (i.e., at 0.5 s for the mole fractions versus 0.2 s for the voltage). As discussed in part I, Alpha is the sum of the electroosmotic drag of water and the diffusion of water from the cathode to the anode. It is negative when the water back diffusion is greater than the electroosmotic drag and this

---

was 2.6 for the anode and 4.4 for the cathode. This relates to 160 % excess hydrogen and 340 % excess oxygen in the stream.



occurs when the membrane is thin and the cathode water activity at the membrane surface is larger than the anode water activity. The negative average value at 0.5 V also results from the operating conditions and the minimal flowrates. Figure 2b shows the relationship of these variables when the cell voltage is changed from 0.7 V to 0.5 V in 0.2 s. When the cell voltage is decreased, the mole fractions of oxygen and hydrogen are lowered due to the increased current. At voltage of 0.505 V, water back diffuses to the anode through the MEA as indicated by the negative value of Alpha. The change of Alpha lags the change in voltage.

It may be important to note that these predictions do not accurately account for water phase change caused by a distribution in the temperature and activity of water in each stream. In fact some of the predicted local activities exceed 1.0 during the simulation and thus the possibility of condensation was indicated. In defense of the predictions and the discussion here, it is our experience with steady state calculations that the local temperature increases at high reaction rates so that the local water activities decrease when the energy balance is included. Thus the predictions here will show slightly higher currents and lower mole fractions because local activities greater than 1.0 increase local conductivity and because condensation will block some reaction sites. Again we show and discuss these transient isothermal predictions because they provide a less computationally intensive solution to the transient problem and because it is our experience that the isothermal equations provide the same general trends as a more complete equation set.

To further explain the overshoot and undershoot behaviors, let us examine the local profiles at the MEA surface at  $x = 0.016$  m across the serpentine flow path as shown in Figure 3. Figures 4a and 4b illustrate the changes in the local current density profiles at different cell voltages and times. Figure 4a shows the transient local current density profiles when the cell voltage is changed from 0.5 V to 0.7 V and Figure 4b presents the profiles when the cell voltage is changed from 0.7 V to 0.5 V. In Figure 4a,

when the cell voltage is 0.5 V and a steady state is maintained, the local current density profile is highly non-uniform. The largest current density is at the inlet region ( $y = 0.0$  m) with the value of  $1.46 \text{ A/cm}^2$  and the lowest is at the outlet region ( $y = 0.032$  m) with the value of almost  $0.0 \text{ A/cm}^2$ . Further, there is the appearance of oscillatory behavior in local current density profile due to the rib spacing between the flow channels. These areas are most restricted to mass transfer and they respond to load changes at rates different from the area adjacent to the flow channels. According to Figure 4a, as the cell voltage is increasing, the local current density profile is becoming uniform with decreasing local values in the first half of the cell (from inlet to about the center) and increasing of the local current density values in the second half of the cell (from center to outlet). At a time of 0.13 s (i.e., at cell voltage of 0.67 V), the current density profile is at about the valley of the current undershoot. On the other hand, when the cell voltage is decreased from 0.7 V to 0.5 V, Figure 4b shows that the local current density profile increases in a somewhat uniform distribution until it reaches the highest profile at a cell voltage of 0.52 V (i.e., 0.13 s). After that, the current density profile becomes more non-uniform with the significant decreases in local current density from the center of the cell toward the outlet region. The local current density changes from a linear profile with width until about 0.13 s (0.52 V) and then the starved conditions produce an exponential distribution after 0.2 s. The reasons for the overshoot/undershoot behavior of current can be discussed by considering the distributions of oxygen concentration and Alpha as shown in Figures 5 and 6.

Figures 5a and 5b show the transient distributions of local oxygen mole fraction across the electrode width for the undershoot (cell voltage changes from 0.5 V to 0.7 V) and overshoot conditions (cell voltage change from 0.7 V to 0.5 V). As shown in Figure 5a at a cell voltage of 0.5 V and steady state, the distribution of oxygen mole fraction is similar to the current density profile due to fixed flow rates corresponding to a starved condition. That is, the oxygen mole fraction decreases along the

electrode width from inlet toward the outlet especially in the first half of the cell where the reaction rate is high. Oxygen is almost depleted in the second half of the cell (i.e., a mole fraction between 0.01 and 0.005) and this limits the current density in these locations. Then, when the cell voltage is increased, the rate of gas consumption is decreased and the oxygen mole fractions increase. Note that the non-uniform profile indicates a time lag of at least 0.13 s (i.e., a cell voltage of 0.67 V) before there is significant reaction toward the outlet and that this lag agrees with the current undershoot presented in Fig 1a. This is because there is a residence time delay of 0.15 s<sup>a</sup> where the unreacted gases have not passed from the inlet to the gas depleted locations. After 0.2 s, the local oxygen distributions become more uniform with significantly increased values in second half of the cell. This corresponds with the increasing local current density as shown in Figure 4a for  $y > 0.016$  m at  $t = 0.2$  s.

When the cell voltage is decreased from 0.7 V to 0.5 V, the reaction rate is increased and the rates of gases consumption increase along with the rate of cathode water production. Figure 5b shows the distributions of oxygen mole fraction that can be compared with Figure 5a. The non-uniformity of oxygen distribution increases as the reaction rate increases. Consequently, the depletion of the reacting gases, especially oxygen, does not occur until after the current density reaches the peak of overshoot (Cell voltage = 0.52 V and time = 0.13 s). This depletion creates the reduction in current density shown in Figure 4b.

Figure 6 shows the transient distributions of local net water flux per proton across the electrode width during the observed undershoot and overshoot behavior. Figure 6a shows the transient water flux distributions when the cell voltage is increased from 0.5 V to 0.7 V. At steady state with 0.5 V and at time equals 0.1 s with 0.6 V, the large negative values, indicating significant back diffusion, are most noticeable. Thus even though the current density is low, any water produced or carried downstream from

---

<sup>a</sup> Calculated with  $v = 4.5$  m/s at the cathode side and a channel length of 0.66 m for the single pass cell. Note that

the first half of the cell, diffuses to anode. The large differences between the area under the ribs and the area in the channel show the effect of oxygen mass transfer resistance. When the cell voltage is increased with time, the difference between electroosmotic transport and back diffusion is reduced due to the supply of oxygen to the cathode, the supply of hydrogen to the anode, and the resumption of current in the second half of the cell. Similar profiles are shown in Figure 6b when the cell voltage is decreased from 0.7 V to 0.5 V.

The undershoot/overshoot behavior of the PEMFC performance can now be summarized based on the discussion of Figs. 2-6. For undershoot behavior, the reaction rate is reduced due to increasing the cell voltage faster than the oxygen that can replenish the starved locations. That is, the decrease in current density and the lowest value of the current density is reached when the partial pressure of oxygen at the downstream (starved) location starts to increase. Thus as the oxygen is replenishing the depleted zones, the cell current (and geometric averaged current density) increase. These figures confirm that the rate of increase in oxygen mole fraction is slower than the increase in cell voltage. For the overshoot behavior, the reaction rate is increased because of the lowering of the cell voltage. Thus the current density increases and reaches the maximum averaged value before the oxygen starts to diminish in the second half of the cell. This lower oxygen in the second half of the cell leads to the oxygen starved operating condition. Thus the rapid lowering of the local current density value correlates with the time at which the oxygen starts to decrease.

## Conclusions

A 3-D transient simulation of PEM fuel cell was studied at minimal stoichiometric fixed flow rates of feed gases. The flowrates correspond to normal fuel and oxygen utilization at the high cell

---

consumption of the gas reduces the velocity along the channel length and that this gives a longer delay.

voltage and a minimal operating condition at the low cell voltage. The cell voltage was changed at a somewhat rapid rate of 1.0 V/s and modest undershoot and overshoot behavior in the current was observed and explained in terms of the distributions of current density, oxygen concentration, and net water transport.

For a change from a minimal condition, the results indicate that when the cell voltage is increased, the response in the local current density decreases faster than the flow of oxygen can replenish the regions that experience a starvation of  $O_2$ . Then, the current density increases after oxygen is relished and the current distribution becomes more uniform. When the cell voltage is decreased, the current density increases and reaches the peak of overshoot while the capacity of the oxygen in the flow channels is used. Then as the local partial pressure decreases toward the exit of the cell, the geometric averaged current density starts to decrease toward the steady state value. This steady state value corresponds to a highly non-uniform local current density distribution, dependent on local concentrations of the reacting gases. For these conditions, oxygen appears to control the distribution. These results may help effort in the design of the flow-field and manifold configuration. These design changes may improve stack performance.

### **Acknowledgements**

The authors wish to acknowledge the financial support of this work by the South Carolina State University/University Transportation Center (Grant # 2000-013), the Department of Energy-EPSCoR (Cooperative Agreement Grant # DE-FG02-91ER75666), and the Office of Naval research (Grant # N00014-98-1-0554).

### **References**

- [1] S-H. Kim, W-K. Lee, S. Shimpalee, and J. W. Van Zee, paper # 127 presented at the 201<sup>st</sup> meeting of the Electrochemical Society, May 2002.
- [2] S. Shimpalee, W-K. Lee, H. Naseri-Neshat, and J. W. Van Zee, submitted to *J. Fuel Cells*, 2002.
-

**Table 1. Inlet conditions and parameters**

Anode channel inlet conditions	Velocity ( $\text{m s}^{-1}$ )	1.2
	Mole fraction of $\text{H}_2$	0.759
	Mole fraction of $\text{H}_2\text{O}$	0.241
	Dew-point temperature ( $^{\circ}\text{C}$ )	65
Cathode channel inlet conditions	Velocity ( $\text{m s}^{-1}$ )	4.5
	Mole fraction of $\text{O}_2$	0.170
	Mole fraction of $\text{N}_2$	0.638
	Mole fraction of $\text{H}_2\text{O}$	0.192
	Dew-point temperature ( $^{\circ}\text{C}$ )	57
Operating conditions	Operating Pressure (kPa)	101
	Permeability of diffusion layer ( $\text{m}^2$ )	$3.3 \times 10^{-15}$
Membrane thickness ( $\mu\text{m}$ )	50	
Density of dry membrane, ( $\text{kg m}^{-3}$ )	2000	
Equivalent weight of a dry membrane ( $\text{kg mol}^{-1}$ )	1.1	
Oxygen exchange current density ( $\text{A m}^{-2}$ )	140	
Hydrogen exchange current density ( $\text{A m}^{-2}$ )	1000	

**Table 2. Cell voltage changes from 0.5 V to 0.7 V in 0.2 s and from 0.7 V to 0.5 V in 0.2 s.**

Time (s)	0.0	0.02	0.04	0.07	0.08	0.09	0.10	0.11	0.12	0.13	0.15	0.175	0.2
Cell voltage (V)	0.50	0.5025	0.505	0.52	0.54	0.57	0.60	0.63	0.65	0.67	0.685	0.695	0.70
Time (s)	0.0	0.025	0.05	0.07	0.08	0.09	0.10	0.11	0.13	0.14	0.16	0.18	0.2
Cell voltage (V)	0.70	0.695	0.685	0.67	0.65	0.63	0.60	0.57	0.52	0.51	0.505	0.5025	0.50

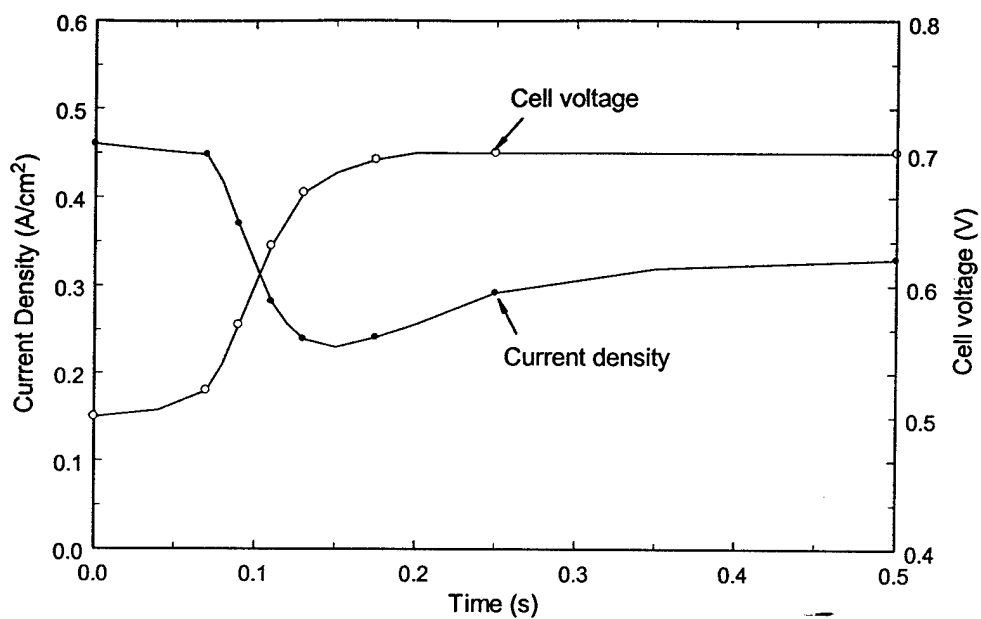


Figure 1a. Averaged current density for change from 0.5 V to 0.7 V. Open circles indicate cell voltage and filled circles indicate current density.

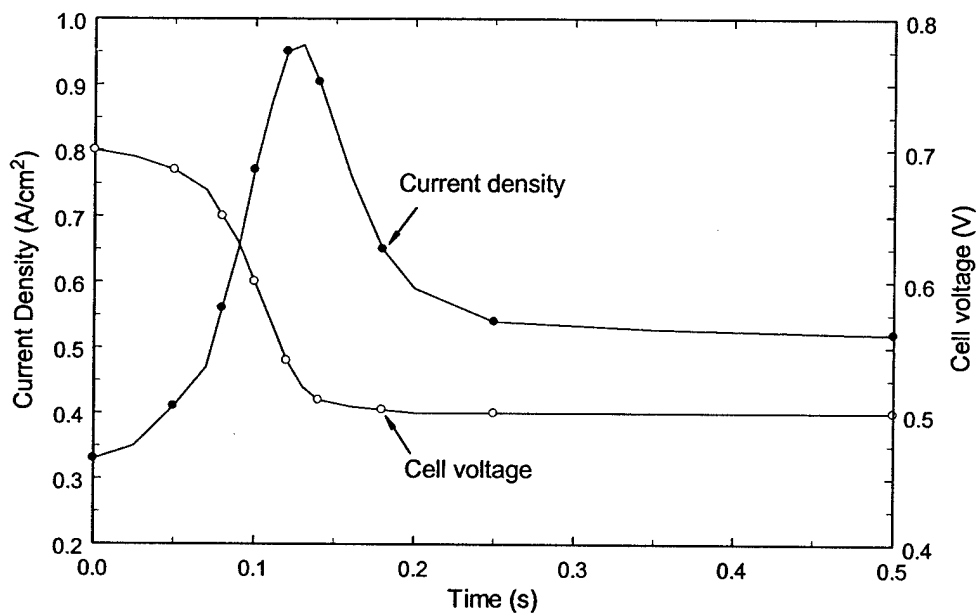


Figure 1b. Averaged current density for change from 0.7 V to 0.5 V. Open circles indicate cell voltage and filled circles indicate current density.



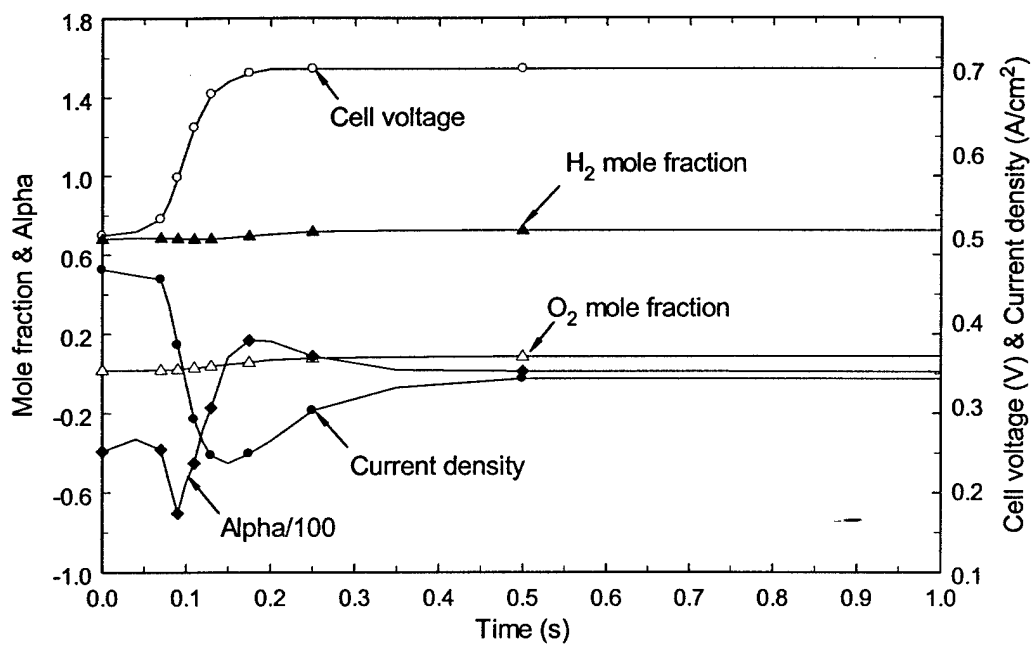


Figure 2a. Averaged cell variables during undershoot behavior.

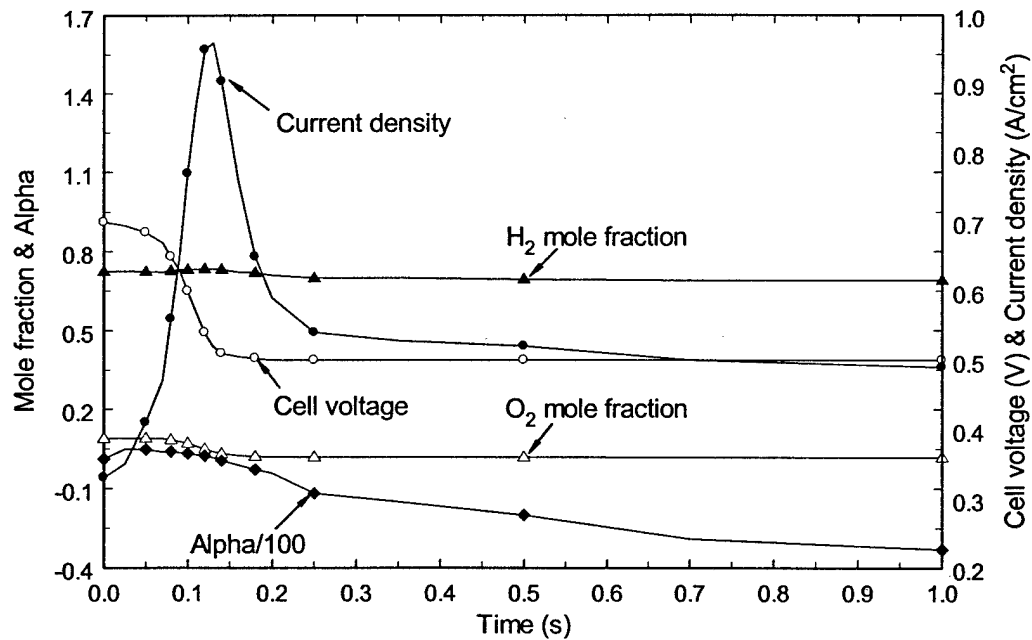


Figure 2b. Averaged cell variables during overshoot behavior.

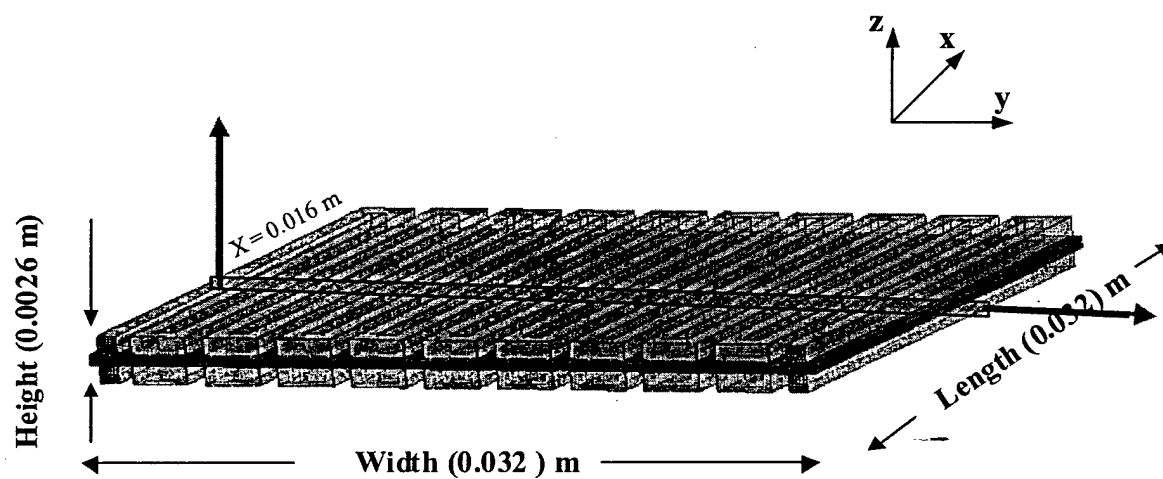


Figure 3. The grid geometry of 10-cm<sup>2</sup> PEMFC with the location where the local profiles at the MEA surface across the serpentine flow path and electrode width are presented.

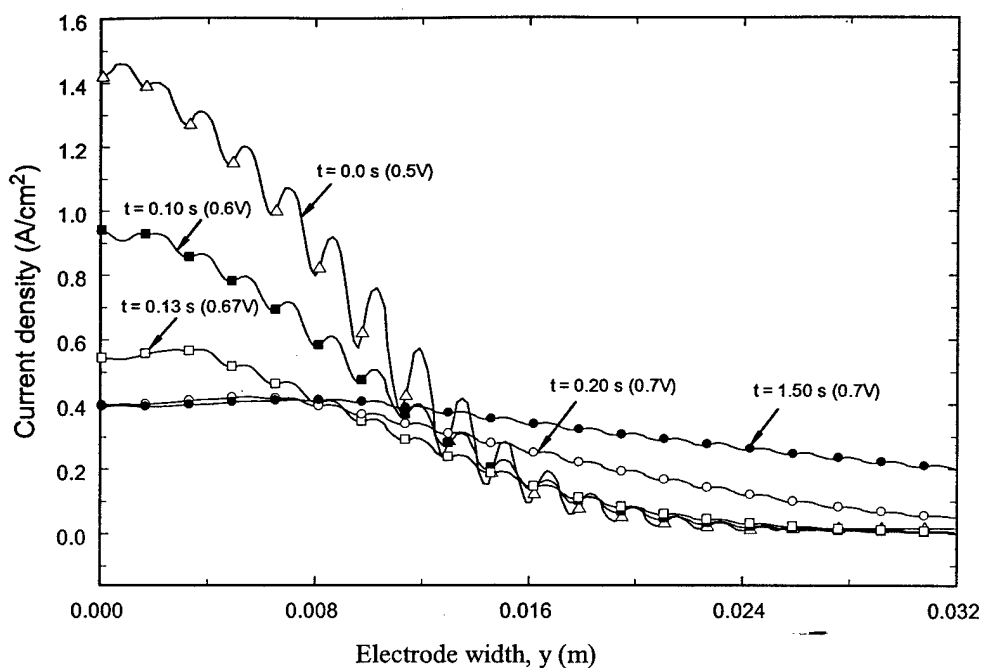


Figure 4a. Variation of current density along electrode width at  $x = 0.016 \text{ m}$  at different times for undershoot behavior.

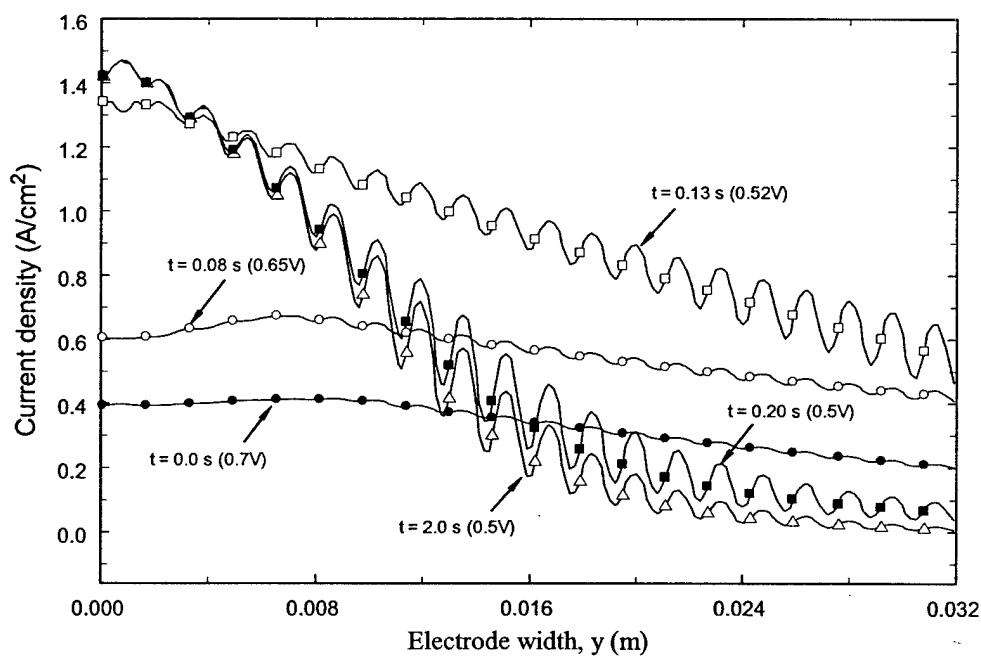


Figure 4b. Variation of current density along electrode width at  $x = 0.016 \text{ m}$  at different times for overshoot behavior.

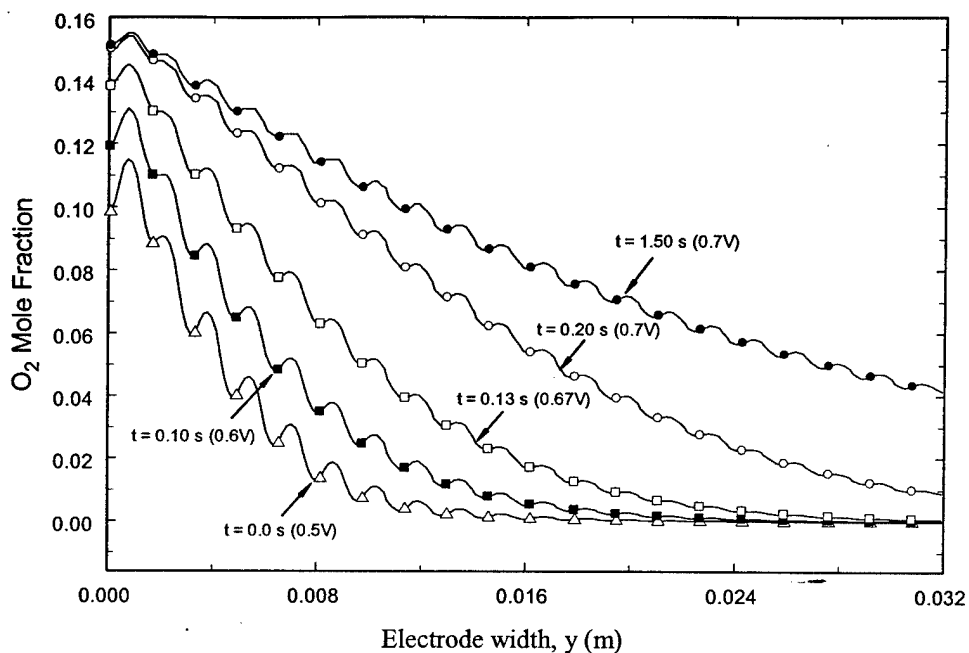


Figure 5a. Variation of oxygen mole fraction along electrode width at  $x = 0.016$  m at different times for undershoot behavior.

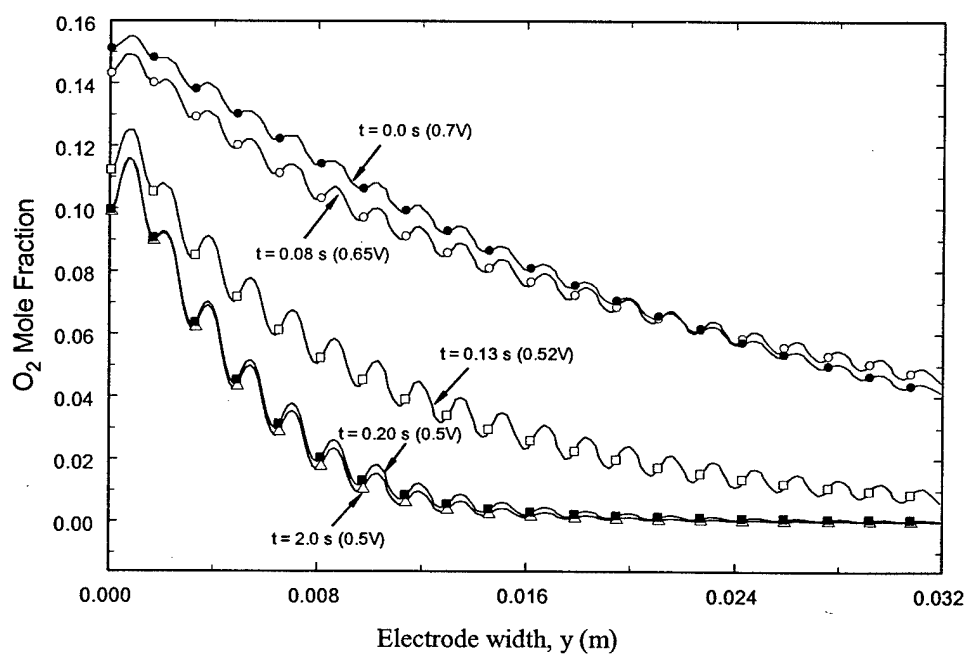


Figure 5b. Variation of oxygen mole fraction along electrode width at  $x = 0.016$  m at different times for overshoot behavior.

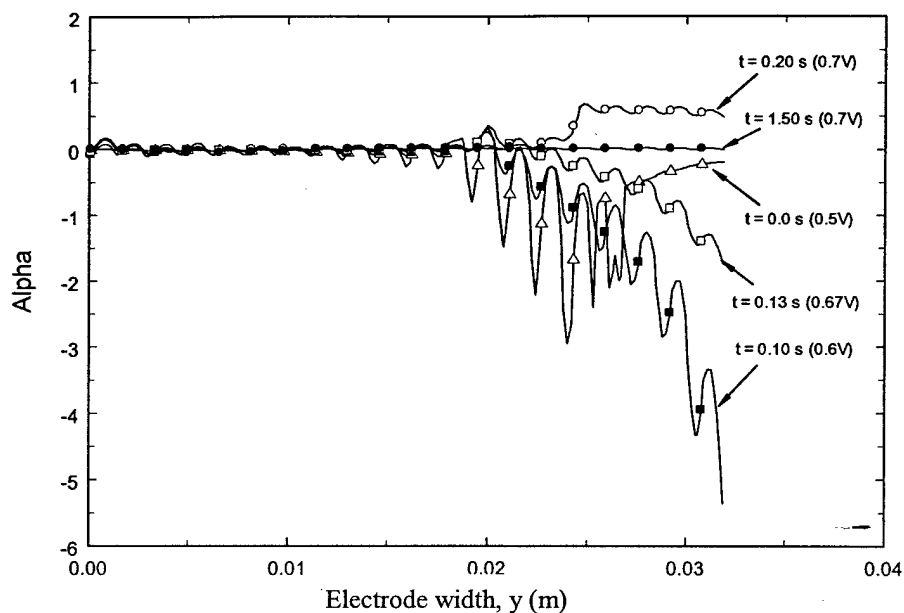


Figure 6a. Variation of net water flux ( $\alpha$ ) along electrode width at  $x = 0.016$  m at different times for undershoot behavior.

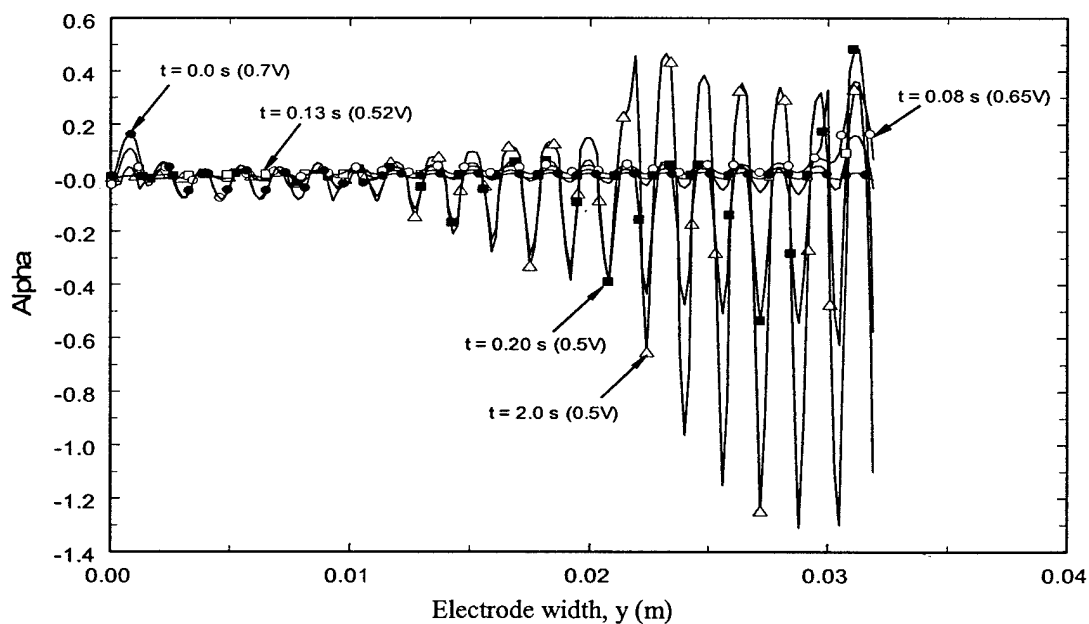


Figure 6b. Variation of net water flux ( $\alpha$ ) along electrode width at  $x = 0.016$  m at different times for overshoot behavior.

## ADVANCES IN COMPUTATIONAL FLUID DYNAMICS MODELING FOR PEM FUEL CELLS

S. Shimpalee, W. K. Lee, and J. W. Van Zee\*

Department of Chemical Engineering, University of South Carolina  
Columbia, SC 29208

H. Naseri-Neshat

Department of Mechanical Engineering  
South Carolina State University, Orangeburg, SC 29072

\*Corresponding author. Tel: 1-803-777-2285; fax: 1-803-777-8625; E-mail: [vanzee@enqr.sc.edu](mailto:vanzee@enqr.sc.edu)

### ABSTRACT

With the development of improved membranes, catalysts and bipolar plates, Polymer Electrolyte Membrane (PEM) fuel cells will play an important role in the near future as a new power source. The design and control of the fuel cells may be advanced by Computational Fluid Dynamics (CFD) techniques. CFD has been used to generate three-dimensional models of PEM fuel cells with the purpose of understanding the physics inside the fuel cells and improving the fuel cell performance. The performance of the fuel cell can be affected significantly by the heat generated inside its polymer electrolyte membrane (PEM). Further, water evaporation and condensation generated by temperature change inside fuel cell control humidity of the membrane and vary the local current density value and all of these phenomena need to be included in the models.

In this paper, the state of the art of models will be reviewed and the limitations of these models for design and control of PEM fuel cells will be discussed. Models for PEM fuel cells that researchers developed beginning with 1-D, 2-D, and 3-D simulations are discussed in terms of model designs, mathematical equations, numerical procedures, and results of studies. The computational requirements for transient predictions will be discussed.

### INTRODUCTION

Fuel cells use continuous transformation of chemical energy into electrical power without thermal-to-mechanical conversion. The PEM fuel cell operates at low temperature and it is a strong runner to be the power of future power generators. Figure 1 shows the major components of a PEM fuel cell, which consists of end plates, current collector, flow-field plates, gaskets, gas diffusion layers, and membrane electrode assembly (MEA) [1]. The MEA is the most important part of the fuel cell system and it consists of a membrane and two electrodes that have dispersed platinum (Pt) catalysts.

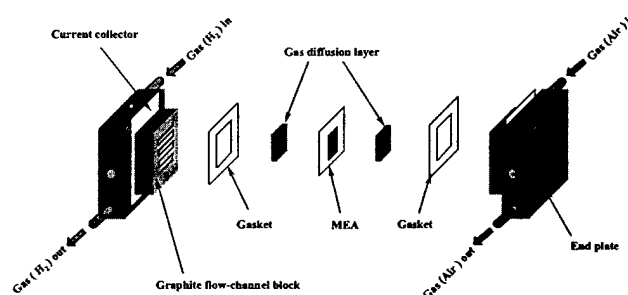
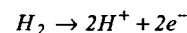
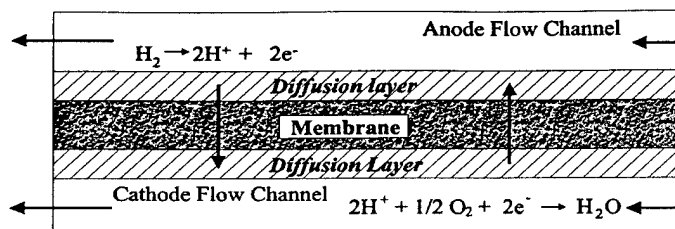


Figure 1. Schematic of a single fuel cell assembly displaying different essential components of the system [1]

The gas diffusion layers are located between the flow-field plates and MEA and they are porous to allow distribution of the gases to the electrodes at unexposed areas of the flow channels. This distribution allows for complete utilization of the electrode areas. The fuel cell case is outside of the flow channel block. It contains gas inlet and outlet ports. The gases go in through the inlet and diffused to the MEA while they are circulating along the gas channel. The current collector is situated between the fuel cell case and flow-field plates and connected to an electric load.

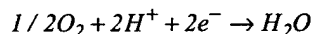
The general concept of fuel cell operation is characterized as gas-mixture transport and transformation of species by electrochemical reactions as shown in Figure 2. The hydrogen from the anode flow channel is transported through the diffusion layer toward the MEA surface. Hydrogen molecules are dissociated to protons and electrons in the catalyst:





**Figure 2. Schematic of the anode and cathode flow channels in a PEM fuel cell showing the transport of  $H^+$  to the cathode and the possibility of back diffusion of water from the cathode to the anode. Note that there is significant transport of water from the anode to the cathode by electro-osmosis [2].**

The water that impregnates the MEA hydrates the protons. Electro-osmosis and diffusion transport the water in the MEA. The air mixture in cathode channel is transported through the diffusion layer toward the MEA where oxygen reacts with protons:



The hydrogen supplies the electrons to one electrode while the oxygen receives them from the other electrode. This flow of electrons can power the electric motor of an automobile or other electrical device. The by-product of this reaction is water, which is only waste product of PEM fuel cell system.

While there are many recent experimental studies of PEM fuel cells (see eg: Nguyen [3], Hirano et al. [4], Stumper et al. [5], Bellows et al. [6], Lee et al. [7], Squadrito et al. [8], Lee [1]), it is important to have the numerical predictions to explain the local physics and to develop PEM fuel cell design tools. In this paper numerical studies of PEM fuel cells will be reviewed and the restrictions of these models for design and control of PEM fuel cells will be discussed. The advantages of using CFD to improve PEM fuel cell models, to simulate the complex geometry of experimental cells, and to include complicated equations to capture the liquid water, transient response will be discussed.

## DISCUSSION

### One-dimensional models

Springer et al. [9] reported an isothermal, one-dimensional, steady state model for a complete PEM fuel cell with a 117 Nafion membrane. Their model was considered the direction perpendicular to the MEA and it is similar to the gas diffusion electrode model of Bernardi and Verbrugge [10]. They considered a pseudo one-dimensional model in which flow channels were treated as being well mixed. Their model employed water diffusion coefficients, electro-osmotic drag coefficients, water sorption isotherms, and membrane conductivities, which they measured experimentally as functions of membrane water content. Equilibrium conditions between membrane liquid water and electrode water vapor at the membrane-electrode interfaces were applied. Their model also predicted an increase in membrane resistance with increased current density and showed the advantage of thinner membranes in alleviating the resistance problem. Their works also provided the key properties of the membrane required for a numerical model.

Bernardi and Verbrugge [11] also developed a one-dimensional mathematical model of the complete cell. They studied the direction perpendicular to the MEA and considered the effects of the transport of reacting gases and water vapor in gas-diffusion electrodes on the performance of PEM fuel cells. In their model the membrane were

assumed to be consistently hydrated with constant transport properties. Their predictions were compared with experimental data.

### Two-dimensional models

The step in PEM fuel cell simulation was the development of two-dimensional models. According to the 1-D model of PEM fuel cell, researchers had followed those fundamental equations and physical properties to improve their models to be more realistic. Different techniques including CFD had been used to satisfy 2-D simulation [12-19]. These models typically consider the dimensions in direction of bulk flow down the channel and in the direction perpendicular to the membrane. We now review the 2-D PEM fuel cell numerical models and the limitations of the models for design and control of PEM fuel cells.

Fuller and Newman [12] developed a two-dimensional model of a membrane electrode assembly of PEM fuel cell to study water management, thermal management, and utilization of fuel. They examined the temperature and membrane hydration along the channels. This model included water transport in the diffusion layer and assumed plug flow in the flow channel. They showed that the equilibrium sorption of water between gas phase and the polymer-electrolyte depends on temperature, water, and thermal management. Therefore, the rate of heat removal was presented to be a critical parameter in the operation of PEM fuel cells.

Nguyen and White [13] developed a model for water and heat management of PEM fuel cells and investigated the effectiveness of various humidification designs. They discussed four different humidification designs to prevent dehydration at the anode side of the membrane. Their model was two-dimensional of heat and water transport that accounted for variation in temperature and membrane hydration conditions along the flow channels. They did not include the diffusion layer for water transport. The results from their model showed that at high current densities ohmic loss in the membrane justify a large fraction of the voltage loss in the cell and back diffusion of water from the cathode side of the membrane is insufficient to keep the membrane hydrated. Therefore, to minimize the ohmic loss the anode gas must be humidified, and when air is used instead of pure oxygen the cathode gas must also be humidified.

West and Fuller [14] used a two-dimensional analysis of PEM fuel cell in their study of the effect of rib sizing that restricts the access of fuel and oxidant gases to the catalyst layer and the thickness of the gas-diffusion electrode. They showed the expected change in cell performance that results from the partial blocking of the substrate layer. However, in their work they considered only the half-cell potential for a given applied current.

Yi and Nguyen [15] modified the previous models of Nguyen and White [13] to include both the liquid and gas phase along the flow path of both anode and cathode sides of a PEM fuel cell. They included the convective water transport by pressure gradient across the membrane, temperature distribution in the solid phase along the flow channel, and heat removal by natural convection, co-flow, and counter-flow heat exchangers. Again their results revealed that the performance of a PEM fuel cell could be improved by anode humidification. Their results also showed that effective heat removal is necessary for preventing excessive temperature that may cause local membrane dehydration.

Later, Yi and Nguyen [16] analyzed the two-dimensional hydrodynamics in the cathode of a PEM fuel cell that was connected to an interdigitated gas distributor. They used a steady state multicomponent transport model. This model explained the two-dimensional cross-flow patterns and the distributions of the gaseous species in the porous electrode. It can be used to predict the current

density generated at the electrode and membrane interface as a function of various operating conditions and design parameters. Their results showed that with the forced flow-through condition created by the interdigitated gas distributor design, the diffusion layer is greatly reduced and with a much thinner diffusion layer, diffusion factor still play a significant role in the transport of oxygen to the reaction surface. In this model, the width of the channel and portion of the gas diffusion layer hidden from the channel were neglected. These models provided a reasonable prediction of the axial water distribution but they overestimated the non-uniformity of the current distribution at the entrance of a PEM fuel cell.

Gurau et al. [17] considered two-dimensional fluid flow in the channels of their PEM fuel cell model but the density change due to species consumption appears to be neglected. Moreover, the connectivity of the main channel and diffusion layer involved a change of primary variables that may lead to numerical discontinuities under some operating conditions. Again, the width of the channel and portion of the gas diffusion layer hidden from the channel were neglected. They showed oxygen and water vapor mole fraction distributions in the coupled cathode gas and channel-gas diffuser for various operating current densities conditions. Moreover, their results were compared with experimental results from literature.

Kazim et al. [18] developed a simple two-dimensional mathematical model of PEM fuel cells to investigate the superiority of the interdigitated flow field over the conventional and compared their results with previous works (Nguyen [3] and Yi and Nguyen, [15]). However, their model was considered only in the cathode side of the fuel cell and therefore, the model neglected the effects of the local over-potential of hydrogen (a small effect) and the net water transport across the membrane (a big effect). Their results revealed that the limiting current density of a fuel cell with an interdigitated flow field is about three times the current density of a fuel cell with a conventional flow field. Furthermore, the results also showed that the interdigitated flow field model can double the maximum power density of a PEM fuel cell. Their results are not comparable with Yi and Nguyen [16] because they neglect the water transport.

Kulikovskiy et al. [19] developed a two-dimensional simulation of the cathode compartment of PEM fuel cell and only investigated the influence of two-dimension effects on cathode performance. Their model was based on continuity equations for concentration of the gases and Poisson's equations for the potentials of membrane and carbon phase, coupled by Tafel relation for reaction kinetics. Their results showed that for a low value of carbon phase conductivity, a "dead zone" in the active layer in front of the gas channel is formed, where the reaction rate is small. The catalyst might be removed from this zone without significant loss in cell performance. Consequently, these results showed the possibilities for a considerable reduction of the amount of catalyst.

CFD technique had been introduced in some of two-dimensional PEM fuel cell models. This technique is general using the concept of Navier-Stokes, species transport, and energy equations and applied to electrochemical reaction of PEM fuel cell in term of mass source/sink. Even though 2-D models give more realistic predictions and enhanced PEM fuel cell knowledge, these models have to neglect the effect of channel length or channel width. Moreover, 2-D model cannot simulate the experimental cell with a complicated flow-field shown in Figure 3. Therefore, these 2-D predictions cannot be perfectly validated with experimental data. This causes problems when one uses 1-D and 2-D models designs.

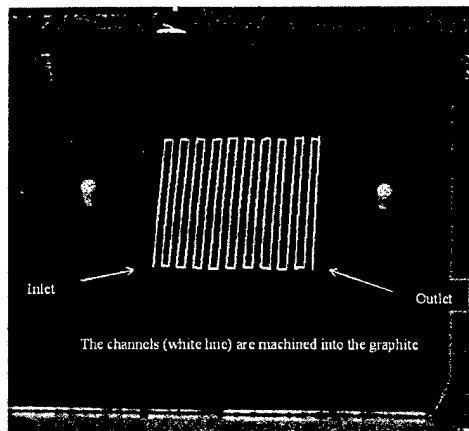


**Figure 3. The picture shows actual flow-field plate with the gas channel. There are twenty straight channels connected in a serpentine fashion [1,20, 23 and 24]. This is an example of flow-field design used in PEM fuel cell application.**

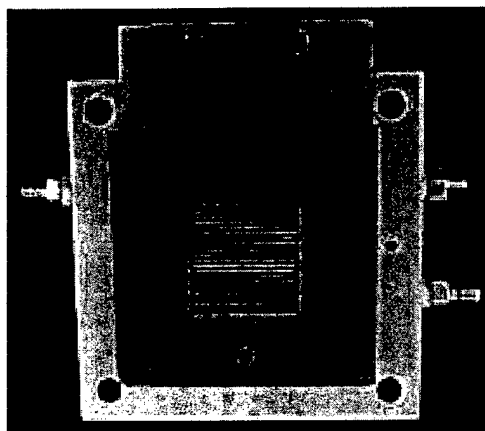
### *Three-dimensional models*

Recently, three-dimensional model of a PEM fuel cell have been developed by using a CFD technique. This code allows one to predict performance, local current density, water distribution, temperature distribution, and electrochemical variables inside actual PEM fuel cells used in experiments. These valuable predictions enhance researchers' understanding of the physics inside PEM fuel cells. This CFD technique can be applied to other patterns of flow-fields and therefore can help in bipolar plate designs that have serpentine flow fields like those shown in Figures 4. The following describes some of 3-D PEM fuel cell models using CFD technique done by different researchers.

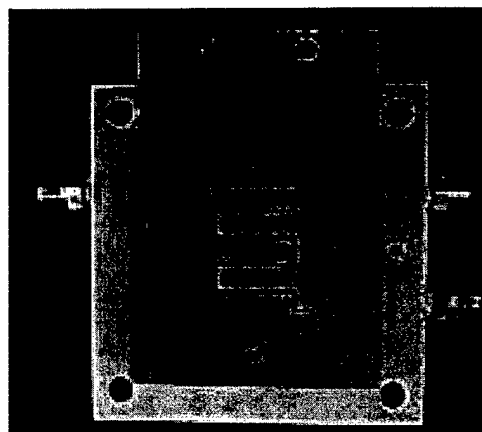
Dutta et al. [2] developed the first three-dimensional straight channel PEM fuel cell using commercial CFD package with their own user-subroutines that modified the electrochemical equations of PEM fuel cell done by Fuller and Newman [12] and Yi and Nguyen [15]. They reported isothermal and single-phase numerical model that included the full three-dimensional solution of Navier-Stokes equations for the flow channel. The solution procedure used in that flow solver was based on SIMPLE algorithm. This work allowed one to account for the effect of the flow channel width on the velocity distribution. Further, they showed that under certain conditions the transport toward the membrane was driven by both pressure and concentration gradients rather than by diffusion alone. Their model included the area hidden from the flow channel by the rib spacer.

Their model [2] was validated by Shimpalee [20]. He modified their model geometry by neglecting the effect of rib spacing or channel width and compared his prediction with 2-D results of Fuller and Newman [12]. Figure 5 shows the current density profiles along the flow channel (channel length). The current density profile of the 3-D model compares well with the predictions of Fuller and Newman [12]. It is important to note that their model fixed the partial pressure of  $H_2$ ,  $H_2O$ ,  $O_2$ ,  $N_2$ , and  $CO_2$  at both anode and cathode at interface between flow channels and diffusion layers. That means the concentration of each species at those positions did not depend on the species consumption/production at the membrane surface of both anode and cathode and porosity of diffusion layers. However, this 3-D model gives well comparison This is because their operating condition had high stoichiometry of the reacting gases and therefore the variation of

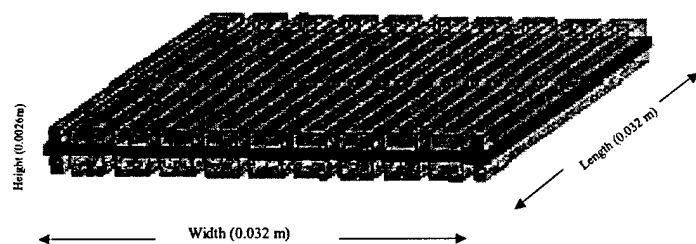




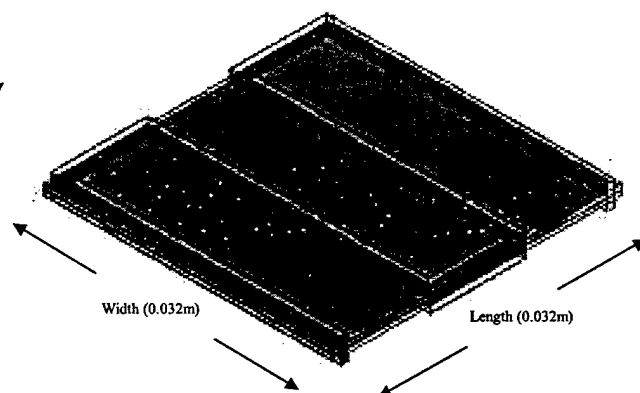
(A)



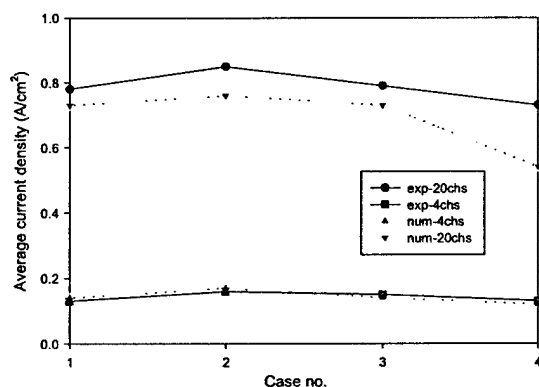
(B)



(C)



(D)



(E)

Figure 4: A) 10-cm<sup>2</sup> PEM fuel cell with 20 channels flow path, B) 10-cm<sup>2</sup> PEM fuel cell with 4 channels flow path, C) model geometry for (A) [20, 23, 24 and 30], D) model geometry for (B), E) comparison between experiment results and numerical predictions at atmospheric 0.5 setting voltage with 4 different inlet humidity conditions between 20 channels and 4 channels flow path.

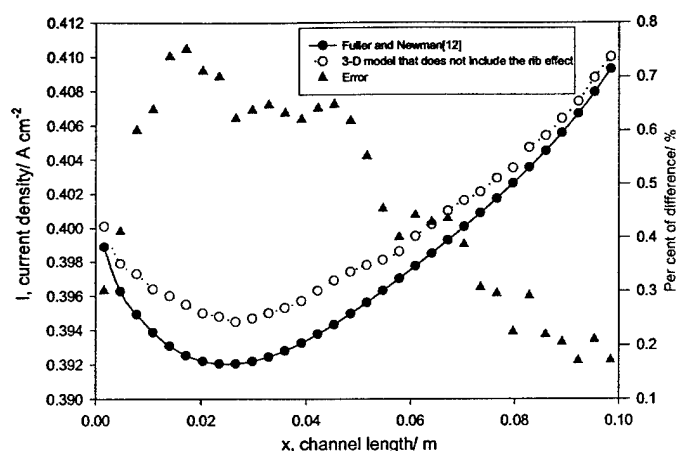


**Figure 5. The current density profiles along the flow channel and the error results between Shimpalee [20]'s model comparing to Fuller and Newman [12].**

species concentration at those positions can be neglect by the high velocity in the flow channels.

Naseri-Neshat et al. [21] continued Dutta et al. [2]'s work by studying the effects of change in diffusion layer with constant diffusion layer thickness and channel cross section area. Their model indicated that in the diffusion layer the reactants are transported by both convective and diffusion transport apparatuses and their predictions confirmed that the width of the flow channel and gas diffusion layer must not be neglected.

Shimpalee [20], Shimpalee et al. [22-23], and Dutta et al. [24] adapted their previous CFD model geometry to actual size of 10-cm<sup>2</sup> reacting area PEM fuel cell used in Lee [1] and Lee et al. [25] as shown in Figure 3. Their predictions were compared with experimental data. This was the first full-cell PEM fuel cell model using the advantage of CFD technique. The model geometry consisted of 20 passes of serpentine gas channels (anode and cathode) as shown in Figure 4C. A thin membrane-electrode-assembly (MEA) is sandwiched between anode and cathode diffusion layers as also shown in Figure 1. In their model, they also included the overpotential for both hydrogen and oxygen reaction. They studied the effects of permeability of the diffusion layer on mass transport behavior. They also presented the effect of inlet humidity conditions on the current density and compared their predictions with experimental results [1 and 23] as shown in Figure 6. This figure shows that in absence of condensation, an increase in the inlet humidity condition increases averaged current density. This can be argued that the experiment has condensation effect in very high inlet humidity condition and created membrane flooding therefore, drops performance.

Due to the important of temperature change inside PEM fuel cell creating condensation/evaporation and affects the performance, Shimpalee and Dutta [26] modified Dutta et al. [2]'s model by including the energy equation to predict the temperature distribution inside a straight channel PEM fuel cell. The CFD method using control volume approach is not complicate to incorporate source terms for transport equations, heat generation, and water phase change. Note that their model was assumed to be homogeneous two-phase flow. Their predictions showed that fuel cell performance depends not only on the inlet humidity condition and initial setup, but also on the temperature rise inside the fuel cell system especially in fuel cell stack operation.

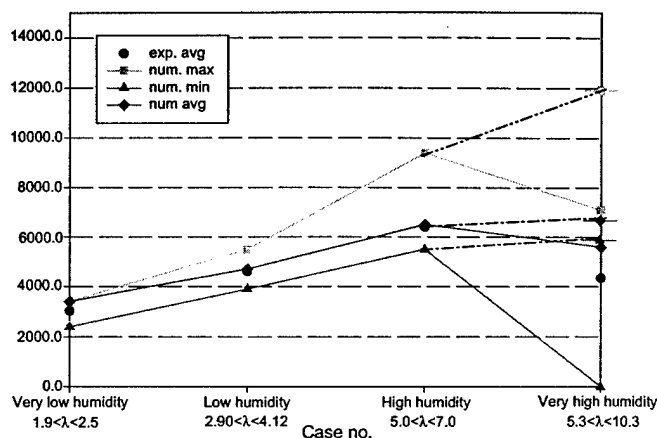


**Figure 6: Comparison of experiment current density (A/m<sup>2</sup>) data with the numerical predictions for each inlet condition (Shimpalee [20] and Shimpalee et al. [23]).**

Um et al. [27] and Um and Wang [28] also used computational fluid dynamics to create three-dimensional PEM fuel cell model. Their model included anode/cathode gas channels, diffusion layers, and catalyst layers and Membrane. However, their isothermal and single-phase PEM fuel cell model considered only straight channel with different flow-field (convectonal and interdigitated) with about 1.8-cm<sup>2</sup> reacting area. They presented that the force convection created by interdigitated flow field improves mass transport of oxygen and water elimination at reaction zone thus increasing the performance as compared to convectonal flow field.

In the mean time, Zhou and Liu [29] showed their three-dimensional model for PEM fuel cell. They also developed their model by using CFD technique in order to couple the governing equations for reactant mass transport and chemical reaction kinetics. Their model included the energy equation to map the temperature distribution inside PEM fuel cell model. However, their model simulated for straight channel with approximately 1.6-cm<sup>2</sup> reacting area. Their model confirmed that the 3-D model could be very necessary for fuel cell design and development.

Shimpalee et al. [30] revised their previous straight channel model [28] to 10-cm<sup>2</sup> reacting area with 20 channels serpentine flow path. Their work revealed that the water evaporation and condensation produced by temperature change direct membrane humidity and so alter the local current density. Again, their model did not include the surface tension and contact angle of the liquid droplet. Therefore, there was not hydrophobic/ hydrophilic effect at both sides of MEA surface. Figure 7 shows the effect of non-isothermal consideration on local current density on the membrane surface comparing with the case with isothermal [30]. In particular condition of their work, the temperature rise inside the PEM fuel cell generated membrane dehydration and drop the rate of electrochemical reactions and therefore decreased the performance.

Computational Fluid Dynamics technique has been used to help researchers developing PEM fuel cell models significantly. Therefore, completed geometries of single PEM fuel cell with different pattern of flow-fields have been achieved and simulated using developing electrochemistry codes associate with Navier Stokes, species transport, and energy equations. The predictions were very useful in order to understand and improve PEM fuel cells. The next approaches of development could be the transient simulation with variable load that

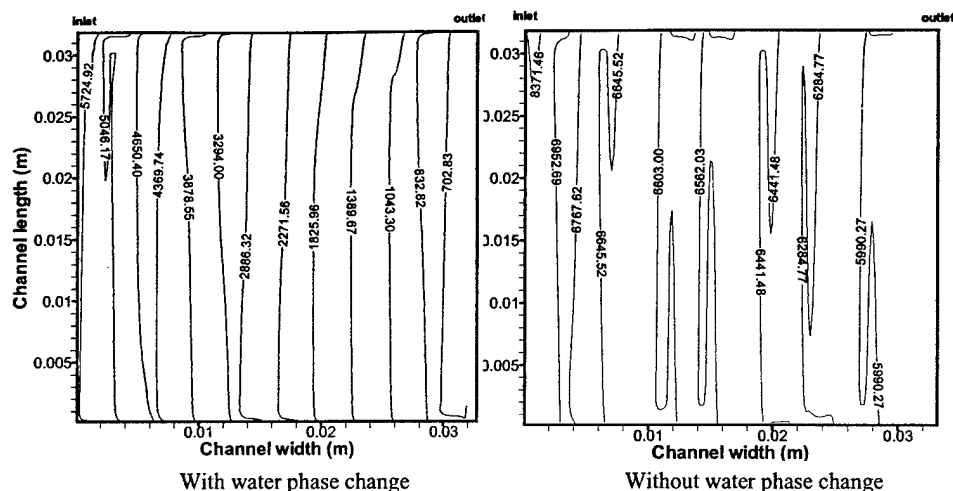


Figure 7. The local current density ( $A/m^2$ ) contours on the membrane surface [30].

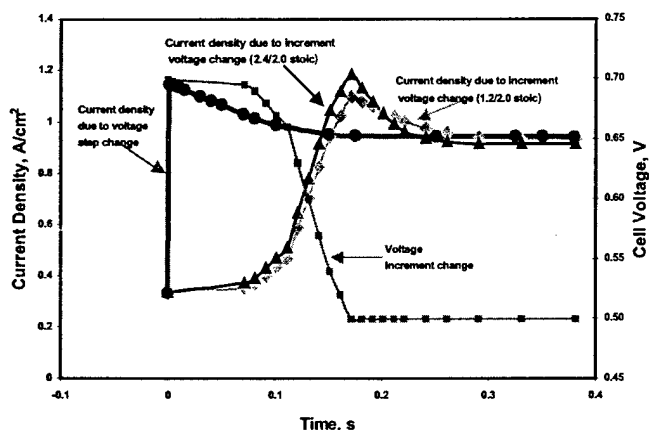


Figure 8. Transient average current density for voltage change from 0.7-0.5V [31].

is designed to reflect parts of a Federal Urban Driving Scenario. Figure 8 shows preliminary transient results of Naseri-Neshat et al. [31]. This figure presents the over shoot of current density for different types of changing in the cell voltage (0.7 - 0.5 V) on 10-cm<sup>2</sup> PEM fuel cell [1, 20, 23 and 24]. Moreover, this will be applied by including carbon monoxide (CO) in order to development hydrocarbon reformat PEM fuel cell as model equations are recently developed by Springer et al. [32] and finally generate PEM stack fuel cell model that will be included the cooling/heating system. To achieve complicated PEM fuel cell model, for example transient response with CO-poisoning, variety flow-field pattern, or stack, capability of computer used have to be considered. This is because those models have to involve with million element cells and each cell has to solve for many variables and this will also increase the computational time drastically. Parallel process or Unix cluster may be suitable for those complexity simulations. In addition, numerical procedure method has to be deliberated from iteration to iteration and time step to time step to speed up the converged solution.

## CONCLUSIONS

1. Improving PEM fuel cell performance could not be satisfactory with only experimental studies.
2. One-dimensional models gave the principal though of physics inside PEM fuel cells and fundamental for multidimensional simulations.
3. Two-dimensional models using computation fluid dynamics technique gave more realistic of PEM fuel cell simulation and enhance understanding of PEM fuel cells. However, this cannot achieve the development of flow-field design, comparison of predictions with experimental data.
4. Three-dimensional simulation using CFD approach presented the most realistic models and significantly comparable with experimental cells with variety of flow-field patterns. This will lead researcher to capture the actual operation of PEM fuel cell, such as transient response, CO poisoning effect, water management in stack, etc.
5. High powerful computers, for example parallel processes, Unix clusters, or super computers, have to be contemplated to develop complexity three-dimensional simulation of single and stack PEM fuel cell. Therefore, this will accelerate convergent solution extensively.

## ACKNOWLEDGEMENTS

This project was supported by DOE through Cooperative Agreement Number DE-FG02-91ER75666, ONR Grant # N00014-98-1-0554, and University Transportation Center/ South Carolina State University.

## REFERENCES

- [1] Lee, W. K., 2000, "The effect of clamp torque, humidity, and Co poisoning on PEM fuel cell," Ph.D. dissertation, Department of Chemical Engineering, University of South Carolina, Columbia, SC.
- [2] Dutta, S., Shimpalee, S., Van Zee, J. W., 2000, "Three-dimensional numerical simulation of straight channel PEM fuel cells," J. of Applied Electrochemistry, 30, pp. 135-146.

- [3] Nguyen, T., 1996, "A gas distribution design for proton-exchange-membrane fuel cells," *J. of Electrochemical Society*, **140**, pp. 2178-2186.
- [4] Hirano, S., Kim, J., and Srinivasan, S., 1997, "High performance proton exchange membrane fuel cells with sputter-deposited Pt layer electrodes," *J. of Electrochimica Acta*, **42**, pp. 1587-1593.
- [5] Stumper, J., Campbell, S., Wilkinson, D., Johnson, and Davis, M., 1998, "In-situ methods for the determination of current distributions in PEM fuel cells," *J. of Electrochimica Acta*, **43**, pp. 3773-3783.
- [6] Bellows, R., Lin, M., Arif, M., Thompson, A., and Jacobson, D., 1999, "Neutron imaging technique for In-situ measurement of water transport gradient within Nafion in polymer electrolyte fuel cells," *J. of Electrochemical Society*, **146**, pp. 1099-1103.
- [7] Lee, W., Ho, C., Van Zee, J., and Murthy, M., 1999, "The effects of compression and gas diffusion layers on the performance of a PEM fuel cell," *J. of Power Sources*, **84**, pp. 45-51.
- [8] Squadrito, G., Maggio, G., Passalacqua, E., Lufrano, F., and Patti, A., 2000, "An empirical equation for polymer electrolyte fuel cell (PEFC) behavior," *J. of Applied Electrochemistry*, **29**, pp. 1449-1455.
- [9] Springer, T., Zawodzinski, and Gottesfeld, S., 1991, "Polymer electrolyte fuel cell model," *J. of Electrochemical Society*, **138**, pp. 2334-2342.
- [10] Bernardi, D. M. and Verbrugge, M. W., 1991, "Mathematical model of a gas diffusion electrode bonded to a polymer electrolyte," *AIChE J.*, **37**, pp. 1151-1163.
- [11] Bernardi, D. M. and Verbrugge, M. W., 1992, "A mathematical model for the solid-polymer-electrode fuel cell," *J. Electrochemical Society*, **139**, pp. 2477-2491.
- [12] Fuller, T. and Newman, J., 1993, "Water and thermal management in solid-polymer-electrolyte fuel cells," *J. of Electrochemical Society*, **140**, pp. 1218-1225.
- [13] Nguyen, T. and White, R., 1993, "A water and heat management model for proton-exchange-membrane fuel cells," *J. of Electrochemical Society*, **140**, pp. 2178-2186.
- [14] West, A. and Fuller, T., 1996, "Influence of rib spacing in proton-exchange-membrane electrode assemblies," *J. of Applied Electrochemistry*, **26**, pp. 557-565.
- [15] Yi, J. and Nguyen, T., 1998, "An along-the channel model for proton exchange membrane fuel cells," *J. of Electrochemical Society*, **145**, pp. 1149-1159.
- [16] Yi, J. and Nguyen, Y., 1999, "Multicomponent transport in porous electrodes of proton exchange membrane fuel cells using the interdigitated gas distributors," *J. of Electrochemical Society*, **146**, pp. 38-45.
- [17] Garua, V., Liu, H., and Kakac, S., 1998, "Two-dimensional model for proton exchange membrane fuel cells," *J. of AIChE*, **44**, pp. 2410-2422.
- [18] Kazim, A., Liu, H., and Forges, P., 1999, "Modeling of performance of PEM fuel cells with conventional and interdigitated flow fields," *J. of Applied Electrochemistry*, **29**, pp. 1409-1416.
- [19] Kulikovskiy, A., Divisek, J., and Kornyshev, A., 1999, "Modeling the cathode compartment of polymer electrolyte fuel cells: Dead and active reaction zones," *J. of Electrochemical Society*, **146**, pp. 3981-3991.
- [20] Shimpalee, S., 2001, "Numerical prediction of gas-humidification effects on energy transfer in PEM fuel cell," Ph.D. dissertation, Dept. of Mechanical Engineering, University of South Carolina, SC.
- [21] Naseri-Neshat, H., Shimpalee, S., Dutta, S., Lee, W.K., and Van Zee, J. W., 1999, "Predicting the effect of gas-flow channel spacing on current density in PEM fuel cells," *Proc. of ASME IMECE*, Nashville, TN., **4**, pp. 341.
- [22] Shimpalee, S., Dutta, S., Lee, W.K., and Van Zee, J. W., 1999, "Effect of humidity on PEM fuel cell performance Part II: Numerical Simulation," *Proc. of ASME IMECE*, Nashville, TN., **5**, pp. 464.
- [23] Shimpalee, S., Lee, W., Dutta, S., and Van Zee, J., 2001, "Effect of inlet humidity on current density in a PEM fuel cell," submitted to *J. Electrochemical Society*.
- [24] Dutta, S., Shimpalee, S., and Van Zee, J., 2001, "Numerical prediction of mass-exchange between cathode and anode channels in a PEM fuel cell," *Intl. J. of Heat and Mass Transfer*, **44/11**, pp. 2029-2042.
- [25] Lee, W.K., Van Zee, J. W., Shimpalee, S., and Dutta, S., 1999, "Effect of inlet humidity on PEM fuel cell performance Part I: Experiments," *Proc. of ASME IMECE*, Nashville, TN., **5**, pp. 454.
- [26] Shimpalee, S. and Dutta, S., 2000, "Numerical prediction of temperature distribution in PEM fuel cells," *Numerical Heat Transfer, Part A*, **38**, pp. 111-128.
- [27] Um, S., Wang, C. Y., and Chen, K. S., 2000, "Computational fluid dynamics of proton exchange membrane fuel cells," *J. of Electrochemical Society*, **147**, pp. 4485-4493.
- [28] Um, S. and Wang, C. Y., 2000, "Three dimensional analysis of transport and reaction in proton exchange membrane fuel cells," *Proc. of ASME IMECE*, Orlando, FL., **1**, pp. 19.
- [29] Zhou, T. and Liu, H., 2000, "3-D model of proton exchange membrane fuel cells," *Proc. of ASME IMECE*, Orlando, FL., **1**, pp. 43.
- [30] Shimpalee, S., Dutta, S. and Van Zee, J. W., 2000, "Numerical prediction of local temperature and current density in a PEM fuel cell," *Proc. of ASME IMECE*, Orlando, FL., **1**, pp. 1.
- [31] Naseri-Neshat, H., Lee, W. K., Shimpalee, S., and Van Zee, J. W., 2001, "Numerical prediction of transient response on a PEM fuel cell performance," submitted to *J. of Electrochemical Society*.
- [32] Springer T. E., Rockward, T., Zawodzinski, T. A., and Gottesfeld, S., 2001, "Model for polymer electrolyte fuel cell operation on reformate feed," *J. of Electrochemical Society*, **148**, pp. A11-A23.



# The effect of stoichiometry on dynamic behavior of a proton exchange membrane fuel cell (PEMFC) during load change

Sunhoe Kim, S. Shimpalee, J.W. Van Zee\*

Department of Chemical Engineering, University of South Carolina, Columbia, SC 29208, USA

Received 24 February 2004; accepted 20 March 2004

## Abstract

Data are presented to show the transient response of a proton exchange membrane fuel cell (PEMFC) subjected to change in the load. Overshoot and undershoot behaviors of the steady-state current density were observed for various rates of change in the voltage during constant inlet flow rate conditions. The results of these experiments with a 25 cm<sup>2</sup> triple serpentine flow field indicate a correlation of the overshoot/undershoot behavior with initial and final stoichiometry. This transient analysis is potentially attractive in the operation of vehicle and stationary application and flow field designs.

© 2004 Published by Elsevier B.V.

**Keywords:** PEM; Fuel cells; Membrane electrode assembly; Electric vehicle; Transient; Stoichiometry; Electric load

## 1. Introduction

The control, design, and optimum operation of PEMFCs will require an understanding of its transient behavior when the current, voltage, or power changes. These dynamics would be important for residential and automotive applications and the transient operation may be a result of a sudden demand as an appliance starts or as a vehicle is accelerated or decelerated. These transients may be of sufficient amplitude and speed that fuel flow rates cannot be adjusted by feedback control and thus electrical capacitors are often used to stabilize the system output. Here we present experimental data to help understand how the fuel cell by default or design can act as a capacitor during the power demand surges.

While most of the studies of PEMFCs have focused on steady-state behavior, a few authors have considered transient operation of stacks [1–5]. For example, Hamelin et al. [1] demonstrated three different transients in their work on with a Ballard fuel cell stack model MK5-E, which has a total of 35 cells, of 10 kW maximum power, connected in series with a cell surface area of 232 cm<sup>2</sup>. The first transient was a continuous load change with various amplitudes by changing the power in a square wave. The second was a higher frequency transient at very short times. In this part

they replaced the back-pressure valve with a metering valve to maintain a fixed outlet flow, while the inlet mass flow controller was completely open to reduce the transient phenomena to the load alone. Finally, they studied DC + AC load communication and the noise from the AC/DC converter in the system. They emphasized the importance of studying transient behavior of fuel cell to understand how the fuel cell stack will behave under extreme conditions, for example, in case of current or voltage exceed certain limits.

Amphlett et al. [2] presented an analysis of a hybrid PEMFC/battery system with a system scaled down from a 400 kW fuel cell stack and 224 cell lead-acid battery suitable for submarine systems. They showed how their hybrid system and components interacted during charging or discharging. Those experiments followed a presentation of the dynamics during start-up, current change, and shut down of a Ballard Mark V 35-Cell 5 kW PEMFC stack where they compared the observed voltage response from a current change to their empirical model [3]. Emonts et al. [4] studied the dynamics of a PEMFC, a compact methanol reformer, and the choice of a short-term storage system for an automotive application. Kötz et al. [5] discussed the combinations of a PEMFC and supercapacitors for automotive applications. These experimental studies [1–5] were conducted under excess initial fuel and oxidant conditions and the load changes were not large enough to study starved fuel conditions.

\* Corresponding author. Tel.: +1-803-777-2285; fax: +1-803-777-8028.  
E-mail address: [vanzee@engr.sc.edu](mailto:vanzee@engr.sc.edu) (J.W. Van Zee).

## Nomenclature

$i$	current density (A/cm <sup>2</sup> )
$K$	steady-state gain (A/cm <sup>2</sup> V)
$t$	time (s)
$V$	cell voltage (V)
$\Delta V$	cell voltage difference (V)

## Greek letters

$\beta$	lead time constant (s)
$\delta$	time constant for cell voltage (s)
$\xi$	damping coefficient
$\rho$	lead-to-lag ratio ( $\rho = \beta/\tau$ )
$\tau$	Time constant (s)

In an effort to understand the dynamics of a PEMFC, we present data for a single cell with fixed flow rates. The transient operation is forced by rapid changes to the voltages and this allows observation of changes in the current and stoichiometry of the cell as discussed below. We are motivated by our recent three-dimensional numerical simulations for the transient response of fuel cell [6,7] in which we observed an overshoot in the current density when the voltage was changed at 1.0 V/s. The dynamics one-dimensional semi-empirical model of Ceraolo et al. [8] also leads discussions of when voltage overshoot observed in [3] may occur. Thus we designed experiments here to expand an understanding of this behavior.

## 2. Experimental

The objective of this work is to study the transient current response when the cell voltage is changed at a rate of approximately 0.2 V/s at fixed feed flow rates. These fixed flow rates result in the cell being exposed to different stoichiometries as the current changes as shown in Table 1. That is, here we present data for the response of the current when the cell voltage was changed from 0.7 to 0.5 V and from 0.5 to 0.7 V.

Four cases can be described as changes in operating conditions, such that the fuel and air are “normal”, “starved”, or “excess” (see Table 1). For example, Case 1a corresponds to the flow rates of 249 and 1040 cm<sup>3</sup>/min at standard conditions<sup>1</sup> for the anode and cathode, respectively. These flow rates yield a stoichiometric change from 2.9/4.8 at  $t \leq 0$  to 1.2/2.0 at  $t = \infty$  for a current density of 0.62 A/cm<sup>2</sup> at 0.7 V and 1.48 A/cm<sup>2</sup> at 0.5 V. Thus Case 1a corresponds to a change in operation from a “excess” to a “normal” stoichiometry. Case 2a uses the same flow rates but we began the experiment at 0.5 V and increased the cell voltage to 0.7 V (i.e. 0.62 A/cm<sup>2</sup>). Case 2a corresponds to a change in oper-

ation from a “normal” to an “excess” condition. For Case 3a, the flow rates were 92 and 384 cm<sup>3</sup>/min, corresponding to 1.2/2.0 stoichiometry for the 0.7 V initial condition (i.e., 0.54 A/cm<sup>2</sup>) and a stoichiometry of 1.0/1.7 for  $t = \infty$  (i.e., 0.5 V and 0.63 A/cm<sup>2</sup>). This corresponds to a change in the fuel stoichiometry from a “normal” to a “starved” condition. Note that for fixed voltage a single cell can never be completely “starved” but we use this as a description. Prior to changing the cell voltage, we waited 30 min to ensure a steady-state value of the current and to ensure a well humidified membrane at the voltage. We replicated the experiment at least twice and the data presented here demonstrates reproducibility of the transient responses as discussed below.

All the data reported here were obtained with PRIMEA® Series 5510 MEA (0.4 mg/cm<sup>2</sup> Pt loading, 25  $\mu$ m nominal membrane thickness, W.L. Gore & Associates, Inc., Elkton, Maryland, USA). The original active electrode area was 25 cm<sup>2</sup>, but sub-gaskets for both anode and cathode sides reduced the area to 20 cm<sup>2</sup>. The gas diffusion media (GDM) used for both anode and cathode were 16 mils (0.41  $\times 10^{-3}$  m) CARBEL™ CL. The cell was tightened with 8 V at the torque of 50 lb<sub>f</sub>-in./bolt. The effect of clamp-torque has been discussed by Lee et al. [9]. The flow fields for both anode and cathode used in this experiment had triple path serpentine channels where the flows were split into three paths at entrance and converged at the end.

High purity hydrogen (99.997%) and industrial grade compressed air were used. The fuel cell test station used to control the electrical load, the fuel supply, and the temperature was manufactured by Fuel Cell Technologies (Los Alamos, NM). A model 6060B (Agilent Technologies) was used for the electronic load bank. Digital mass flow controllers (MKS model) were used to control the flow rates and these were calibrated with a bubble flow meter as discussed in [10]. The inlet gases were bubbled through the humidity bottles and from the temperature of those bottles a correlation was used to determine the humidity of inlet fuel gas [10].

The operation of a laboratory scale PEMFC involves inlet gas and water vapor diffusing from flow channels through the GDM to electrode, where the electrochemical reaction takes place. The non-reacted gas and water vapor exit the cell and pass through the back-pressure regulator to a vent. The back-pressure of both anode and cathode sides was 101 kPa. The fuel cell was operated at the temperature of 70 °C and the anode and cathode dew point temperatures were 80 and 70 °C, respectively. These dew point temperatures were calculated from calibration data as discussed in [10].

The experiment was conducted in two parts. First, we measured the polarization behavior of the PEMFC at fixed stoichiometry and those familiar with these experiments will recognize this indicates that fixed the flow rates were varied according to the measured current. These polarization data were obtained between a voltage of 0.45 V and the open circuit voltage in randomized steps of 0.05 V. The flow rates were manually changed according to the current in an iter-

<sup>1</sup> We defined the standard condition as 298 K and 101 kPa.

Table 1

Flow rates, stoichiometries, and voltage change rates for experiments

	Flow rates, A/C (cm <sup>3</sup> /min)	Stoichiometry (A/C)		Current density (A/cm <sup>2</sup> )		Approximate linear cell voltage change rate (V/s)	Voltage time constant, $\delta$ (s)	Overshoot/undershoot(A/cm <sup>2</sup> )
		$t = 0$	$t = \infty$	$t = 0$	$t = \infty$			
Case 1, 0.7–0.5 V (excess to normal)								
1a	249/1040	2.9/4.8	1.2/2.0	0.62	1.48	0.17	0.6	N/A
1b	501/1040	5.8/4.8	2.4/2.0	0.62	1.48	0.17	0.6	N/A
1c	301/1260	3.5/8.7	1.2/3.0	0.62	1.80	0.17	0.8	N/A
Case 2, 0.5–0.7 V (normal to excess)								
2a	249/1040	1.2/2.0	2.9/4.8	1.48	0.62	0.17	0.4	N/A
2b	501/1040	2.4/2.0	5.8/4.8	1.48	0.62	0.17	0.4	N/A
2c	301/1260	1.2/3.0	3.5/8.7	1.80	0.62	0.17	0.5	N/A
Case 3, 0.7–0.5 V (normal to starved)								
3a	92/384	1.2/2.0	1.0/1.7	0.54	0.58	0.22	0.4	0.95
3b	185/385	2.4/2.0	1.5/1.2	0.57	0.90	0.22	0.5	0.95
3c	96/600	1.2/3.0	1.0/2.7	0.58	0.58	0.22	0.6	1.15
Case 4, 0.5–0.7 V (starved to normal)								
4a	92/384	1.0/1.7	1.2/2.0	0.58	0.54	0.22	0.2	0.39
4b	185/385	1.5/1.2	2.4/2.0	0.90	0.57	0.22	0.2	N/A
4c	96/600	1.0/2.7	1.2/3.0	0.58	0.58	0.22	0.2	0.35

active manner to maintain the fixed stoichiometry. The data (Fig. 1) were obtained at three normal stoichiometric sets: a (standard), b (anode-rich), and c (cathode-rich), corresponding to anode/cathode stoichiometries of 1.2/2.0, 2.4/2.0, and 1.2/3.0, respectively. That is, for example, a stoichiometry of 1.2/2.0 corresponds to flow rates that were 1.2 times greater than required (by the measured current) for hydrogen and 2.0 greater than that required on the cathode for air.

The second part of this experiment measured the transient behavior of the PEM fuel cell. A two channel digital oscilloscope (TDS 210, Tektronix Inc.) was used to record simultaneously both the current response and the voltage forcing function. The current was measured using a “hall effect current sensor” so that it would be converted into voltage sig-

nals. Fig. 2 shows a schematic diagram of the experimental setup. The current was converted into voltage signal and then recorded at the first channel (CH-1) of the oscilloscope. The cell potential was measured directly from the fuel cell and recorded at the second channel (CH-2) of the oscilloscope. The cell voltage was changed after a steady-state current was achieved at the initial voltage. These signals were recorded in the oscilloscope from 10 s before the triggering point, at  $t = 0$ , until 40 s after the triggering point.

We focused the transient experiment on voltages changes either to or from 0.7 and 0.5 V. The test station, computer interface, and electronic load bank limited the rates of voltage change to about 0.2 V/s. Variation in this change was  $\pm 0.05$  V/s. The change rates were not linear but rather can

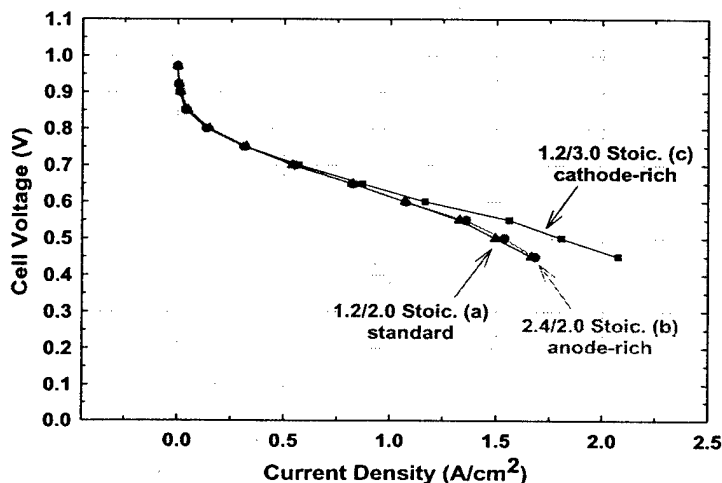


Fig. 1. Steady-state polarization curves for various stoichiometric flows of the anode/cathode: (▲) 1.2/2.0, (●) 2.4/2.0, and (■) 1.2/3.0.

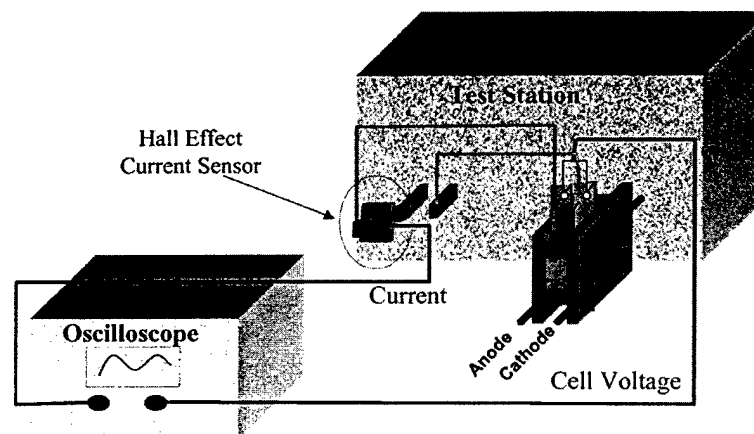


Fig. 2. Schematic diagram of oscilloscope and fuel cell for transient experiments.

be approximated by a first-order system. That is, for Case 1a in Table 1. The cell voltage change rate for this case is approximately 0.17 V/s based on a linear estimate between 0.7 V at  $t = 0$  s and 0.5 V at  $t = 1.18$  s. Note, however, that the change is not linear but best described as a first-order change:

$$V(t) = V(t=0) + \Delta V(1 - e^{-t/\delta}) \quad (1)$$

where  $\delta$  is a time constant that depends on the load characteristics and thus on total current from the PEMFC. For Case 1a,  $V(t=0) = 0.7$  V and  $\Delta V = -0.2$  V and for Case 2a  $V(t=0) = 0.5$  V and  $\Delta V = +0.2$  V. The time constant,  $\delta$ , is shown in Table 1. Also for Cases 3 and 4 as shown in Table 1, the linear voltage change rate was approximately 0.22 V/s and thus  $\delta$ ,  $V(t=0)$ , and  $\Delta V$  follow from Table 1.

### 3. Results and discussions

Fig. 3 shows a voltage–current cycle for a normal-to-excess-to-normal experiment of Cases 1a and 2a. Note that we performed Case 1a followed by Case 2a four times over a period of approximately 4.1 h. Fig. 4 shows the second and third cycles of Fig. 3 and by expanding the time scale for Case 1a it allows comparison of the data obtained at 75 and 135 min. There is some noise in the voltage data corresponding to the  $\pm 5$  mV accuracy of the load but, in general, the experimental data were reproducible. The response for Case 1a can be described as a first-order (FO) system and one does not observe any overshoot in the current density. That is, the value of 1.16 A/cm<sup>2</sup> occurs at the time constant,  $\tau$ , of 0.2 s corresponds to 63.2% of the final value of the current density difference between final and initial values. That is, the current density value for this case is

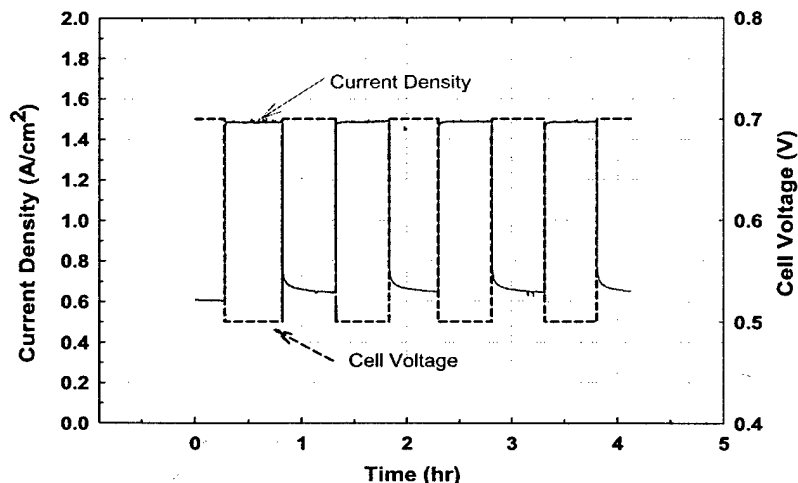


Fig. 3. Overall view of voltage change and current density response for Cases 1a and 2a.



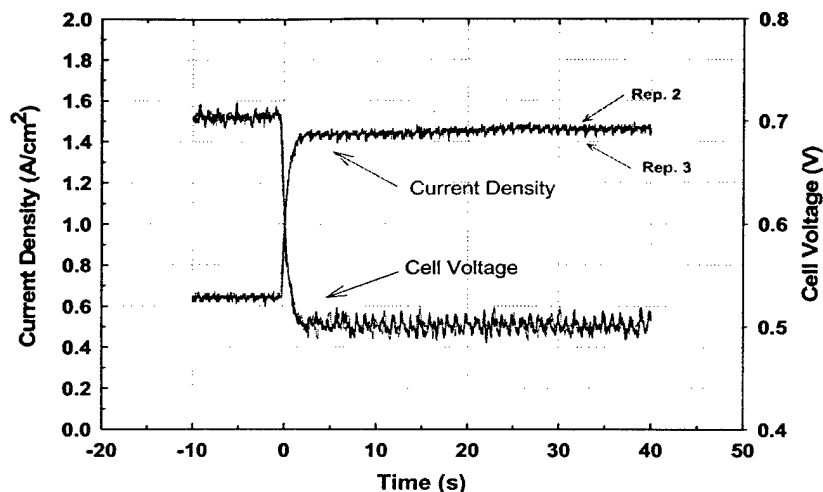


Fig. 4. Case 1a (expanded view with oscilloscope), flow rates: 249/1040 cm<sup>3</sup>/min. The cell voltage changes from 0.7 to 0.5 V. Stoichiometry change: 2.9/4.8–1.2/2.0.

$$i(t = \tau) = i(t = 0) + 0.632(i(t = \infty) - i(t = 0)) \quad (2)$$

where  $i(t = 0)$  and  $i(t = \infty)$  are at initial and final current density, respectively. The transfer function of this FO response system to the voltage change can be written as Laplace domain [11]:

$$i(s) = \frac{K_1}{\tau s + 1} V(s) \quad (3)$$

and by taking the inverse Laplace transform, one can obtain the time domain equation for a step change in  $V(s)$ :

$$i(t) = i(t = 0) + K_1(1 - e^{-t/\tau})(V(t) - V(t = 0)) \quad (4)$$

The gain,  $K_1$ , is shown in Table 2 to be negative because the forcing function  $\Delta V = V(t) - V(t = 0)$  is negative (i.e., 0.5–0.7 V). Note that most FO analyses use a step function but that we used (Eq. (1)) for  $V(t)$  from the experiments to obtain the value of  $K_1$  with MATLAB® Simulink® as described in [12]. As discussed below the response of current density with a cell voltage change depends mainly on the time constant for the case where the stoichiometry is in excess. The quality of the fit of equation to the data is also discussed below.

Fig. 5 shows the expanded time scale response for Case 2a, a change from 0.5 to 0.7 V at the same flow rates as Case

Table 2  
Observations and dependent variables analysis parameters

Type of response		Gain (A/cm <sup>2</sup> V)		Time constant, $\tau$ (s)	FO lead time constant, $\beta$ (s)	Damping factor, $\xi$	$R^2$
		$K_1$	$K_2$				
Case 1, 0.7–0.5 V (excess to normal)							
1a	FO	–4.4		0.2			0.9970
1b	FO	–4.4		0.2			0.9970
1c	FO	–5.9		0.2			0.9983
Case 2, 0.5–0.7 V (normal to excess)							
2a	FO	–3.6		0.6			0.9941
2b	FO	–3.6		0.6			0.9941
2c	FO	–5.1		0.6			0.9931
Case 3, 0.7–0.5 V (normal to starved)							
3a	SO L/L	2.4	–2.4	1.5		0.4	0.9643
3b	FO	–1.9		0.02			0.9956
3c	SO L/L	2.8	–2.8	1.1		0.4	0.9472
Case 4, 0.5–0.7 V (starved to normal)							
4a	FO L/L	–0.1		2.0	19		0.9715
4b	FO	–1.4		0.4			0.9816
4c	FO L/L	–0.1		2.0	30		0.9762

The types of responses are abbreviated: FO, first-order system response; FO L/L, first-order lead/lag system response; SO L/L, second-order lead/lag system response (two gains,  $K_1$  and  $K_2$ ).

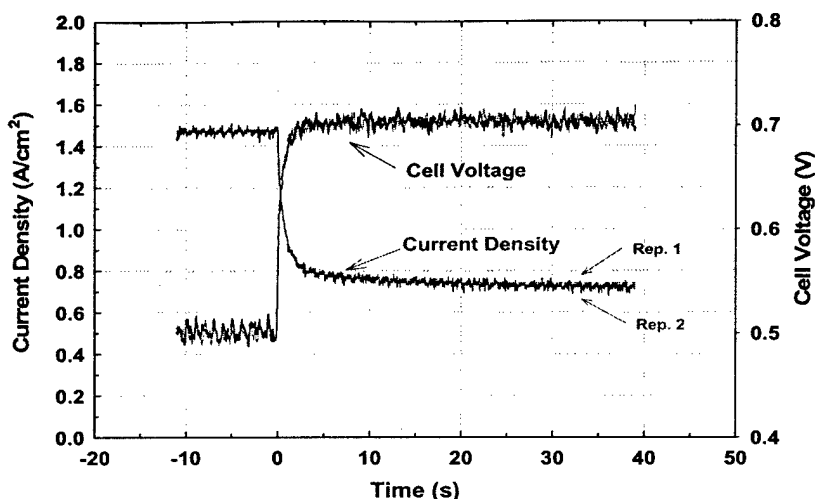


Fig. 5. Case 2a (expanded view with oscilloscope), flow rates: 249/1040 cm<sup>3</sup>/min. The cell voltage changes from 0.5 to 0.7 V. Stoichiometry change: 1.2/2.0–2.9/4.8.

1a. Thus, we observed a change from normal stoichiometry to excess (from 1.2/2.0 to 2.9/4.8 stoichiometry). The reproducibility is shown to be good by rescaling the time axis for the data starting at 45 and 105 min and plotting Rep. 1 and Rep. 2 data from Fig. 3. As the cell voltage increases, the current density decreases and this response is also a FO system with the time constant corresponding to about 0.6 s. Note that this FO model and parameters corresponds to the short time response until 0.8 A/cm<sup>2</sup> and that there is a gradual decrease in the current during the next 30 min until the value 0.62 A/cm<sup>2</sup> is obtained at 0.7 V. This current density change for 30 min after a cell voltage change to 0.7 V is reproducible as shown in Fig. 3 and it is typical for this MEA when there are transients at “excess” conditions. The experiments reported here do not yield information on the cause

of this long-term decrease. No undershoot behavior is observed for this case. Case 2a can be described by Eqs. (3) and (4) with the parameters of Table 2. For Case 2a the cell voltage change is a positive value and thus the current density decreases so that the gain,  $K_1$ , has negative value. Again the comparison of the FO model and the data is discussed after the data for the other cases are presented.

Fig. 6 shows the voltage and current density changes for Cases 3a and 4a. These results were obtained over 2.0 h. The current was unstable (non-periodic oscillations were observed) at the cell voltage of 0.5 V because the hydrogen flow approaches starved conditions. This stoichiometry was estimated based on the average current density at 0.5 V. At a stoichiometry of 1.0 the flow of hydrogen out of the fuel cell will approach zero because all of the hy-

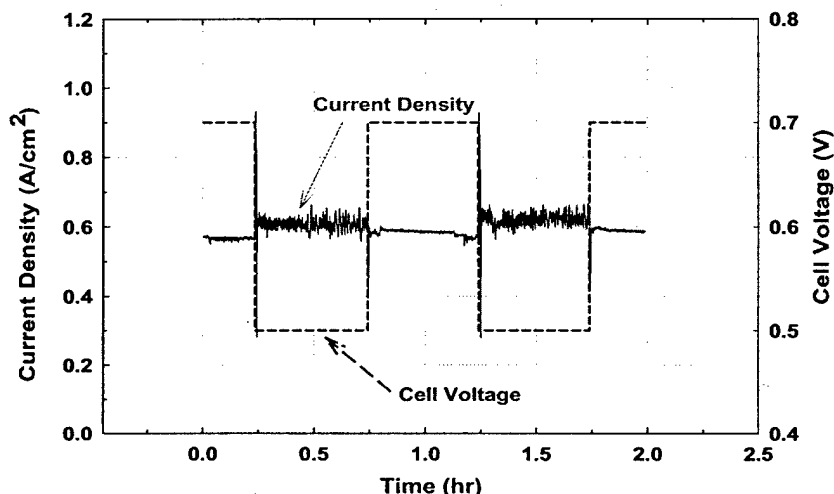


Fig. 6. Overall view of voltage change and current density response for Cases 3a and 4a.

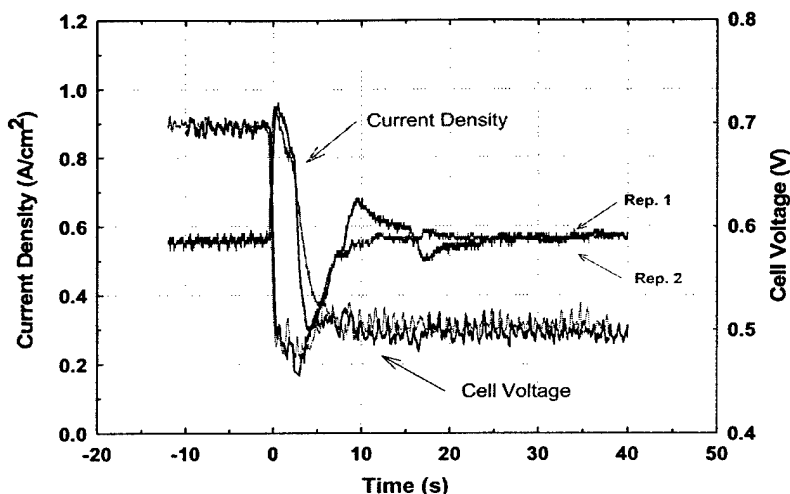


Fig. 7. Case 3a (expanded view with oscilloscope), flow rates:  $92/384 \text{ cm}^3/\text{min}$ . The cell voltage changes from 0.7 to 0.5 V. Stoichiometry change: 1.2/2.0–1.0/1.7.

drogen into the cell will be reacted before reaching the end of the flow channel. This is consistent with our numerical predictions [6,7] that indicate for these conditions that all the hydrogen is consumed before reaching the end of the flow channel and that not all the reaction area is utilized.

Fig. 7 expands the scale of Fig. 6 for Case 3a. The stoichiometry changes from a normal (1.2/2.0) to a starved (1.0/1.7) condition (see Table 1) and overshoot behavior is observed here. That is, as the voltage decreases from 0.7 to 0.5 V, the current density increases from  $0.54 \text{ A/cm}^2$ , at 0.7 V, to about  $0.95 \text{ A/cm}^2$  after 0.22 s. This maximum is obtained after the cell voltage reaches 0.5 V and after this maximum, the current density decreases to about  $0.38 \text{ A/cm}^2$  for Rep. 1 at 5.5 s and about  $0.30 \text{ A/cm}^2$  for Rep. 2 at about 4.5 s. Then at about  $t = 10 \text{ s}$  the current density has increased from 0.38 to  $0.58 \text{ A/cm}^2$  for Rep. 1. Rep. 2 shows a slightly different behavior where the current density increases from  $0.30 \text{ A/cm}^2$  to an apparent second overshoot of  $0.68 \text{ A/cm}^2$  at about  $t = 10 \text{ s}$ . Typically, we could not confirm that this apparent second overshoot was different from noise but this second overshoot, shown in Fig. 7, corresponds to the maximum value we observed over many replicates. Fig. 7 also shows second undershoot behavior at about  $t = 17 \text{ s}$  which again was the extreme that we observed over many replicates. Note that there is some undershoot with the cell voltage in the first 3 s but that this undershoot was only slightly responsible for the width of the overshoot current peak as determined by other experiments.

We now explain the overshoot behavior: Since the electrochemical reaction is greater at 0.5 than at 0.7 V and because the potential of the electrodes follows the cell voltage without any appreciable time lag, the local reaction (i.e., current) uses the excess hydrogen and oxygen without limi-

tation. (The time constants for limitations are discussed below.) This unlimited use continues until  $0.95 \text{ A/cm}^2$  (based on  $20 \text{ cm}^2$  of MEA area). The current density starts to decrease at 0.22 s because all of the “excess” hydrogen in the GDM and flow channels is consumed. Note that hydrogen is still flowing into the cell but that the distribution of current is highly non-uniform at 0.22 s and becomes more uniform as discussed in [7]. Note also that the overshoot is greater than the 20% that would be expected based on the average stoichiometry. One might be concerned that the MEA hydration may also limit reaction but our experience and measurements indicate that dehydration occurs at a slower time scale than the response shown in Fig. 7 for this MEA.

The undershoot behavior for Case 3a can be explained by considering the current distribution. That is, we hypothesize that the overshoot behavior results in a highly non-uniform current distribution so that the consumption of hydrogen allows for a significant portion of the PEMFC on the hydrogen side to contain ambient air. Ambient air flows into the hydrogen side to equilibrate the atmospheric pressure much like a spring in a spring-dashpot. We label this a “vacuum” effect. This description requires the highly non-uniform current distribution at the peak current density to become more uniform after 10 s as the current density decreases from the peak and it requires time to expel the ambient air and use all of the electrode area. The time between the crossing under the final current density values and the return to the final current density is approximately 9 s for Rep. 1 and 7 s for Rep. 2. The Case 3a can be described with a second-order lead/lag (SO L/L) current response model as discussed below.

Fig. 8 shows the expanded time scale behavior for Case 4a, a change from 0.5 to 0.7 V at the same flow rates as Case 3a. Thus we observe the behavior as the stoichiometry changes from a starved to normal condition (i.e., stoichiometry

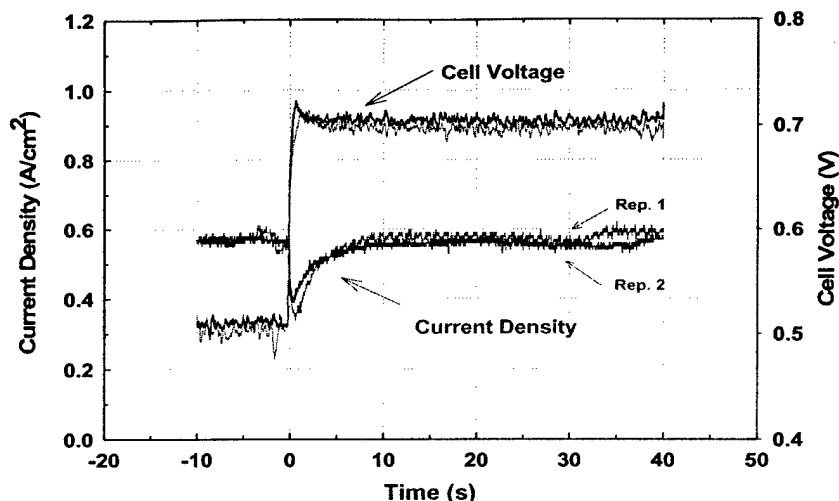


Fig. 8. Case 4a (expanded view with oscilloscope), flow rates: 92/384 cm<sup>3</sup>/min. The cell voltage changes from 0.5 to 0.7 V. Stoichiometry change: 1.0/1.7–1.2/2.0.

etry: 1.0/1.7 to 1.2/2.0). Here, we observe undershoot behavior in the current density. At the cell voltage of 0.5 V, which is a staved condition, the reaction is probably not uniform and the active area utilization is not complete. However, when the cell voltage is changed to 0.7 V, the electrochemical driving force is less and the current density decreases. The lower current density yields unused fuel. Then, the unused fuel expels the ambient air and the non-utilized reaction area becomes exposed to hydrogen. This re-exposure leads to an increase of current density after about 1 s. The time for the recovery of the undershoot behavior is about 8 s. The responses of Case 4a can be described with a first-order lead/lag (FO L/L) current response model as describe below.

Fig. 9 shows a comparison of the Cases of 1a–1c and it allows analysis of the stoichiometry effect. The three cases,

a, b, and c, show similar first-order trends. The response for Cases 1a–1c can be classified as a first-order system because one does not observe an overshoot in the current density when the fuel is excess. The final performance of Case 1c (cathode-rich stoichiometry) shows the highest current density (1.80 A/cm<sup>2</sup>) and the initial current densities are equal indicating ohmic limitations at the high initial stoichiometries consistent with Fig. 1 shown in Table 1. Cases 1a and 1b show identical current density responses (0.65 and 1.48 A/cm<sup>2</sup> for initial and final values, respectively). The linear-approximated cell voltage change rates for these three cases are 0.17 V/s and the time constant,  $\delta$ , for Eq. (1) are close for all three cases. The FO model for the response of the current and a FO response occur for all of these cases because they are not hydrogen-staved condition. Table 2

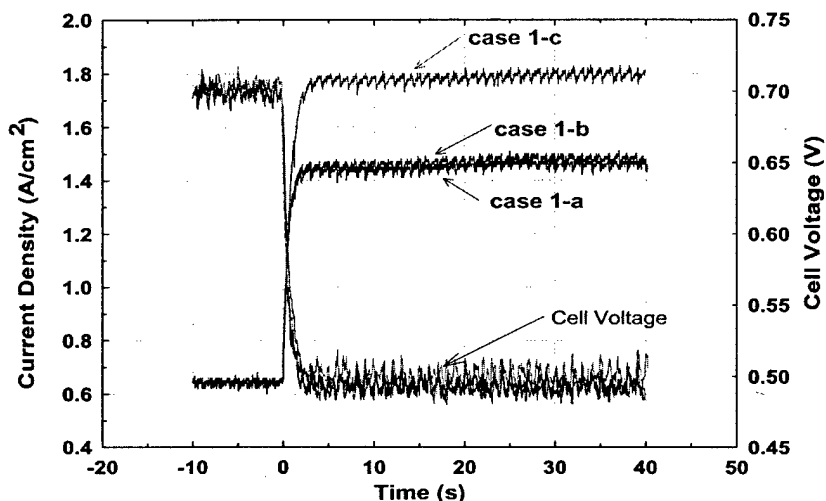


Fig. 9. Comparison of the stoichiometry effect for Cases 1a–1c (excess to normal). See Table 1 for flow rates.

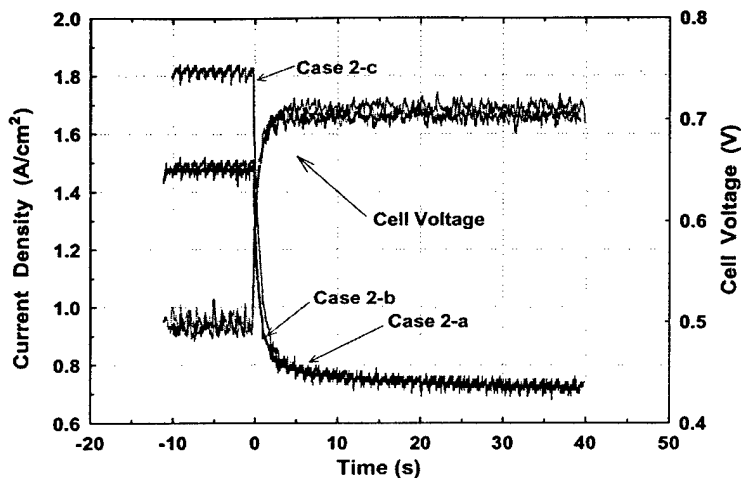


Fig. 10. Comparison of the stoichiometry effect for Cases 2a–2c (normal to excess). See Table 1 for flow rates.

shows that the time constant for each case is the same and that the gain is controlled by the air stoichiometry. This gain could be obtained from steady-state polarization curves such as those shown in Fig. 1 and thus for this configuration of MEA, GDL, gasket, flow field, and membrane water content the FO response can be calculated for design purposes. Future work will quantify the effect of  $\Delta V$  on  $\tau$  and  $K_1$  for the excess stoichiometry and other configurations. The lack of a starved condition conditions yields no overshoot behavior. The  $R^2$  shown in Table 2 is one measure of good agreement between the FO model and the data and Ref. [12] contains graphs of these comparisons.

Fig. 10 shows a comparison of Cases 2a–2c. These graphs show similar FO current density responses where the current density decreases when the cell voltage increases. The initial performance of the Case 2c is higher than that of other two cases because the higher cathode stoichiometry air reduces mass transfer limitations. This response system can be characterized with FO response of exponential decay because there is excess fuel. The FO model with the parameters in Table 2 agrees with the experimental data and no undershoot behavior is observed. Note that although the time constants are equal, the gain reflects the initial stoichiometry. Note also that these parameters correspond to short time since the final approach to steady-state requires about 30 min (see Fig. 3 and discussion above). This slow long-term decaying is responsible for the difference in  $K_1$  for the respective conditions of Cases 1 and 2. Thus  $K_1 = -5.9 \text{ A/cm}^2 \text{ V}$  for Case 1c but  $K_1 = -5.1 \text{ A/cm}^2 \text{ V}$  for Case 2c.

Fig. 11a shows a comparison of Cases 3a–3c. These data have more noise due to the “starved” condition but the data are sufficiently reproducible to compare. Case 3b does not show the overshoot/undershoot behavior because there is excess hydrogen. Cases 3a and 3b start at the same current density at 0.7 V (consistence with Fig. 3) but only Case 3b shows a FO responses as indicated in Table 2. Note that the

small time constant of 0.02 s indicating the lack of limitations consistent with the lack of mass transfer or membrane hydration issues. Case 3c has the higher air stoichiometry than Case 3a and thus the initial current density for Case 3c is slightly the larger (0.58 versus 0.54  $\text{A/cm}^2$ ). The responses of Cases 3a and 3c can be classified as a modified second-order response called as second-order lead/lag system (SO L/L). The details of this modification can be found in [12]. The model can be written in the Laplace domain:

$$i(s) = \left( K_2 + \frac{K_1}{\tau^2 s^2 + 2\tau\xi s + 1} \right) V(s) \quad (5)$$

The time domain function for this system can be obtained by taking inverse Laplace transformation:

$$i(t) = i(t=0) + \left( K_2 + K_1 \left[ 1 - e^{-(\xi/\tau)t} \left\{ \cosh \left( t \sqrt{\frac{\xi^2 - 1}{\tau^2}} \right) + \frac{\xi}{\sqrt{\xi^2 - 1}} \sinh \left( t \sqrt{\frac{\xi^2 - 1}{\tau^2}} \right) \right\} \right] \right) (V(t) - V(t=0)) \quad (6)$$

MATLAB® [13] was used to fit this to the data and the second-order response would be obtained by using MATLAB®. The parameters, steady-state gains,  $K_1$  and  $K_2$ , the time constant,  $\tau$ , and the damping factor,  $\xi$ , listed in Table 2. When the cell voltage is decreased to 0.5 V,  $\Delta V = -0.2 \text{ V}$ , and the current density increases instantaneously to 0.95 and 1.15  $\text{A/cm}^2$  for Cases 3a and 3c, respectively. We model this instantaneous increase with the gain  $K_2$ . The condition of  $K_2$  with  $\Delta V$  is explored in our next paper [12]. The cell voltage difference,  $\Delta V$  has negative value in this case,  $-0.2 \text{ V}$ , and  $K_2$  has negative value so

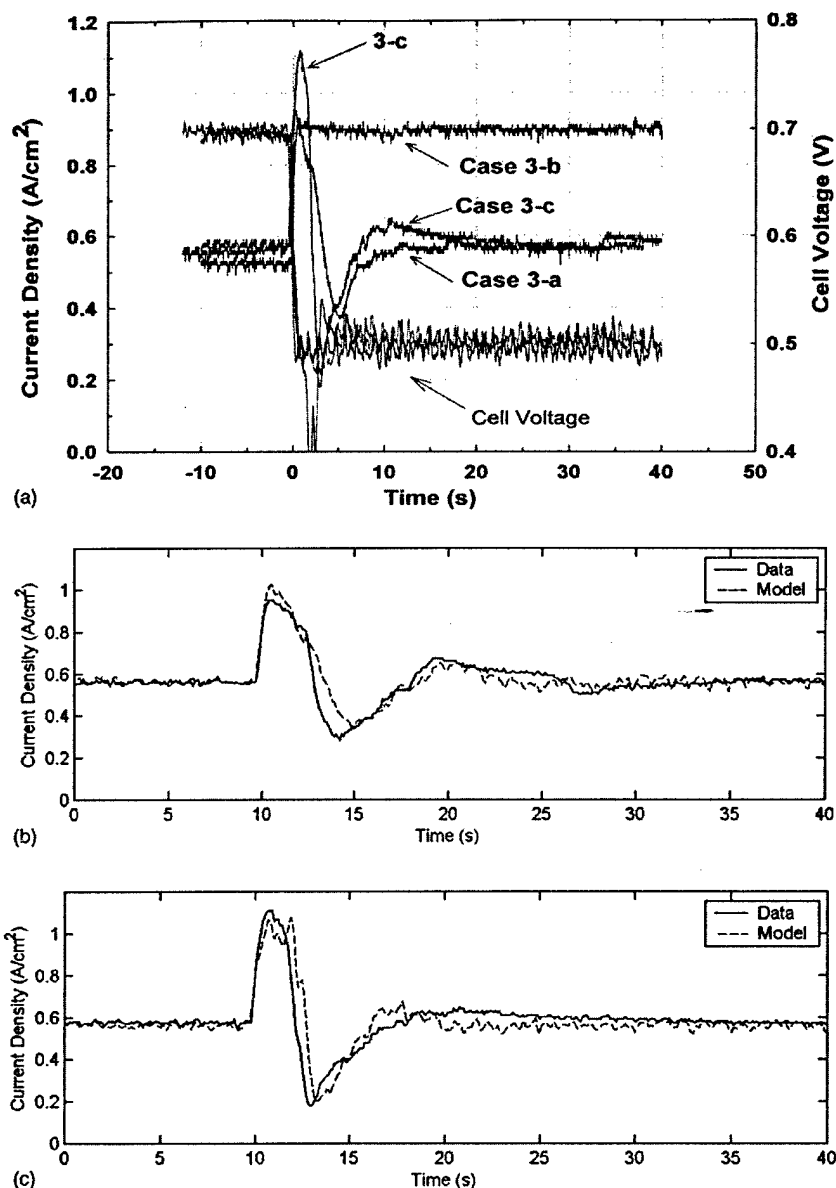


Fig. 11. (a) Comparison of the stoichiometry effect Cases 3a–3c (normal to starved). See Table 1 for flow rates. (b) Fitting of second-order lead/lag response for Case 3a. (c) Fitting of second-order lead/lag response for Case 3c.

that the current density response has positive value. After the maximum current density, all the hydrogen stored in the cell is used and the current density begins to decrease. This decrease is modeled with the second-order part of Eqs. (5) and (6). The gain,  $K_1$ , has positive value and the  $\Delta V$  has negative value so that the current begin to decay from the overshoot peak. The time constant can be obtained at 63.2% of this decrease. The current density value at  $t = 0$  in that equation in this case is the overshoot peak and that of  $t = \infty$ . The undershoot behavior is affected by the damping coefficient in the second-order term. The time constants,

$\tau$ , for Cases 3a and 3c are 1.5 and 1.1 s, respectively. This indicates that the hydrogen consumption is about 1.4 times faster for Case 3c. These parameters could be used for interpolation for any cathode stoichiometry ratio between these two cases. The instantaneous gains,  $K_2$ , for Cases 3a and 3c are different based on the difference in overshoot at  $t \rightarrow 0$  listed in Table 2. Note that the  $R^2$  values are somewhat smaller for Cases 3a and 3c indicating less agreement between the equation and the data. Fig. 11b and c shows that these comparisons are adequate for a description of the dynamics.

It is interesting to note that the overshoot peak at about 0.95 A/cm<sup>2</sup> for Case 3a is only slightly larger than the value of about 0.90 A/cm<sup>2</sup> observed for Case 3b. The hydrogen is not starved for Case 3b (stoichiometry change from 2.4 to 1.5 for the anode) and thus one might believe that the maximum peak is related to the ohmic drop across the MEA. Thus Case 3b is controlled by oxygen electrode and the IR since there is sufficient hydrogen. Thus Case 3b gives the stable cell performance at 0.5 V, while other two cases show “vacuum” effects and unstable oscillations due to insufficient hydrogen. Also, the undershoot behavior due to the “vacuum” effect after overshoot peak for Case 3c is more significant than that of Case 3a, due to the cathode-rich stoichiometry. The overshoot peak values for Cases 3a and 3c are about 0.95 and 1.15 A/cm<sup>2</sup>, respectively. The undershoot behaviors were shown at about  $t = 5$  s with a depth of about 0.37 A/cm<sup>2</sup> for Case 3a and at about  $t = 2.5$  s and 0.2 A/cm<sup>2</sup> of undershoot value for Case 3c. With similar hydrogen flow rates for Cases 3a and 3c are similar, 92 and 96 cm<sup>3</sup>/min, respectively, the hydrogen is consumed faster for Case 3c than for Case 3a because the oxygen is not limited. The electrochemical reaction is more limited by oxygen mass transfer at cell voltage of 0.5 V than 0.7 V. Abundant oxygen for Case 3c results in faster consumption of hydrogen than Case 3a and a larger “vacuum” effect with more ambient air flowing in. Also the second overshoot is observed in Case 3c because we used Rep. 2 of Fig. 7 in Fig. 11a. Again while we cannot completely distinguish, the second peak observed at about  $t = 10$  s with the value of about 0.62 A/cm<sup>2</sup> from the noise, one would expect that a second oscillation corresponding to the dashpot system mentioned above is more significant with excess air.

Fig. 12 shows a comparison of the Cases 4a–4c. Case 4b does not show undershoot behavior because the hydrogen flow is not starved. Also, the initial current density,

0.90 A/cm<sup>2</sup>, is the same as the final of Case 3b from Fig. 11a. The transient behavior of Case 4b can be classified as a FO response system as explained above. The final current density value in Fig. 12 is about 0.6 A/cm<sup>2</sup> for all cases. However, the undershoot behavior of cathode-rich condition, Case 4c, shows similar behavior as that shown in Case 4a. The undershoot depth for Cases 4a and 4c are about 0.40 and 0.38 A/cm<sup>2</sup> and the recovery times for both cases are also very similar with similar hydrogen flow rates. We explain this similarity as, the cell performance at 0.7 V is more affected by ohmic limitations rather than oxygen mass transfer limitation. Thus the extent of recovering from hydrogen starved conditions is similar for both cases. This similarity strongly supports the hypothesis that the undershoot behavior and recovery rate depends on the hydrogen utilization.

Cases 4a and 4c can be described by a first-order lead/lag (FO L/L) response of current density. The FO L/L system can be written in the Laplace domain as:

$$i(s) = K_1 \frac{\beta s + 1}{\tau s + 1} V(s) \quad (7)$$

The time domain of the transfer function above is

$$i(t) = i(t=0) + K_1(1 - (1 - \rho)e^{-t/\tau})(V(t) - V(t=0)) \quad (8)$$

where  $\rho$  is the lead-to-lag ratio ( $=\beta/\tau$ ) [11,13]. The parameters, lead time constant,  $\beta$ , lag time constant,  $\tau$ , and steady-state gain,  $K_1$ , are listed in Table 2. The gain,  $K_1$ , and lead time constant,  $\beta$ , affect the instantaneous undershoot response. The gain represents the difference between initial and final values. Although the initial current density values for Cases 4a and 4c shown in Table 1 are 0.58, the average current density at 0.5 V as mentioned in Fig. 8, for both cases, the model fittings were calculated based on Fig. 12.

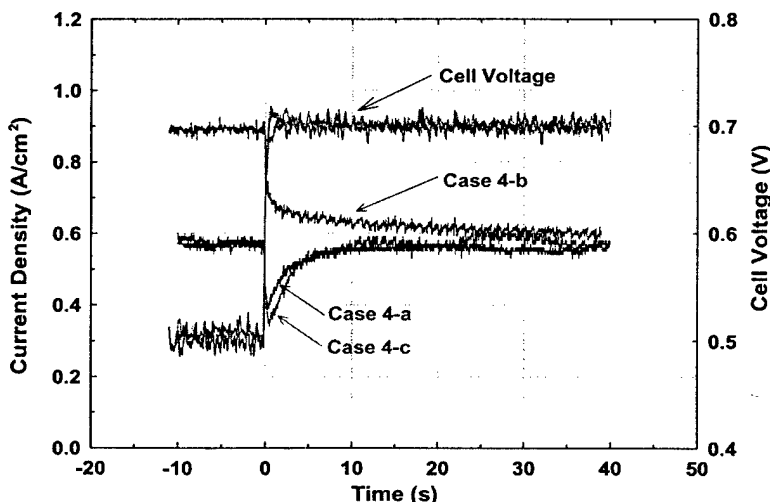


Fig. 12. Comparison of the stoichiometry effect in Cases 4a–4c (starved to normal). See Table 1 for flow rates.

The undershoot peak is determined by lead-to-lag ratio,  $\rho$  and  $K_1$ . The  $\Delta V$  has positive value, 0.2 V, and the gain has negative value so that the current response is negative with the cell voltage change. Then the lag time constant in this case,  $\tau$ , affects the current density makeup. The lag time constants,  $\tau$ , were obtained from experimental data by applying Eq. (2). The initial current density in this case is the undershoot peak value. While the other two cases show first-order lead/lag system, Case 3b shows a modified first-order exponential decay. The hydrogen stoichiometry is changed from 1.5 to 2.4 for Case 3b.

#### 4. Conclusions

Data were presented to show the current density response when the cell voltage was changed rapidly for fixed flow rates. The responses depend on the relative stoichiometry at  $t = 0$  and  $\infty$ . Overshoot, undershoot, and overshoot/undershoot behavior was observed. For excess stoichiometry, the response was modeled with a FO equation. Thus no overshoot or undershoot behaviors were observed for the excess stoichiometries. For “starved” conditions, pseudo-second-order behavior was observed and classified with lead/lag models. Parameters for these models were presented and the models agree well with the experimental data. Undershoot behaviors were observed when hydrogen stoichiometry is changed from starved to normal condition. The undershoot behavior was explained in terms of a non-uniform hydrogen controlled current distribution. The undershoot peak is affected by the gain,  $K$ , and lead-time constant,  $\beta$ , with the cathode stoichiometry. Overshoot behavior was explained in terms of excess hydrogen consumption, non-uniform hydrogen controlled current density, and a sufficient consumption of hydrogen to draw ambient air into the flow field at the exit of the cell. These overshoot peaks are affected by the gain,  $K_2$ , for instant, current density increase with cell voltage decrease.

Finally, overshoot followed by undershoot behavior was observed and explained in terms of hydrogen replacing the ambient air as the current density distribution became more uniform. The undershoot following the overshoot peak is af-

ected by second-order gain,  $K_1$ , for the steady-state value at  $t = \infty$  and damping coefficient,  $\xi$  for its magnitude. The cathode stoichiometry affected the time constant,  $\tau$ , and magnitude of overshoot peak. It supports that the overshoot or undershoot behaviors were mainly dependent on hydrogen utilization.

#### Acknowledgements

Financial support by the South Carolina State University/University Transportation Center (Grant no. 2000-013), Department of Energy-EPSCoR (Cooperation Agreement DE-FG02-91ER75666), and Office of Naval Research, ONR (Grant no. N00014-98-1-0554) is gratefully acknowledged. The authors gratefully acknowledge that W.L. Gore & Associates, Inc., supplied the MEAs used in this work.

#### References

- [1] J. Hamelin, K. Agbossou, A. Laperriere, F. Laurencelle, T.K. Bose, *Int. J. Hydrogen Energy* 26 (2001) 625–629.
- [2] J.C. Amphlett, E.H. De Oliveria, R.F. Mann, P.R. Roberge, A. Rodrigues, J.P. Salvador, *J. Power Sour.* 65 (1997) 173–178.
- [3] J.C. Amphlett, R.F. Mann, B.A. Peppley, P.R. Roberge, A. Rodrigues, *J. Power Sour.* 61 (1997) 183–188.
- [4] B. Emonts, J. Bøgild Hansen, H. Schmidt, T. Grube, B. Hohlein, R. Peters, A. Tschauder, *J. Power Sour.* 86 (2000) 228–236.
- [5] R. Kötze, S. Müller, M. Bärtschi, B. Schnyder, P. Dietrich, F.N. Büchi, A. Tsukada, G.G. Scherer, P. Rodatz, O. Garcia, P. Barrade, V. Hermann, R. Gallay, in: G. Nazri, et al. (Eds.), *Advanced Batteries and Supercapacitors*, ECS Proceedings, vol. PV 2001-21, 2001.
- [6] S. Shimpalee, W.-k. Lee, J.W. Van Zee, H. Naseri-Neshat, *J. Fuel Cells* (2002), submitted for publication.
- [7] S. Shimpalee, W.-k. Lee, J.W. Van Zee, Presented at the 2002 Meeting of the Electrochem. Soc., Paper No. 1136, Philadelphia, PA, May 2002.
- [8] M. Ceraolo, C. Miulli, A. Pazio, *J. Power Sour.* 113 (2003) 131.
- [9] W.-k. Lee, C. Ho, J.W. Van Zee, *J. Power Sour.* 84 (1999) 45.
- [10] W.-k. Lee, Ph.D. Dissertation, Department of Chemical Engineering, University of South Carolina, SC, 1999.
- [11] B.A. Ogunnaike, W.H. Ray, *Process Dynamics, Modeling, and Control*, Oxford, 1994, pp. 139–211.
- [12] S. Kim, Ph.D. Dissertation, Department of Chemical Engineering, University of South Carolina, SC, 2004.
- [13] MATLAB® Simulink®, version 6.5.1. <http://www.mathworks.com>.





## The effect of reservoirs and fuel dilution on the dynamic behavior of a PEMFC

Sunhoe Kim, S. Shimpalee, J.W. Van Zee\*

Department of Chemical Engineering, University of South Carolina, Columbia, SC 29208, USA

Received 23 April 2004; accepted 15 May 2004

### Abstract

Data are presented to characterize the effects of reservoir size and hydrogen dilution on the dynamic behavior of a proton exchange membrane fuel cell (PEMFC) subjected to rapid changes in the voltage when the flowrates are constant. The data consist of the responses of the current density during low fuel stoichiometries in an effort to expand an understanding of the previously observed overshoot/undershoot behavior. That is, recent studies of the dynamic behavior of a PEMFC have shown pseudo-second-order dynamics of the current response to a change in voltage [J. Power Sources (2004); J. Electrochem. Soc. (2004)]. The data reported here lend further evidence that under fuel starved conditions, rapid changes in the cell voltage between 0.7 and 0.5 V yield pressure differences sufficient to create a “vacuum” effect. This vacuum effect may cause fuel to be drawn from the manifold in a stack or cause ambient air to enter a laboratory scale cell. The vacuum effect explained in our previous work [J. Power Sources (2004)] is shown here to depend on diameter and volume of fuel reservoirs and on the concentration of hydrogen in the fuel.

© 2004 Published by Elsevier B.V.

**Keywords:** PEM; Fuel cells; Membrane electrode assembly; Electric vehicle; Transient; Electric load; Reservoir effect; Dilution effect; Dynamic behavior

### 1. Introduction

As discussed previously [1,2], transient operation of PEMFCs during stationary and automotive applications may be a result of a sudden demand as appliance starts or as a vehicle is accelerated or decelerated. Further these transients may be of sufficient magnitude and speed that gas flowrates cannot be adjusted by feedback control or that the capacitors in the system cannot accommodate the demand. We recently showed that these transients result in pseudo-second-order dynamics in the current response when the voltage was changed during operation with low fuel stoichiometry in a 25 cm<sup>2</sup> laboratory cell. We believe these transients expose the MEA to various degrees of stoichiometry and distributions of the current density, temperature, and water as predicted recently, by three-dimensional simulations presented by Shimpalee et al. [3,4]. Here we present experimental data for this second-order response of the current that shows both the effects of a fuel reservoir and the effects of diluting the hydrogen fuel with nitrogen.

The objective of this paper is to test two hypotheses by presenting an experimental study of the second-order dynamic behavior observed during changes in the voltage. The terms and definitions used for this study are shown in Fig. 1a and b for an idealized forcing function and response. During an increase in the load at a fixed set of anode and cathode flowrates, the voltage is changed from a high value to a low value (e.g., 0.7–0.5 V in Fig. 1a). This change results in an increase in the measured current and if we use the geometric area we can obtain a response such as that shown for the current density. This response may overshoot the final value of the current density value due to residual hydrogen in the cell and the degree of overshoot can be labeled “O” in Fig. 1a. Then we typically observe a period of time before the current starts to decrease and we label this time as the “Peak Length.” The overshoot “O” may then be followed by an undershoot “U<sub>o</sub>” [1,2]. On the other hand, as shown in Fig. 1b, we observed an undershoot “U<sub>u</sub>” without an overshoot when we change the cell voltage from 0.5 to 0.7 V for a starved condition. Fig. 1a and b also gains,  $K_1$  and  $K_2$ , used in the mathematical analysis as discussed below.

One of the hypotheses to be tested here is a result of observations in references [1,2]. There we suggested that the “U<sub>o</sub>” was due to a “vacuum” effect dependent on the ve-

\* Corresponding author. Tel.: +1 803 777 2285; fax: +1 803 777 8142.  
E-mail address: [vanzee@engr.sc.edu](mailto:vanzee@engr.sc.edu) (J.W. Van Zee).

## Nomenclature

$i$	current density (A/cm <sup>2</sup> )
$K$	steady state gain (A/cm <sup>2</sup> V)
$t$	time (s)
$V$	cell voltage (V)
$\Delta V$	cell voltage difference (V)

## Greek letters

$\beta$	lead time constant (s)
$\delta$	time constant for cell voltage (s)
$\xi$	damping coefficient
$\rho$	lead-to-lag ratio ( $\rho = \beta/\tau$ )
$\tau$	time constant (s)

“ $U_0$ ” was observed when a triple path flow field is used because the velocity in each channel is less thereby allowing more ambient air to enter the cell [2]. Also a larger fraction of the MEA is exposed to air when a triple path flow field is used because the air can enter three channels. It is important to note also that the undershoot discussed here follows an overshoot and that it is therefore fundamentally different than the undershoot observed when the cell voltage is increased. That undershoot appears to be a result of the current distribution becoming more uniform as the load is decreased and as the apparent stoichiometry is increased [3,4]. Thus, to test this first hypothesis, we used diluted fuel to change the velocity in a triple path flow field cell so that comparisons could be made at the same stoichiometry.

The second hypothesis to be tested here also involves the “vacuum” effect but it relates to the peak length in Fig. 1a. We hypothesize that the peak length can be increased or decreased depending on the volume and diameter of a hydrogen reservoir at the exit of the cell. This reservoir may be a model for part of the manifold in a stack of cells and our

locity of the fuel in the flow channels. That is, undershoot behavior is not observed when a single path flow channel is used because the faster exit velocity of hydrogen decreases the amount of air that penetrates the cell. On the other hand,

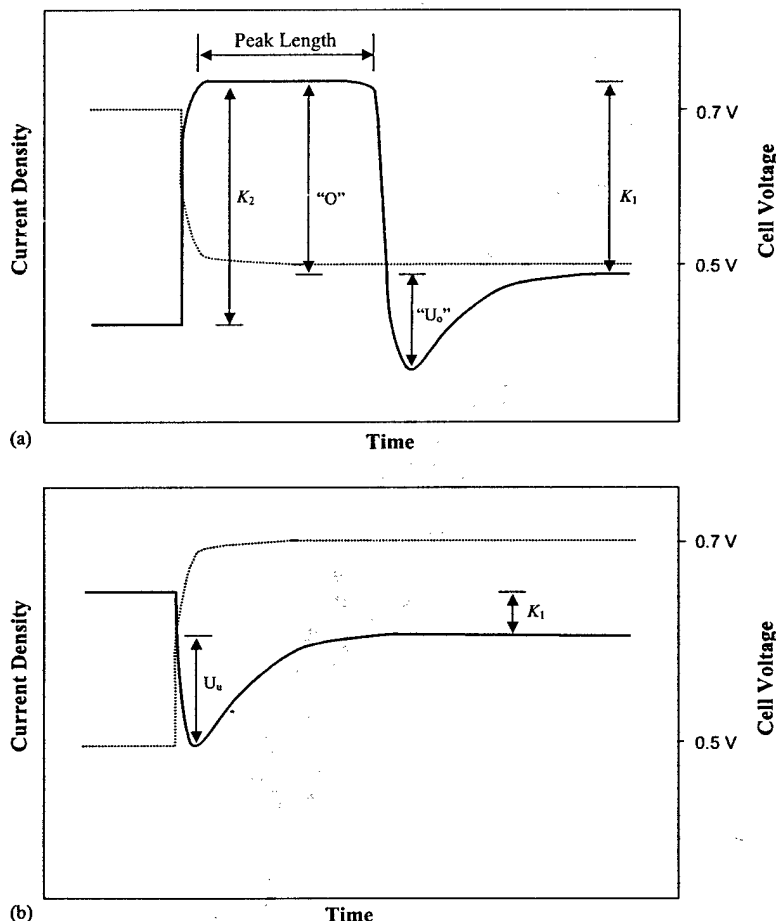


Fig. 1. (a) Schematic of overshoot-undershoot behavior during a voltage change from 0.7 to 0.5 V at fixed flow rates: (---) cell voltage and (—) current density. (b) Schematic of undershoot behavior during a voltage change from 0.5 to 0.7 V at fixed flow rates: (---) cell voltage and (—) current density.

focus here is to study the interaction of this “vacuum” effect and the manifold size by isolating a single cell. The hypothesis includes the diameter of the reservoir because, again, we want to test the component that velocity at the exit is a major effect for the overshoot/undershoot behavior. Thus a manifold with more hydrogen should have a longer peak length and the depth of the resulting undershoot should be a function of reservoir diameter since the “vacuum” effect is influenced by the velocity of the fuel flowing into the channel.

Our reviews of the literature [1,2] indicate that experimental analysis of the behavior in Fig. 1a and b are new for PEMFCs. On the other hand, there have been studies on system performance of PEMFC stacks [5] and battery–PEMFC hybrid systems [6–8]. In Reference [1] we considered the effect of stoichiometry on the dynamics behavior and we showed that for fixed flowrates, voltage changes yielded current densities that could be described by a simple first-order decay or increase:

$$i(t) = i(t=0) + K \Delta V(1 - e^{-t/\tau}) \quad (1)$$

when those changes resulted in stoichiometries that changed from excess conditions to a 1.2/2.0 condition for hydrogen and air, respectively. On the other hand, the overshoot and “undershoot” behavior, illustrated in Fig. 1a, occurs when the voltage change results in a stoichiometry change from 1.2/2.0 to a ‘starved’ condition. This behavior was classified as a second-order lead/lag (SO L/L) response system and described by Eqs. (2a)–(2c) below [1]:

$$\tau^2 \frac{d^2 i_1}{dt^2} + 2\xi\tau \frac{di_1}{dt} + i_1 = K_1[V(t) - V(t=0)] \quad (2a)$$

$$i_2 = K_2[V(t) - V(t=0)] \quad (2b)$$

$$i(t) = i_1(t) + i_2(t) \quad (2c)$$

Thus transient behavior after the peak was described by the second-order differential equation for  $i_1$  and the initial peak in the current density,  $i_2$ , was described by the product of a constant gain,  $K_2$ , and the voltage difference. In Reference [1] the peak length was ignored and this resulted in some lack of fit. Here we include the peak length, as discussed below, and the fit is improved. The undershoot behavior shown when the stoichiometry changes from a ‘starved’ to a normal condition, illustrated in Fig. 1b, can be classified as a first-order lead/lag (FO L/L) system [1,9]:

$$i(t) = i(t=0) + K_3[1 - (1 - \rho)e^{-t/\tau}][V(t=0) - V(t)] \quad (3)$$

## 2. Experimental

The same single cell PEMFC and MEA from our other work [1,2] was used for these experiments. The MEAs were PRIMEA® Series 5510 MEA (0.4 mg/cm<sup>2</sup> Pt loading, 25 μm nominal membrane thickness, W.L. Gore & Associates Inc. Elkton, Maryland, USA). The original active electrode area

was 25 cm<sup>2</sup>. The active reaction area of MEA is reduced from 25 to 20 cm<sup>2</sup> by sub-gaskets for both anode and cathode sides. The gas diffusion layers (GDLs) used in this work were CARBEL™ CL (16 miles = 0.41 × 10<sup>−3</sup> m of nominal thickness produced by W.L. Gore & Associates Inc. Elkton, Maryland, USA). The cell was tightened with eight volts with equivalent torques of 50 lb<sub>f</sub> in./bolt. This was determined previously to give the optimal degree of internal compression according to the experiments of Lee et al. [10].

A triple serpentine flow field (SFF) was used in this experimental paper to investigate the length of peak and the “undershoot” after overshoot. The electrical load to control the cell voltage was a Model 6060B (Agilent Technologies) that had a capability of 60 A and 300 W. The fuel cell test station used to control the electrical load, inlet fuel flowrates, and cell and humidity bottle temperature was a product of Fuel Cell Technology (Los Alamos, NM). The digital mass flow controllers (MKS), which were calibrated by bubble flow meters as discussed in reference [11], were used to control the fuel and air flowrates. The inlet hydrogen and air pass through the humidity bottles to be heated and humidified. The humidity of the inlet flows is determined by using previously obtained calibration curves at fixed temperatures of the humidity bottles. In the data reported here we estimate the dew point temperatures of anode and cathode to be 80 and 70 °C, respectively. The hydrogen and air enter into the cell in co-current flow and diffuse through the GDLs to reach the electrode where electrochemical reaction takes place. Usually the non-reacted gas and air exit the cell, pass through the backpressure regulators and then through lengths of tubing that can be considered reservoirs before they are vented. Note that these regulators are not check valves and the outlets of hydrogen and air are open to atmosphere in this work because the backpressures of both the anode and cathode sides were set to atmospheric pressure, 101 kPa. The gases in this experimental work were high purity hydrogen (99.997%) and industrial grade compressed air.

Prior to performing the transient experiments the steady state performance was measured to establish a well humidified MEA baseline with different concentrations of hydrogen (i.e., 100, 80, and 40%) diluted with nitrogen while keeping a stoichiometry of 1.2 and 2.0 for the anode and cathode, respectively. The stoichiometry 1.2/2.0 corresponds to flowrates that were 1.2 times greater than required (by the measured current) for hydrogen and 2.0 greater than that required on the cathode for air. The polarization curves were obtained at the cell voltage from 0.45 V to open circuit voltage (OCV) in 0.05 V randomized steps to insure that no hysteresis is included with the reported polarization curves. The constant stoichiometry requires different flowrates, according to current, for each cell voltage and these flowrates were adjusted manually in an iterative manner according to measured current to maintain the fixed stoichiometry. Note that, for example, if the hydrogen requirement is 80 cm<sup>3</sup>/min, for 80% hydrogen in mixture gas, the total flowrates of the mixture gas is 100 cm<sup>3</sup>/min.

Table 1

Overshoot and undershoot comparison for dilution effect when  $\Delta V = 0.2$  V at  $V(t=0) = 0.7$  or  $0.5$  V

	Voltage change (V)	Stoichiometry		Current density at $t = 0$ (A/cm <sup>2</sup> )	Peak or minimum current density (A/cm <sup>2</sup> )	Change in current density (A/cm <sup>2</sup> )	Current density at $t = \infty$ (A/cm <sup>2</sup> )	Recovery time from undershoot (s)	Flow rates, A/C (cm <sup>3</sup> /min)
		$t = 0$	$t = \infty$						
Neat H <sub>2</sub>	0.7–0.5	1.2/2.0	1.0/1.7	0.49	0.79	<i>O</i>	0.51	N/A	86/357
	0.5–0.7	1.0/1.7	1.2/2.0	0.51	0.32	<i>U<sub>u</sub></i>	0.49	5.8	86/357
80% H <sub>2</sub>	0.7–0.5	1.2/2.0	1.0/1.7	0.40	0.69	<i>O</i>	0.42	N/A	89/295
	0.5–0.7	1.0/1.7	1.2/2.0	0.42	0.30	<i>U<sub>u</sub></i>	0.40	2.2	89/295
40% H <sub>2</sub>	0.7–0.5	1.2/2.0	1.0/1.7	0.35	0.62	<i>O</i>	0.40	N/A	155/258
	0.5–0.7	1.0/1.7	1.2/2.0	0.40	0.28	<i>U<sub>u</sub></i>	0.35	1.0	155/258

Linear approximated voltage changes are 0.22 V/s for all cases.

A two channel digital oscilloscope (TDS 210, Tektronix Inc.) was used to record simultaneously both the current response and the voltage forcing function as illustrated in our previous work [1]. The current was recorded in a form of a voltage signal, via a “hall effect” current sensor at the first channel of the oscilloscope. The cell voltage was measured directly at the cell’s current collector plates and then recorded in second channel of the oscilloscope. For the cell voltage changes from 0.7 to 0.5 V in this work, the test station, computer interface, and electronic load bank limited the rate of voltage change to be about  $0.2 \pm 0.05$  V/s. This approximate rate can be calculated as a linear change from 0 to  $t$  (s) corresponding to the time,  $t$ , when the voltage crosses 0.5 V. In actuality, the cell voltage change rate was non-linear and it can be characterized best with a first-order exponential response [1,2]:

$$V(t) = V(t=0) + \Delta V(1 - e^{-t/\delta}) \quad (4)$$

where  $\Delta V$  is cell voltage difference ( $-0.2$  V for the voltage change from 0.7 to 0.5 and  $0.2$  V for from 0.5 to 0.7 V), and the time constant,  $\delta$ , is equal to  $0.4$  s for the data shown in this paper.

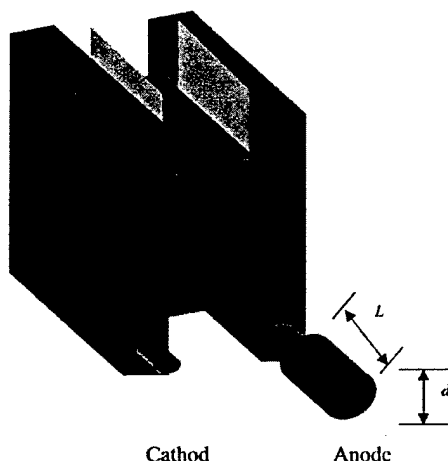


Fig. 2. Schematic diagram of experimental setup for reservoir effect experiment. There are three different volumes of reservoirs and six different lengths corresponding to the three reservoir volumes of Table 2 (i.e., 5, 10, 15 cm<sup>3</sup>).

The dilution effect was measured with three different hydrogen/nitrogen mixture concentrations (100, 80, and 40% hydrogen) at a stoichiometry of 1.2 and 2.0, for the anode and cathode, respectively. There are two cases for the dilution effect experiments, corresponding to  $\Delta V = -0.2$  V and  $\Delta V = 0.2$  V yielding overshoot and undershoot behaviors, respectively. Note that the stoichiometry changed from a normal to a ‘starved’ conditions and from a ‘starved’ to a normal conditions depending on  $\Delta V$  and  $V(t=0)$  for the constant inlet flowrates shown in Table 1.

The “reservoir” was constructed at the exit with tubes of different sizes to study the overshoot peak length. Three volumes of tube (5, 10, and 15 cm<sup>3</sup>) were used in this work. Also, there were two different diameters of the tubes and the volumes were adjusted by cutting the length of the tube. The outer diameters of the tubes were nominally 0.64 and 1.27 cm and the inner diameters were 0.46 and 0.95 cm, respectively. Fig. 2 illustrates the schematic diagram of the experiment setup for the reservoir effect. The details of the sizes and diameters are discussed with the results below. In addition to these reservoir sizes, the volume of the cell may be of interest and it is calculated based on the channel volume, GDL’s thickness and porosity, and the actual 25 cm<sup>2</sup> of the cell. The channel volume is the multiplication of depth of 0.07 cm, width of 0.1 cm, and length of 66 cm and there are three channels in the triple path serpentine flow field. This yields a channel volume of 1.39 cm<sup>3</sup>. Also, the GDL volume was 1.02 cm<sup>3</sup> based on the 25 cm<sup>2</sup> area, the 16 mils thickness (i.e., 0.0406 cm), and the porosity of 0.7. Thus the total volume inside of the cell is 2.4 cm<sup>3</sup>.

### 3. Results and discussion

We conducted the experiments for quantifying the overshoot behavior of PEMFC. These data are best described after a typical overshoot/undershoot response is analyzed (Fig. 1a) and after a typical undershoot response is analyzed (Fig. 1b). It is important to note that as discussed in previous papers [1,2] the overshoot/undershoot behavior and the undershoot behavior occur only for starved conditions. Fig. 3 was shown as a guide to the normal steady state voltage/current behavior for fixed flowrates corresponding to a

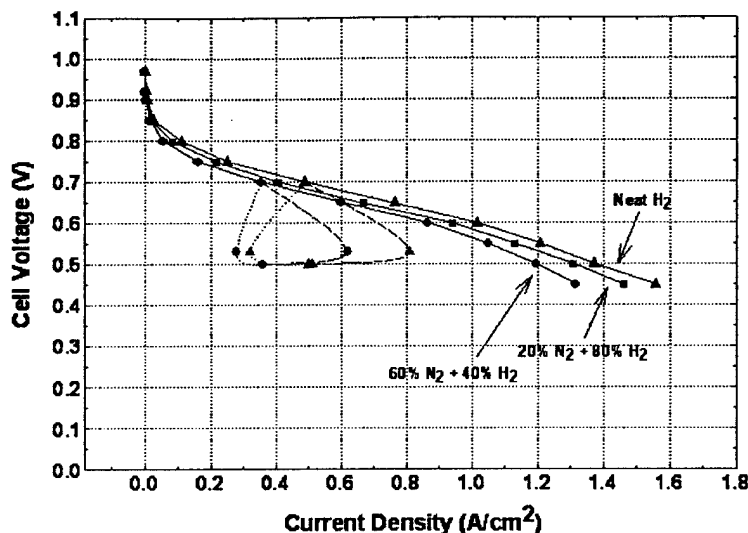


Fig. 3. Polarization behaviors of a PEMFC for various concentrations of hydrogen. The cell temperature of 70 °C. The dew point temperatures of anode and cathode are 80 and 70 °C. The dashed lines (---) indicate that the approximate path of the current during the overshoot behavior as the cell voltage is changed from 0.7 to 0.5 V. The dotted line (···) indicates that the approximate path of the current during the undershoot behavior as the cell voltage is changed from 0.5 to 0.7 V.

1.2/2.0 stoichiometry. The dashed lines indicate that the approximate path of the current during the overshoot behavior as the cell voltage is changed from 0.7 to 0.5 V. The dotted line indicates that the approximate path of the current during the undershoot behavior as the cell voltage is changed from 0.5 to 0.7 V. When, as a result of the voltage decrease (the independent variable), the current (a dependent variable) increases to its limit at a fixed flowrate, the stoichiometry (a dependent variable for fixed flowrates) changes from the normal to the 'starved' condition, and an overshoot behavior was observed. The normal condition defined in this experimental work is 1.2 and 2.0, anode and cathode, respectively. Note that because we are controlling the voltage, the stoichiometry can never be truly 'starved' since the current will respond to the applied voltage and the availability of reactant. However, we use the term 'starved' to indicate the condition when the current corresponds to a stoichiometry close to 1.0.

Fig. 4a and b shows the dimensional and dimensionless comparison of overshoot behavior with different concentrations of hydrogen for the case when there is no reservoir. The dimensionless comparison is useful because these dilution effect experiments have different initial current densities and thus it is difficult to compare changes in the current densities directly. Thus, we introduce the dimensionless current density which is obtained by dividing the transient current density by the respective steady state value  $i = \infty$ . These current densities at  $t = 0$  and  $t = \infty$  are listed in Table 1. In Fig. 4a, the overshoot peaks for neat hydrogen, 80, and 40% of hydrogen are about 0.79, 0.69, and 0.62 A/cm<sup>2</sup>, respectively. As shown in Fig. 4b, the dimensionless magnitude of the overshoot is independent of hy-

drogen concentration. For the neat hydrogen case the overshoot peak length is approximately 2.0 s, while for the diluted hydrogen the peak length was zero. The current density with 40% hydrogen decreased the fastest and this is consistent with less hydrogen in the flow channel and GDL. Also, the dimensionless value of  $U_0$  is largest for neat hydrogen and we argue that the apparent undershoot for the diluted gases is really a function of the inability of the load to precisely control the cell voltage during the first 2.5 s. As discussed in our previous work [1], the "undershoot" after overshoot peak is a result of air flowing back into the cell at the end of the anode. To check this hypothesis, we attached a u-shaped site tube filled with a soap-bubble solution at the anode exit and we observed bubbles flowing away from the cell during operation with diluted fuel. We observed the bubbles moving towards the cell during operation with neat hydrogen. The dimensional current density, values of overshoot peak, and stoichiometries are listed in Table 1.

Fig. 5a shows the comparison of undershoot behavior for the different concentration of hydrogen fuel. The undershoot behavior in this figure corresponds to  $U_u$  from Fig. 1b and it occurs when the fuel supply condition is changed from a starved to a normal condition. The minimum current density at the undershoot depths for neat, 80, and 40% hydrogen concentrations are 0.32, 0.30, and 0.28 A/cm<sup>2</sup>. The dimensionless values of undershoot are similar for each cases (i.e., Fig. 5b). However, the current density recovery times are different. The recovery times for 100, 80, and 40% hydrogen are approximately 5.8, 2.2, and 1.0 s, respectively. The more dilute the hydrogen, the faster the current density recovers. This can be explained if there is a non-uniform distribution

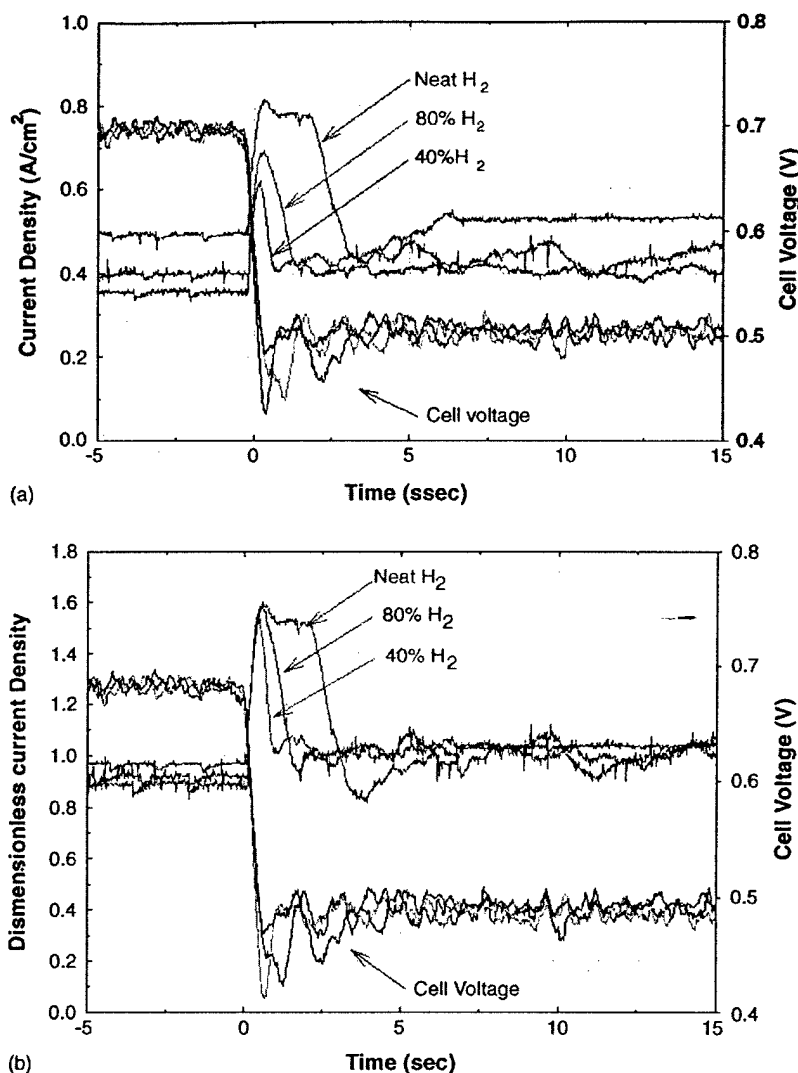


Fig. 4. (a) Comparison of dilution effects on overshoot behavior for different concentrations of hydrogen, neat, 40, and 80% diluted with nitrogen. Here, the resulting fuel stoichiometry condition changes from a normal condition to a starved. (b) Dimensionless comparison of dilution effects on overshoot behavior for different concentrations of hydrogen, neat, 40, and 80% diluted with nitrogen. Cell Voltage changes from 0.7 to 0.5 V.

of current density at the beginning of the cell so that the higher velocities due to the dilution of the fuel lead to faster replenishment of hydrogen throughout the cell, which yields faster recovery. The values of the undershoot recovery time and the minimum currents are listed in Table 1.

The parameters in Eqs. (2a)–(2b) that yield a good fit for the SO L/L model system are listed in Table 2. Note that for the neat hydrogen the  $R^2$  is lower because we applied Eq. (2a) from the time the peak current was obtained and thus we neglect a parameter for the peak length in a manner consistent with reference [1]. Note that the parameters in the table are based on dimensionless current density. The gain  $K_2$ , represents the overshoot peak current density relative to the current density at  $t = 0$  as shown in Fig. 1a. The other

gain,  $K_1$ , corresponds to the current density decay from the peak to final current density values. The undershoot following overshoot peak that were observed in neat hydrogen case were affected by damping coefficients,  $\xi$ , as explained in ref-

Table 2  
Parameters for the dimensionless overshoot SO L/L system for dilution effect experiment

	Gains ( $V^{-1}$ )		Time constant, $\tau$ (s)	Damping coefficient, $\xi$	$R^2$
	$K_1$	$K_2$			
Neat $H_2$	3.1	-3.1	1.0	0.6	0.915
80% $H_2$	2.8	-3.2	0.6	0.8	0.947
40% $H_2$	2.4	-2.9	0.4	0.8	0.950

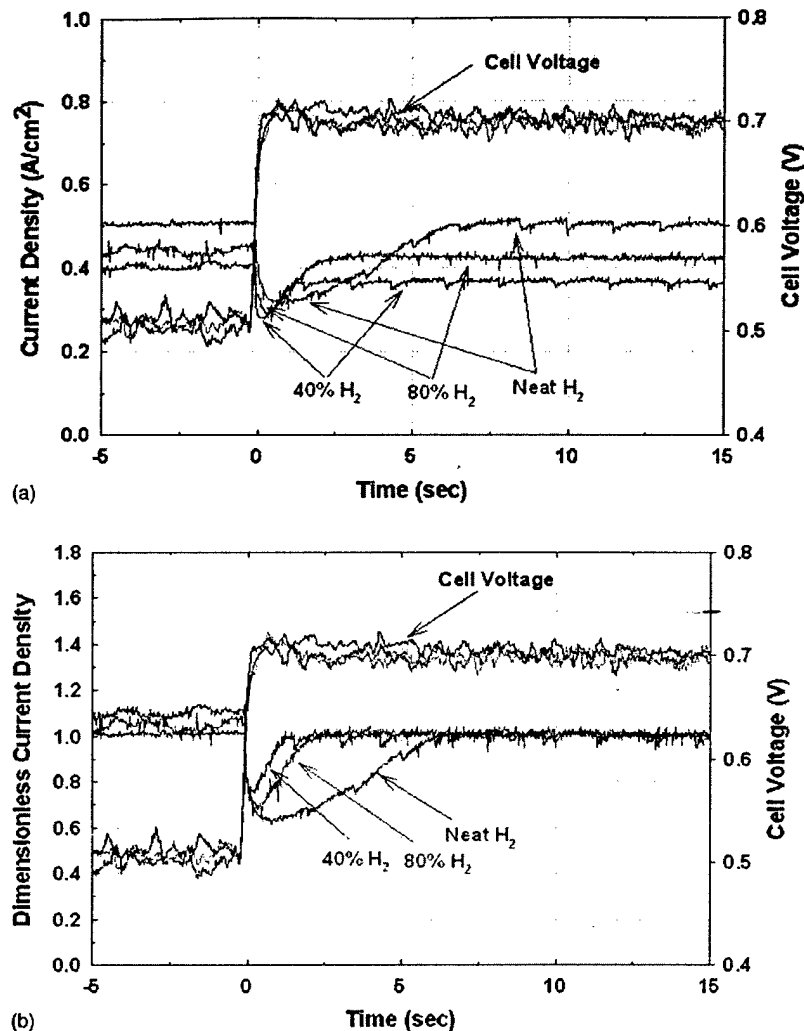


Fig. 5. (a) Comparison of dilution effects on undershoot behavior for different concentrations of hydrogen, neat, 40, and 80% diluted with nitrogen. Here, the resulting fuel stoichiometry condition changes from a starved to a normal condition. (b) Dimensionless comparison of dilution effects on undershoot behavior for different concentrations of hydrogen, neat, 40, and 80% diluted with nitrogen. Cell Voltage changes from 0.5 to 0.7 V.

erence [1]. Also, the time constants,  $\tau$ , for each case affects the current decay after overshoot peak. The time constants were obtained from experimental data with the same manner discussed in our previous work [1]. The corresponding parameters for Eq. (3), a FO L/L system, are listed in Table 3. The gain,  $K_3$ , and lead to lag ratio,  $\rho$ , determine the instant-

Table 3  
Parameters for the dimensionless undershoot behaviors FO L/L system for dilution effect

	Gain, $K_3$ ( $V^{-1}$ )	Lead time constant, $\tau$ (s)	Lag time constant, $\beta$ (s)	$R^2$
Neat $H_2$	-0.2	3.0	38	0.959
80% $H_2$	-0.3	1.2	11	0.980
40% $H_2$	-0.5	0.8	3	0.973

aneous undershoot peak and the time constant,  $\tau$ , determines the rate of recovery to the final steady state value. These values were obtained using MATLAB Simulink<sup>®</sup> from experimental data as explained in our previous work [1]. The gain  $K_3$  is illustrated in Fig. 1b. Again, these parameters were calculated based on dimensionless current density data.

Fig. 6 shows the effect of reservoir connected at the end of anode as illustrated in Fig. 2. Neat hydrogen was used in this experiment. Note that the cell voltages shown in the figure indicate that the cell voltage change rates were the same for all cases. Data for four experiments are shown in this figure corresponding to four volumes: Vol. = 0  $cm^3$  (i.e., without reservoir tube) and Vol. = 5, 10, and 15  $cm^3$ . The overshoot peak is approximately 0.79  $A/cm^2$  for all cases when the cell voltage is 0.5 V. This value of the current density in the overshoot peak is lower than what would be ex-

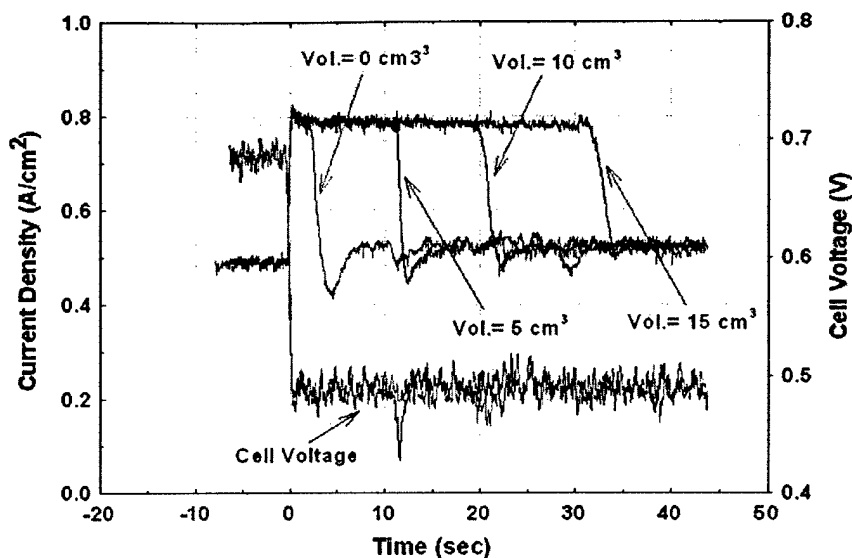


Fig. 6. Comparison of overshoot peak length and “undershoot” with three different volumes of 5, 10, and 15 cm<sup>3</sup>, of reservoir tubes with quarter inches of outer diameter (inside diameter of 0.4572 cm).

pected for a stoichiometry of 1.2/2.0 shown in the polarization curve because the cathode stoichiometry is actually 1.7 at this flowrate [1]. The lowest “undershoot” current density is about 0.42 A/cm<sup>2</sup>, after this “undershoot” the current density increases, and reaches a steady state value for the case without reservoir. The “undershoot” current density peak for the reservoir sizes of 5, 10, and 15 cm<sup>3</sup> are 0.43, 0.45, and 0.48 A/cm<sup>2</sup>, respectively. The values of “ $U_o$ ” corresponding to Fig. 1a are 0.10, 0.09, 0.07 and 0.04 A/cm<sup>2</sup> for the 0, 5, 10 and 15 cm<sup>3</sup> volumes of the reservoir tube, respectively. The flowrates in these experiments are 86 and 357 cm<sup>3</sup>/min for the anode and cathode, respectively. Note that the flow condition at 0.7 V corresponds to stoichiometries of 1.2/2.0 and that at 0.5 V these conditions correspond to stoichiometries of 1.0/1.7. The current density at 0.5 V with these flowrates

corresponds to a starved condition, and thus there are some small oscillations as discussed in our previous work [1]. For Fig. 6, the volume of the reservoir is determined with the tube length and one can observe that the bigger the reservoir volume yields a longer the overshoot peak as expected. Also, the “undershoot” after overshoot behavior is less with longer reservoir tubes as is consistent with the hypothesis that the “undershoot” is caused by ambient air entering the cell. The peak length and reservoir sizes are listed in the Table 4 and one will note that the theoretical peak length is longer than that of actual experimental result. This theoretical peak length is calculated assuming plug flow conditions with the volume of flow channel, GDL, and reservoir sizes and one explanation for the difference is that the reservoir does not empty into the cell as plug flow but rather some

Table 4

Peak length and “undershoot” comparison in the cell voltage changes from 0.7 to 0.5 V with flow rates of 86/357 cm<sup>3</sup>/min, neat hydrogen and parameters for the SOPDT for reservoir effect

Tube volume (cm <sup>3</sup> )	Tube diameter	Tube length (cm)	Stoichiometry		Peak length (s)	“Undershoot” depth (A/cm <sup>2</sup> )	Velocity in reservoir (cm/s)	Damping coefficient, $\xi$	Time delay, $\alpha$ (s)	$R^2$
			$t = 0$	$t = \infty$						
0		0.00	1.2/2.0	1.0/1.7	2.0	0.42	—	0.6	0	0.913
5	1/2 in. o.d.	7.02	1.2/2.0	1.0/1.7	6.1	0.44	0.34	0.6	6	0.995
	1/4 in. o.d.	30.45	1.2/2.0	1.0/1.7	11.1	0.43	1.48	0.6	10	0.988
10	1/2 in. o.d.	14.03	1.2/2.0	1.0/1.7	9.1	0.48	0.34	0.6	11	0.998
	1/2 in. o.d.	60.90	1.2/2.0	1.0/1.7	19.4	0.45	1.48	0.6	19	0.992
15	1/2 in. o.d.	21.04	1.2/2.0	1.0/1.7	13.3	N/A	0.34	0.6	15	0.995
	1/4 in. o.d.	91.35	1.2/2.0	1.0/1.7	31.4	0.48	1.48	0.6	32	0.996

Calculated peak lengths for tube volume of 0, 5, 10, 15 cm<sup>3</sup> are 2.90, 15.1, 27.3 and 39.5 s, respectively) overshoot peak is 0.79 A/cm<sup>2</sup>. Initial and final current density is 0.49 and 0.51 A/cm<sup>2</sup>, respectively. Gains for all cases are 1.6 and -1.6 (A/cm<sup>2</sup> V) for  $K_1$  and  $K_2$ , respectively. Time constant,  $\tau$ , for all cases is 1.0 s.



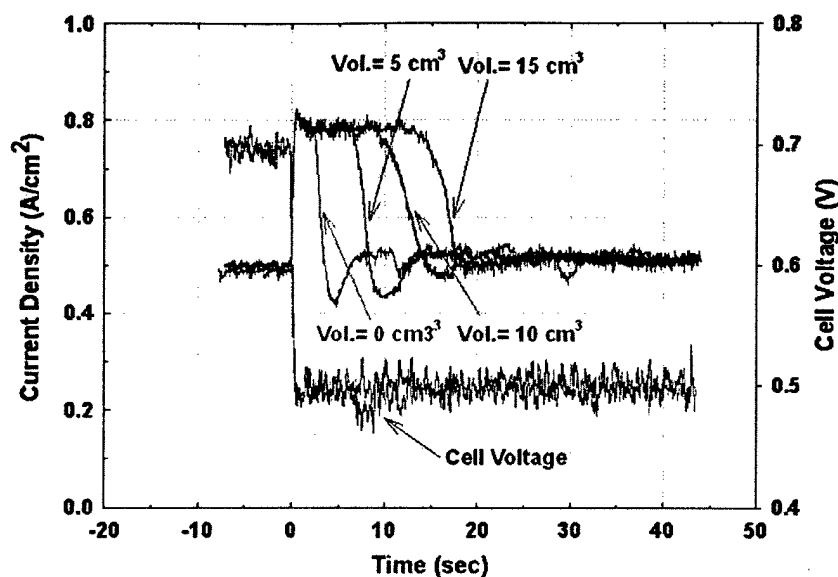


Fig. 7. Comparison of overshoot peak length and "undershoot" with three different volumes of 5, 10, and 15 cm<sup>3</sup> of reservoir tubes with half inches of outer diameter (inside diameter of 0.9525 cm).

ambient air also enters the cell enter because the boundary between hydrogen and ambient air is not clear at the end of the reservoir tube.

Fig. 7 shows the response for reservoirs with a bigger diameter tubes (i.e., the inner diameter is 0.95 cm for the 1/2" o.d. tube) for the same three volumes as in Fig. 6. As mentioned in the previous figure, the theoretical peak lengths shown in Table 4 are longer than those of actual experiment but this difference is more significant with the bigger diam-

eter of tubes. Again, this may be a result of deviations from plug flow and this deviation also explains the more pronounced "undershoot" with the larger diameter tubes. The peak is the same as that in Fig. 6, about 0.79 A/cm<sup>2</sup>. The value of the "undershoot" for the 5 cm<sup>3</sup> of reservoir tube is 0.43 A/cm<sup>2</sup>, for the 10 cm<sup>3</sup> of reservoir tube is 0.48 A/cm<sup>2</sup>, and for the 15 cm<sup>3</sup> the "undershoot" is barely observable in the figure. The values of "*U*<sub>0</sub>" corresponding to Fig. 1a are 0.09, 0.03, and 0 A/cm<sup>2</sup> for the 5, 10 and 15 cm<sup>3</sup> volumes.

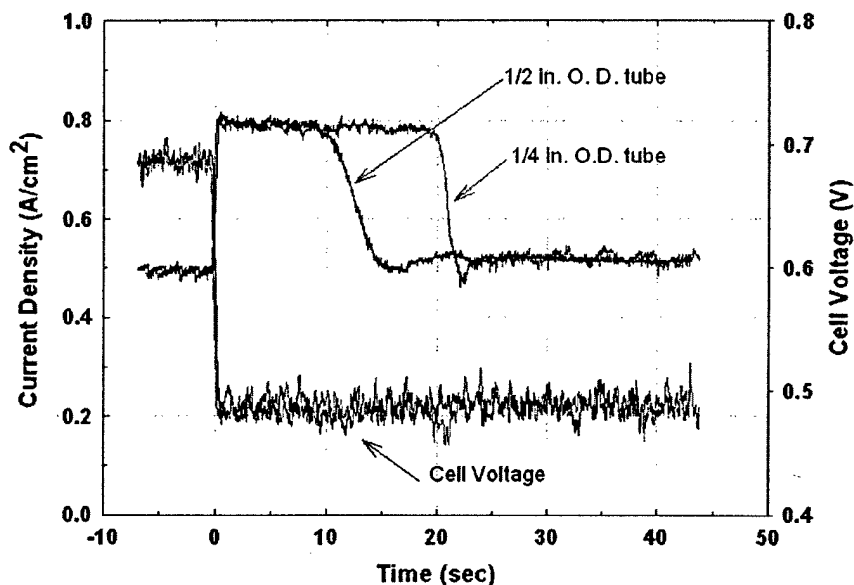


Fig. 8. Direct comparison of two different diameters of tubes, 1/4 and 1/2 in. o.d. with volume of 10 cm<sup>3</sup>.

The current density values of  $t = \infty$  approaches the same value,  $0.52 \text{ A/cm}^2$ , for all the cases. Fig. 8 compares the different diameters of reservoir tubes for the  $10 \text{ cm}^3$  volume. For the bigger tube diameter the undershoot/overshoot behavior is barely observable because the hydrogen/ambient air boundary is less defined at the end of large diameter reservoir tube. The initial exit flowrate of hydrogen in the reservoir tube is  $14.6 \text{ cm}^3/\text{min}$  at the cell voltage of  $0.7 \text{ V}$  and thus the velocity of hydrogen in the  $1/4 \text{ in. o.d.}$  tube is  $1.48 \text{ cm/s}$  while that of  $1/2 \text{ in.}$  is  $0.34 \text{ cm/s}$ . This significantly slower velocity allows ambient air to flow into the tube so that the volume of hydrogen that reenters the cell after a voltage change from  $0.7$  to  $0.5 \text{ V}$  is less than the size of the reservoir and this yields the shorter peak length for the larger diameter reservoir.

The response with a reservoir can be describe as a modified SO L/L system second-order plus dead time (SOPDT). The transfer function for this system is:

$$i(s) = \left[ K_2 + \frac{K_1}{\tau^2 s^2 + 2\xi\tau s + 1} e^{-\alpha s} \right] V(s) \quad (5)$$

The time domain function for this system can be described by the sum of two current densities,  $i_1$  and  $i_2$ , where  $i_2$  corresponds to the current density at the peak and during the peak length. Thus the peak length is modeled as a dead time  $\alpha$  and the time dependent current after the peak length,  $i_1$ , applies to times after the dead time. The fitted parameters for each diameter and volume are listed in Table 4. The transient responses of this system are determined by damping coefficient,  $\xi$ , and the dead time,  $\alpha$ . This SOPDT system explains the overshoot/undershoot behavior and peak length and it is an improvement to the analysis given in Reference [1]. Future work can now focus on a first principles description or model for damping coefficient,  $\xi$ , and the dead time,  $\alpha$ .

#### 4. Conclusions

Reservoir and dilution effects on dynamic behavior of a PEMFC fuel cell were studied at fixed flow rates of feed gases. The flowrates correspond to normal fuel and oxygen (air) utilization at the high cell voltage and a minimal operating condition at the low cell voltage. The results support the conclusion of our recent work [2] in that the increased velocity with diluted anode feed gas eliminates the “vacuum” effect and “undershoot” after overshoot behavior. Thus reformat fuel will yield less “undershoot” and less of a “vacuum” effect. The vacuum effect with neat hydrogen will provide local conditions of starvation due to a more non-uniform reaction rate during transient load changes. Also, the dilution effect affects the undershoot behavior in the current density recovery time when the initial voltage is  $0.7 \text{ V}$  (i.e., stoichiometry change from a ‘starved’ to a nor-

mal condition). The dilute fuel yields faster recovery time. We have shown that the volume of the reservoir influences the transient behavior of PEMFCs and thus, under proper design, the excess hydrogen in the manifold could serve the function of a capacitor and perhaps lower the need for a hybrid designs to handle the transient loads of the system. The ability to remove the battery/capacitor simplifies the system, may provide for increased reliability, and reduced cost.

The data also show that not just the volume of the reservoir but also the structure of the reservoir affects the transient behavior. The length and diameter of the reservoir affect the peak length as well as the undershoot after overshoot behavior. These ideas may lead one to better designs of flow fields so that the PEMFC can survive transient conditions. For example, changing the path length to the manifolds of fuel cell stack, may improve the response during unsteady operation.

#### Acknowledgements

Financial support by the South Carolina State University/University Transportation Center (Grant no. 2000–013), Department of Energy-EPSCoR (Cooperation Agreement DE-FG02-91ER75666), and Office of Naval Research, ONR (Grant no. N00014-98-1-0554) is gratefully acknowledged. The authors gratefully acknowledge that W.L. Gore & Associates Inc. supplied the MEAs used in this work.

#### References

- [1] S. Kim, S. Shimpalee, J.W. Van Zee, J. Power Sources (2004), in press.
- [2] S. Kim, S. Shimpalee, J.W. Van Zee, J. Electrochem. Soc. (2004), in press.
- [3] S. Shimpalee, W.-k. Lee, J.W. Van Zee, H. Naseri-Neshat, J. Fuel Cells (2002), in press.
- [4] S. Shimpalee, W.-k. Lee, J.W. Van Zee, Presented at the 2002 Meeting of the Electrochemical Society, Philadelphia, PA, May 2002, paper #1136.
- [5] J. Hamelin, K. Agbossou, A. Laperriere, F. Laurencelle, T.K. Bose, Int. J. Hydrogen Energy 26 (2001) 625–629.
- [6] J.C. Amphlett, E.H. De Oliveria, R.F. Mann, P.R. Roberge, A. Rodrigues, J.P. Salvador, J. Power Sources 65 (1997) 173–178.
- [7] B. Emonts, J. Bøgild Hansen, H. Schmidt, T. Grube, B. Hohlein, R. Peters, A. Tschauder, J. Power Sources 86 (2000) 228–236.
- [8] R. Kötz, S. Müller, M. Bärtschi, B. Schnyder, P. Dietrich, F.N. Büchi, A. Tsukada, G.G. Scherer, P. Rodatz, O. Garcia, P. Barrade, V. Hermann, R. Gallay, in: G. Nazri, et al. (Eds.), Advanced Batteries and Supercapacitors, ECS Proceeding Volume, PV 2001–21 (2001).
- [9] B.A. Ogunnaike, W.H. Ray, Process Dynamics, Modeling, and Control, Oxford, 1994, pp. 139–211.
- [10] W.-k. Lee, C. Ho, J.W. Van Zee, J. Power Sources 84 (1999) 45–51.
- [11] W.-k. Lee, Ph.D. dissertation, Department of Chemical Engineering, University of South Carolina, SC, 29208, 1999, pp. 16–21.

## Distribution List

Copies of this report have been mailed to the following addresses.

1 copy to:

Office of Naval Research  
Ballston Centre Tower One  
800 North Quincy Street  
Arlington, VA 22217-5660

1 copy to:

Office of Naval Research Regional Office Atlanta  
100 Alabama Street NW Suite 4R15  
Atlanta, GA 30303-3104

1 copy to:

Defense Technical Information Center  
8725 John J. Kingman Road Ste 0944  
Fort Belvoir, VA 22060-6218

1 copy to:

Naval Research Laboratory  
ATTN: Code 5227  
4555 Overlook Avenue SW  
Washington, DC 20375-5320

END OF REPORT